

Development of a Hierarchical Zinc Oxide Photocatalyst for the Removal of Emerging Contaminants from Water

Amir Mirzaei

A Thesis
In the Department
of
Building, Civil and Environmental Engineering

Presented in Partial Fulfillment of the Requirements
For the Degree of
Doctor of Philosophy (Civil Engineering) at
Concordia University
Montreal, Quebec, Canada

October 2018

© Amir Mirzaei, 2018

CONCORDIA UNIVERSITY
SCHOOL OF GRADUATE STUDIES

This is to certify that the thesis prepared

By: Amir Mirzaei

Entitled: Development of a Hierarchical Zinc Oxide Photocatalyst for the
Removal of Emerging Contaminants from Water

and submitted in partial fulfillment of the requirements for the degree of

Doctor Of Philosophy (Civil Engineering)

complies with the regulations of the University and meets the accepted standards with respect to originality and quality.

Signed by the final examining committee:

_____ Chair
Dr. Ion Stiharu

_____ External Examiner
Dr. Julian X.X. Zhu

_____ External to Program
Dr. Paula Wood-Adams

_____ Examiner
Dr. Fuzhan Nasiri

_____ Examiner
Dr. Catherine Mulligan

_____ Thesis Supervisor
Dr. Zhi Chen

_____ Thesis Co-Supervisor
Dr. Fariborz Haghighat

_____ Thesis Co-Supervisor
Dr. Laleh Yerushalmi

Approved by _____
Dr. Fariborz Haghighat, Graduate Program Director

November 29, 2018

Dr. Amir Asif, Dean
Gina Cody School of Engineering and Computer Science

Abstract

Development of a Hierarchical Zinc Oxide Photocatalyst for the Removal of Emerging Contaminants from Water

Amir Mirzaei, Ph.D.

Concordia University, 2018

The presence of emerging contaminants (ECs) such as antibiotics in water bodies has raised increasing concern since they are continuously introduced in aquatic ecosystem and may cause unpredictable environmental hazards and risks, even at trace concentrations. Conventional water treatment processes are known to be generally inadequate for the elimination of these persistent contaminants. As an alternative to conventional biological water treatment processes, photocatalytic degradation of antibiotics has been identified as a promising technique, as it may lead to the mineralization of contaminants into carbon dioxide, water and mineral acid. However, high energy consumption, fast recombination of photo-generated charges, low stability and difficulty in the separation of photocatalysts from treated solution are the main limitations of this process. Herein, to address these obstacles, a low energy consuming photoreactor was designed and built. Besides, the efficiency of process was improved by fluorination and exfoliation of synthesized hierarchical photocatalysts with magnetic properties based on ZnO and graphitic carbon nitride (g-C₃N₄) as a wide and narrow band gap photocatalyst, respectively. The synthesized photocatalysts were characterized by several characterization tests. The effect of operating parameters such as catalyst dosage, solution pH and airflow rate on the antibiotics removal efficiency and the optimization of process was studied by response surface methodology (RSM). Under the optimum conditions, the photocatalytic removal performance was examined in terms of sulfamethoxazole (SMX), ampicillin (AMP) and amoxicillin (AMX) removal and mineralization as well as detoxification of the solution and by-product formation. Moreover, the reaction kinetics, energy consumption, stability and reusability of photocatalysts were evaluated. Based on the LC-HR-MS/MS method, the formation of several by-products during the degradation of antibiotics was evaluated and a degradation pathway for SMX and AMX was proposed. The results showed that in

comparison with a 500 W visible lamp, using a UV lamp (10 W) was considerably more effective for AMX removal, its mineralization and detoxification of the solution. Compared to reported values in the literature, the removal efficiency, mineralization, detoxification and energy consumption for the removal of examined antibiotics were improved in this study.

ACKNOWLEDGMENT

First of all, I would like to express my truthful gratitude to my supervisors, Prof. Zhi Chen, Prof. Fariborz Haghighat and Dr. Laleh Yerushalmi, for their motivation, encouragement, inspiration and priceless support throughout my study. I am grateful for the valuable advice, both technical and personal, which they gave me during my study. They kept their office door open whenever I needed their precious advice and I continuously benefited from their wise guidance.

I am deeply grateful to Professor Peter Edwards, Dr. Tiancun Xiao and Dr. Sergio González-Cortés from Oxford University. They offered me an opportunity to use the resources and facilities of their research labs in the Department of Chemistry at Oxford University.

I am indebted to Mr. Luc Demers, Mr. Josef Hrib, and Ms. Hong Guan, the experienced technicians of the Department of Building, Civil & Environmental Engineering at Concordia University.

My very sincere thanks to Professor David Ménard and Dr. Djamel Seddaoui from Polytechnique Montreal who allowed me to use some of the facilities in their research Lab.

Finally, I would like to sincerely thank my thesis committee Prof. Julian Zhu, Prof. Paula Wood-Adams, Prof. Catherine Mulligan and Prof. Fuzhan Nasiri for their interest in my work and their valuable and constructive questions and insightful comments.

DEDICATION

To:

My beloved parents, Parviz and Zahra

For their unconditional love and support from the very first day and their warmest spiritual support in the toughest days of my life

My dearest love, Zahra

For her endless love, ongoing encouragement to follow my dreams, always being by my side, and her heartfelt assistance throughout all arisen hardships

My amazing siblings, Manizheh, Davoud and Fatemeh

For their continuous inspiration, endless love and unconditional support in my life.

TABLE OF CONTENTS

List of Figures.....	xi
List of Tables	xv
Nomenclature	xvi
1. Introduction	1
1.1. Background.....	1
1.2. Problem statement.....	2
1.3. Research objectives.....	3
1.4. Thesis outline	5
2. Literature Review	6
2.1. Introduction.....	6
2.2. Zinc oxide based photocatalytic degradation.....	7
2.2.1. ZnO structure	7
2.2.2. Mechanism of ZnO based photocatalysis	8
2.2.3. Strategies for modification of zinc oxide photocatalyst.....	9
2.2.3.1. Doping.....	9
2.2.3.2. Surface modification	10
2.2.3.3. Couple semiconductors	13
2.2.3.3.1. Fe ₃ O ₄ /ZnO.....	13
2.2.3.3.2. g-C ₃ N ₄ /ZnO.....	14
2.2.3.3.3. Magnetic g-C ₃ N ₄	15
2.2.3.3.4. Exfoliation of g-C ₃ N ₄	16
2.3. Impact of controlling parameters on photodegradation efficiency	17
2.3.1. Effect of photocatalyst loading	17
2.3.2. Effect of contaminant concentration	17
2.3.3. Effect of pH on photocatalytic efficiency	18
2.3.4. Effect of ion presence in water on photocatalytic efficiency	19
2.3.5. Effect of air bubbling into the solution on photocatalytic degradation.....	21
2.4. Method of ZnO synthesis.....	25
2.4.1. Hierarchical photocatalysts	26

2.4.1.1.	Strategies for fabrication of hierarchical photocatalysts	28
2.5.	Summary of literature review	29
3.	Methodology.....	30
3.1.	Experimental setup.....	31
3.2.	Experimental design.....	32
3.3.	Chemicals.....	33
3.4.	Synthesis of photocatalysts	34
3.4.1.	Surface fluorination of ZnO	34
3.4.2.	Zn(OH)F	34
3.4.3.	Fe ₃ O ₄ -ZnO@g-C ₃ N ₄	35
3.4.4.	Mesoporous Fe ₃ O ₄ @g-C ₃ N ₄	36
3.5.	Characterization of photocatalysts	37
3.6.	Performance evaluation.....	38
3.6.1.	Adsorption capacity	38
3.6.2.	Removal efficiency and reaction kinetics in photocatalysis	39
3.6.3.	By-product formation and degradation mechanism	39
3.6.4.	Toxicity assessment	40
3.6.5.	Durability and stability of photocatalysts	41
3.6.6.	Energy consumption	41
4.	Results and Discussion	43
4.1.	Photocatalytic degradation of SMX by surface fluorinated ZnO.....	43
4.1.1.	Experimental condition	43
4.1.2.	Results and discussion of photocatalytic removal of SMX by fluorinated ZnO.....	43
4.1.2.1.	Analysis of CCD	43
4.1.2.2.	Effect of operating parameters on removal efficiency of SMX	46
4.1.2.3.	Determination of optimal conditions	50
4.1.2.4.	Mechanism of SMX removal reaction	50
4.1.2.5.	COD removal	53
4.1.2.6.	Kinetics of reaction	54
4.1.2.7.	Stability of photocatalyst	55
4.1.2.8.	Energy consumption	57
4.1.2.9.	Toxicity assessment	58
4.1.3.	Conclusions and remarks related to the photocatalytic degradation of SMX by surface fluorinated ZnO.....	60

4.2.	Adsorption behavior of ZnO and Zn(OH)F	60
4.2.1.	Experimental condition	60
4.2.2.	Results and discussion	61
4.2.2.1.	Characterization of adsorbent/catalyst	61
4.2.2.2.	Hydrophobic behavior of adsorbent.....	66
4.2.2.3.	Equilibrium study.....	67
4.2.3.	Conclusions and remarks related to the adsorption behavior of ZnO and Zn(OH)F	69
4.3.	Catalytic performance of Zn(OH)F for the removal of AMP	70
4.3.1.	Experimental condition	70
4.3.2.	Results and discussion	70
4.3.2.1.	Removal of AMP by sonolysis and sonocatalysis by ZnO and Zn(OH)F	70
4.3.2.2.	Effect of operating parameters on the AMP sonocatalytic degradation rate.....	73
4.3.2.3.	COD and TOC removal	79
4.3.2.4.	By-product formation.....	80
4.3.2.5.	Toxicity assessment	82
4.3.2.6.	Stability of catalyst.....	84
4.3.3.	Conclusions and remarks related to the catalytic performance of Zn(OH)F for the removal of AMP.....	85
4.4.	Removal of SMX by Fe ₃ O ₄ @Zn-O@g-C ₃ N ₄	86
4.4.1.	Experimental condition	86
4.4.2.	Results and discussion	86
4.4.2.1.	Characterization of photocatalysts	86
4.4.2.2.	Optimization of photocatalysts	94
4.4.2.3.	Experimental design and data analysis	98
4.4.2.4.	Effect of operating parameters on the removal efficiency of SMX	100
4.4.2.5.	Kinetics of SMX removal	105
4.4.2.6.	COD and TOC removal	106
4.4.2.7.	Toxicity assessment	106
4.4.2.8.	Transformation pathway and by-product formation	108
4.4.2.9.	Stability of the synthesized catalyst	109
4.4.3.	Conclusions and remarks related to the removal of SMX by Fe ₃ O ₄ @ZnO@g-C ₃ N ₄	111
4.5.	Removal of AMX by magnetic fluorinated g-C ₃ N ₄ under UV and visible light.....	112
4.5.1.	Experimental condition	112
4.5.2.	Results and discussion	112
4.5.2.1.	Characterization of photocatalysts	112

4.5.2.2.	Photocatalytic performance and kinetics of contaminant removal	121
4.5.2.3.	Mechanism of reaction.....	123
4.5.2.4.	Identification of intermediates and AMX degradation pathway	125
4.5.2.5.	Mineralization	129
4.5.2.6.	Toxicity assessment	130
4.5.2.7.	Stability of photocatalyst	132
4.5.3.	Conclusions and remarks	134
5.	Conclusions and Recommendations	136
5.1.	Conclusions, remarks and contribution of research	137
5.2.	Recommendations for future work	139
	References.....	141
	Appendix A: Extracted ion chromatograms of SMX and its by-products.....	162

List of Figures

Figure 2.1. (a) Rocksalt, (b) zinc blende and (c) wurtzite structures model of ZnO (Lee et al. 2016).	8
Figure 2.2. General mechanism of the photocatalysis process (Lee et al. 2016).	9
Figure 2.3. Zeta potential of TiO ₂ particles in aqueous suspensions ([TiO ₂]=2 mg/L) as a function of pH and fluoride ion concentration (Park and Choi 2004).	11
Figure 2.4. The change of adsorption mode of Rhodamine B (RhB) on the surface fluorinated TiO ₂ (a) in comparison to that on pure TiO ₂ (b) (Wang et al. 2008b).	12
Figure 2.5. Changing the mechanism of reactions by surface fluorination of TiO ₂ (Yu et al. 2009).	13
Figure 2.6. Schematic synthesis process of g-C ₃ N ₄ through thermal polymerization of nitrogen-rich different precursors (Shen et al. 2018).	15
Figure 2.7. Distribution of published papers considering magnetic materials coupled with g-C ₃ N ₄ (Mousavi et al. 2018).	16
Figure 2.8. Schematic illustration of liquid-exfoliation process from bulk g-C ₃ N ₄ to ultrathin nanosheets (Dong et al. 2016).	16
Figure 2.9. Typical hierarchical structures of photocatalyst (Li et al. 2016) and significance of hierarchical nanostructures in enhancing photocatalysis.	27
Figure 2.10. Schematic illustration of the reflecting and scattering effects in interiors of cavities (A) and hierarchical microspheres (B) (Xiong et al. 2014).	27
Figure 2.11. Three-dimensional mesoporous architecture with a continuous and periodically porous network that offers transport routes for reactants to move in and out of the framework (Yu et al. 2004).	28
Figure 3.1. Schematic of designed photoreactor set-up (left), UVC lamp and protective sleeve (right).	31
Figure 3.2. (a) Photocatalytic set-up under UV light, (b) and visible light.	32
Figure 3.3. Central composite design for three operating parameters (Li et al. 2015).	33
Figure 3.4. The possible chemical structures of simple ligand exchange between F ⁻ and surface hydroxyl groups (Liu et al. 2012).	34
Figure 3.5. (a) crystalline structure of ZnO and (b) Zn(OH)F. black, red, purple and green color represent, zinc, oxygen, fluorine and hydrogen atoms, respectively.	35
Figure 3.6. Pressurized autoclave, the capacity of the Teflon-lined autoclave: 200 ml.	35
Figure 4.1. Correlation between the experimental and predicted photodegradation efficiencies of SMX.	45
Figure 4.2. Pareto graphic analysis for the photodegradation efficiency of SMX.	46
Figure 4.3. The response surface (A) and contour plots (B) of photocatalytic removal efficiency of SMX as the function of pH of solution and concentration of NH ₄ F (mM); the response surface (C) and contour plots (D) of photocatalytic removal efficiency of SMX as the function of catalyst dosage (g/L) and air flow rate (L/min); (reaction time = 30 min, temperature= 21 °C).	47
Figure 4.4. Variation of SMX dimensionless concentration with time in the presence and absence of scavengers; [SMX] ₀ = 1 mM, [catalysts]= 1.487 g/L, pH= 4.8, airflow rate= 2.5 L/min, ([F ⁻]=2.505 mM for F-ZnO), temperature= 21 °C, [TBA] =20 mM, [KI] ₀ =20 mM.	52
Figure 4.5 Time evolution of hydrogen peroxide concentration formed during the photocatalytic oxidation of sulfamethoxazole by ZnO and F-ZnO, [SMX] ₀ = 1 mM, [catalysts]= 1.487 g/L, pH= 4.8, airflow rate= 2.5 L/min, ([F ⁻]=2.505 mM for F-ZnO), temperature= 21 °C.	53
Figure 4.6. COD removal by photolysis, and photocatalysis by using ZnO, F-ZnO and TiO ₂ Degussa P25 after 20, 60 and 90 min; [SMX] ₀ = 1 mM, [catalysts]= 1.487 g/L, pH= 4.8, airflow rate= 2.5 L/min, ([F ⁻]=2.505 mM for F-ZnO), temperature= 21 °C.	54
Figure 4.7. Pseudo-first-order reaction rate of and first order initial rate constant of SMX removal; [SMX] ₀ = 1 mM, [catalysts]= 1.487 g/L, pH= 4.8, airflow rate= 2.5 L/min, ([F ⁻]=2.505 mM for F-ZnO), temperature= 20 °C, inset: reaction rate constants.	55

Figure 4.8. (A) Cycling photocatalytic tests by using F-ZnO, ZnO and TiO ₂ (P25), [SMX] ₀ = 1 mM, [catalysts]= 1.487 g/L, pH= 4.8, airflow rate= 2.5 L/min, ([NH ₄ F] =2.505 mM for F-ZnO), temperature= 20 °C; (B) Release of Zn ²⁺ ions into the solution in the presence of fluoride ions in various concentration.	56
Figure 4.9. Changes in toxicities (as measured by inhibition to E. coli bacteria) before treatment and after different stages of photocatalytic degradation of SMX by different photocatalysts.	59
Figure 4.10. The growth inhibition zone of E. coli bacteria against the SMX (right) and after 30 min treatment (left).	59
Figure 4.11. SEM images of (a-c) ZnO and (d-f) Zn(OH)F at different magnifications; (g) elemental mapping of Zn(OH)F.	61
Figure 4.12. (a) X-ray diffraction patterns, (b) FT-IR spectra, (c) N ₂ adsorption–desorption isotherm, (d) ultraviolet-visible diffuse reflectance spectra, (e) Tauc plots and (f) photoluminescence spectra of ZnO and ZF1 samples.	63
Figure 4.13. (a) XPS survey spectrum of ZnO and ZF1, (b) high-resolution XPS spectra of Zn, (c) F, and (d) O elements.	65
Figure 4.14. Zeta potentials (ζ) of suspended ZnO and ZF1 particles as a function of pH.	65
Figure 4.15. Removal percentage of anionic dyes (MB and AO7) by bare ZnO, FZ1; C _{0,dyes} =100 mg/L, adsorbent dosage= 5 mg/mL, pH (6.5) (not adjusted), temperature=20±1 °C, adsorption time = 30.	66
Figure 4.16. Relative water dispersibility of (A) Zn(OH)F and (B) ZnO.	66
Figure 4.17. Single-component adsorption of: (A) MB and (B) AO7 onto ZF1; adsorbent dosage= 5 mg/mL, pH (6.5) (not adjusted), temperature=20±1 °C. Lines represent adsorption models.	67
Figure 4.18. Removal ratio of AMP by different processes during 90 min treatment. Experimental conditions: [AMP] ₀ = 30 mg/L, pH = 7, [Catalyst] = 1 g/L, temperature = 26 ±2 °C and ultrasonic power = 100 W.	72
Figure 4.19. (a) Effect of ZF1 loading (pH=7, [AMP] ₀ = 30 mg/L), (b) pH of solution ([catalyst] ₀ = 1.5g/L, [AMP] ₀ = 30 mg/L), and (c) initial concentration of AMP ([catalyst] ₀ = 1.5 g/L, pH=5) on the rate of AMP removal in sonocatalytic process.	76
Figure 4.20. Effect of scavengers on the removal efficiency of AMP. Experimental conditions: [AMP] ₀ = 30 mg/L, [ZF1] = 1.5 g/L, pH=5, [scavenger] ₀ = 30 mg/L, reaction time = 90 min, temperature = 26 ±2 °C and ultrasonic power = 100 W.	79
Figure 4.21. TOC and COD removal during the sonocatalytic degradation of AMP. Experimental conditions: [AMP] ₀ = 30 mg/L, [ZF1] = 1.5 g/L, pH=5, temperature = 26 ±2 °C and ultrasonic power = 100 W.	80
Figure 4.22. LC-HR-MS/MS extracted-ion screening chromatograms of (a) ampicillin, [m/z=350.12], (b) ampicillin –CO, -H ₂ O, +O, [m/z=312.12], (c) ampicillin + H ₂ O, -CO ₂ , [m/z=324.14], (d) ampicillin + O ₂ , - COOH, [m/z=338.12], (e) ampicillin + O, -NH ₂ , -H, [m/z=349.09], (f) ampicillin + O, [m/z=366.11].	82
Figure 4.23. Changes in toxicities (as measured by the inhibition to E. coli bacteria) before treatment and after different stages of sonocatalytic degradation of AMP by ZF1 at the optimum condition.	83
Figure 4.24. Magnified images of the growth inhibition zone of AMP solution against E. coli bacteria before treatment and after 1 and 2h treatment by US/ZF1 process at the optimum condition.	83
Figure 4.25. (a) Reusability of the F-ZnO nanoparticles within four consecutive experimental runs. (b) Fluoride ion concentration into the solution. Experimental conditions: [AMP] ₀ = 30 mg/L, [F-ZnO] = 1.5 g/L, pH=5, temperature = 26 ±2 °C and ultrasonic power = 100 W.	84
Figure 4.26. (a) XRD spectra of Fe ₃ O ₄ , pristine ZnO, g-C ₃ N ₄ and FZG, inset: magnified XRD pattern of FZG and presence of g-C ₃ N ₄ and Fe ₃ O ₄ peaks; (b) Nitrogen adsorption/desorption isotherm of ZnO, g-C ₃ N ₄ and FZG; (c) pore size distribution of ZnO, g-C ₃ N ₄ and FZG; (d) DRS spectra of pristine ZnO, g-	

C ₃ N ₄ and FZG; (e) Tauc plot of pristine ZnO, g-C ₃ N ₄ and FZG; and (f) PL spectra of pristine ZnO, g-C ₃ N ₄ and FZG excited at 325 nm.....	88
Figure 4.27. FTIR spectra of ZnO, g-C ₃ N ₄ , Fe-ZnO and FZG1.	89
Figure 4.28. TGA curve of Fe-ZnO and FZG1.....	89
Figure 4.29. Zeta-potential of FZG as a function of pH value (Radjenovic and Petrovic 2017).....	90
Figure 4.30. SEM images of ZnO (a-c), Fe-ZnO (d-f) and FZG1 (g-i) in three different magnifications. .	91
Figure 4.31. EDS spectra of (a) ZnO, (b) Fe-ZnO and (c) FZG1.	92
Figure 4.32. (a), TEM images of Fe-ZnO, inset: HAADF-STEM imaging Fe-ZnO, (b), high resolution TEM image of Fe-ZnO sample, inset: SEAD pattern for Fe-ZnO, (c-d) TEM images of FZG1, inset: SEAD pattern for FZG1.....	93
Figure 4.33. Magnetization curves of Fe ₃ O ₄ -ZnO and FZG1.....	94
Figure 4.34. Photocatalytic degradation of SMX by photolysis and photocatalytic degradation by using ZnO, Fe ₃ O ₄ -ZnO, FZG0.5, FZG1, and FZG2, experimental condition:	95
Figure 4.35. Band positions diagram and charge carriers transfer between ZnO, g-C ₃ N ₄ and Fe ₃ O ₄	98
Figure 4.36. (a-b) 3D and contours surface plots of SMX degradation efficiency (%) for catalyst dosage vs pH, (c-d) catalyst dosage vs airflow rate.	101
Figure 4.37. Different forms of sulfamethoxazole (SMX) at various pH values (Radjenovic and Petrovic 2017).	102
Figure 4.38. (a) First-order kinetic plots for SMX removal by commercial ZnO and FZG in the absence and presence of anions; (b) first-order kinetic rate constants. Experimental condition: [SMX] ₀ = 30 mg/L, [catalyst] ₀ = 0.65 g/L, pH= 5.87, airflow rate=1.89 L/min, [scavenger] ₀ = 1 mM.	105
Figure 4.39. Degree of mineralization of SMX as COD and TOC removal; experimental condition: [SMX] ₀ = 30 mg/L, [catalyst] ₀ = 0.65 g/L, pH= 5.87, airflow rate =1.89 L/min.....	106
Figure 4.40. Changes in toxicity as the percentage inhibition of E. coli bacteria before and after the treatment of SMX solution by FZG under the optimum conditions.	107
Figure 4.41. Well-agar diffusion method and magnified images of wells after (a) 0 min, (b) 20 min, and (c) 60 min treatment.....	107
Figure 4.42. Evolution of major degradation products (DPs) with (a) high-peaks intensities and (b) low intensities in photocatalytic degradation of SMX under optimum conditions.....	109
Figure 4.43. Proposed degradation pathway of SMX by photocatalytic degradation by using FZG.	109
Figure 4.44 (a) Recyclability of FZG1 photocatalyst (five successive experiments) for the degradation of SMX, (b) release of zinc and iron ions into the solution as a function of time for Fe-ZnO and FZG1, experimental conditions: [SMX] ₀ = 30 mg/L catalyst dosage: 0.5 g/L, initial solution pH=7, air flow rate = 1.5 L/min.....	110
Figure 4.45. (a) XRD patterns, (b) FTIR spectra, (c) Nitrogen adsorption–desorption isotherms (inset: pore size distribution), (d) UV–vis diffuse reflectance spectra, (e) PL emission spectra, and (f) band gaps (E _g) of g-C ₃ N ₄ ,GF, FeGF1, FeGF2 and FeGF3	114
Figure 4.46. Magnified (002) peak of XRD pattern of g-C ₃ N ₄ and exfoliated g-C ₃ N ₄ (GF).....	115
Figure 4.47. XPS survey spectra (a), high-resolution XPS spectra of the C1s region (b), N1s region (c), Fe2p (d), F1s (e) and O1s region (f) of FeGF2.....	117
Figure 4.48. (a-c) SEM images of FeGF1, (d-f) FeGF2, (g-i) FeGF3, (i-l) Fe ₃ O ₄ samples at different magnifications, (m) elemental mapping of N, C, Fe, O and F of FeGF2.....	119
Figure 4.49. (a-c), TEM images of FeGF2 samples, (d) high angle annular dark field (HAADF) STEM image of FeGF2.	121
Figure 4.50. (a) Photocatalytic activity of photocatalysts for the degradation of AMX under UV and visible light, (b), apparent first-order rate constant; experimental condition: [AMX] ₀ = 0.25 mM, pH 7, [photocatalyst] ₀ = 1 g/L, [scavenger] ₀ = 2.5 mM airflow rate = 1.5 L/min.	123

Figure 4.51. Absorbance spectrum of AMX in water and the maximum emission wavelength of UVC lamp.	124
Figure 4.52. (a) Photographs of GF nanosheets after storage for 24 h and (b) bare g-C ₃ N ₄ nanosheets after storage for 30 min.	125
Figure 4.53. Species-trapping experiments for degradation of AMX by FeGF2 photocatalysts; experimental condition: [AMX] ₀ = 0.25 mM, pH 7, [photocatalyst]= 1 g/L, [scavenger] ₀ = 2.5 mM airflow rate = 1.5 L/min.	125
Figure 4.54. Schematic diagram of the proposed photocatalytic degradation mechanisms of AMX under UV light. The transformation products (TPs) marked with (*) were detected during UV/g-C ₃ N ₄ process and TPs marked with (**) were detected during UV/FeGF2 processes.	127
Figure 4.55. Presence of [m/z=189.06] fragment during hydroxylation.....	128
Figure 4.56. Presence of [m/z=155.015] fragment during the hydroxylation of TP 349.....	128
Figure 4.57. Evolution of transformation products (TP) with low (a) and high (b) peak intensities during the UV/g-C ₃ N ₄ process; and with low (c) and high (d) peak intensities during the UV/FeGF2 process..	129
Figure 4.58. (a) TOC removal during UV/g-C ₃ N ₄ and UV/FeGF2 and Vis/FeGF2 processes; evolution of nitrate and nitrite UV/g-C ₃ N ₄ and UV/FeGF2 processes.....	130
Figure 4.59. Evaluation of changes in the toxicity of AMX solution by using (a), petri dish (b), agar-well diffusion and (c) inhibition percentage (Toxtrac™ kit) in UV/g-C ₃ N ₄ , UV/FeGF2 and Vis/FeGF2 processes.	131
Figure 4.60. (a) Magnetization curves of Fe ₃ O ₄ and FeGF2, (b) repeated photocatalytic degradation of AMX by FeGF2 under UV irradiation, (c) fluoride ion leaching from FeGF2 structure during UV/FeGF2 process.	133
Figure 4.61. High-resolution XPS spectra of fresh and spent FeGF2 of (a) Fe2p and (b) F1s.....	134

List of Tables

Table 2.1. Photocatalytic degradation of pharmaceuticals by ZnO-based photocatalysts	21
Table 2.2. Photocatalytic degradation of endocrine disruptive compounds (EDCs) by ZnO-based photocatalysts.....	23
Table 4.1. Actual and coded levels of the independent parameters of the experimental design for SMX removal by using F-ZnO	43
Table 4.2. Four factors experimental design and observed and predicted values for the central composite design.	44
Table 4.3. Analysis of variances (ANOVA) for SMX removal.....	45
Table 4.4. Optimum operating conditions of the parameters of process.....	50
Table 4.5. Comparison of energy consumption for removal of SMX by photocatalytic removal under UV irradiation based on calculated E_{EO}	58
Table 4.6. Band gap parameters for single sonocatalysts	64
Table 4.7. Isotherm parameters, SSRE and R^2 values for MB and AO7 adsorption onto ZF1 in single-component adsorption.....	68
Table 4.8. By-products identified during the sonocatalytic degradation of AMP after 90 min reaction by US, US/ZnO and US/ZF1 processes.....	81
Table 4.9. Band gap parameters for single photocatalysts.....	88
Table 4.10. By-products identified during the photocatalytic degradation of SMX after 90 min reaction by UV/ZnO, UV/FZG0.5, UV/FZG1 and UV/FZG2 processes.....	96
Table 4.11. Ranges and levels of independent variables for SMX removal by using Fe_3O_4 -ZnO@g- C_3N_4	98
Table 4.12. Experimental design conditions and responses of each experimental run.	99
Table 4.13. ANOVA test for the response function Y.....	100
Table 4.14. Optimum values of operating conditions and comparison of experimental and predicted values for SMX removal under the optimal conditions ^a	103
Table 4.15. Comparison of reported efficiencies of removal and mineralization of SMX by photocatalytic process under UVC irradiation.	104

Nomenclature

AAS	atomic absorption spectroscopy
AOP	advanced oxidation process
AO7	acid orange 7
AMP	ampicillin
AMR	antimicrobial resistance
AMX	amoxicillin
ANOVA	analysis of variance
APS	average particle size
BET	Brunauer–Emmett–Teller
BJH	Barrett-Joyner-Halenda
BQ	benzoquinone
CB	conduction band
CCD	central composite design
CEC	contaminants of emerging concern
CFU	colony forming unit
CLX	cloxacillin
COD	chemical oxygen demand
CPX	ciprofloxacin
DBS	dynamic background subtraction
DIW	deionized water
DOC	dissolved organic compound
DP	degradation product
D-R	Dubinin-Radushkevich
e ⁻	electron
ECs	emerging contaminants
EDCs	endocrine disrupting compounds
EDS	energy dispersive spectroscopy
EDTA	ethylenediaminetetraacetic acid
EE ₀	electrical energy per order
EG	ethylene glycol
FeGF	Fluorinated Fe ₃ O ₄ -g-C ₃ N ₄
FTIR	fourier-transform infrared spectroscopy
FZG	Fe ₃ O ₄ -ZnO@g-C ₃ N ₄
GPD	global domestic product
h ⁺	hole
HAADF	high-angle annular dark-field
HP	high pressure
HR	high resolution

IDA	information dependent acquisition
IUPAC	International Union of Pure and Applied Chemistry
LC	liquid chromatography
LP	low pressure
MB	methyl blue
MMT	montmorillonite
N.D.	not detected
PCO	photocatalytic oxidation
PFCs	polyfluorinated compounds
PL	photoluminescent
QqTOF	quadrupole-quadrupole-time-of-flight
RhB	rhodamine B
ROS	reactive oxygen species
RSM	response surface methodology
SAED	selected area electron diffraction
SEM	scanning electron microscopy
SMX	sulfamethoxazole
TBA	<i>tert</i> butyl alcohol
TEM	transmission electron microscopy
TGA	thermal gravimetric analysis
TP	transformation products
US	ultrasound
UV	ultraviolet
VB	valence band
Vis	visible
VLD	visible light driven
VSM	vibrating sample magnetometer
WWTP	water and wastewater treatment plant
XIC	extracted ion chromatogram
XPS	X-ray photoelectron spectroscopy
XRD	X-ray powder diffraction
ZPC	zero point charge

1. Introduction

1.1. Background

The presence of “emerging contaminants” (ECs) or “contaminants of emerging concern” (CEC) such as pharmaceuticals in natural waters has raised increasing concern due to their frequent appearance as a result of their continuous input in the aquatic media and persistence in the aquatic ecosystem (Mirzaei et al. 2016, Yuan et al. 2013). Emerging contaminants such as pharmaceuticals appear in the water and wastewater treatment plants mainly through excretion and/or improper disposal of outdated or unused medication (Boix et al. 2016). These pollutants are labeled as “emerging contaminants” since they have recently been detected due to the rapid development of new analytical techniques (Terzić et al. 2008). For instance, the flame retardant compounds are very toxic and were dispersed in the environment due to a strong industrial use from 1929. However, in Canada, a regulation was first set in 2006 for these compounds (Sauvé and Desrosiers 2014).

The presence of pharmaceuticals in water bodies has raised concerns since they are potentially toxic to aquatic organisms even at trace concentrations (ng/L or µg/L) (Yuan et al. 2013). Besides, some pharmaceuticals exhibit non-target effects as well as mixture toxicity in the environment. This means that pharmaceuticals have the potential to show specific effects, which are irrelevant to their therapeutic purposes (Catalá et al. 2015, Escher et al. 2006). Specifically, the presence of antibiotics in the environment is a matter of concern due to their frequent detection, low biodegradability and their potential to induce antimicrobial resistance (AMR) even at trace concentrations (Gong and Chu 2018). As a result of AMR, even simple infections and minor injuries can kill humans, which is a very real possibility for this century. AMR develops when microorganisms such as bacteria, viruses, parasites and fungi no longer respond to pharmaceutical, as they either mutate or acquire genetic information from other microorganisms to develop resistance. It is predicted that AMR will cause up to 10 million deaths per year by 2050, which is more than cancer, and will cause a loss of US\$100 trillion from global GDP (Sugden et al. 2016)

Unfortunately, most antibiotics persist in the environment mainly because of their recalcitrance and low biodegradability since these pharmaceuticals have been designed to resist

biodegradation (Sin et al. 2013). Therefore, wastewaters containing pharmaceuticals should be effectively treated prior to their discharge into the surface waters.

1.2. Problem statement

Antibiotics are widely used for both human and veterinary medicine to prevent or treat diseases. However, antibiotics are poorly metabolized in the body and most of them are excreted via urine or feces (Zhang et al. 2018). Due to seasonal variation of the water and waste water treatment plants (WWTPs) performance and variability of antibiotic concentrations and different characteristics of antibiotics, a diverse range of removal efficiency from ~0% for enrofloxacin (Watkinson et al. 2007) to 85% for sulfamethoxazole (Zhou et al. 2013a) is reported in the literature by using conventional biological treatment. In most cases, due to the poor removal of antibiotics in conventional water treatment systems, these chemical compounds end up in soil, surface waters or even in drinking water (Hu et al. 2011, Krzeminski et al. 2019, Matamoros et al. 2012, Mompelat et al. 2009, Veloutsou et al. 2014).

Photocatalytic degradation method may be considered as an alternative to this problem due to the relatively low cost and possible operation at ambient temperature and natural pH (Mirzaei et al. 2016, Yuan et al. 2013). Various types of photocatalysts such as titanium dioxide (TiO_2), zinc oxide (ZnO), iron (III) oxide (Fe_2O_3), vanadium (V) oxide (V_2O_5), and tungsten trioxide (WO_3) have been used in water and wastewater treatment operations (Kudo and Miseki 2009). However, none of the abovementioned photocatalysts completely satisfies all requirements such as the lack of toxicity and safety, long lifetime of photo-generated electron-hole pairs, low cost, ability of utilization of solar light energy and high efficiency and stability, which significantly hinder their practical applications. The high recombination rate of photo-induced charge significantly reduces the removal efficiency of contaminants and may lead to the generation of by-products which are sometimes more toxic than the parent compounds (Ballesteros Martín et al. 2008, Oller et al. 2011, Prieto-Rodríguez et al. 2013, Veloutsou et al. 2014). In addition, the high energy consumption during photocatalytic oxidation is considered as a major obstacle to the commercial application of photocatalysis (Chi et al. 2013, Nakada et al. 2007).

Among photocatalysts, TiO_2 and ZnO are the most frequently used materials for photocatalytic processes in water treatment operations (Samadi et al. 2016). However, the higher removal efficiency of ZnO compared to TiO_2 under certain operating conditions has been

reported in several studies (Elmolla and Chaudhuri 2010a, Hariharan 2006, Kansal et al. 2007, Li et al. 2010, Liu and Gao 2014, Palominos et al. 2009, Pardeshi and Patil 2008, Pare et al. 2008, Patil et al. 2010, Sin et al. 2013, Wu 2004, Zhao et al. 2012). The main limitations of ZnO photocatalysts are the low quantum efficiency because of high recombination of the photo-generated electron-hole pairs (Ba-Abbad et al. 2013) and photocorrosion (Liu et al. 2011). The photocorrosion of ZnO in aqueous solution under UV irradiation limits its application as an efficient photocatalyst in wastewater treatment operations (Lee et al. 2016). Moreover, photocatalyst separation and recovery from solution after treatment is a real hindrance to the application of photocatalysis process. In summary, photocatalytic degradation process is facing the following challenges:

- 1) High energy consumption of process
- 2) Low quantum yield of photocatalyst
- 3) Low stability of photocatalyst
- 4) Separation and recovery of photocatalysts particles from solution after treatment

1.3. Research objectives

Based on the above-mentioned problems, the modification of ZnO photocatalyst to enhance its efficiencies for the effective removal of antibiotics from water is a promising approach. So far, numerous modifying strategies have been proposed for the preparation of highly efficient photocatalysts (Li et al. 2016). However, most efforts have focused on narrowing the band gap of semiconductors by introducing dopant(s) into the semiconductor structure in order to harvest visible light instead of UV light. Utilizing visible light instead of UV light can be considered as a sustainable approach and reduces the energy cost (Mirzaei et al. 2016). However, replacing UV light with visible light usually needs an exorbitant area footprint. It is reported about 2.6 m² of solar exposure would be needed to achieve the treatment power of one 1000W UV lamp with 40% efficiency (Cates 2017). Moreover, from thermodynamic viewpoint, narrowing the band gap of semiconductors leads to the reduction of oxidation and reduction potential (Li et al. 2016). Therefore, incomplete mineralization of antibiotics due to the low redox potential may lead to the formation of additional toxic chemicals (Catalá et al. 2015, Escher et al. 2006). Therefore, improving the efficiency of photocatalysts under UV light will not only decrease the operating

costs, but it may also advance the disinfection process and further reduce the operating cost by process intensification.

Besides the band gap, the overall photocatalytic performance of semiconductors can be significantly influenced by their adsorption capacity, surface/interface morphology and crystallinity of the materials (Li et al. 2016). Based on the existing limitations of photocatalysis process, the following objective is specifically considered as the main objectives of this research:

- **Development of a novel hierarchical zinc oxide photocatalyst with magnetic properties for effective removal of antibiotics with low energy consumption.**

In order to achieve this objective, the following tasks are followed:

- ✓ Design and build an annular photoreactor by using a low energy consuming UV lamp.
- ✓ Modify the surface of photocatalysts by surface fluorination for enhancing the adsorption capacity and quantum yields.
- ✓ Synthesize hierarchical photocatalysts for enhancing quantum yields and specific surface area.
- ✓ Synthesize photocatalysts with magnetic characteristics for improving separation ability and recovery of photocatalysts in consecutive runs.
- ✓ Synthesize composite photocatalysts with a protective layer to reduce photocorrosion, which is the main drawback of ZnO-based photocatalysts.
- ✓ Synthesize a visible-driven photocatalyst in an effort to evaluate the effect of light type on the performance of photocatalyst.
- ✓ Optimize operating parameters of photocatalytic method for increasing the degradation and mineralization efficiencies of antibiotics.

1.4. Thesis outline

Chapter 1 presents a brief introduction, problem statements, and the objectives of this study. Chapter 2 reviews the previous investigations for pharmaceuticals removal and the mechanism of photocatalysis process with focus on ZnO-based photocatalyst, and discusses the necessary background for developing the proposed methodology. In addition, Chapter 2 provides a literature review focusing on the limitations ZnO-based photocatalysts. Chapter 3 discusses the methodology of this research, including experimental setup and apparatus design, materials and chemicals, including the examined antibiotics, synthesizing and characterization facilities, removal efficiency criteria and analytical methods. The experimental design and key operating parameters are also identified in this chapter. The major findings of the present research for removal of (sulfamethoxazole) SMX, (ampicillin) AMP and (amoxicillin) AMX antibiotics are presented and discussed in Chapter 4. At the end, Chapter 5 presents the concluding remarks and contributions of the thesis and makes recommendations for future development of the present study.

2. Literature Review

2.1. Introduction

Since penicillin was discovered by Fleming (1944), antibiotics have been extensively produced, consumed and used to treat bacterial diseases worldwide (Wang et al. 2019). However, after a short residence time in body, a large portion of antibiotics is excreted as metabolized or partially metabolized (Ikehata et al. 2006). Such behavior and extensive use for both human and veterinary medicine, resulted the presence of high levels of antibiotic residues in water and wastewater treatment effluents (Cheng et al. 2018). The presence of these contaminants in water poses a serious environmental threat due to their adverse effects on the environment and the human health (Tijani et al. 2013). The continuous introduction of antibiotics and their metabolites into the natural aquatic increases the number of antibiotic resistant bacteria, which is an important public health concern (Gao et al. 2018, Su et al. 2016). It is expected that a continued rise in antibiotic resistant bacteria by 2050 would kill people more than cancer by 10 million individuals every year (Sugden et al. 2016). Different treatment techniques can be applied to remove organic compounds from the effluents. Physical-chemical processes such as filtration (Shamsuddin et al. 2015) and reverse osmosis (Dolar et al. 2012) are unable to destroy contaminants and only transfer the pollutants from one phase to another (Elmolla and Chaudhuri 2010a). Biological treatment processes, commonly used in wastewater treatment plants, are usually inefficient in the removal of toxic and refractory organic contaminants such as antibiotics (Kansal et al. 2007, Pardeshi and Patil 2008, Qamar and Muneer 2009). Hence, the development of reliable, efficient and economical methods for the elimination of antibiotics in the aquatic environment is urgently needed. Advanced oxidation processes (AOPs) such as ozonation, O₃/UV, H₂O₂/UV and photocatalytic degradation processes potentially can eliminate ECs without producing secondary waste in the environment (Shemer et al. 2006, Vogna et al. 2004). Among them, photocatalytic degradation process has been shown to be a promising technique due to its non-toxicity, lack of mass transfer limitation, and possible operation at ambient temperature (Elmolla and Chaudhuri 2010a, Hariharan 2006).

2.2. Zinc oxide based photocatalytic degradation

Among different type of AOPs, undoubtedly, photocatalytic degradation process is a promising approach for the removal of toxic and recalcitrant contaminants such as pharmaceuticals and antibiotics. TiO₂ and ZnO and are among the most widely used photocatalysts for degradation of antibiotics in water due to their non-toxicity, chemical inertness, and low cost (Kanakaraju et al. 2015, Mirzaei et al. 2016, 2018a, Zhang et al. 2013). Since ZnO and TiO₂ have nearly the same band gap energy, their photocatalytic performances are anticipated to be similar (Lee et al. 2016, Peng et al. 2006). However, the difference in the morphology, charge-transfer dynamics and surface interactions can influence the performance of semiconductors (Hariharan 2006, Kamat et al. 2002). Due to certain intrinsic characteristics such as high electron mobility (about 10-100 times more than TiO₂) and higher quantum yield, ZnO can be considered as an effective photocatalyst and a suitable alternative to TiO₂ (Kansal et al. 2007, Kumar and Rao 2015, Li et al. 2014, Mai et al. 2008, Yu et al. 2016). The higher removal efficiency of ZnO compared to TiO₂ under certain operating conditions is reported in several studies (Elmolla and Chaudhuri 2010a, Hariharan 2006, Kansal et al. 2007, Li et al. 2010, Liu and Gao 2014, Palominos et al. 2009, Pardeshi and Patil 2008, Pare et al. 2008, Patil et al. 2010, Sin et al. 2013, Wu 2004, Zhao et al. 2012). Elmolla and Chaudhuri (2010a) showed that under optimized operating conditions, UV/ZnO process is considerably more effective than UV/TiO₂ for the removal of pharmaceuticals and chemical oxygen demand (COD) and for (dissolved organic carbon) DOC reduction.

2.2.1. ZnO structure

ZnO as a wide band-gap (3.2 eV) semiconductor is a promising candidate in industrial applications and environmental engineering due to its unique characteristics such as low cost, strong oxidation ability, good photocatalytic property, and insolubility in water. ZnO has three well-defined crystal structures namely, rocksalt, zinc blende and wurtzite as shown in Fig. 2.1. Among the three structures, wurtzite with a hexagonal structure has the highest thermodynamic stability and is the most commonly used structure (Wang 2004).

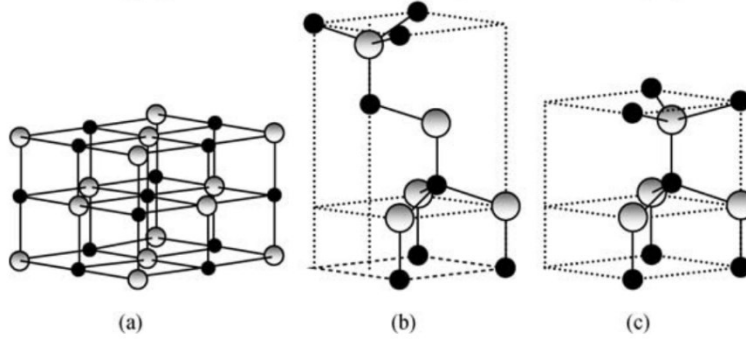
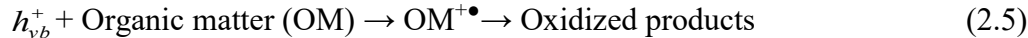


Figure 2.1. (a) Rocksalt, (b) zinc blende and (c) wurtzite structures model of ZnO (Lee et al. 2016).

2.2.2. Mechanism of ZnO based photocatalysis

The mechanism of photocatalysis process under UV irradiation is based on the excitation of a semiconductor by irradiation of photons with an equal or higher amount of energy than its band gap (Fig. 2.2). Under this condition, the electrons of valence band (VB) advance to the conduction band (CB) energy level to generate electron-hole pairs and reactive oxygen species (ROS) (Gaya and Abdullah 2008) (Eqs. 2.1-2.5).



The generated pairs of electron/holes can directly react with organic matter (Eq. 2.5) or indirectly by producing free radicals (Eqs. 2.2 -2.4) (Chong et al. 2010). Under optimized operating conditions, the organic contaminants can be totally mineralized to carbon dioxide, water and non-toxic anions. However, in some cases, total mineralization does not occur and the contaminants are converted to by-products. The main limitation of ZnO photocatalysts are the fast recombination of photo-generated charges (Ba-Abbad et al. 2013) and photocorrosion (Lee et al. 2016). Therefore, modification of the ZnO structure for enhancing its efficiency and

stability is urgently needed. If these improvements are achieved, ZnO can represent an effective photocatalyst for environmental applications.

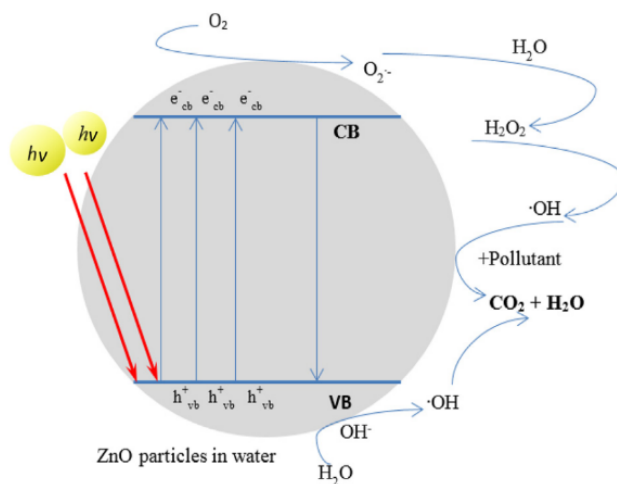


Figure 2.2. General mechanism of the photocatalysis process (Lee et al. 2016).

2.2.3. Strategies for modification of zinc oxide photocatalyst

2.2.3.1. Doping

It is worth mentioning that the rapid recombination of generated electron/holes in a photocatalyst considerably limits its application. A novel, effective and practical approach to enhancing the photocatalytic activity of ZnO is doping some elements for inter-particle electron transfer, since the chemical properties of materials, their atoms and the bonds between them considerably alter photocatalyst characteristics including the interfacial electron-transfer rate, charge carrier and recombination rate (Mirzaei et al. 2016). It is stated that the doping of a cation with a valence lower than that of the parent cation in the semiconductor (such as Na, K, etc. in ZnO) produces abundant oxygen vacancies (Takata and Domen 2009). Benhebal et al. (2012) reported that Na-doped and Li-doped ZnO produced higher efficiencies of phenol photodegradation.

Doping with inorganic elements such as sulfur improves optical, electrical, and photocatalytic activities of ZnO, due to the large electronegativity and size difference between sulfur and oxygen. Patil et al. (2010) reported that the COD removal efficiency by using S-doped ZnO was almost two times higher compared with the bare ZnO under solar irradiation. Doping

can also shift the absorption edge of photocatalyst from UV region to visible light region by narrowing the band gap of semiconductor. Chen and Liu (2016) reported that tetracycline was totally removed after 90 minutes of reaction under xenon lamp as a source of visible light by nitrogen-doped TiO₂. However, dopant modification needs accurate control and experiment to evaluate the optimum amount of dopant. This occurs because the addition of dopant higher than the optimum value can act as recombination center and promote the recombination of electron and hole (Lee et al. 2016). In addition, using high concentrations of metals doped onto the catalyst surface will reduce the available active sites of ZnO for the absorption of light and adsorption of pollutants, deteriorating the catalytic efficiency of the semiconductor (Arabatzis et al. 2003). To achieve the photocatalytic removal of a pollutant, the photo-induced electron/hole (e^-/h^+) on the surface of a photocatalyst should have an appropriate reduction and oxidation ability to generate free radicals ($O_2^{\bullet-}$, OH^{\bullet} , etc.). Any effort to narrow the band gap of semiconductor leads to reducing the redox and oxidation potential of semiconductor and the efficiency of mineralization (Li et al. 2016). For instance, from thermodynamic point of view, standard oxidation potentials required for the production of hydroxyl radicals based on Eq. (2.4) is 2.69 eV (Li et al. 2016). Therefore, by reducing oxidation potential lower than 2.69 eV by narrowing the band gap, the generation of OH^{\bullet} radicals as a strong reactive species will be limited. Generally, complete mineralization is more desirable than the elimination of specific target contaminants. This is important since a complete removal of total organic carbon (TOC) will ensure the complete mineralization of contaminants and potential intermediate compounds, and their transformation into CO₂ and H₂O. The by-products produced during the degradation of pharmaceuticals are sometimes more toxic than the parent compounds (Mirzaei et al. 2018c). Surface modification as an alternative strategy can be performed in order to slow down the recombination rate and enhance the photocatalytic removal efficiency without changing the band gap.

2.2.3.2. Surface modification

The performance of semiconductors as photocatalyst for the removal of aquatic contaminants is strongly dependent on the type of contaminant and surface interactions, kind of reactive oxygen species, charge transfer efficiency and recombination rate of the photo-induced electron and holes (Ryu et al. 2017). Among various surface modification methods, the surface

fluorination of semiconductors has recently attracted much attention as it is highly efficient, simple, and inexpensive to perform (Chen et al. 2009).

Effect of surface fluorination

Generally, surface fluorination does not greatly affect the structure and optical characteristics of semiconductors. In contrast, it significantly modifies the surface characteristics such as acidity, surface charge, polarity, etc., which influence the adsorption of reactants, surface charge separation and transfer, production of active radical species, and thus surface photocatalytic reaction kinetics and mechanism (Liu et al. 2012, Minero et al. 2000). For instance, the presence of fluoride ions leads to a more negatively charged surface, and reduces the zero point charge (ZPC) of surface. Therefore, the adsorption of the positively charged organic pollutants is usually favored by surface fluorination, while adsorption of negatively charged organic pollutant is normally inhibited (Kim et al. 2010). Notably, the surface fluorination process and the resulting surface properties of photocatalyst are affected by the pH value. Therefore, the adsorption behavior on fluorinated photocatalyst surface is also pH dependent (Liu et al. 2012). Fig. 2.3 illustrates the effects of surface fluorination on zeta potential of TiO₂ particles.

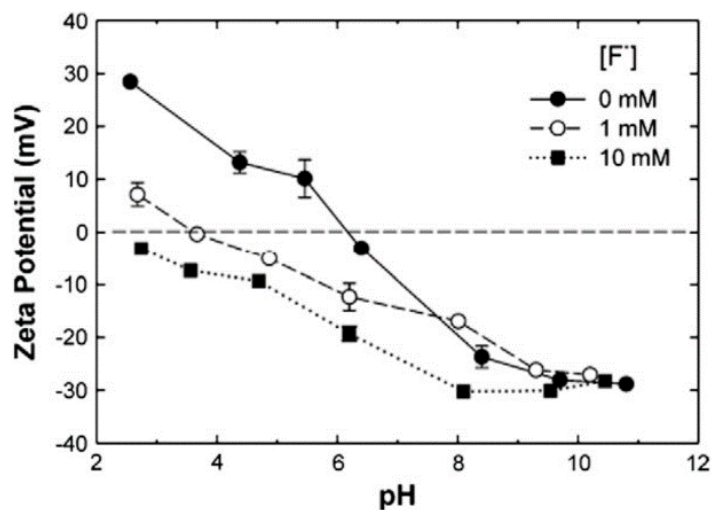


Figure 2.3. Zeta potential of TiO₂ particles in aqueous suspensions ([TiO₂]=2 mg/L) as a function of pH and fluoride ion concentration (Park and Choi 2004).

Beside adsorption capacities, surface fluorination of photocatalyst may significantly alter the adsorption capacities and modes of adsorption of molecules. Wang et al. (2008b) demonstrated

that the adsorption mode of RhB dye on bare TiO₂ was changed from carboxylic (-COOH) group to the cationic moiety (-NEt₂ group) by surface fluorination (see Fig. 2.4).

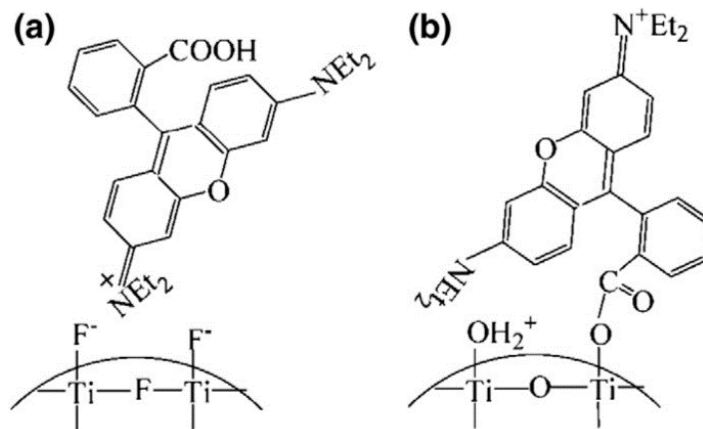
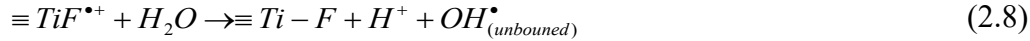


Figure 2.4. The change of adsorption mode of Rhodamine B (RhB) on the surface fluorinated TiO₂ (a) in comparison to that on pure TiO₂ (b) (Wang et al. 2008b).

Normally, the photocatalytic reactions occur on the surface of photocatalysts. Therefore, the change of adsorption capacity may considerably change the photocatalytic reaction efficiency. Generally, a higher adsorption capacity leads to a higher photocatalytic activity. This happens because the adsorbed molecules on the surface of photocatalyst can be oxidized directly by photo-induced holes (Eq. 2.5). In addition, the adsorbed molecules may react more efficiently with photo-generated short-living hydroxyl radicals, which are mostly bound on the photocatalysts surface and may be rapidly transformed to inactive surface -OH group (Liu et al. 2010). The modification of TiO₂ surface with fluoride anions and generation Ti-F bounds also enhances UV light photocatalytic activity due to the formation of mobile free OH• radicals (Eqs. 2.6-2.8), while most hydroxyl radicals generated on pure TiO₂ surface prefer to remain adsorbed (Eq. 2.9) (Xing et al. 2012).





The unbounded radicals not only possess higher oxidation potential than adsorbed radicals (2.3 eV vs 1.7 eV) but also they are more reactive due to the facile homogeneous photocatalytic reactions (Xu et al. 2007). As shown in Fig. (2.5), electron storage in the surface fluorinated moiety retards electron transfer to dissolve oxygen. As a result, surface fluorination inhibits recombination of photo-induced electron and hole which significantly facilitates the interfacial hole transfer and production of hydroxyl radicals.

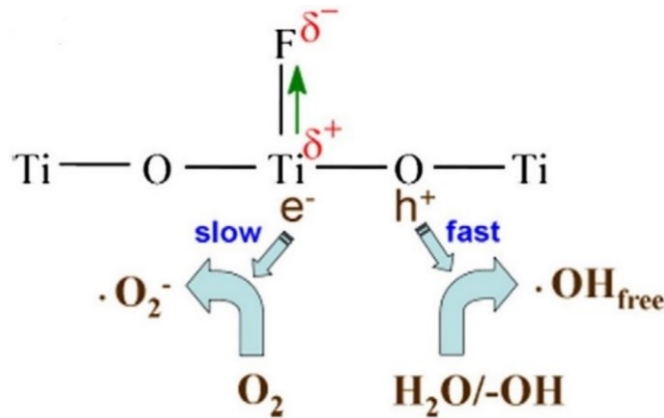


Figure 2.5. Changing the mechanism of reactions by surface fluorination of TiO_2 (Yu et al. 2009).

In summary, the modification of semiconductors' surface to achieve synergistic effects of adsorption and photodegradation is an effective way to promote the performance of photocatalysts.

2.2.3.3. Couple semiconductors

2.2.3.3.1. $\text{Fe}_3\text{O}_4/\text{ZnO}$

It is proven that coupling semiconductors with different band gap value or band gap position would increase the separation of charge carriers which enhances the lifetime of electron and hole (Serpone et al. 1995). For instance, coupling Fe_3O_4 as a narrow band gap (2.2 eV) with ZnO as a wide band gap semiconductor (3.2 eV) not only can improve the photocatalytic activity of composites, but it also facilitates the separation of particles from solution after treatment as the

result of magnetic properties (Feng et al. 2014, Hong et al. 2008, Xia et al. 2011). Feng et al. (2014) reported that the hybrid Fe₃O₄/ZnO nanocomposite enhanced the phenol degradation efficiency from 52% for pure ZnO to of 82.3%. Hong et al. (2008) successfully used Fe₃O₄/ZnO nanocomposite in four repeated cycles by using a magnet for speeding up the sedimentation of magnetic photocatalyst.

2.2.3.3.2. g-C₃N₄/ZnO

After reporting the photocatalytic activity of graphitic carbon nitride (g-C₃N₄) by Wang et al. (2009c), many studies have considered g-C₃N₄ either as a standalone photocatalyst ((Ding et al. 2017) and references therein) or as a heterojunction with other semiconductors ((Huang et al. 2018) and references therein). Graphitic carbon nitride, as a metal-free semiconductor, has gained remarkable acceptance as a visible-light-driven (VLD) photocatalyst due to its high chemical stability, response to visible-light and environmentally benign character (Dong et al. 2015, Hao et al. 2016, Papailias et al. 2018). Moreover, g-C₃N₄ can be easily synthesized by thermal polymerization of inexpensive nitrogen-rich precursors such as urea, melamine, dicyandiamide, thiourea and cyanamide (Fig. (2.6)) (Shen et al. 2018).

In particular, g-C₃N₄ with nanosheet structure reduces perpendicular migration distance of photo-induced charge carriers from the bulk to the surface and accelerates electrons transport along the in-plane direction (Ou et al. 2017). However, low charge mobility, low specific surface area, as well as high recombination rate of electrons and holes restrict g-C₃N₄ applications as a stand-alone photocatalyst (Mirzaei et al. 2018b, Zhou et al. 2017). Furthermore, with nanosheet structure, its separation from the solution after photocatalytic process is difficult. Therefore, different strategies such as preparation of mesoporous g-C₃N₄ (Hao et al. 2016), exfoliation (Dong et al. 2015), coupling with other materials (Mirzaei et al. 2018a, Zhou et al. 2017) and preparation of magnetic g-C₃N₄ ((Mousavi et al. 2018) and references therein) have been applied to improve the photocatalytic performance of g-C₃N₄. Despite the beneficial effects of hybrid photocatalysts, the poor attachment of the produced composites restricts the charge carriers transfer between heterojunction interfaces and reduces the stability of the resultant photocatalysts (Chen et al. 2016, Pan et al. 2012). Therefore, the design of an efficient conjugated composite of semiconductors and g-C₃N₄ remains a challenge (Chalasanani and Vasudevan 2013, Qin et al. 2016).

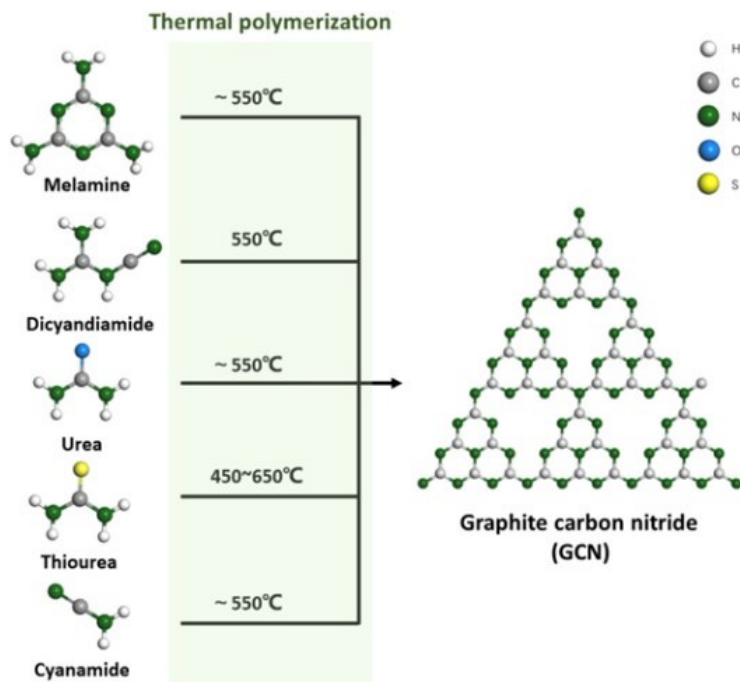


Figure 2.6. Schematic synthesis process of $g\text{-C}_3\text{N}_4$ through thermal polymerization of nitrogen-rich different precursors (Shen et al. 2018).

2.2.3.3.3. *Magnetic $g\text{-C}_3\text{N}_4$*

Among different modification methods, the introduction of a magnetic material over the $g\text{-C}_3\text{N}_4$ nanosheets is promising since the separation of particles from solution would be facilitated via this method (Mousavi et al. 2018). In addition, the coupling of a magnetic component would synergistically improve the photocatalytic activity by developing a heterojunction between the $g\text{-C}_3\text{N}_4$ and the magnetic material and will increase the separation of the electron and hole pairs (Abazari et al. 2016). Hematite ($\alpha\text{-Fe}_2\text{O}_3$), maghemite ($\gamma\text{-Fe}_2\text{O}_3$), magnetite (Fe_3O_4), and metal ferrites (MFe_2O_4) with magnetic properties have been widely used for synthesizing magnetic $g\text{-C}_3\text{N}_4$ (Mousavi et al. 2018). However, Fe_3O_4 owing to its super-magnetic properties is the most studied magnetic material coupled with $g\text{-C}_3\text{N}_4$ (Mousavi et al. 2018) (see Fig. 2.7). Zhou et al. (2013b) reported three times higher methyl orange removal by using 2% Fe_3O_4 loaded on $g\text{-C}_3\text{N}_4$.

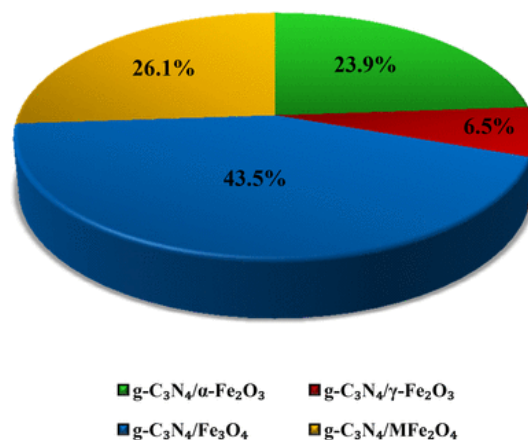


Figure 2.7. Distribution of published papers considering magnetic materials coupled with g-C₃N₄ (Mousavi et al. 2018).

2.2.3.3.4. Exfoliation of g-C₃N₄

As mentioned above, the photocatalytic activity of bulk g-C₃N₄ is low due to low surface area and high recombination of charge carriers. The van der Waals interaction between layers of bulk g-C₃N₄ reduces the surface area and active sites. Exfoliation is often achieved by applying external forces to overcome the van der Waals interactions between sheets (Cai et al. 2012). Among different methods to improve the optical properties and photocatalytic activity of g-C₃N₄, exfoliation appears to be very effective and easy to apply (Papailias et al. 2018). Moreover, without exfoliation, bulk g-C₃N₄ usually suffers from poor dispersity in solution (Dong et al. 2016). Exfoliated g-C₃N₄ with a thickness of ~2 nm, not only provides high specific surface area and pore volume and abundant reactive sites, but also promotes the charge transport. Mechanical (ultrasonic), thermal and chemical exfoliation have been developed as the major techniques of exfoliation (Cai et al. 2012). Fig. (2.8) presents the schematic illustration of liquid-exfoliation process from bulk g-C₃N₄ to nanosheets.

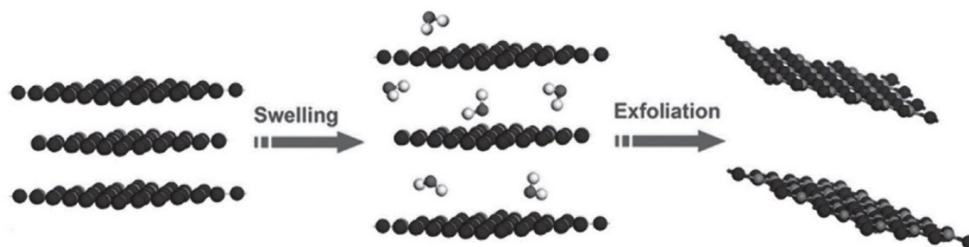


Figure 2.8. Schematic illustration of liquid-exfoliation process from bulk g-C₃N₄ to ultrathin nanosheets (Dong et al. 2016).

2.3. Impact of controlling parameters on photodegradation efficiency

2.3.1. Effect of photocatalyst loading

The total efficiency and removal rate of photocatalytic reactions are affected by the photocatalyst loading. Generally, the removal of contaminants by photocatalytic degradation increases with the increase of ZnO concentration until it reaches an optimum loading. This effect is observed since the increase of catalyst dosage provides a larger number of active sites and consequently, a higher electron-hole generation, leading to increased generation of hydroxyl and superoxide radicals, which facilitate the degradation of organic contaminants (Patil et al. 2010). However, excess photocatalyst loading may reduce the removal efficiency of contaminants by unfavorable light scattering and reduction of light penetration into the solution that may result from the turbidity of solution and shielding of target contaminants from direct radiation (Pardeshi and Patil 2008, Patil et al. 2010, Qamar and Muneer 2009). Furthermore, the high concentration of catalyst may cause particle agglomeration and reduce the homogeneity of suspension, thus reducing the availability of active sites (Rabindranathan et al. 2003). Mahalakshmi et al. (2007) reported that 1 g/L of ZnO was the optimum concentration for carbofuran removal. Table 2.1 and Table 2.2 show that a high dosage of catalyst (0.5-2.5 mg/L) is usually needed in order to efficiently remove pharmaceuticals in water. The relatively high cost of the catalyst and its regeneration as well as the separation of catalyst from water after treatment limit the application of photocatalytic processes at high water flow rates. The use of nanostructure ZnO will significantly reduce the required dosage of the catalyst, improving its economic prospects. This is because nano structure of ZnO provides a larger surface area and more active sites (Hayat et al. 2011). For instance, 50% ciprofloxacin removal was achieved by using only 20 mg/L of nano-ZnO (El-Kemary et al. 2010). In addition, 90% and 59% removal of tetracycline and ibuprofen were reported, respectively, by using 20 mg/L of nano-ZnO (Choina et al. 2015).

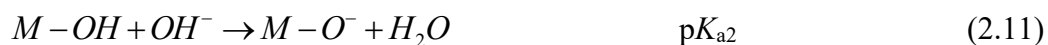
2.3.2. Effect of contaminant concentration

The concentration of contaminants is an important factor that affects the efficiency and kinetics of removal as well as the optimum catalyst dosage (Mahalakshmi et al. 2007). Generally, at low concentrations of contaminants, the rate of degradation increases with the increase of substrate concentration since there are sufficient amounts of radicals and holes for the reaction with contaminants at low substrate concentration. However, beyond the optimal

concentration, the removal rate decreases due to the insufficient amount of reactive radicals (Shankar et al. 2004). As the concentration of contaminants increases, more reactant molecules are adsorbed on the surface of ZnO, reducing the generation of OH• radicals since there are fewer active sites for the adsorption of hydroxyl anions. On the other hand, at higher contaminants concentrations, the photons are absorbed by the contaminants before they can reach the catalyst surface. Therefore, the absorption of light by the ZnO surface decreases the photocatalytic efficiency (Patil et al. 2010, Sin et al. 2013). The high concentration of substrate may also cause the deactivation of photocatalyst. During the removal of tetracycline, the increase of contaminant concentration from 5 to 60 ppm, reduced its removal efficiency from 65 to 5% after 180 min of irradiation (Choina et al. 2015). The above studies indicated that the optimum contaminant concentration depends on the photocatalyst-to-substrate mass ratios. Mahalakshmi et al. (2007) reported an optimum photocatalyst-to-substrate ratio of 5:1, whereas Choina et al. (2015) reported an optimum ratio of 2:1. The deactivation of photocatalyst was not only attributed to the structure of catalyst, but it was also affected by the nature of substrate. For instance, ZnO had undergone more deactivation during the removal of tetracycline compared to ibuprofen (Choina et al. 2015). This could be due to the higher polarity of tetracycline compared to ibuprofen.

2.3.3. Effect of pH on photocatalytic efficiency

The pH of solution is an important factor in photochemical reaction since it controls the size of the generated aggregates and the surface charge properties of the photocatalyst (Qamar and Muneer 2009). The surface of catalyst can be positively or negatively charged, depending on the pH of solution. This is due to the amphoteric behavior of most metal hydroxide surfaces. Depending on the pH, the following reactions are expected to take place on the surface of photocatalyst (Sin et al. 2013):



where K_a is the acid dissociation constant. The pK_{a1} and pK_{a2} value for ZnO have been reported as 7.6 and 11, respectively. Consequently, the zero point charge of ZnO is determined as 9.3, ($zpc = 0.5 (pK_{a1} + pK_{a2})$) (Comparelli et al. 2005). Above the pH of 9.3, the surface of ZnO is

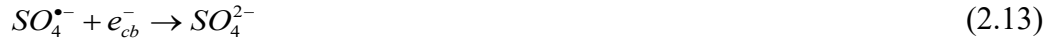
principally negatively charged by the adsorbed OH⁻ ions (Ba-Abbad et al. 2013, Kansal et al. 2007). As a result, the adsorption of organic matter onto ZnO is affected by the pH of solution. Li et al. (2014) observed that the highest removal efficiency of 17 α -ethinylestradiol was achieved at pH 9 by using Ag/ZnO hollow sphere composites. The electric charge property of contaminant is another important factor in this process. The contaminant is in molecular form when the pH is less than its pK_a, while at pH > pK_a the compound loses a proton and becomes negatively charged. Hence, when the charge of catalyst and the dissociated contaminates are the same, the removal efficiency decreases due to the repulsion force between the catalyst surface and substrate. At pH < pK_a the water solubility is reduced, so the adsorption of organic contaminants on photocatalyst is increased (Talebian et al. 2012). Hariharan (2006) reported a steady increase of degradation of 4-chlorophenol with pH up to 9. This was mainly due to the availability of more hydroxyl ions to react with the holes (h⁺). The optimum conditions summarized in Tables 2.1 and 2.2 show that the photocatalytic degradation by ZnO was more efficient under neutral or alkaline conditions. According to Eq. (2.4), the presence of abundant hydroxyl ions (OH⁻) under alkaline condition, leads to the production of high amount of hydroxyl radicals. Conversely, at low pH values, because of the lack of hydroxyl ions (OH⁻), the photo-generated holes are the sole oxidizing species (Patil et al. 2010, Wenhua et al. 2000). However, the interpretation of pH effect on the photocatalytic process is complicated because of the multiplicity of factors such as interactions with the photocatalyst surface, substrate and charged radicals as well as the controlling effect of pH on the dissociation of species (Kansal et al. 2007, Qamar and Muneer 2009, Talebian et al. 2012). In addition, different mechanisms such as direct reduction with the produced electron and oxidation with holes and indirect reaction with OH[•] radicals could contribute to degradation at different pH values and under different experimental conditions.

2.3.4. Effect of ion presence in water on photocatalytic efficiency

The presence of ions has a significant impact on the effectiveness of photocatalytic reactions. Pare et al. (2008) reported that persulfate ions act as electron scavenger and improve the removal efficiency of acridine orange due to the generation of highly reactive SO₄^{•-} (E^o=2.6 eV) radicals, according to Eq. (2.12):



These authors suggested three possible pathways for the production of persulfate with organic compounds: i) by removing a hydrogen atom from the saturated carbon, ii) by reacting with unsaturated or aromatic carbon and, iii) by removing one electron from the carboxylate ions. In addition, persulfate may react with the generated electron in the conducting band and/or with water molecules to produce sulfate ions or hydroxide radicals, respectively, as presented in the following reactions:



The reaction shown in Eq. (2.13) improves the photocatalytic reaction by reducing electron-holes recombination. However, at high concentrations of persulfate ions beyond the optimum value, the degradation of organic contaminants decreases due to the reaction with sulfate ions formed on the ZnO surface that contribute to the deactivation of a fraction of photocatalyst sites. Other ions commonly found in the water are carbonate ions that are present in the effluent of water and wastewater treatment plants. Textile industries use sodium carbonate for fixing dyes on the fabric, and produce effluents that contain high concentrations of carbonate ions. The carbonate ions act as the inner filter to absorb the light energy and radical scavengers, and decrease the rate of degradation according to the following reactions (Pare et al. 2008) :



The photocatalytic efficiency is considerably reduced when inert salts such as sodium chloride, sodium phosphate and sodium sulfate are present in the water. This is because of the preferential adsorption of the cationic or anionic molecules on the photocatalyst surface, while the inert salts inhibit degradation due to the competitive reaction of ions with the generated holes on the surface of photocatalyst. For instance, in the case of NaCl, the following hole scavenging reactions are expected:



As mentioned before, the photo-generated holes act as an oxidation agent and produce hydroxyl radicals (Eq. 2.4). The hole scavenging effect of chloride ions leads to the deactivation of holes and inhibits the removal of contaminants (Pare et al. 2008).

2.3.5. Effect of air bubbling into the solution on photocatalytic degradation

The effects of oxygen and nitrogen bubbling into the solution have been investigated (Bohdziewicz et al. 2016, Qamar and Muneer 2009). The introduction of N₂ gas into the solution negatively affected the rate of degradation by absorbing a fraction of UV radiation and expelling the beneficial dissolved oxygen molecules from the reactor (Pare et al. 2008). Conversely, the bubbling of oxygen enhanced the rate of reaction by acting as the electron acceptor on the surface of catalyst and reducing the probability of electron hole combination (Eq. 2.2). Qamar and Muneer (2009) and Bohdziewicz et al. (2016) observed that supplying oxygen not only improved the suspension state of the ZnO particles in the solution, but also reduced the rate of recombination of electron-holes process by providing oxygen as electron scavenger on the surface.

Tables 2.1 and 2.2 summarize the findings of the existing literature on the use of photocatalytic processes for the removal of pharmaceutical and endocrine disrupting compounds from water, respectively.

Table 2.1. Photocatalytic degradation of pharmaceuticals by ZnO-based photocatalysts

Pharmaceutical	Type of catalyst	Water matrix/Light source/ Irradiation time	Experimental conditions	Findings/ Remarks	Reference
Amoxicillin Ampicillin Cloxacillin	ZnO Commercial	Distilled water, UV lamp 6 W at (\approx 365 nm). Irradiation time = 300 min	[Catalyst]= 0.5 g/L [AMX] ₀ =104 mg/L [AMP] ₀ =104 mg/L [CLX] ₀ =104 mg/L Temperature = 22°C pH 8	<ul style="list-style-type: none"> •100 % AMX, AMP and CLX removal was achieved. •With [COD]₀=520 mg/L, 33% of COD removal was also achieved, •The half-life time for COD removal was 1238 min 	(Elmolla and Chaudhuri 2010a)
Ciprofloxacin	Nano ZnO (Precipitation) APS# \approx 2.1 nm	Distilled water, Xenon lamp (365 nm) Irradiation time = 60 min	[Catalyst]= 0.02 g/L, [EC] ₀ =5 mg/L pH 10	<ul style="list-style-type: none"> •50% CPX removal was achieved. •The reaction was more efficient in basic condition. •The loading of nano-catalyst was very low; First-order-rate constant was 0.0043 (min⁻¹). 	(El-Kemary et al. 2010)
Alprazolam	Synthesized Mg/ZnO annealed at 700 °C (Mg \approx 5% wt)	Distilled water, 125 W high-pressure Hg lamp Irradiation time : 10 min	[Catalyst] = 1 g/L [EC] ₀ =0.03 mM	<ul style="list-style-type: none"> •About 87 % removal was achieved by Mg/ZnO. •In same condition this value for bare ZnO was about 78 %. 	(Ivetić et al. 2014)
Tetracycline	Nano ZnO Commercial	Distilled water Simulated solar light Xe lamp, (250 W m ⁻²) (300-800 nm) Irradiation time =10 min	[Catalyst] = 1 g/L [EC] ₀ =20 mg/L pH 11	<ul style="list-style-type: none"> •Total removal of TC was achieved after 10 minutes. •Also, total mineralization of TC was achieved after 45 min of irradiation. 	(Palominos et al. 2009)
Metronidazole	Nano ZnO	Distilled water	[Catalyst] = 1.5 g/L	<ul style="list-style-type: none"> •96.5 % EC removal and 95.5% 	(Farzadki

	Commercial	(8 W) low pressure Irradiation time =180 min	[EC] ₀ = 80 mg/L pH 10 Room temperature	COD removal were achieved.	a et al. 2014)
Carbofuran	ZnO Commercial	Distilled water Low pressure Hg lamp, (8 ×8 W) (254 nm), Irradiation time = 6 h	[Catalyst] = 1 g/L [EC] ₀ =200 mg/L Temperature =25-30 °C pH 7	•~ 90% TOC removal was achieved.	(Mahalaks hmi et al. 2007)
Combination of 14 different PhACs	ZnO Commercial	Real sewage effluent [COD] ₀ = 37 mg/L [BOD] ₀ = 4 mg/L TKN < 5.0 mg/L Hg lamp, (6 ×8 W) (365 nm), intensity = 1.6 mW.cm ⁻² . Irradiation time = 40 min	[Catalyst] = 1 g/L Room temperature pH 7.5 [carbamazepine]= 1.29 µg/L [gabapentin]=11.30 µg/L [lamotrigine]= 0.98 µg/L [oxcarbazepine]= 0.63 µg/L [venlafaxine]= 0.58µg/L [bisoprolol]= 0.58 µg/L [celiprolol]= 0.35µg/L [talinolol]= 0.43 µg/L [bezafibrate]= 0.48µg/L [tramadol]= 0.624 µg/L [candesartan]= 1.30µg/L [eprosartan]= 0.56 µg/L [irbesartan]=1.5 µg/L [valsartan]= 3.59 µg/L	<ul style="list-style-type: none"> •After 40 minutes, about 95% removal was achieved for all ECs. •The average first order rate constant for all considered pharmaceuticals was 8.6 ×10⁻² (s⁻¹) 	(Teixeira et al. 2016)
Ibuprofen Tetracycline	Synthesized nano ZnO _w (solvent water), ZnO _e (solvent ethanol)	Distilled water Four UV-Vis solarium lamps (60 W), Irradiation time= 180 min	[Catalyst] = 0.02 g/L pH 9 [Ibuprofen] ₀ = 5 ppm [TC] ₀ = 10 ppm	<ul style="list-style-type: none"> •For ibuprofen, 59% and 36% removal were archived by ZnO_e and ZnO_w, respectively. •For TC, 90 % and 85 % removal were archived by ZnO_e and ZnO_w, respectively. •~50% deactivation of both catalysts was shown after 3 cycles. 	(Choina et al. 2015)
Paracetamol	Synthesized ZnO (sol-gel) Annealing at 500 °C	Distilled water UV lamp (18W) (315–400 nm) Intensity= 5×10 ⁻⁵ W cm ⁻² Irradiation time = 4 h	[Catalyst] = n.a (Thin film) pH= 5.58–6.69 (natural) [Paracetamol] ₀ = 15 ppm [Chloramphenicol] ₀ = 8 ppm Temperature = 25 °C	<ul style="list-style-type: none"> •About 14 % removal paracetamol was achieved. •First-order-rate constant for paracetamol removal was 0.0362 (min⁻¹). •~40 % chloramphenicol removal was achieved. •First-order-rate constant was 0.1373 (min⁻¹). 	(Pronin et al. 2014)
Diclofenac Ibuprofen Carbamazepine	ZnO Commercial	Distilled water Low pressure Hg lamp (150 W) (λ < 300nm) Irradiation time = 30 min	[Catalyst] = 0.05 g/L pH 7 [EC] ₀ =1 mg/L Temperature = 20 °C	<ul style="list-style-type: none"> •68% diclofenac removal was achieved. •First-order-rate constant for diclofenac removal was 0.0574 (min⁻¹). •The half-life of diclofenac removal was 8.58 min. •60% ibuprofen removal was achieved. • First-order-rate constant for ibuprofen was 0.0328 (min⁻¹). • The half-life of Ibuprofen was 13.04 min. •60% removal was achieved for 	(Bohdzie wicz et al. 2016)

				carbamazepine. • First-order-rate constant for carbamazepine removal was 0.0152 (min ⁻¹). • The half-life of carbamazepine removal was 36.45 min.	
Metronidazole	Synthesized nano ZnO (Precipitation)	Distilled water Ultrasound irradiation time = 27 min	[Catalyst] = 0.02 g/L [EC] ₀ = 10 mg/L pH (n.a) Temperature = 30 °C	• 100% removal was achieved. • First order rate constant was 0.072 (min ⁻¹). • Excellent activity (recyclability) after five cycles.	(Bhuyan et al. 2016)
Phenazopyridine	Synthesized nano Sm/ZnO (0.4 % mol) (Sonochemical)	Distilled water Ultrasound (700 W, 20 kHz) Irradiation time = 45 min	[Catalyst] = 1 g/L [EC] ₀ = 10 mg/L pH 6.1 [Oxidants] = 0.7 g/L	• With H ₂ O ₂ as oxidant the removal was = 81.5%, • With S ₂ O ₈ ²⁻ as oxidant the removal was = 87.6 %, • With HSO ₅ ⁻ as oxidant the removal was = 72.2 %. • With IO ₄ ⁻ as oxidant the removal was = 95.5%	(Eskandarloo et al. 2016)
Naproxen	Synthesized nano ZnO/MMT	Distilled water Ultrasound (650 W, 60 kHz) Irradiation time = 120 min	[Catalyst] = 0.5 g/L [EC] ₀ = 10 mg/L pH 4.5 Room temperature	• 73.2 % removal was achieved. • Only 2% of reduction in activity was shown after five cycles.	(Karaca et al. 2016)

Average Particle Size

na: not available

[EC]= Initial concentration of emerging contaminants

Table 2.2. Photocatalytic degradation of endocrine disruptive compounds (EDCs) by ZnO-based photocatalysts

Contaminant	Type of catalyst	Light source/ Irradiation time	Experimental conditions	Findings/ Remarks	Reference
Resorcinol	Synthesized S/ZnO	Distilled water, Sunlight, (1.7×10^{-7} Einstein s ⁻¹ cm ⁻²) Irradiation time: 7 h	[Catalyst] = 2.5 g/L, [EC] ₀ = 150 ppm pH 6.7	• By pure ZnO, ~55% of COD removal was achieved. • By S/ZnO, 100% of COD removal was achieved. • First order reaction constants for S/ZnO and ZnO were, 2.51×10^{-1} h ⁻¹ and 8.09×10^{-2} h ⁻¹ , respectively. • The activity of modified ZnO remained unchanged after five cycles.	(Patil et al. 2010)
17 α -ethinylestradiol (EE2)	Synthesized Ag/ZnO hollow spheres (Ag= 6.7% mol)	Distilled water UV lamp 8 W (254 nm) UV fluxes = 145 W m ⁻² , Irradiation time: 50 min	[Catalyst] = 0.5 g/L, [EC] ₀ = 2.719 mg/L pH (neutral)	• 100 % and 53%.of removal was achieved by Ag/ZnO, and bare ZnO, respectively. • The activity of modified ZnO remained unchanged after three cycles. • The Maximum first-order-rate constant was 0.067 (min ⁻¹)	(Li et al. 2014)
4-Nitrophenol	Synthesized Ag/ZnO By polyacrylamide-gel method (Ag \approx 0.5%)	Distilled water UV-light Irradiation time: 3 h	[Catalyst] = 2 g/L [EC] ₀ = 10 ppm	• 100 % and 15% removal was achieved by using Ag/ZnO prepared by polyacrylamide-gel method and bare ZnO, respectively. • Maximum first-order-rate constant was 0.0484 (min ⁻¹).	(Divband et al. 2013)
Phenol	M/ZnO (M= Li, Na, K) by sol-gel methods	Distilled water 125 W Hg lamp Irradiation time=2 h	[Catalyst] = 1 g/L [EC] ₀ = 200 mg/L temperature = 20°C	• The removal percentage by bare ZnO was about 68%.	(Benhebal et al. 2012)

	(M:Zn ratio = 10% wt)		pH 6.5	<ul style="list-style-type: none"> 70% and 74% removal were achieved by doping with Li and Na, respectively. 	
2-Chlorophenol	Synthesized Fe/ZnO nanoparticles (0.5% wt), Calcined at 400 °C	Distilled water Solar radiation (23 W.m ⁻²) Irradiation time=90 min	[Catalyst] = 1 g/L [EC] ₀ =50 mg/L temperature =28-38°C	<ul style="list-style-type: none"> For bare ZnO the first order rate constant and removal efficiency were 1.71×10⁻² (min⁻¹) and 65%, respectively. Maximum first-order-rate constant and removal efficiency, were, 2.63×10⁻² (min⁻¹) and 85%, respectively. 	(Ba-Abbad et al. 2013)
Phenol, 4-Aminophenol, 4-Nitrophenol	Nano ZnO/SnO ₂ /ZnO /SnO ₂ /ZnO five-layers (sol-gel) Annealing at 550 °C	Distilled water Four UV lamps (8 W) (365 nm) Irradiation time = 150 min	[Catalyst] = n.a (coated on glass) pH= 11 [Phenol] ₀ = 5 ppm [4-Aminophenol] ₀ = 5 ppm [4-Nitrophenol] ₀ = 5 ppm	<ul style="list-style-type: none"> 31%, 91% and 73% phenol, 4-aminophenol and 4-Nitrophenol removal were achieved, respectively. First-order-rate constant for phenol, 4-aminophenol and 4-Nitrophenol removal was 0.006, 0.017 and 0.011 (min⁻¹), respectively. 	(Talebian et al. 2012)
2,4,6-Trichlorophenol	Synthesized nano ZnO (thermal evaporation)	Distilled water UV lamp (6 W) (254 nm) Irradiation time = 60 min	[Catalyst] = n.a (Thin film) pH 6 [EC] ₀ = 100 ppm temperature = 25 °C	<ul style="list-style-type: none"> 95.4 % removal was achieved. The removal by ZnO (sol-gel) in same condition was 80.7 %. First-order-rate constant for (thermal evaporation) and (sol-gel) were 0.0455 (min⁻¹) and 0.0272 (min⁻¹), respectively. 	(Abdel Aal et al. 2009)
Estrone; 17β-estradiol; 17α-ethinylestradiol; Bisphenol A	Synthesized ZnO nanorod arrays	Distilled water UVA (365 nm) Intensity= 0.57 mW cm ⁻² Irradiation time = 6 h	[Catalyst] = n.a (coated on glass) [ECs] ₀ = 1.85×10 ⁻³ mmol/L pH (n.a)	<ul style="list-style-type: none"> About 90 %, 80%, 80% and 75% Estrone, 17β-estradiol, 17α-ethinylestradiol and bisphenol A removal were achieved, respectively. 	(Liu and Gao 2014)
Phenol	ZnO Commercial	Distilled water UV (365 nm) (15 W) Intensity= 0.840 mW cm ⁻² Irradiation time = 30 min	[Catalyst] = 2.5 g/L [EC] ₀ = 5 mg/L pH 5.2 temperature =26°C	<ul style="list-style-type: none"> 100% removal was achieved. Only about 4% decline was shown in performance of catalyst after 3 cycles. The maximum first order rate constant was 0.1278 (min⁻¹). 46.5 % of TOC removal was reported after 20 min of irradiation. 	(Sin et al. 2013)
Resorcinol	ZnO Commercial	Distilled water UV (365 nm) (15 W) Intensity= 0.840 mW cm ⁻² Irradiation time = 30 min	[Catalyst] = 2 g/L [EC] ₀ = 5 mg/L pH 11 temperature =26°C	<ul style="list-style-type: none"> 100% removal was achieved. Only about 4% of decline was shown in performance of catalyst after 3 cycles. The maximum first order rate constant was 0.2345 (min⁻¹). 50.1% of TOC removal was reported after 20 min of irradiation. 	(Sin et al. 2013)
Phenol	ZnO Commercial	Distilled water UV medium pressure mercury (400 W) Ultrasound (100 W 40 kHz) Irradiation time = 120 min	[Catalyst] = 0.1 g/L [EC] ₀ = 40 mg/L pH 5.5 temperature = 29 °C [H ₂ O ₂] = 15 mg/L	<ul style="list-style-type: none"> 94.6% removal was achieved. 	(Jyothi et al. 2014)

4-Chlorophenol	ZnO Commercial	Distilled water UV (365 nm) (6 W) Irradiation time = 180 min	[Catalyst] = 2 g/L [EC] ₀ = 50 mg/L pH 7.1-7.5 temperature = 26 °C	<ul style="list-style-type: none"> • 100% removal was achieved. 	(Gaya et al. 2009)
4-Chlorocatechol	ZnO Commercial	Distilled water and also real industrial effluent. Seven UV tubes (36 W), (365 nm) Intensity = 25 W m ⁻² Irradiation time = 120 min. And also, Solar radiation = 6 h, Intensity = 35 W m ⁻²	[Catalyst] = 1.5 g/L [EC] ₀ = 50 ppm pH 8 temperature = 30 °C	<ul style="list-style-type: none"> • 98.6 % removal was achieved under 120 min of irradiation of UV lamp. • First order rate constant was 0.0173 (min⁻¹). • By utilizing solar energy, 99.1% removal was achieved after 6 h. • In real effluent, about 44% of COD removal was achieved by (ZnO/solar) after 6 h. 	(Dhir et al. 2012)
Phenol	ZnO Commercial	Distilled water, UV lamp (medium pressure Hg). (400 W), Ultrasound (100 W 40 kHz) Irradiation time = 120 min.	[Catalyst] = 0.1 g/L [EC] ₀ = 40 mg/L pH 5.5 temperature = 29 °C	<ul style="list-style-type: none"> • 85% degradation was achieved. 	(Anju et al. 2012)

Average Particle Size

na: not available

[EC]= Initial concentration of emerging contaminants

2.4. Method of ZnO synthesis

The photocatalytic performance of ZnO depends on many factors such as the surface area, phase purity, crystallite size, method of preparation and type and concentration of dopant as modifier (Etacheri et al. 2012). Generally, the nano structural properties of catalyst such as crystallinity, morphology, size, electronic structure, and surface defects substantially differ from those of the bulk catalyst (Wu and Huang 2010). For instance, the nanostructure form of ZnO not only provides a larger surface area and catalytic activity, but also increases the effective band gap of nano catalyst when the crystallite dimension of a catalyst particle falls below the critical radius of about 50 nm (Mirzaei et al. 2016). As a result, an improvement in driving force resulting from the increase of the oxidation/reduction potential is expected. In addition, the use of nanostructure ZnO will significantly reduce the required dosage of the catalyst, improving its economic prospects. This is because the nano structure of ZnO provides a larger surface area and more active sites (Hayat et al. 2011). For instance, 50% ciprofloxacin removal was achieved by using only 0.020 g/L of nano-ZnO (El-Kemary et al. 2010). In addition, 90% and 59% removal of tetracycline and ibuprofen were reported, respectively, by using 0.020 g/L of nano-ZnO (Choina et al. 2015). In the case of nano-ZnO, the amount of electron-hole recombination is considerably less than that in the micro-size catalyst (Hayat et al. 2011) since the nanostructure catalyst commonly has more defects and oxygen vacancies on the surface (Wang et al. 2009b,

Wu and Huang 2010). In the photocatalyst process, defects and oxygen vacancies become centers to trap the photo-generated electrons on the surface (Lee et al. 2016). The temperature of calcination process is also a critical factor, which considerably alters the morphology, surface hydroxyl groups and performance of the ZnO photocatalyst (Hayat et al. 2011, Kong et al. 2010). At high temperatures of calcinations, the crystallites tend to agglomerate. Consequently, the surface area decreases and particle size increases due to the growth and sintering of the nanoparticles. Since both crystallinity and high surface area are important to the catalytic activity, a trade-off must be found between these two competitive parameters. Different types of solvents used in the synthesise process also affect the surface characteristics and the performance of photocatalysts. For example, using ethanol instead of water in the preparation of ZnO improved the activity and stability of photocatalyst (Choina et al. 2015).

2.4.1. Hierarchical photocatalysts

ZnO photocatalysts can be prepared by various techniques such as precipitation (Sepulveda-Guzman et al. 2009), sol-gel (Mahdavi and Talesh 2017), and hydrothermal/solvothermal (Muñoz-Fernandez et al. 2017) methods. Among these methods, the hydrothermal synthetic route has advantages to obtain high-crystallized powders with high purity and narrow grain size-distribution without the expensive precursors (Wirunmongkol et al. 2013). By hydrothermal/solvothermal techniques, different forms of photocatalyst such as nanoparticles, nanorods, mesoporous structure, or nanotubes can be prepared. However, none of these photocatalysts completely satisfies all practical requirements such as high surface area, reusability and lack of mass transfer limitations. The hierarchical structures have been known as the state-of-the-art forms of photocatalysts due to their unique shape and structure (Li et al. 2016). “Hierarchical photocatalysts” are usually referred to as the nanostructured semiconductors having multidimensional domains at different levels or multimodal pore structures.

Different forms of hierarchical photocatalysts such as urchin-like, brush-like, flower-like and tree-like (Fig. 2.9) possess interconnected and readily accessible porous networks and high specific surface areas, which not only enhance the adsorption of reactants and light harvesting, but also facilitate the mass transfer of guest species to the binding sites (Li et al. 2016).

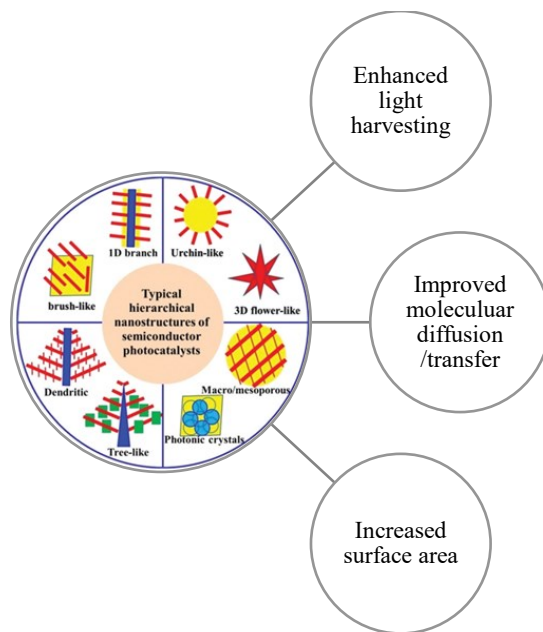


Figure 2.9. Typical hierarchical structures of photocatalyst (Li et al. 2016) and significance of hierarchical nanostructures in enhancing photocatalysis.

Hierarchical structures of photocatalysts usually provide a rough surface, which is beneficial for light harvesting. Hierarchical photocatalyst with macro/mesoporous or appropriate inner structures offer multiple reflections and scattering of light inside their pore channels as well as within the interiors of cavities, which results in enhanced light absorption (Li et al. 2007) (Fig. 2.10).

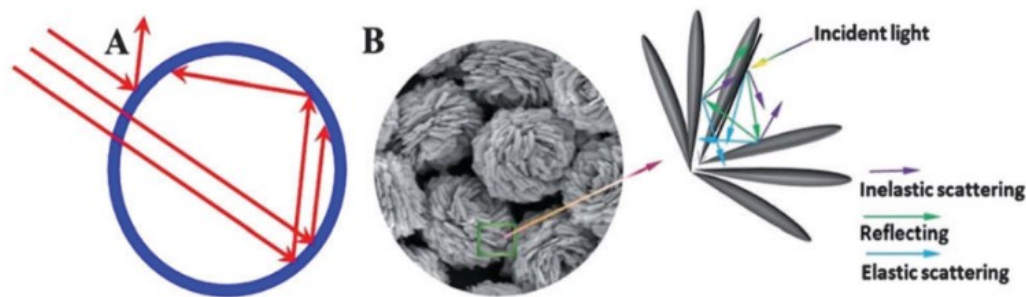


Figure 2.10. Schematic illustration of the reflecting and scattering effects in interiors of cavities (A) and hierarchical microspheres (B) (Xiong et al. 2014).

The design of novel hierarchical morphologies and interconnected porous networks can also facilitate the diffusion of reactants and products inside the porous structure of photocatalyst (Yu

et al. 2004). In the case of photocatalysts with properly interconnected pores of different sizes, the reactant molecules can easily diffuse into the reaction sites, while the intermediates and products can freely move out of them (Fig. 2.11).

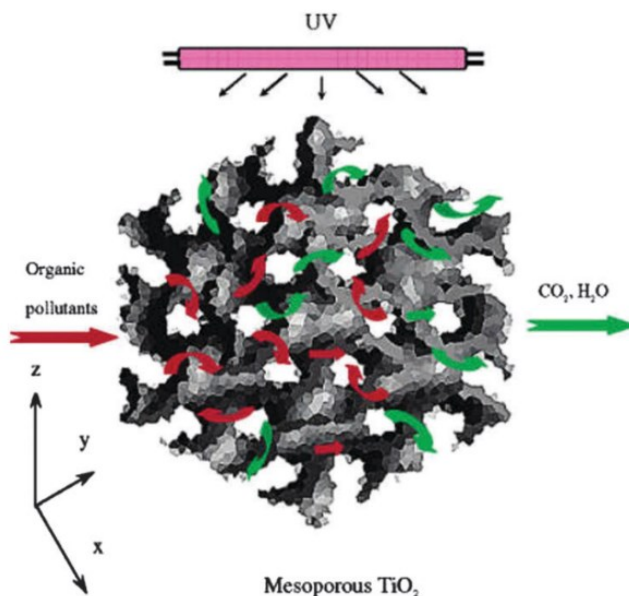


Figure 2.11. Three-dimensional mesoporous architecture with a continuous and periodically porous network that offers transport routes for reactants to move in and out of the framework (Yu et al. 2004).

Besides improving the light harvesting and mass transfer, hierarchical structures also improve the efficiency of removal by increasing the specific surface area. For instance, Lu et al. (2008) synthesized a hierarchical ZnO photocatalyst with $185.6 \text{ m}^2/\text{g}$ by solvothermal method, which possesses a significantly higher specific surface area compared to the commercial ZnO nanoparticles ($\sim 30.6 \text{ m}^2/\text{g}$). The higher specific surface area is obviously beneficial for enhancing the photocatalytic performance.

2.4.1.1. Strategies for fabrication of hierarchical photocatalysts

Mostly, the 3D hierarchical structures are synthesized via the self-assembly of nanosized building blocks (including nanoparticles, 1D nanowires, and 2D nanosheets). However, it is very difficult to directly design and fabricate various kinds of hierarchical photocatalysts such as brush-like, flower-like, and forest-like with highly controlled hierarchical morphologies (Li et al. 2016). Templating is one of the most important techniques, using a pre-existing guide with desired nanoscale features to control the oriented growth of hierarchical nanomaterials (Liu et al.

2013). Based on the physical properties of the employed templates, this method can be performed by relatively rigid shaped material such as SiO₂ (hard templating) (Yu et al. 2008) and soft templates such as poly (ethylene glycol) (Yu et al. 2013).

2.5. Summary of literature review

The presence of antibiotics in the aquatic ecosystem has raised increasing concern due to their frequent appearance and the threat to health and safety of aquatic life, even at trace concentrations. Conventional water treatment processes are known to be generally inadequate for the elimination of these persistent contaminants. Therefore, the use of AOPs, such as photocatalytic oxidation, which is able to efficiently oxidize organic pollutants, has attracted a great amount of attention. Photocatalytic removal of emerging contaminants by using zinc oxide photocatalyst is a promising process due to the unique characteristics of this catalyst such as wide band gap, non-toxicity and low cost. The main limitations of ZnO photocatalysts are the fast recombination of photo-generated charges and photocorrosion. Recently, a considerable effort has been made to improve the photocatalytic performance of ZnO by surface modification, doping with elements, optimizing preparation methods, and using hierarchal structure. Hierarchal structure not only enhances light absorption and specific surface area of photocatalysts, but also reduces the mass transfer limitations. In addition, surface fluorination of photocatalysts can be considered as an effective surface modification method to improve the efficiency of contaminant removal. Finally, the efficiency of photocatalytic degradation processes have been shown to be dependent on the pH of solution, type and amount of ZnO, concentration of contaminants, presence of natural organic matter (NOM) and electron acceptor. Therefore, optimizing the controlling parameters during the synthesis or utilization of photocatalysts (operating parameters) is necessary.

3. Methodology

In this study, first, a low-energy-consuming photoreactor (10 W) was designed and built. An immersed UVC lamp with a protective quartz sleeve was used in an annular stainless steel reactor to increase the quantum yield of process. The effect of physically fluorination (F-ZnO) and chemically fluorination (Zn(OH)F) of ZnO on the adsorption capacity and photocatalytic activity were evaluated. Preliminary experiments were conducted to select the affecting parameters and their corresponding ranges for photocatalytic degradation of SMX. Response surface methodology (RSM) coupled with central composite design (CCD) was employed to evaluate the importance of affecting parameters as well as optimization of process for maximizing SMX removal. Under the optimum conditions, the photocatalytic activity of F-ZnO was assessed in terms of SMX removal and mineralization, kinetic of reaction and detoxification of solution. The energy consumption of process based on *electrical energy per order* (E_{EO}) was calculated and compared with reported values in the literature for SMX removal by using UVC.

In the next step, Fe_3O_4 -ZnO@g-C₃N₄ was synthesized with hierarchical structure for facile separation of photocatalysts from solution by magnetic force and increasing stability of ZnO against photocorrosion. The synthesized Fe_3O_4 -ZnO@g-C₃N₄ was first optimized by changing ZnO:g-C₃N₄ ratio and the optimum photocatalyst after characterization with several tests was used for SMX removal. The effect of operating parameters including, photocatalyst dosage, pH of solution and air flowrate on SMX removal was evaluated by using RSM, and the removal efficiency, kinetic of reaction, by-products formation and detoxification of solution were investigated under the optimum condition.

Finally, the effect of light type on the removal of AMX was examined by using exfoliated magnetic Fe_3O_4 @g-C₃N₄ as a UV-Visible driven photocatalyst. Similarly, after the synthesis and characterization of photocatalyst, its performance was assessed in terms of AMX removal and mineralization, by-products formation and detoxification of solution. Based on the evolution of intermediates compounds during removal, degradation pathways of SMX and AMX were proposed in this study.

3.1. Experimental setup

The photocatalytic performance of commercial and synthesized photocatalysts under UV light was examined using an annular photoreactor. The photoreactor set-up is illustrated in Figs. 3.1 and 3.2(a). The photocatalytic experiments were performed in a stainless steel photoreactor working in slurry mode with 700 mL volume. The light source was provided by a UVC lamp (9 W, Trojan Technologies, USA), the intensity of UVC radiation was 3.5 mJ/cm^2 , measured by a radiometer (Trojan Technologies, USA). In all cases, air was continuously bubbled into the solution mixture through a sparger located at the bottom of the reactor to achieve sufficient agitation and provide dissolved oxygen as the electron acceptor. An external reservoir (300 mL) was used to purge the air, and for sampling and further mixing by the stirrer. The pH of solution was measured by a Q46 digital pH meter (Analytical Technology, Inc.). At given time intervals, 10 mL of solution was withdrawn and the catalyst particles were removed by a $0.22 \mu\text{m}$ filter for subsequent analysis.

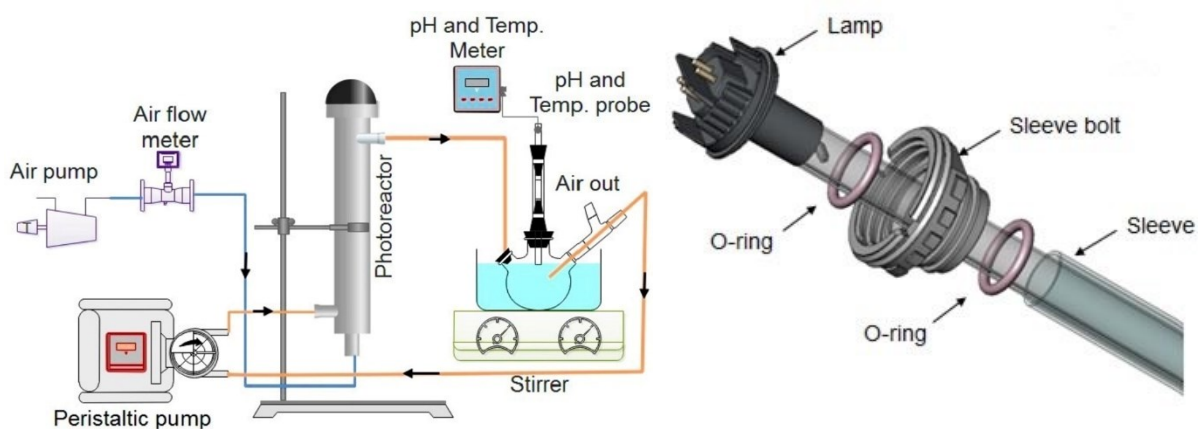


Figure 3.1. Schematic of designed photoreactor set-up (left), UVC lamp and protective sleeve (right).

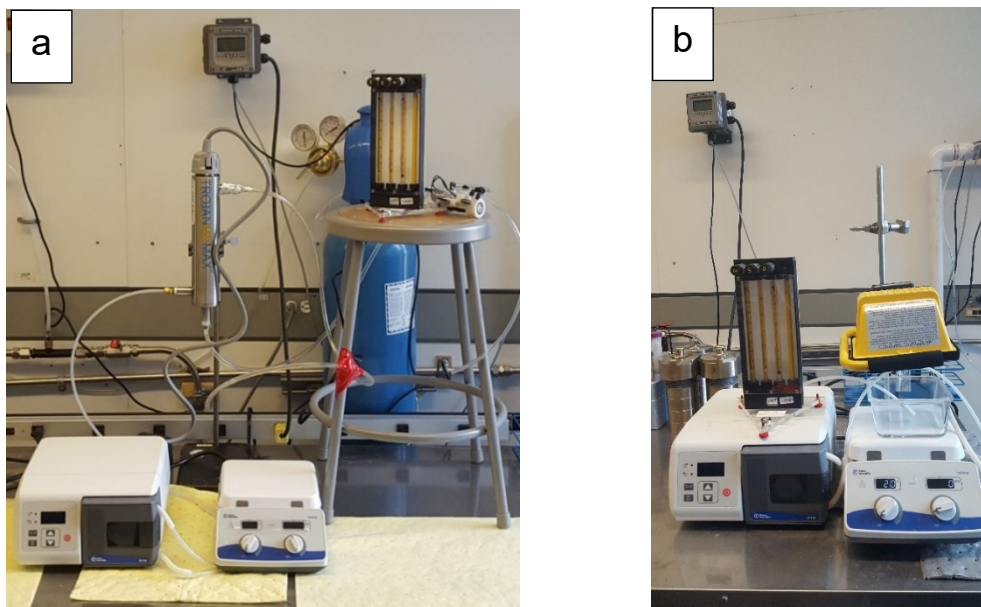


Figure 3.2. (a) Photocatalytic set-up under UV light, (b) and visible light.

A 500 W halogen lamp with a UV cutoff filter (>400 nm) was used as the light source in visible-driven experiments. Similar to the UV-driven experiments, air was continuously introduced into the solution mixture by an air stone diffuser. The distance between the solution surface and lamp was 10 cm. Ice bath was used in order to cool down the solution during the experiments (Fig. 3.2b).

3.2. Experimental design

Conventional experimental design approach by varying one-variable-at-a-time while other parameters are held constant involves a large number of experiments and does not consider interaction among parameters (Subramonian et al. 2017). As an alternative method, response surface methodology (RSM) is a collection of mathematical and statistical techniques useful for optimizing processes and evaluating possible interactions between parameters. In this study, RSM based on central composite design (CCD) was employed to evaluate the effects of independent operating parameters. It is reported that the photocatalyst loading, solution pH and dissolved oxygen concentration are among the most effective parameters in the photocatalysis process (Lin et al. 2009, Mirzaei et al. 2018a). In addition, in surface fluorination experiments, the concentration of fluoride ion in the solution was considered as the fourth controlling parameter since the amount of fluoride ion has a decisive influence on the photocatalytic degradation

reaction (Liu et al. 2012). With three parameters, the experimental design consisted of twenty experiments including six axial, eight factorial and six central points (Fig. 3.3).

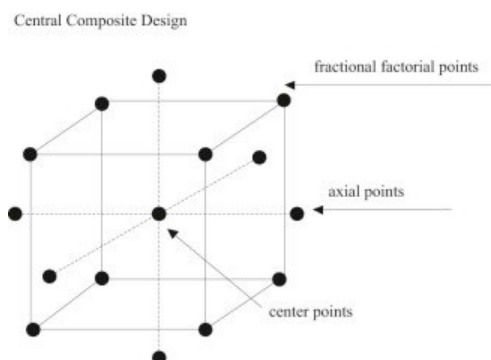


Figure 3.3. Central composite design for three operating parameters (Li et al. 2015).

A second-order equation was used to model the interaction between the dependent and independent variables (Eq. 3.1) (Hou et al. 2012, Xiao et al. 2017):

$$Y = \beta_0 + \sum_{i=1}^n \beta_i x_i + \sum_{i=1}^n \beta_{ii} x_i^2 + \sum_{1 \leq i < j}^n \beta_{ij} x_i x_j + \varepsilon \quad (3.1)$$

where Y (%) is the SMX removal percent, x_i and x_j are dependent parameters, β_0 is the model intercept coefficient; β_i , β_{ii} and β_{ij} are the coefficients of linear, quadratic and second order terms, respectively, n is the number of dependent parameters and ε is the residual term. Regression analysis were performed using Minitab 16 statistical software. Analysis of variance (ANOVA) was employed to evaluate the significance and suitability of the predicted model (Shayegan et al. 2013). Optimization was carried out on the basis of desirability function in order to find the optimum point where the removal efficiency of SMX is maximum at a certain reaction time.

3.3. Chemicals

Acid orange 7 (AO7), methyl blue (MB), calcium sulfate, sodium chloride, sodium carbonate, and sodium nitrate were supplied by Acros Organic Co. (Canada). Zinc acetate, ammonium fluoride, urea, ethylene glycol (EG) anhydrous ethanol, potassium iodide, tert-butanol, and zinc oxide nanoparticles were supplied by Fisher Scientific (ON, Canada). EDTA disodium salt and p-benzoquinone (BQ) were purchased from Alfa-Aesar. FeCl_3 , $\text{FeCl}_2 \cdot 4\text{H}_2\text{O}$, Fe_3O_4 nanoparticles, sulfamethoxazole, ampicillin and amoxicillin were supplied by Sigma-

Aldrich Inc., USA. Deionized Milli-Q water (DIW) ($18 \mu\text{S cm}^{-1}$) was used throughout this study for the preparation of photocatalysts and during the experiments.

3.4. Synthesis of photocatalysts

3.4.1. Surface fluorination of ZnO

As shown in Fig. 3.4, the surface fluorination of semiconductor can be easily performed by a simple ligand exchange reaction between surface hydroxyl groups on semiconductor and fluoride ions (F^-) under acidic condition (Yu et al. 2009).

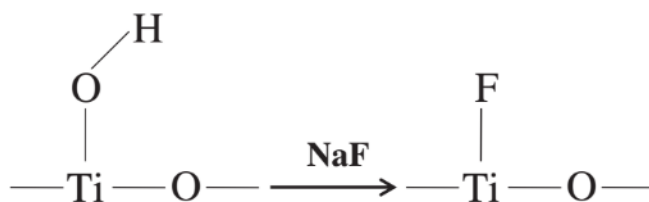


Figure 3.4. The possible chemical structures of simple ligand exchange between F^- and surface hydroxyl groups (Liu et al. 2012).

In post-synthesis fluorination, the effect of surface fluorination largely depends on the amount of fluoride ion adsorbed on the surface (Liu et al. 2012). Therefore, the amount of fluoride ion in the solution is optimized for the removal of SMX. Although, post-synthesis fluorination (addition of fluoride ion directly into the solution at acidic condition) is very convenient and effective, the remaining fluoride ion in the solution after the treatment is a matter of concern. Consequently, *in-situ* fluorination or participation of fluoride in the crystallization processes of a photocatalyst is also examined by synthesizing zinc hydroxide fluoride (Zn(OH)F).

3.4.2. Zn(OH)F

The post-synthesis solvothermal method was used to prepare Zn(OH)F sonocatalysts by using NH_4F as a precursor of fluorine according to the literature with minor modifications (Yang et al. 2017b). Briefly, NH_4F was dissolved in 150 mL isopropanol and the solution was stirred for 30 min at room temperature. Then, ZnO with (F/Zn) molar ratio of 0.5:1, 1:1 and 2:1 was added to the above solution. After 1 hour stirring, the solution was transferred into a 200 mL Teflon-lined autoclave and was heated to $160 \text{ }^\circ\text{C}$ for 16 h. After cooling naturally to room

temperature, the sonocatalyst was retrieved, washed and dried at 60 °C, and was labeled as ZF0.5, ZF1 and ZF2, respectively. Fig. 3.5 (a) and (b) shows the crystalline structure of ZnO and Zn(OH)F, respectively.

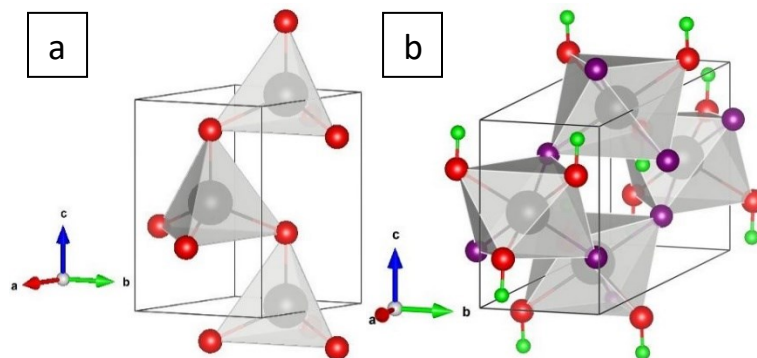


Figure 3.5. (a) crystalline structure of ZnO and (b) Zn(OH)F. black, red, purple and green color represent, zinc, oxygen, fluorine and hydrogen atoms, respectively.

3.4.3. Fe₃O₄-ZnO@g-C₃N₄

The ZnO photocatalyst was synthesized via a facile solvothermal method. Hydrothermal synthesis includes crystallization of substances from high-temperature aqueous solutions at high vapor pressures. The crystal growth is performed in a Teflon-lined vessel, which is confined by a pressure vessel called an autoclave (Fig. 3.6). Solvothermal method is very similar to the hydrothermal route, the only difference being that the precursor solution is not water.



Figure 3.6. Pressurized autoclave, the capacity of the Teflon-lined autoclave: 200 ml.

Hydrothermal technique is generally used for the growth of high quality crystals (Sharma et al. 2017a). In a typical experiment, zinc acetate (3.96 g) and urea (3.28 g) were dissolved in 150 mL of EG and DIW with a volume ratio of 1:1. Afterwards, 39.6 mg Fe₃O₄ nanoparticles (Fe₃O₄: zinc acetate = 1% wt.) was added to the solution and it was mixed by sonication for 15 min. The obtained solution was transferred into a 200 mL Teflon-lined autoclave and was maintained for 12 h at 160 °C before cooling down naturally to room temperature. The obtained particles were collected and washed with ethanol and DIW several times. Then, the grey products were dried at 60 °C in an oven for 10 h followed by annealing at 500 °C for 2 h in air. The resulted product was denoted as Fe-ZnO. The Fe₃O₄-ZnO@g-C₃N₄ composites (FZG) were obtained by the *in situ* growth of g-C₃N₄ on Fe-ZnO petals. Accordingly, a certain amount of urea was completely dissolved in 20 mL of ethanol to form a yellowish solution. Then, Fe-ZnO particles were added to the solution and were well dispersed by sonication. Afterwards, the solvent was evaporated at 60°C. The subsequent heating treatment at 500 °C for 2 h transformed the coated urea on the nano-petals surface to g-C₃N₄, resulting in the production of hierarchical magnetic FZG structure. The obtained photocatalysts with different initial urea and Fe-ZnO weight ratios of 0.5:1, 1:1, 2:1 were labeled as FZG0.5, FZG1, FZG2, respectively. The g-C₃N₄ powder was obtained by one-step polymerization of urea according to the literature (Sharma et al. 2017b). Briefly, 7 g of urea as the precursor were heated in a muffle furnace at 500 °C for 2 h with a heating rate of 10 °C/min under atmospheric air. After cooling to room temperature, the obtained yellow color product was collected and ground into powder g-C₃N₄. The pristine ZnO was synthesized with a similar procedure but without the addition of iron and without *in situ* coating with g-C₃N₄.

3.4.4. Mesoporous Fe₃O₄@g-C₃N₄

The *in situ* growth of Fe₃O₄ nanoparticles on exfoliated porous g-C₃N₄ nanosheets was used in this study. Accordingly, carbon nitride (g-C₃N₄) was synthesized by heating urea up to 550 °C for 4 h (Sharma et al. 2017b). Fluorinated g-C₃N₄ nanosheets were prepared by acid-assisted exfoliation of g-C₃N₄ as follows: 2 g g-C₃N₄ were added into 150 mL DIW containing (4 g) NH₄F and then transferred into a 200 mL Teflon-lined autoclave and heated to 180 °C for 12 h. After cooling to room temperature, the photocatalyst was retrieved, washed and dried at 60 °C overnight, and was labelled as GF. Magnetic surface fluorinated g-C₃N₄ (FeGF1) was prepared according to (Zhu et al. 2018) with a minor modification. Briefly, GF powder (2 g) was added to

150 ml of ethanol/water (v/v=1:1) and was sonicated for 10 min. Then, $\text{FeCl}_2 \cdot 4\text{H}_2\text{O}$ (1 mmol) and FeCl_3 (2 mmol) were added into the solution and were mixed for 30 min at 60 °C. Afterward, 15 ml ammonia solution was quickly added to the mixed solution and was continuously stirred for 30 min. The prepared particles were separated by magnet and were rinsed several times with ethanol and DIW and, then the particles were dried at 60 °C overnight. The photocatalysts prepared by using 2 and 3 mmol $\text{FeCl}_2 \cdot 4\text{H}_2\text{O}$ were designated as FeGF2 and FeGF3, respectively. Pure Fe_3O_4 was synthesized using a similar process as FeGF, but in the absence of GF.

3.5. Characterization of photocatalysts

The crystallinity of as-synthesized samples was characterized using XRD with a Bruker D8 Advance X-ray diffractometer with $\text{Cu K}\alpha$ radiation ($\lambda=1.5406 \text{ \AA}$) in the 2θ range from 10° to 80°. Fourier Transform Infrared (FTIR) spectroscopy was performed using Thermo Scientific Nicolet 6700 spectrometer (USA). An emission scanning electron microscope (Hitachi S-3400N) equipped with energy-dispersive spectroscopy (EDS) was used for taking scanning electron microscopy (SEM) and elemental mapping. The transmission electron microscopy (TEM) images were taken using a Tecnai F20 S/TEM operated at 200 kV. X-ray photoelectron spectroscopy (XPS) was used for the characterization of photocatalysts after fluorination using Thermo Scientific K-alphaTM spectrometer (USA) equipped with an $\text{Al K}\alpha$ X-ray source (1486.6 eV, 0.843 nm) and X-ray spot size of 400 μm in diameter. Ultraviolet–visible (UV–vis) spectroscopy was performed by a Lambda 750, PerkinElmer (USA) equipped with an integrating sphere. The specific surface area of the photocatalysts was measured by BET method (Autosorb-1, Quantachrome, USA). Photoluminescence spectra were taken by using a spectrofluorimeter, Perkin Elmer, LS45, USA. The magnetic properties of samples were measured using a Vibrating Sample Magnetometer (VSM, model EV9, ADE Technologies). An atomic absorption spectrophotometer (PinAAcle 900F, PerkinElmer, USA) was used for the measurement of iron and zinc ions concentration in the solution. The pH at the point of zero charge (pHpzc) of catalysts was determined using a ZetaPlus (Brookhaven Instrument Corp.).

3.6. Performance evaluation

3.6.1. Adsorption capacity

As mentioned before, most photocatalytic reactions take place on the surface of photocatalyst and increase the adsorption capacities of photocatalyst towards contaminants, leading to an increase in the overall removal efficiency of the process. Therefore, the evaluation of the effect of fluorination on the photocatalysts performance is performed in two steps. In the first step, the adsorption capacity of commercial ZnO and *in situ* fluorinated ZnO (Zn(OH)F) were examined and evaluated using dyes as model organic compounds. In the second step, the effect of fluorination on photocatalytic performance was examined using AMP as target compound (Section 3.6.2).

The batch adsorption experiments were conducted in 10 mL glass vials using different initial concentrations of dyes. The solutions were agitated in a fixed speed rotator for a minimum of 2 h at 600 rpm in order to achieve equilibrium at room temperature. Preliminary experiments had indicated that the required time for equilibrium was less than 30 minutes for all examined dyes. The uptake (q_{eq}) and the removal percentage of dyes by adsorption were calculated according to Eq. (3.2) and Eq. (3.3), respectively:

$$q_{eq} = \frac{(C_0 - C_{eq})V}{m} \quad (3.2)$$

where q_{eq} is the equilibrium surface loading (mg/g), C_0 and C_{eq} are the initial and equilibrium concentrations of dyes (mg/L), respectively, m is the mass of adsorbent (g), and V is the solution volume (L).

$$Removal\% = \frac{(C_0 - C_{eq})}{C_0} \times 100 \quad (3.3)$$

Among several isotherm models available in the literature, four isotherm models namely, Langmuir, Freundlich, the correct form of BET equation for liquid phase (Ebadi et al. 2009) and Dubinin–Radushkevich (D–R) isotherms are selected in the present study to correlate the adsorption experimental data. The isotherm equations, their parameters and regression analysis data for adsorption of dyes are given in Table 4.7.

3.6.2. Removal efficiency and reaction kinetics in photocatalysis

The removal efficiency of antibiotics, COD and TOC at different time intervals were determined based on Eq. (3.4):

$$R(\%) = (1 - \frac{x_t}{x_0}) \times 100 \quad (3.4)$$

where R (%) is the percentage of antibiotic, COD or TOC removal. x_t is the concentration of antibiotic (mM or mg/L), COD (mg/L) or TOC (mg/L) at time t and x_0 is the initial antibiotic concentration or initial COD or TOC value. The concentration of nitrate, nitrite, H_2O_2 and fluoride ion was measured by using nitrate, nitrite and fluoride ion kits supplied by HACH Co. USA. The measurements of TOC, COD, nitrate, nitrite and fluoride ion were carried out using (HACH DRB/200) and a spectrophotometer (HACH DR/2800). Low range COD and TOC vials were used as indicators to evaluate the mineralization of antibiotics. The kinetics of photocatalytic reaction can commonly be explained by the Langmuir-Hinshelwood model:

$$r = \frac{-dC}{dt} = \frac{k_r C}{1+KC} \quad (3.5)$$

where C is the concentration of contaminant, k_r and K are the reaction rate constant and adsorption constant, respectively. At the low contaminant concentration and low adsorption amount, the term KC can be neglected and the Langmuir-Hinshelwood equation can be transformed into pseudo-first order kinetic equation (Eq. 3.6) (Długosz et al. 2015):

$$-\ln \frac{C}{C_0} = kt \quad (3.6)$$

However, considering the difference between the total volume (V_T) and volume of photoreactor (V_P) in this study, illumination time is considered in all kinetics calculations (Eq. 3.7) (Prieto-Rodriguez et al. 2012):

$$t_i = t_e \times \frac{V_P}{V_T} \quad (3.7)$$

were, t_i and t_e are the time of illumination and time of experiment, respectively.

3.6.3. By-product formation and degradation mechanism

The measurement of antibiotics concentrations and identification of their transformation products (TPs) of SMX, AMP and AMX were conducted by LC-HR-MS/MS method. Accordingly, samples were injected (1 μ L) onto a Phenomenex Kinetex C18 column (2.1 \times 50

mm, 1.7 μm), using a Nexera UHPLC system (Shimadzu, Columbia, MD). The mobile phases were (A) water with 0.1% formic acid and (B) acetonitrile with 0.1% formic acid at the flow rate of 0.3 mL/min. A linear gradient was used starting with 3% (B), and changing to 85% (B) in 8 min. The column temperature was 40 °C. The MS and MS/MS spectra were collected on a hybrid quadrupole-time-of-flight (QqTOF) TripleTOF 5600 mass spectrometer (SCIEX, Concord, ON, Canada) equipped with a DuoSpray ion source in positive ion mode set at 5 kV source voltage, 450 °C source temperature, and 50 psi for GS1/GS2 gas flows. Data were acquired in IDA (information-dependent acquisition) mode, with a survey TOF-MS acquisition from m/z 80-925, followed by MS/MS on the 3 most intense ions from m/z 200-450 with dynamic background subtraction (DBS) with a total cycle time of 1.0 s. The MS/MS analysis of precursor ions was performed at the collision energy of 30 \pm 10 V. The data were analyzed qualitatively with PeakView v2.2 and quantitatively with MultiQuant v3.02.

3.6.4. Toxicity assessment

The antibacterial activity assays of solutions before and after treatments were conducted to evaluate the impact of applied processes on the reduction of solution toxicity. In the first method (Alsager et al. 2018), petri dishes were prepared by mixing appropriate amounts of nutrient broth and agar, followed by boiling the mixture and allowing the formation of gel for at least 1 hour. Approximately 50 μL of *E. coli* ($\sim 1 \times 10^8$ CFU/mL) from a stock solution was subsequently spread over the surface of the agar. A control experiment was conducted using agar made by irradiated water in photocatalytic experiment for 2 h in order to ensure that the observation is due to the antibiotic degradation rather than probable leachate of catalyst and/or a change in the water chemistry. The treated solutions by different processes sampled at different intervals were also used for preparation of agar and assessment of changing the toxicity by examined processes. After incubation overnight at 37 °C, the growth of *E. coli* on prepared agars was compared.

Agar-well diffusion method was also utilized to visualize the change of toxicity before and after the treatment (Gmurek et al. 2015). In this method, after the streaking of agar surface by *E. coli*, a few holes with the diameter of ~ 5 mm were punched into the agar and 50 μL of solution was introduced into the wells. The petri dishes were placed in incubator at 37 °C overnight to promote the formation of inhibition zone around the wells.

A commercial toxicity test kit (Toxtrac™, HACH, USA) was also utilized to quantitatively assess the toxicity in the term of percentage inhibition (PI) of samples according to the manufacturer's protocol. Toxtrac™ is a colorimetric method for toxicity assessment. In this method resazurin, which is a redox-active dye, changes from pink to blue when it is reduced. Bacterial respiration occurring in the sample reduces resazurin. If toxic substances are present, they inhibit the rate of resazurin reduction. The sample color is compared to a toxin-free control tube to determine how toxic the sample is to a culture of *E. coli*. The inhibition of *E. coli* strain was calculated by Eq. (3.8) (Gmurek et al. 2015):

$$\% \text{ inhibition} = \left(1 - \frac{\Delta A_{\text{sample}}}{\Delta A_{\text{control}}}\right) \times 100 \quad (3.8)$$

where: ΔA = (initial absorbance value)-(final absorbance value) at 603 nm.

3.6.5. Durability and stability of photocatalysts

The long-term stability of photocatalyst is one of the most important parameters that governs their utilization in water treatment processes (Kovacic et al. 2017). In order to evaluate the stability of photocatalysts, consecutive experiments were carried out under optimum operating conditions and the photocatalytic performance was compared in the repeated experiments. The decrease of photocatalytic activity of ZnO-based photocatalysts resulted from the photocorrosion phenomenon, as reported before (Mirzaei et al. 2016, Zou et al. 2017a). Photocorrosion consists of the release of Zn^{2+} and the collapse and deactivation of the ZnO structure under UV irradiation due to the self-oxidation of photocatalytic (Eq. 3.9) (Vu et al. 2013):



In this study, the concentration of zinc, iron and fluoride ions in filtrates of the experiments at different time intervals was measured as an indicator of photocatalysts stability.

3.6.6. Energy consumption

The process optimization in order to minimize the operation cost for industrial wastewater treatment processes is crucial in AOPs. Thus, electrical energy per order (E_{EO}), which is approved by the Photochemistry Commission of the International Union of Pure and Applied Chemistry (IUPAC) (Cater et al. 2000), as a figures-of-merit for AOPs is used in this study as a criteria to evaluate and compare the efficiency of contaminant removal based on energy consumption according to Eq. (3.10) (Lam et al. 2013):

$$E_{EO} = \frac{P \times t \times 1000}{V \times 60 \times \log\left(\frac{C_i}{C_f}\right)} \quad (3.10)$$

where P is the power to drive the UV lamp(s) (kW), t is the irradiation time (min), V is the volume of the water in the reactor (L), C_i and C_f are the initial and final concentrations of contaminants. E_{EO} is defined as the amount of kilowatt hours of electrical energy needed to decrease the concentration of a contaminant by one order of magnitude (90 %) in one m³ of solution (Cater et al. 2000).

4. Results and Discussion

4.1. Photocatalytic degradation of SMX by surface fluorinated ZnO

4.1.1. Experimental condition

The experimental setup is described in section (3.1). The solution pH was adjusted at the required value by 0.1 N HCl or 0.1 N NaOH. Before illumination, the solutions were circulated for 30 min in the dark to reach adsorption/desorption equilibrium between photocatalysts, SMX and fluoride ions. At given time intervals, a 10 mL sample of the solution was withdrawn from the reactor for the ensuing analyses. The corresponding range of independent parameters including catalysts dosage, pH of solution, airflow rate and fluoride ion concentration, were determined based on the preliminary experiments, as presented in Table 4.1.

Table 4.1. Actual and coded levels of the independent parameters of the experimental design for SMX removal by using F-ZnO

Factors	Symbol	Real values of coded levels				
		$-\alpha$ (-2)	-1	0	+1	$+\alpha$ (+2)
Catalyst dosage (g/L)	X ₁	0.3	0.6	0.9	1.2	1.5
pH of solution	X ₂	1	3	5	7	9
Airflow rate (L/min)	X ₃	0.5	1	1.5	2	2.5
Concentration of NH ₄ F (mM)	X ₄	0	1	2	3	4

4.1.2. Results and discussion of photocatalytic removal of SMX by fluorinated ZnO

4.1.2.1. Analysis of CCD

Based on the experimental results presented in Table 4.2, a polynomial function was found to adequately represent the response, predicting the percentage of SMX removal (R) at the examined levels of selected parameters. Eq. (4.1) expresses the relative importance of each parameter as well as their interaction.

$$R = 89.82 + 12.53X_1 + 3.89X_2 - 14.41X_3 + 3.37X_4 - 5.69X_1^2 - 0.45X_2^2 + 3.59X_3^2 - 1.43X_4^2 - 0.33(X_1 \times X_2) + 0.65(X_1 \times X_3) + 1.73(X_1 \times X_4) + 0.45(X_2 \times X_3) - 0.1(X_2 \times X_4) + 0.69(X_3 \times X_4) \quad (4.1)$$

The analysis of variance (ANOVA) was carried out and details are provided in Table 4.3. The P -value of the model, which was <0.0001 , and the F -value of 35.21 confirmed that the model was highly significant, which is supported by the good agreement between the predicted values and observed results in Fig. 4.1 and Table 4.3. The polynomial equation fitted the

experimental results within a 98.01% confidence interval, which is in good agreement with the adjusted R^2 (95.25%). Fig. 4.1 shows the goodness of fit between the predicted and observed values where the line of the best fit with $R^2 = 0.9814$ was obtained, further confirming the reliability of model. The F -value and P -value were used to determine the significance of each term. The smaller P -value and higher F -value for each term indicate the significance of its corresponding coefficient and the higher contribution towards the response variable (Shayegan et al. 2013).

Table 4.2. Four factors experimental design and observed and predicted values for the central composite design.

Run	levels of variables				Response (% removal of SMX)		Residual
	X ₁	X ₂	X ₃	X ₄	R _{observed}	R _{predicted}	
1	1.2	7	2.0	1	90.50	89.97	0.53
2	0.6	3	1.0	1	90.44	89.61	0.83
3	0.6	3	2.0	3	88.16	87.85	0.32
4	0.6	3	2.0	1	88.55	88.38	0.17
5	0.3	5	1.5	2	86.60	86.92	-0.32
6	0.9	5	1.5	4	84.97	85.66	-0.69
7	0.9	1	1.5	2	86.00	86.67	-0.67
8	0.9	5	1.5	2	92.00	92.00	0
9	1.5	5	1.5	2	92.59	92.99	-0.40
10	1.2	3	2.0	3	93.23	92.51	0.72
11	0.6	7	1.0	3	85.68	84.86	0.82
12	0.9	5	1.5	2	92.06	92.00	-0.06
13	1.2	3	2.0	1	90.67	90.98	-0.31
14	1.2	7	1.0	1	89.22	89.02	0.20
15	0.9	5	1.5	2	92.03	92.00	-0.03
16	0.6	7	2.0	3	86.99	86.79	0.20
17	1.2	3	1.0	1	91.82	91.81	0.01
18	0.9	5	1.5	0	86.84	86.87	-0.032
19	0.9	5	1.5	2	91.81	92.00	0.19
20	0.9	9	1.5	2	82.78	82.83	-0.047
21	0.6	7	1.0	1	87.09	87.61	-0.52
22	0.6	7	2.0	1	88.03	88.17	-0.14
23	1.2	3	1.0	3	92.62	91.97	0.65
24	0.9	5	1.5	2	91.67	92.00	0.33
25	0.9	5	2.5	2	95.91	96.14	-0.23
26	0.6	3	1.0	3	87.36	87.69	-0.33
27	0.9	5	1.5	2	92.17	92.00	-0.17
28	1.2	7	2.0	3	90.35	90.67	-0.32
29	1.2	7	1.0	3	88.37	88.34	0.031
30	0.9	5	0.5	2	94.55	95.04	-0.49

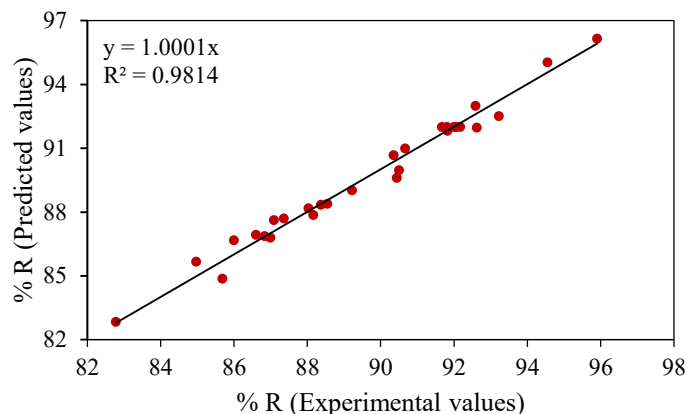


Figure 4.1. Correlation between the experimental and predicted photodegradation efficiencies of SMX.

Table 4.3. Analysis of variances (ANOVA) for SMX removal.

Source	Sum of squares	Degree of freedom	Adjusted mean square	F-value	P-value
Model	239.908	14	17.14	35.21	<0.0001
Linear factors	81.581	4	20.39	41.91	<0.0001
Quadratic factors	147.470	4	36.87	75.75	<0.0001
Interaction factors	10.857	6	1.81	3.72	0.033
Residuals	4.867	10	0.4867	--	--
Total	244.775	24	--	--	--

$R^2=98.01\%$, $adj\text{-}R^2=95.23\%$

In order to evaluate the importance of factors in Eq. (4.1), the Pareto equation is used and the percentage effect of each parameter on the removal of SMX was calculated according to the following equation (Chen et al. 2012):

$$P_i = \left(\frac{a_i^2}{\sum a_i^2} \right) \times 100 \quad (4.2)$$

where P_i is the percentage effect of each variable and a_i represents statistically significant coefficients in Eq. (4.1). The result of the Pareto graphic analysis is illustrated in Fig. 4.2. As shown in the figure, the most important parameters for the photodegradation of SMX were airflow rate (X_3) followed by the amount of photocatalyst (X_1).

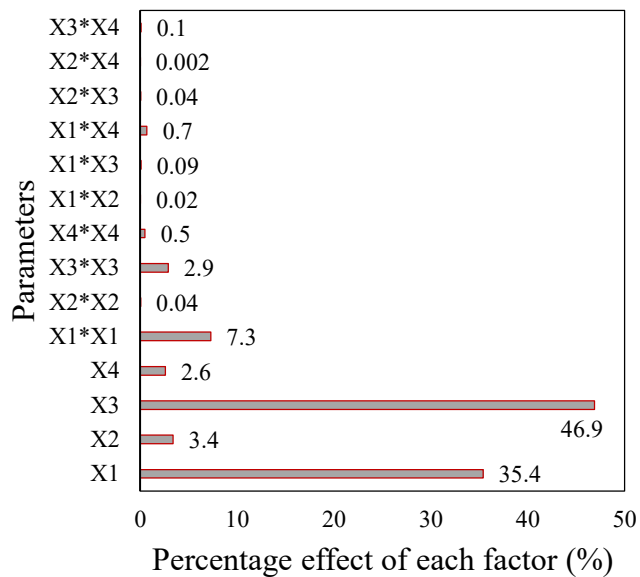


Figure 4.2. Pareto graphic analysis for the photodegradation efficiency of SMX.

4.1.2.2. Effect of operating parameters on removal efficiency of SMX

The 3D response surface and contour plots were used to illustrate the effects of independent parameters and of interactions between independent parameters on the removal of SMX (Fig. 4.3).

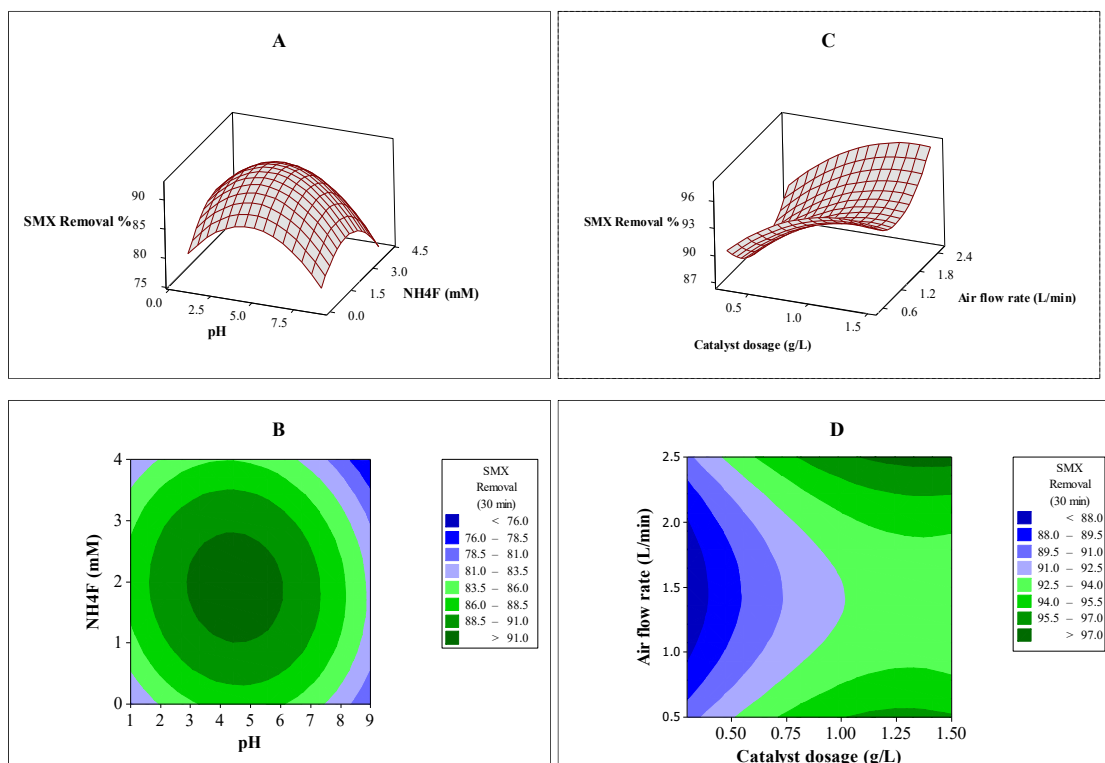


Figure 4.3. The response surface (A) and contour plots (B) of photocatalytic removal efficiency of SMX as the function of pH of solution and concentration of NH₄F (mM); the response surface (C) and contour plots (D) of photocatalytic removal efficiency of SMX as the function of catalyst dosage (g/L) and air flow rate (L/min); (reaction time = 30 min, temperature= 21 °C).

Effect of photocatalyst dosage

The heterogeneous photocatalytic degradation usually increases with the photocatalyst concentration towards a limit at high catalyst concentrations (Prieto-Rodriguez et al. 2012). From Figs. 4.3C and 4.3D, the positive effect of increasing the photocatalyst dosage on the percentage of SMX degradation is clearly indicated. The addition of photocatalyst enhanced the removal efficiencies of SMX and COD. This could be attributed to the higher generation of ROS on active surface sites of the photocatalyst (Ding et al. 2013). As illustrated in Fig. 4.6, the addition of optimum concentration of photocatalyst also increased the COD removal from 4.8%, obtained by photolysis, to 85% by photocatalysis after 90 min of reaction. However, at concentrations higher than the optimum value (1.48 g/L), the increase in removal efficiency demonstrated a slower rate. This was caused by the increase in turbidity and the ensuing scattering phenomena which reduced the UV light penetration into the suspension (Abellán et al. 2009, Elmolla and

Chaudhuri 2010b). In addition, the SMX molecules and the catalyst particles compete for the photons emitting from the UV lamp.

Effect of solution pH

The pH of solution plays an important role in the degradation and mineralization of contaminants in photocatalytic processes (Elmolla and Chaudhuri 2010b, Mirzaei et al. 2016). Generally, photocatalytic degradation efficiency improves by increasing the pH of solution (Mirzaei et al. 2016). This is due to the availability of higher amounts of hydroxyl ions at basic condition as the main precursor of $\text{OH}\cdot$ radical by reacting with the photo-generated holes. However, the removal of SMX was shown to be more efficient under acidic conditions and at an optimum pH of 4.8 (Fig. 4.3A) since surface fluorination of photocatalysts can be carried out in acidic media (Liu et al. 2012, Park and Choi 2004). Therefore, a trade-off should be found between these two competitive parameters. In addition, in very acidic solutions, ZnO will dissolve as zinc ions, which will reduce the photocatalyst active sites and the efficiency of removal. When the solution pH was equal to 1 (run 7, Table 4.2), the photocatalyst particles were totally dissolved and the reaction proceeded as direct photolysis. Since the pH of solution affects the extent and efficiency of surface fluorination, the ionization potential of SMX as well as the photocatalyst surface properties and homogenous reactions, it is difficult to evaluate the effect of pH and the exact contribution of each phenomenon.

Effect of fluoride ion concentration

As seen from Figs. 4.3A and 4.3B, the addition of NH_4F as the surface modifier had a positive impact on the removal of SMX, up to the optimum concentration (2.505 mM). It has been shown that the surface charge separation and transfer, production of active radical species, and the resulting surface photocatalytic reaction mechanisms and kinetics can be altered by surface fluorination of photocatalysts (Liu et al. 2012). In addition, surface fluorination leads to the production of unbound hydroxyl radicals, instead of attached surface radicals. Photo-generated short-living $\text{OH}\cdot$ radicals which are attached to the surface of photocatalyst would be transformed to inactive OH functional groups on the surface of photocatalysts (Liu et al. 2010). Considering that the redox potential of free hydroxyl radicals (2.3 eV vs NHE) is larger than that

of bound hydroxyl radicals, ($\sim 1.5\text{--}1.7$ eV vs NHE) (Xu et al. 2007), it is expected that surface fluorination enhances the efficiency of SMX removal and mineralization. Moreover, the presence of fluoride ions as the most electronegative element on the surface of photocatalyst causes a stronger electron storage capacity compared to the pristine ZnO, thus inhibits charge recombination and enhances free $\text{OH}\cdot$ radicals generation (Liu et al. 2012). However, the presence of fluoride ions at higher than the optimum concentration (2.505 mM), led to the reduction in SMX removal. This was probably due to the reduction of O_2° species as a result of hindering electron separation and transfer on the surface of ZnO. The effect of O_2° radicals on the photodegradation efficiency is discussed in the following section.

Effect of airflow rate

Aeration improves the mixing of solution in the photoreactor and reduces mass transfer limitations, while providing oxygen as the electron acceptor to separate the photo-generated electron/holes and produce O_2° species which can promote the degradation of organic contaminants (Ding et al. 2013). Moreover, a linear dependence between dissolved oxygen concentration and hydroxyl radical generation has been reported (Abellán et al. 2007, Wang and Hong 2000). Without an electron acceptor such as oxygen molecules, the photo-generated electron/ hole pairs will recombine rapidly (Wang and Hong 2000). In addition, the importance of O_2° species in the mineralization of organic contaminants has been reported (Ryu et al. 2017). As illustrated in Fig. 4.2, the airflow rate (X_3) was the most significant parameter and had the highest impact on the removal of SMX. Wang et al. (2007) demonstrated that beside the conventional electron-scavenging effect, dissolved O_2 played a critical role in the degradation of produced intermediates. As shown in Fig. 4.3, the removal efficiency of SMX was reduced until a critical point and then it was enhanced and there was a minimal point about 1.5 L/min of airflow rate. This is because the increase of airflow rate may decrease the removal efficiency due to the scattering of light by smooth surface of bubbles and shielding effects, which hinder the removal of SMX via photolysis and photocatalysis. Therefore, a trade-off should be made between providing dissolved oxygen and scattering effect in order to achieve high SMX removal. Airflow rates higher than 2.5 L/min were not examined in this study due to the limitation of photoreactor.

4.1.2.3. Determination of optimal conditions

The main objectives of process optimization were to determine the optimum values of operating and process parameters for the photocatalytic removal of SMX and to further evaluate the mechanism of photocatalytic reactions under optimum conditions. For this purpose, the desired objective in term of the removal efficiency of SMX was defined as “maximize” to achieve the highest removal percentage after 30 min of reaction. The obtained optimum values are listed in Table 4.4. To validate that the model was satisfactory for predicting the maximum photodegradation of SMX, an additional experiment was conducted at the optimum condition. As presented in Table 4.4, the obtained SMX removal percentage (95.76%) was close to the predicted value (96.23%), which indicates that RSM is a useful mathematical tool for modeling and optimization of SMX photocatalytic removal process. Therefore, the optimum values estimated by the RSM were selected for use in the ensuing experiments.

Table 4.4. Optimum operating conditions of the parameters of process.

Parameter	Optimum values
Catalyst dosage (g/L) (X_1)	1.48
pH of solution (X_2)	4.72
Airflow rate (L/min) (X_3)	2.5
Concentration of NH_4F (mM) (X_4)	2.505
Predicted SMX removal (%) after 30 min	96.23
Experimental SMX removal (%) after 30 min	95.76

4.1.2.4. Mechanism of SMX removal reaction

As shown in Fig. 4.4, the adsorption of SMX on the surface of photocatalysts was very low. Therefore, the photosensitization mechanism is unlikely to occur since it would require efficient adsorption of contaminants on the surface of photocatalysts and electron transfer from the excited SMX molecule to the conduction band of photocatalysts (Liu et al. 2010). The low adsorption of SMX on the surface of other photocatalysts such as TiO_2 has also been reported before (Nasuhoglu et al. 2011). Surface fluorination slightly enhanced the adsorption capacity of ZnO. The presence of KI as the scavenger of hole and hydroxyl radical totally hindered the adsorption of SMX on the photocatalyst. This occurred because the concentration of KI was 20

times higher than SMX, hence the iodide ions in the solution could compete with the SMX molecules for adsorption on the surface of photocatalyst. In addition, a considerable removal of SMX was observed by direct photolysis in the absence of photocatalyst. This happened because SMX can absorb UV light up to 310 nm (maximum absorption at 263 nm) (Abellán et al. 2007), which is close to the wavelength of the examined UVC lamp (254 nm). The high removal of SMX by photolysis under UVC irradiation has been reported before (Kim and Kan 2016, Nasuhoglu et al. 2011). After a short reaction time of photolysis, the color of solution changed to brownish which indicated the formation of intermediate compounds. Under these conditions, only 4.8% COD removal was obtained after 90 minutes of reaction. This means that in contrast to SMX that was shown to be prone to photolysis, photo-induced intermediates were not susceptible to photolysis. Under optimum conditions, 95.76% SMX removal was achieved after 30 min reaction, which is higher than the efficiencies obtained with bare ZnO (82%) and with TiO₂ (P25) with 79%. This is due to the higher amount of photo-generated OH• radicals and adsorption capacity of F-ZnO compared to bare ZnO and P25. To evaluate the role of OH• radicals in the removal of SMX, the photocatalytic reaction was carried out in the presence of 20 mM *tert*-butanol (TBA), a well-known OH• radical scavenger. As illustrated in Fig. 4.4, the addition of TBA as the hydroxyl radical scavenger resulted in a significant decrease in the degradation rate of SMX removal by ZnO. This further confirmed the role of OH• radicals in the degradation of SMX. Długosz et al. (2015) also emphasized the role of hydroxyl radicals formation in the photocatalytic degradation of SMX. The reduction of SMX removal efficiency in the presence of TBA was more evident for F-ZnO in comparison with bare ZnO. Since TBA can selectively scavenge hydroxyl radicals, the higher difference between removal efficiency in the absence and presence of TBA for UV/F-ZnO, compared to UV/ZnO process, further confirmed the higher contributions of hydroxyl radicals in the F-ZnO process. The addition of KI, which acts as both h⁺ and OH• scavenger, considerably hindered the removal of SMX, which was even lower than the removal obtained by photolysis. However, this reduction was more evident in the case of F-ZnO system due to the generation of additional OH• radicals as well as a higher contribution of holes in this system. The higher contribution of holes in the presence of fluoride ions is result of holding of photo-induced electrons on the surface by fluorine as the most electronegative element, which has been reported before (Ryu et al. 2017). However, due to the electronegativity of fluoride ions on the surface of ZnO, the production of O₂^{-•} is reduced.

Therefore, the addition of KI in the F-ZnO process not only scavenged both radicals and holes, but also due to the presence of photocatalyst particles and the ensuing scattering effect, it reduced the efficiency of SMX removal below the efficiency observed by direct photolysis. In summary, the surface fluorination is an effective method to increase hydroxyl radical production, but it decreases $O_2^{\cdot-}$ generation. Considering the fact that OH^{\cdot} radicals are more powerful than $O_2^{\cdot-}$ radicals (2.69 eV vs. NHE and -0.33 eV vs. NHE, respectively) (Li et al. 2016), the efficiency of SMX removal was increased by surface fluorination. However, the reduction of SMX efficiency at high concentrations of NH_4F (beyond the optimum value) revealed that the generation of $O_2^{\cdot-}$ radicals is somewhat essential. It is reported that some produced intermediates will undergo reduction reactions by $O_2^{\cdot-}$ species, which will be used in the reaction as a main reductant species (Ryu et al. 2017).

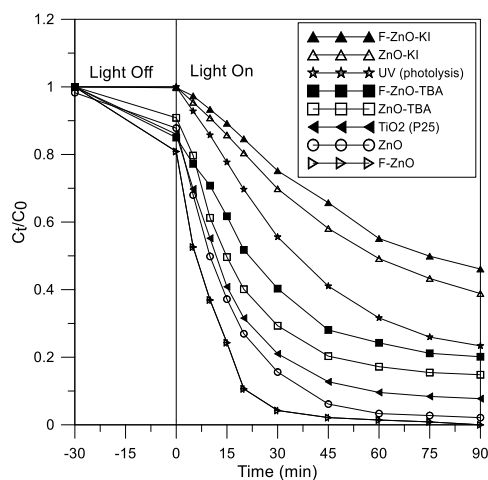


Figure 4.4. Variation of SMX dimensionless concentration with time in the presence and absence of scavengers; $[SMX]_0 = 1 \text{ mM}$, $[catalysts] = 1.487 \text{ g/L}$, $pH = 4.8$, $airflow \text{ rate} = 2.5 \text{ L/min}$, $[F^-] = 2.505 \text{ mM}$ for F-ZnO, $temperature = 21 \text{ }^\circ\text{C}$, $[TBA] = 20 \text{ mM}$, $[KI]_0 = 20 \text{ mM}$.

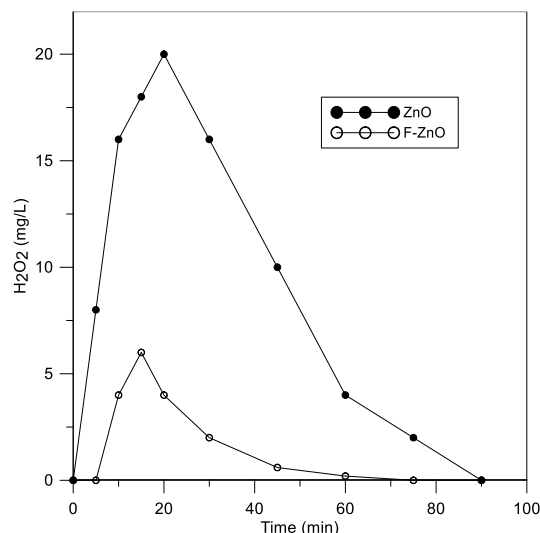
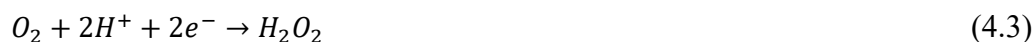


Figure 4.5 Time evolution of hydrogen peroxide concentration formed during the photocatalytic oxidation of sulfamethoxazole by ZnO and F-ZnO, $[SMX]_0 = 1 \text{ mM}$, $[catalysts] = 1.487 \text{ g/L}$, $pH = 4.8$, airflow rate = 2.5 L/min , $[F^-] = 2.505 \text{ mM}$ for F-ZnO, temperature = $21 \text{ }^\circ\text{C}$.

The photo-generated H_2O_2 concentration during the photodegradation experiments was monitored by titration method. Hydrogen peroxide can directly participate in the oxidation of contaminants or it will produce extra hydroxyl radicals. Fig. 4.5 illustrates the concentration profile of H_2O_2 produced during SMX photodegradation by bare ZnO and by F-ZnO at the optimum condition. While the photocatalytic removal of SMX and COD by F-ZnO were higher than that of bare ZnO, H_2O_2 concentration during the photodegradation by F-ZnO was lower, possibly due to the hindering interfacial electron transfer to dissolved oxygen which is required for H_2O_2 generation based on Eq. (4.3) (Kim et al. 2018).



The maximum concentration of H_2O_2 produced during the photocatalytic process by F-ZnO was about three times lower than that obtained with bare ZnO.

4.1.2.5. COD removal

Chemical oxygen demand is an important water quality parameter since, it provides an index to evaluate the effect discharged wastewater will have on the receiving water bodies. Higher COD levels mean a greater amount of oxidizable organic compounds in the effluent, which will reduce dissolved oxygen (DO) levels. A reduction in DO can lead to anaerobic conditions, which is deleterious to higher aquatic life forms. Changed in COD also has been considered as an

indicator of the extent of mineralization in some studies (Kim and Kan 2016, Nasuhoglu et al. 2011). The persistence of SMX and intermediates in the solution was evaluated by conducting experiments for 90 minutes using photolytic and photocatalytic processes under the optimum operating conditions. According to Fig. 4.6, the mineralization of SMX required a considerably longer reaction time than its degradation. Approximately 85% of the initial COD was removed by F-ZnO; however only 4.8% COD removal was achieved for photolysis even after 90 min of irradiation. It is concluded that, although SMX can be partially degraded by photolysis, the degradation of intermediates that were generated by the photolytic reaction is more difficult. The COD removal efficiencies were improved when F-ZnO was used at the optimum condition at three considered time intervals compared to bare ZnO and TiO₂ Degussa P25.

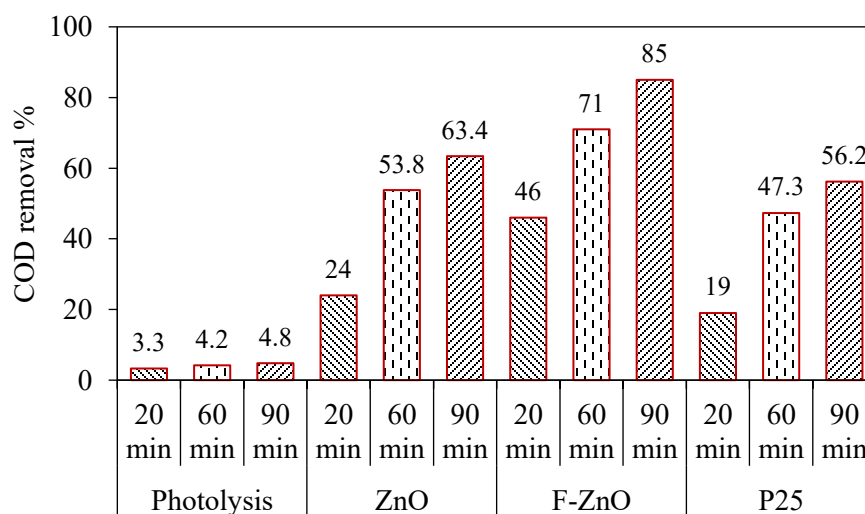


Figure 4.6. COD removal by photolysis, and photocatalysis by using ZnO, F-ZnO and TiO₂ Degussa P25 after 20, 60 and 90 min; [SMX]₀ = 1 mM, [catalysts] = 1.487 g/L, pH = 4.8, airflow rate = 2.5 L/min, ([F^{•-}] = 2.505 mM for F-ZnO), temperature = 21 °C.

4.1.2.6. Kinetics of reaction

In order to study the kinetics of photocatalytic degradation of SMX removal, experiments were conducted under the optimum operating conditions and initial SMX concentration of 1mM. As shown in Fig. 4.7, the kinetics of SMX removal photocatalytic degradation was also compared to the results obtained with bare ZnO and TiO₂ Degussa P25.

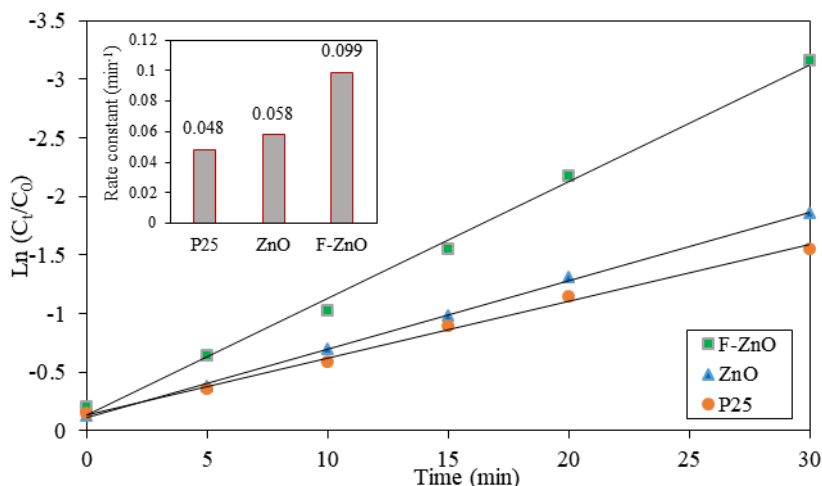


Figure 4.7. Pseudo-first-order reaction rate of and first order initial rate constant of SMX removal; $[SMX]_0 = 1 \text{ mM}$, $[catalysts] = 1.487 \text{ g/L}$, $pH = 4.8$, $airflow \text{ rate} = 2.5 \text{ L/min}$, $([F] = 2.505 \text{ mM for F-ZnO})$, $temperature = 20 \text{ }^\circ\text{C}$, inset: reaction rate constants.

The photocatalytic removal rate of SMX was relatively high during the first 30 minutes of reaction, but the reaction rate decreased as the reactions proceeded. This could be related to the formation of intermediates and ionic species such as SO_4^{2-} during the reaction which can compete with SMX, either for adsorption on the photocatalyst, absorption of available UV light and/or reaction by ROS (Abellán et al. 2007, Abellán et al. 2009, Ding et al. 2013). The highest rate constant (0.099 min^{-1}) for the degradation of SMX was achieved by F-ZnO, followed by bare ZnO (0.058 min^{-1}) and TiO_2 Degussa P25 (0.048 min^{-1}), respectively.

4.1.2.7. Stability of photocatalyst

The long-term stability of photocatalysts is one of the most important parameters that governs their utilization in water treatment processes (Kovacic et al. 2017). In order to evaluate the stability of photocatalysts, recycled experiments for photocatalytic degradation of SMX were carried out under the optimum operating conditions. As illustrated in Fig. 4.8A, at the first cycle, the removal efficiency of SMX by F-ZnO was higher than that of ZnO and P25. However, a sharp drop in SMX removal efficiency was shown after the first cycle. After four cycles, the efficiency of F-ZnO for the removal of SMX was lower than bare ZnO and P25. The SMX removal was reduced from 82% to 60% after four cycles by bare ZnO, while by using F-ZnO the efficiency drop was more obvious and declined from 95% to 55%. It should be noted that P25 displayed a relatively lower photocatalytic activity compared to bare ZnO and F-ZnO at the first

cycle. However, the results showed that its performance in long-term stability is better than ZnO-based photocatalysts. The substantial decrease of photocatalytic activity of ZnO-based photocatalysts resulted from the photocorrosion phenomenon, as reported before (Mirzaei et al. 2016, Zou et al. 2017a). It is known that the photocorrosion of photocatalyst (Eq. 3.9) and photocatalytic reactions are two competitive processes (Zhao et al. 2017).

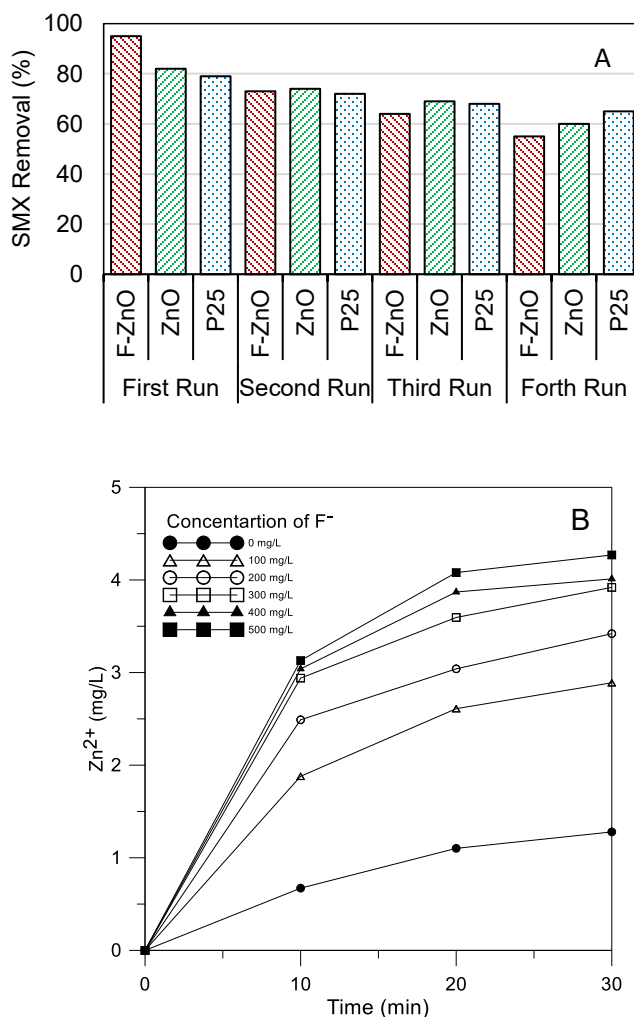


Figure 4.8. (A) Cycling photocatalytic tests by using F-ZnO, ZnO and TiO₂ (P25), [SMX]₀ = 1 mM, [catalysts] = 1.487 g/L, pH = 4.8, airflow rate = 2.5 L/min, ([NH₄F] = 2.505 mM for F-ZnO), temperature = 20 °C; (B) Release of Zn²⁺ ions into the solution in the presence of fluoride ions in various concentration.

Fig. 4.8B shows that the amount of Zn²⁺ released into the solution by photocorrosion is proportional to the concentration of fluoride ion in the solution. Based on the Eq. (3.9), the photo-induced h^+ could be the main reason for the photocorrosion of ZnO (Ma et al. 2017). The reason behind the enhancement of Zn²⁺ ion leaching by surface fluorination is the higher

availability of photo-induced h^+ by holding of electrons on the surface. The higher availability of holes and their contribution to the reaction leads to the self-corrosion of ZnO, release of Zn^{2+} and reductions in the photocatalytic efficiency in consecutive runs. It should be emphasized that despite the higher efficiency of F-ZnO for the removal of SMX and COD and the higher rate of degradation, the results indicated a negative effect of surface fluorination on the photostability of ZnO photocatalyst.

4.1.2.8. Energy consumption

The high-energy consumption of AOP is the main obstacle to the utilization of photocatalytic process in water and wastewater treatment plants. The process economic is often the dominant factor in selecting an advanced oxidation process (Saien et al. 2014). Photocatalytic degradation of aqueous organic contaminants is an electric-energy-intensive process, and the electric energy represents the major fraction of the operating costs. The *electrical energy per order* (E_{EO}) (Eq. 3.10), is used in this study as a criteria to evaluate and compare the removal efficiency based on energy consumption. As presented in Table 4.5, the electrical energy required in the process developed in this study is lower than that reported in most previous studies of photocatalytic degradation of SMX. Table 4.5, lists a high diverse range of energy consumption for SMX removal by photocatalysis process under UV irradiation. The main reasons for the low energy consumption in this study could be summarized as follow: (i) enhancing the removal efficiency and removal rate by slowing down the recombination rate and increasing the hydrophobicity of photocatalyst, which led to the promotion of hydroxyl radical generation and oxidation of SMX, (ii) utilizing low energy consuming UVC lamp, which had a substantial overlap with maximum absorption wavelength of SMX and led to the photolysis of SMX in addition to photocatalytic oxidation, (iii) using a annular narrow photoreactor which led to utilizing all emitted radiation and increasing the quantum yield. Based on Eq. (3.10), the energy consumption of process depends on the rate of reaction. In addition, different parameters such as the mixing efficiency and mass transfer limitations, type and concentration of photocatalyst, pH and temperature of solution, geometry of reactor etc. can considerably affect the reaction rate and consequently the energy consumption (Friedmann et al. 2010). Therefore, in order to reduce the energy consumption of process and promote the feasibility of photocatalytic process, the above-mentioned parameters should all be taken into consideration.

Table 4.5. Comparison of energy consumption for removal of SMX by photocatalytic removal under UV irradiation based on calculated E_{EO} .

Photocatalyst	Lamp(s)	Maximum k (min^{-1})	Solution volume (mL)	(E_{EO}) ($\text{kWh/m}^3 \cdot \text{order}$)	Ref.
TiO ₂ -2.7% rGO nanocomposites	160 W (UVA)	0.0126	25	19504.7	(Lin et al. 2017)
Immobilized TiO ₂	24 W (UVA)	0.0568	45	360.5	(Ramasundaram et al. 2016)
P25/CoFe ₂ O ₄ heterojunction	96 W (UVA)	0.0542	150	449.2	(Gong and Chu 2015)
TiO ₂ -expanded perlite	48 W (UVA)	0.00289	30	21060.2	(Długosz et al. 2015)
TiO ₂ (Degussa P25)	15 W (UVA)	90% removal in 400 min	50	52115.3	(Yang et al. 2015)
TiO ₂ (Degussa P25)	450 W (UVA)	0.054	50	6435.75	(Hu et al. 2007b)
Immobilized TiO ₂	75 W (UVA)	0.013	325	681.67	(Carbonaro et al. 2013)
TiO ₂ and FeCl ₃ mixture	160 W (UVA)	0.078	100	787.7	(Adamek et al. 2012)
TiO ₂ /hydroxyapatite	18 W (UVA)	0.267	1000	2.59	(Chun et al. 2014)
TiO ₂ (Degussa P25)	9 W (UVA)	0.225	350	4.39	(Xekoukoulotakis et al. 2011)
biochar-supported TiO ₂	15 W (UVC)	90 % in 6h	100	390.8	(Kim and Kan 2016)
F-ZnO	10 W (UVC)	0.099	1000	3.88	This study

4.1.2.9. Toxicity assessment

During the degradation of antibiotics, many intermediate compounds are formed that may be more toxic than the parent compounds. Therefore, total mineralization or at least their transformation into non-toxic compounds should be considered in addition to the removal of parent antibiotics contaminant (Mirzaei et al. 2017b, Nasuhoglu et al. 2011, Ryu et al. 2017). Fig. 4.10 shows the percentage inhibition (PI) of solution by ZnO, F-ZnO and TiO₂ (P25) at two reaction intervals. The results showed a high inhibition percentage of SMX solution towards *E. coli* before the photocatalytic degradation. The results obtained after 15 minutes of reaction indicated that the oxidation of SMX led to the generation of intermediates which showed some degree of toxicity (PI >10%), although lower than the initial samples. After 30 minutes of reaction, the toxicity of solutions treated by all photocatalysts fell within the non-toxic range, which demonstrated the effectiveness of photocatalytic degradation in the reduction of toxicity. It should be noted that the reduction in toxicity towards *E. coli* by F-ZnO was obtained at a

shorter time compared to ZnO and TiO₂ (P25). F-ZnO was the most appropriate process to reduce the toxicity or even eliminate it. This is due to the generation of more OH[•] radicals by F-ZnO and ring cleavage of SMX and intermediates by hydroxyl radical oxidation mechanism.

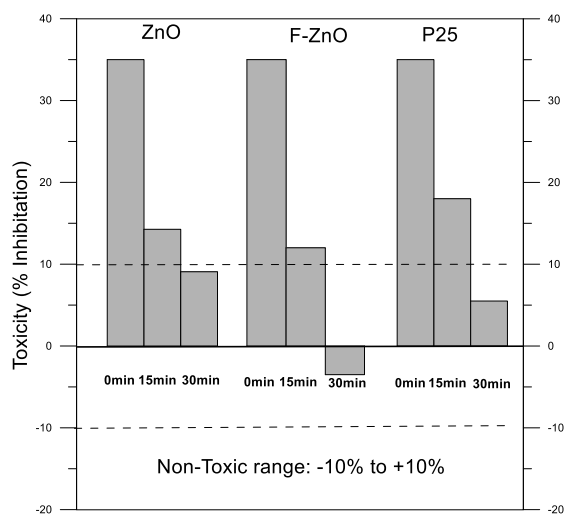


Figure 4.9. Changes in toxicities (as measured by inhibition to *E. coli* bacteria) before treatment and after different stages of photocatalytic degradation of SMX by different photocatalysts.

The magnified images of cultured plates with the zone of inhibition for the *E. coli* strain is presented in Fig. 4.10. An untreated sample of SMX was added to the well at the right side of the picture, while the treated solution by F-ZnO after 30 min reaction was added to the well at the left side of the picture. The zone of inhibition around the untreated sample and the growth of bacterial colonies around the treated sample further confirmed the non-toxic characteristics of the treated solution.

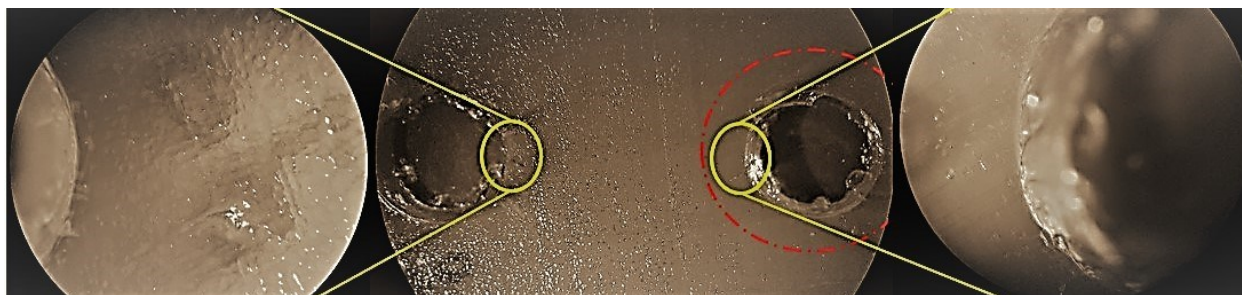


Figure 4.10. The growth inhibition zone of *E. coli* bacteria against the SMX (right) and after 30 min treatment (left).

4.1.3. Conclusions and remarks related to the photocatalytic degradation of SMX by surface fluorinated ZnO

The photocatalytic degradation of sulfamethoxazole (SMX) by ZnO in the presence of fluoride ions (F-ZnO) was evaluated. The effects of operating parameters on the efficiency of SMX removal were investigated by using RSM. Under the optimum condition, i.e. photocatalyst dosage = 1.48 g/L, pH 4.7, airflow rate = 2.5 L/min and the concentration of fluoride ions = 2.505 mM, about 97% SMX removal was achieved by F-ZnO after 30 min of reaction. The mechanism of reactions, COD removal efficiency and reaction kinetics were also investigated under optimum operating conditions. In addition, about 85% COD reduction was obtained after 90 min photocatalytic reaction. The pseudo-first-order kinetics rate constants for the photodegradation of SMX were found to be 0.099, 0.058 and 0.048 min^{-1} by F-ZnO, ZnO and TiO₂ (P25), respectively. The figure-of-merit electrical energy per order (E_{EO}) was used for estimating the electrical energy efficiency, which was shown to be considerably lower than the energy consumption for the reported research on removal of SMX by photocatalytic degradation under UV irradiation. Toxicity assays were conducted by measuring the inhibition percentage (PI) towards *E. coli* bacteria strain and by agar well diffusion method. The results showed that after 30 minutes of reaction, the toxicity of the treated solutions by all photocatalysts fell within the non-toxic range; however, the reduction in toxicity by F-ZnO was faster than those by ZnO and P25.

Despite the positive effects of surface fluorination of ZnO on the SMX and COD removal and reaction kinetics, its lower stability compared to ZnO and P25 in the repeated experiments gave rise to some doubts about its performance from a practical point of view. Moreover, as mentioned in Section 3.4.1, the remaining fluoride ion in the solution after treatment should be taken into the account. In the following sections, *in situ* fluorination of ZnO and its performance in the adsorption of organic contaminants and photocatalysis process were investigated.

4.2. Adsorption behavior of ZnO and Zn(OH)F

4.2.1. Experimental condition

Equilibrium adsorption experiments were performed at 20 ± 1 °C under batch conditions. For single-component adsorption experiments, 25 mg of adsorbent were added to 5 ml of freshly prepared dye solutions in the range of 25-250 mg/L at natural pH of solution (pH 6.5). To assure

the reproducibility of the data, all the isotherm experiments were repeated in triplicate and average values were reported. Eq. (3.2) and Eq. (3.3) were used to evaluate the adsorption capacity and removal percentage during the adsorption, respectively.

4.2.2. Results and discussion

4.2.2.1. Characterization of adsorbent/catalyst

SEM was used to evaluate the surface morphology of the bare ZnO and ZF1. Fig. 4.11(a–c) show the SEM images of the bare ZnO particles at different magnifications. Fig. 4.11(d–f) illustrate that the ZF1 particles formed a hierarchical structure during the solvothermal process. Fig. 4.11(f) reveals that some needle-like catalysts, possibly Zn(OH)F, are attached on the surfaces of ZnO microparticles. EDS mapping images of ZF1 are presented in Fig. 4.11(g) where the Zn, O and F elements are clearly detected, confirming that fluorine has been embedded uniformly into the ZnO structure.

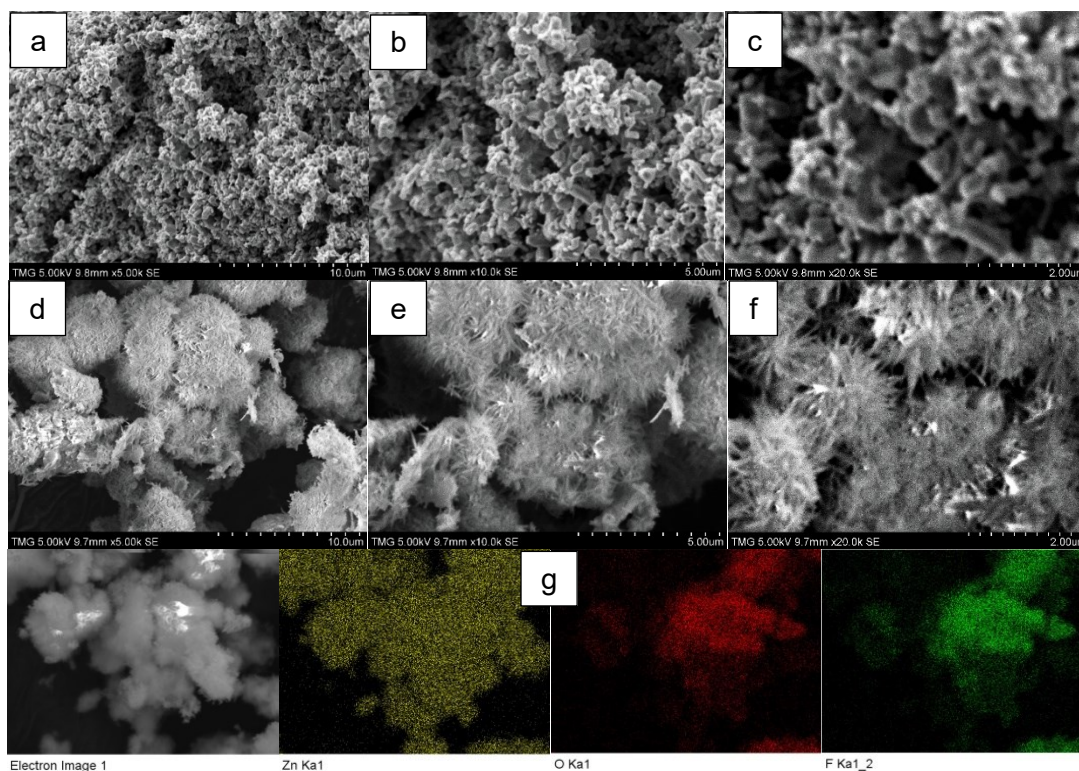


Figure 4.11. SEM images of (a–c) ZnO and (d–f) Zn(OH)F at different magnifications; (g) elemental mapping of Zn(OH)F.

Fig. 4.12(a) shows the XRD patterns of ZnO and ZF1. The pure ZnO with sharp peaks is in good agreement with the hexagonal wurtzite ZnO structure (JCPDS: 65-3411) (Mirzaei et al. 2018a). In the ZF1 XRD pattern, beside the peaks of Zn(OH)F (JCPDS: 74-1816) (Yang et al. 2017b), the peaks corresponding to the ZnO phase are also presented in the XRD pattern. This happens because, during the solvothermal process, the Zn(OH)F nuclei grow and assemble on the ZnO particles in a self-assembly process (Yang et al. 2017b). Fig. 4.12(b) illustrates the FT-IR spectra of the ZnO and ZF1 samples. The peak at 798 cm^{-1} is attributed to Zn-F vibration (Sangari et al. 2015). The spectrum of both samples is relatively similar. However, the band at 1510 cm^{-1} , which is associated with the combination of the symmetric and asymmetric stretching modes of H_2O molecules adsorbed on the surface (Castañeda et al. 2016), was slightly larger for ZF1. The vibration of surface $-\text{OH}$ groups assigned at $3200\text{-}3600\text{ cm}^{-1}$ was also slightly increased as a result of the enhancement of surface acidity in the presence of fluorine element (Chen et al. 2009). Nitrogen adsorption–desorption isotherm for ZnO and ZF1 are provided in Fig. 4.12(c). Both isotherms are identified as type IV, which correspond to the mesoporous materials. The specific surface area of ZF1 is about $38.23\text{ m}^2/\text{g}$, which is lower than that of ZnO powder with a BET surface area of $58.6\text{ m}^2/\text{g}$. The reduction in specific surface area of ZnO after solvothermal process is in accordance with observation in SEM images where macroparticles are formed.

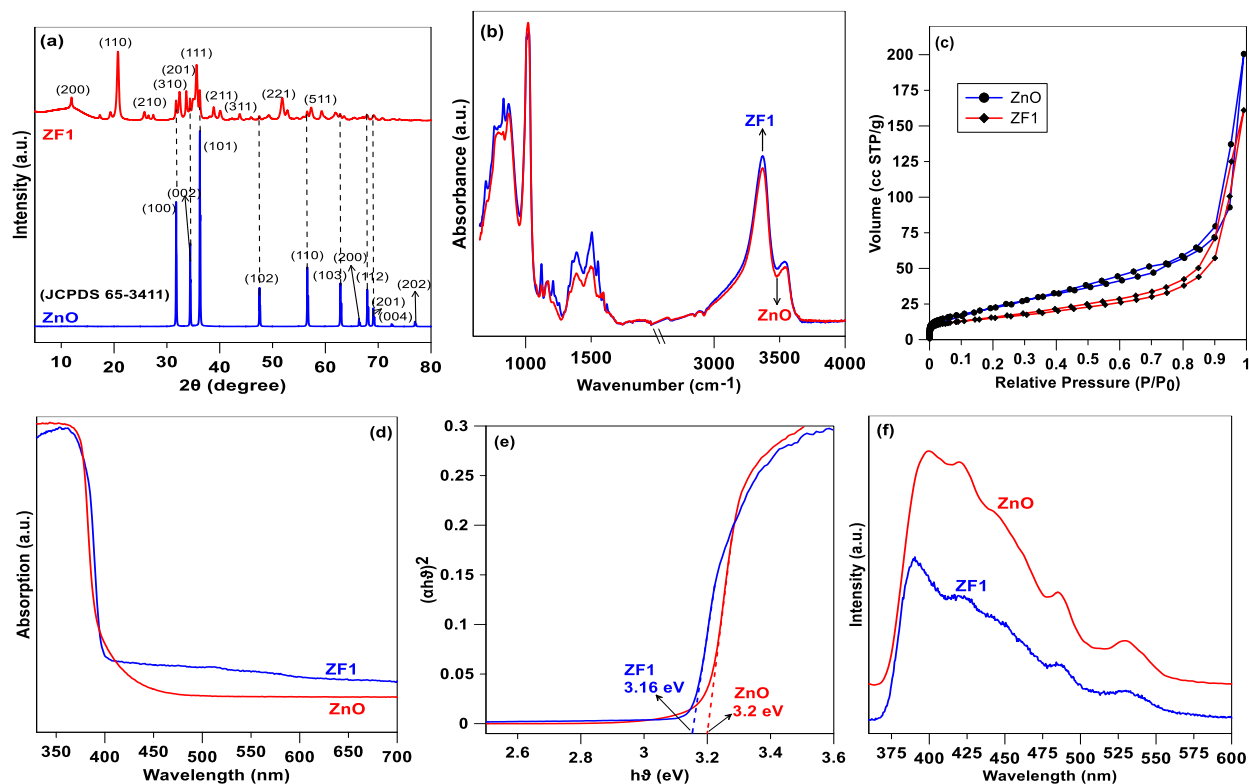


Figure 4.12. (a) X-ray diffraction patterns, (b) FT-IR spectra, (c) N_2 adsorption–desorption isotherm, (d) ultraviolet-visible diffuse reflectance spectra, (e) Tauc plots and (f) photoluminescence spectra of ZnO and ZF1 samples.

Optical properties of ZnO and ZF1 are shown in Fig. 4.12(d) and 4.12(e). As shown in Fig. 4.12(d) the light absorption of ZF1 was slightly enhanced in the visible region. Fig. 4.12(e) shows the Tauc plots of ZnO and ZF1 for the calculation of band gap of catalysts according to the following equation (Yang et al. 2017b):

$$\alpha h\nu = A(h\nu - E_g)^n \quad (4.4)$$

where, α , h , ν and E_g are the absorption coefficient, Planck's constant (eV s), light frequency (s^{-1}), and the band gap (eV), respectively. A is a constant and the power (n) is assumed to be 1/2 and 2 for direct and indirect transitions, respectively (Mirzaei et al. 2018a). It is reported that both ZnO and Zn(OH)F are direct band gap semiconductors (Yang et al. 2017b). As shown in Fig. 4.12(e) and Table 4.6, the band gap of ZnO and ZF1 is determined as 3.2 (eV) and 3.16 (eV), respectively. The position of band edges was also determined by using the following equations (Mirzaei et al. 2018a, Yang et al. 2017b):

$$E_{VB} = X - E_e + 0.5E_g \quad (4.5)$$

$$E_{CB} = E_{VB} - E_g \quad (4.6)$$

where E_{VB} is the valence band and E_{CB} is the conduction band edge potential. E_e is the energy of electrons on hydrogen scale (~ 4.5 eV) and X is the geometric mean of the absolute electronegativity of the constituent atoms on Pearson scale (PAE) (Mirzaei et al. 2018a). The band gaps and band edges as determined are listed in Table 4.6. As shown in the Table 4.6, compared to ZnO, the VB and CB potentials of ZF1 have down shifted, suggesting that an effective heterojunction can be formed between ZnO and Zn(OH)F, which would favor for the charge separation and decrease the recombination rate of electrons and holes. As shown in Fig. 4.12(f), the photoluminescence (PL) emission of ZF1, which was conducted at an excitation wavelength of 325 nm was reduced in comparison to ZnO, presenting the reduction in the recombination of electron/hole pairs.

Table 4.6. Band gap parameters for single sonocatalysts

Sonocatalysts	X (PAE)	E_{VB} (eV)	E_{CB} (eV)	E_g (eV)
ZnO	5.79	2.89	-0.31	3.2
ZF1	7.08	4.16	0.96	3.16

The XPS measurements were used to investigate the chemical compositions of ZnO and ZF1. As shown in Fig. 4.13, the XPS spectra of ZnO and ZF1 present the coexistence of Zn and O elements in both sonocatalysts. Besides these two elements, the fluorine element was detected on the spectrum of ZF1. The Zn($2p_{3/2}$) peak was found at 1022.38 eV and 1023.28 eV for ZnO and ZF1, respectively. This slight shift is due to the differences between the fluoride and oxygen environments, which exists in the ZF1 structure. As shown in Fig. 4.13(c), the F1s region of ZF1 spectrum is composed of two peaks. The main peak at 685.9 eV is associated with F in the $ZnO_{1-x}F_x$ lattice (Wu et al. 2009), while the minor peak at 684.4 eV is related to F^- ions, physically adsorbed on the surface of ZnO (Yu et al. 2002). In contrast to Zn, a significant change was shown in the O(1s) spectrum as illustrated in Fig. 4.13(d). For ZnO two peaks appeared at 530.6 eV and 532.2 eV which are attributed to the oxygen atoms in the ZnO lattice and to surface OH groups, respectively (Chiarello et al. 2014). The binding energies of O(1s) in ZF1 was determined at 533.3 eV (Wu et al. 2009) which is slightly higher than the binding energy of

oxygen in ZnO. The higher binding energy may be due to the stronger interaction between O and H in the ZF1, as reported before (Zhu et al. 2009). The peak at 287.3 eV is related to a trace amount of carbon contamination.

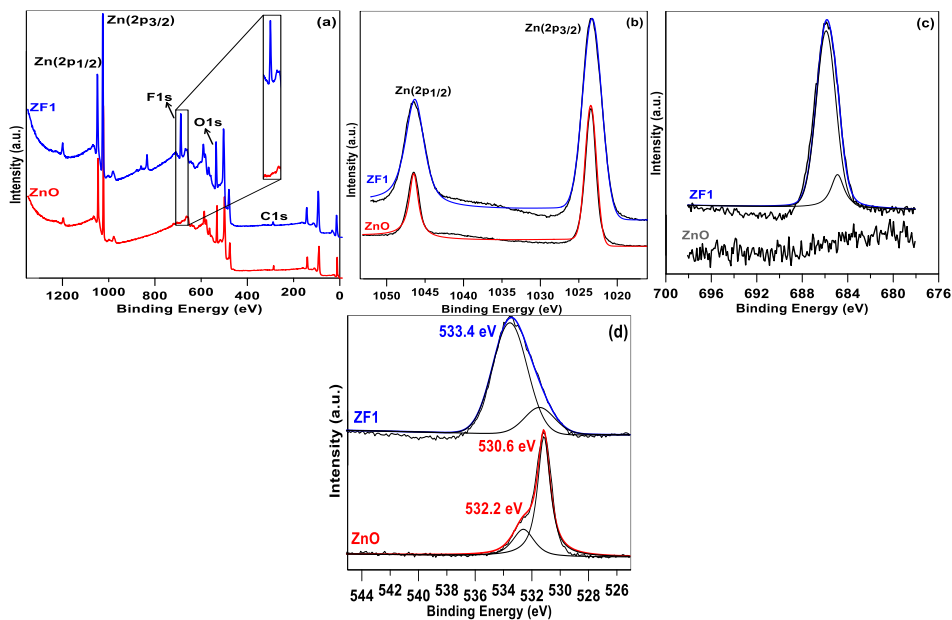


Figure 4.13. (a) XPS survey spectrum of ZnO and ZF1, (b) high-resolution XPS spectra of Zn, (c) F, and (d) O elements.

The variations of zeta potentials (ζ) of ZnO and ZF1 as a function of pH are shown in Fig. 4.14.

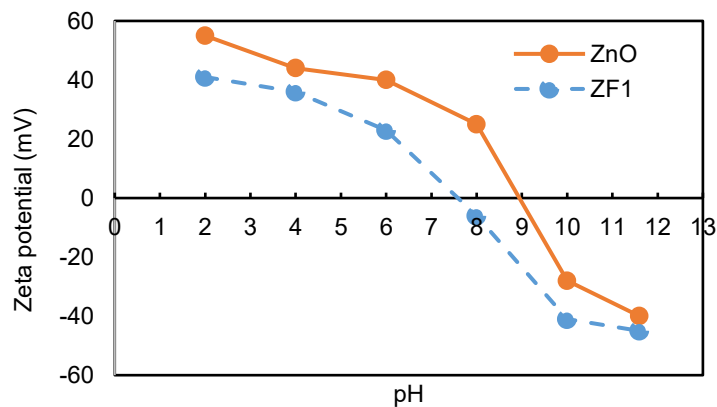


Figure 4.14. Zeta potentials (ζ) of suspended ZnO and ZF1 particles as a function of pH.

4.2.2.2. Hydrophobic behavior of adsorbent

The impact of surface fluorination of ZnO on the adsorption of anionic dyes including methyl blue (MB) and acid orange 7 (AO7) was examined. As illustrated in Fig. 4.15, surface fluorination was effective for increasing the adsorption capacity of ZnO for the adsorption of anionic dyes. In the present study, different hydrophobic behaviors of ZnO and Zn(OH)F led to different dispersion stability of the adsorbents in the dye solutions. As shown in Fig. 4.16, ZnO sunk to the bottom of solution, while Zn(OH)F floated on the solution surface and took a long time to settle down. The same trend has been reported in the case of surface fluorination of TiO₂ composites (Qi et al. 2014, Xing et al. 2012). The higher hydrophobic characteristic of Zn(OH)F leads to the higher adsorption capacity of organic contaminants such as dyes. This is because, the hydrophobic surface of adsorbent provides more available sites for electrostatic attraction of anionic dyes when compete with water molecules for adsorption.

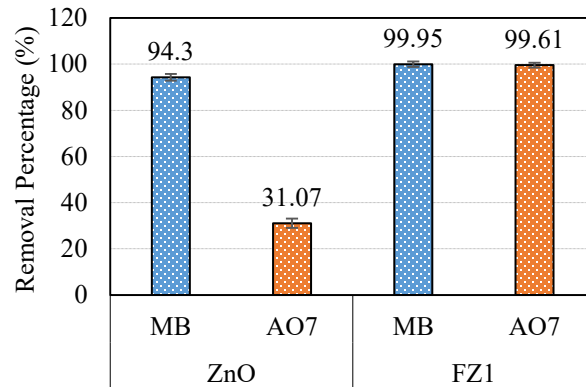


Figure 4.15. Removal percentage of anionic dyes (MB and AO7) by bare ZnO, FZ1; $C_{0,dyes}=100$ mg/L, adsorbent dosage= 5 mg/mL, pH (6.5) (not adjusted), temperature= 20 ± 1 °C, adsorption time = 30.



Figure 4.16. Relative water dispersibility of (A) Zn(OH)F and (B) ZnO.

Fig. 4.14 shows the variation of zeta potentials (ζ) of ZnO and ZF1 in water as a function of pH. The pH at the point of zero charge (pH_{zpc}) of ZnO is determined as 9, which is in agreement with the value reported in the literature (Mohd Omar et al. 2014). In the case of ZF1, the isoelectric point was shifted to a lower value (7.6) since some surface Zn-OH_2^+ groups are replaced by Zn-F species. The decrease of pH_{zpc} by surface fluorination of semiconductors was also reported (Wang et al. 2008b). Accordingly, at the pH of solutions in this research (pH 6.5) a large number of sites are available for the adsorption of the anionic dyes due to the electrostatic attraction between the positively charged ZF1 and anionic dyes in the solutions. Therefore, ZF1 was an effective adsorbent for the removal of anionic dyes in natural pH of experiment (about 6.5) in this research.

4.2.2.3. Equilibrium study

The adsorption isotherms describe the adsorption behavior and the interactions between adsorbate and adsorbent at equilibrium condition. Herein, single-component experiments were performed in order to evaluate the adsorption capacity of ZnO and ZF1. Fig. 4.17 shows the comparison of experimental data by using the Langmuir, Freundlich, BET and D-R isotherms. From the results presented in Fig. 4.17 and the correlation coefficients (R^2 and SSRE) in Table 4.7 it is concluded that the Freundlich and BET models provide the best correlation between the experimental data and theoretical predictions for MB and AO7, respectively.

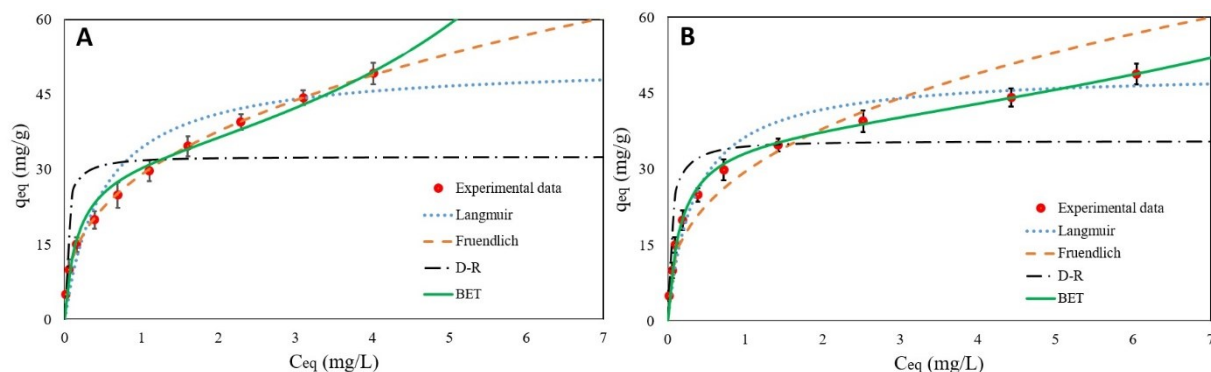


Figure 4.17. Single-component adsorption of: (A) MB and (B) AO7 onto ZF1; adsorbent dosage= 5 mg/mL, pH (6.5) (not adjusted), temperature=20±1°C. Lines represent adsorption models.

The Freundlich isotherm parameters for the adsorption of MB and AO7 onto ZF1 are listed in Table 4.7. In the Freundlich isotherm, higher value of n indicates better bonding and a more favorable adsorption process between the adsorbent and adsorbate. The n values higher than unity for both dyes indicate that the adsorption of dyes onto ZF1 is favorable. However, in contrast to the Langmuir model, Freundlich isotherm is not able to consider the saturation concentration of adsorbent which is an inherent drawback of this isotherm (Kayvani Fard et al. 2016).

Table 4.7. Isotherm parameters, SSRE and R^2 values for MB and AO7 adsorption onto ZF1 in single-component adsorption.

Isotherm	Equation	Parameters	FZ1	
			MB	AO7
Freundlich	$q_{eq}^0 = K_F^0 (C_{eq}^0)^{\frac{1}{n_F^0}}$	K_F^0	29.01	29.47
		n_F^0	2.657	2.739
		SSRE	0.0034	0.3341
		R^2	0.9993	0.9375
Langmuir	$q_{eq}^0 = q_{mL}^0 \frac{K_{sL}^0 C_{eq}^0}{1 + K_{sL}^0 C_{eq}^0}$	q_{mL}^0	51.28	49.26
		K_{sL}^0	2.031	2.819
		SSRE	1.0203	0.4636
		R^2	0.9658	0.9918
BET	$q_{eq}^0 = q_{mB}^0 \frac{K_{sB}^0 C_{eq}^0}{(1 - K_L^0 C_{eq}^0)(1 - K_L^0 C_{eq}^0 + K_{sB}^0 C_{eq}^0)}$	q_{mB}^0	31.354	36.512
		K_{sB}^0	6.133	6.225
		K_L^0	0.0956	0.0441
		SSRE	0.4902	0.05071
		R^2	0.9940	0.9997
Dubinin–Radushkevich	$q_{eq}^0 = q_{mD}^0 \exp(-\beta(RT \ln(1 + \frac{1}{C_{eq}^0}))^2)$	q_{mD}^0	32.524	35.497
		E	3.56	2.99
		SSRE	16.8035	5.2812
		R^2	0.8379	0.9503

In spite of very restrictive assumptions, Langmuir isotherm is the most widely used isotherm to describe the adsorption process in water because of its rigorous theoretical bases (Erto et al. 2015, Erto et al. 2011). As presented in Table 4.7, the adsorption capacity obtained from the Langmuir isotherm (q_{mL}), for both dyes were higher than that obtained from the BET isotherm (q_{mB}). This is because in the Langmuir isotherm, the entire adsorption amount is considered as monolayer adsorption. However, at high concentrations, some dyes are adsorbed on already adsorbed molecules; therefore, the surface affinity for dyes will be reduced compared to the direct adsorption on the surface. The correct form of BET isotherm for liquid phase is a theoretical isotherm that was developed to derive multilayer adsorption in liquid phase (Ebadi et al. 2009). This model is a three-parameter isotherm, which can be applied for multilayer adsorption at high concentrations and reduces to the Langmuir and Henry's law at low

concentrations. The empirical Dubinin–Radushkevich (D-R) isotherm is used to define the nature of adsorption (Foo and Hameed 2010). The mean free energy adsorbed per molecule of the adsorbate (E) obtained from the D-R isotherm (Eq. 4.7) is a convenient way to assess the mechanism of adsorption process (Foo and Hameed 2010, Noorpoor and Nazari Kudahi 2016).

$$E = \left[\frac{1}{\sqrt{2\beta}} \right] \quad (4.7)$$

where E (kJ mol^{-1}) and β are mean free energy and D-R isotherm constant, respectively. If the E value is larger than 16 kJ/mol, the process is chemisorption, while for E value between 8 and 16 kJ/mol, the adsorption process can be defined by ion-exchange mechanism. E values less than 8 kJ/mol show that the adsorption is of physical nature (Mirzaei et al. 2013). As can be seen in Table 4.7, since the E values were significantly lower than 8 kJ/mol, in spite of the low R^2 and high SSRE values, with a reasonable estimation the adsorption of both MB and AO7 could be indicated as physical adsorption in this study.

4.2.3. Conclusions and remarks related to the adsorption behavior of ZnO and Zn(OH)F

Normally, the photocatalytic reactions occur on the surface of photocatalysts. Therefore, the change of adsorption capacity may considerably change the photocatalytic reaction efficiency. In this study, first, Zn(OH)F was synthesized by solvothermal method in order to incorporate fluorine element into the structure of ZnO. The synthesized catalyst was characterized by XRD, XPS, SEM, EDS, FTIR, BET, DRS, PL and zeta potential analyzer. Then the effect of fluorination on the adsorption capacity of organic compounds was evaluated by using methyl blue and acid orange 7 as model organic compound. In the equilibrium adsorption tests, four adsorption isotherm models, including the Freundlich, Langmuir, BET and Dubinin–Radushkevich (D–R) were investigated. The results showed that the adsorption capacity of Zn(OH)F was improved compared to ZnO. Considering that most antibiotics are manufactured in anionic form, such as ampicillin sodium salt and amoxicillin sodium salt, the evaluation of the effect of fluorination on the adsorption of anionic compounds is of importance. The performance of Zn(OH)F for removal of AMP antibiotic is examined in the following section.

4.3. Catalytic performance of Zn(OH)F for the removal of AMP

4.3.1. Experimental condition

So far, the beneficial effect of ZnO fluorination on the enhancement of removal efficiency is confirmed through the adsorption and photocatalytic degradation of organic contaminants. After incorporation of fluorine element into the ZnO structure (Zn(OH)F), we evaluated its performance for the degradation of AMP antibiotic. Since, the stability of Zn(OH)F during the degradation process was the main objective of this study, instead of photocatalysis we employed Zn(OH)F under ultrasound waves irradiation (sonocatalysis) to examine its stability and fluoride ion leachate from its structure under severe condition of sonocatalysis process. A Branson 450 sonifier, at a fixed frequency of 35 kHz, was used for sonication experiments. The initial volume of aqueous solution was 250 mL. The sonoreactor temperature was kept constant at 26 ± 2 °C by circulating water around the cylindrical glass reactor. At different intervals, 10 mL samples were collected from the reactors during the course of experiments to analyze for the concentration of AMP, COD TOC, by-product formation and toxicity assessment. All experiments were conducted in batch mode of operation.

4.3.2. Results and discussion

4.3.2.1. Removal of AMP by sonolysis and sonocatalysis by ZnO and Zn(OH)F

Screening experiments were conducted to evaluate the efficiency of different processes in terms of the removal percentage of AMP during 90 min of treatment. The examined processes included ultrasonic irradiation (US) and sonocatalytic degradation by ZnO (US/ZnO) and Zn(OH)F (US/ZF) with different amounts of fluorine embedded into the structure of catalyst. As shown in Fig. 4.18 the removal of AMP by ultrasound irradiation was negligible and only 5.2% of AMP was removed after 90 min treatment. Moreover, the rate constant of AMP removal by sonolysis was $6.1 \times 10^{-4} \text{ min}^{-1}$. In the sonolysis process, three different sites are available for eliminating contaminants, namely: (i) the gaseous region of the cavitation bubbles by pyrolytic reactions of volatile contaminants, (ii) the bubble–liquid interface where the generated radicals are localized and (iii) the liquid bulk where the elimination reactions take place, either via OH· radicals generated by the pyrolysis of water or the free radicals which have escaped from the bubble–liquid interface and migrated to the liquid bulk (Velegraki et al. 2006). Considering that ampicillin is a highly soluble and non-volatile compound, the pyrolysis in the gas phase is

unlikely to occur, and can be considered to be negligible. Hence, the hydroxyl radical-mediated reactions occurring in the bubble–liquid interface and the bulk of solution are the dominant elimination pathways in the sonolysis of AMP. Under ultrasound irradiation, water molecules can cleave to produce OH• and H• radicals (Eq. 4.8) (Güyer and Ince 2011).



where))) denotes ultrasonic irradiation. Hydroxyl radicals can also be generated by the reaction between oxygen radical and water molecules (Eqs. 4.9 and 4.10) (Hassani et al. 2017).



However, the generated radicals may combine to form H₂O (Eq. 4.11) or H₂O₂ (Eq. 4.12), which are less reactive compared to hydroxyl radicals.



It has been reported that the H° radicals are reducing agents and their contribution to the elimination of organic compounds is insignificant (Benito et al. 2017). On the other hand, the rate of OH• radicals generation by sonolysis process is low (Khataee et al. 2017a). Therefore, the elimination of organic contaminants by sonolysis usually requires large amounts of energy or long reaction times, which limit its application (Hassani et al. 2017). As shown in Fig. 4.18, only 5.2% AMP removal was achieved by sonolysis after 90 min treatment, while the percentage removal of AMP by using ZnO, ZF0.5, ZF1 and ZF2 was about 48, 68, 87 and 80%, respectively. The presence of catalyst in the medium increases the removal efficiency due to the formation of more radicals on the catalyst surfaces by heterogeneous nucleation of bubbles in the sonocatalysis process (Eren and Ince 2010). Moreover, the presence of particles accelerates the breakup of generated microbubbles into smaller ones, thus enhancing the number of high temperature and pressure regions (Anju et al. 2012, Chen and Smirniotis 2002). It is reported that sonoluminescence or “hot spot” may play a significant role in sonocatalytic degradation of organic compounds (Pang et al. 2010, Shimizu et al. 2007, Wang et al. 2009a). In this mechanism, the semiconductor as sonocatalyst would be excited and produces hole and electron pairs and reactive radicals under the light irradiation created at the time of sonoluminescence

(Jyothi et al. 2014, Khataee et al. 2017b, Khataee et al. 2016, Soltani et al. 2016, Zhang et al. 2017b). Shimizu et al. (2007) reported that methylene blue was effectively eliminated in the presence of semiconductor (TiO_2) under a low frequency ultrasonic irradiation, while using insulator (Al_2O_3) had no effect on the degradation of methylene blue under similar conditions. However, the mechanism of sonoluminescence phenomenon in the presence of semiconductors is not fully discovered (Wang et al. 2008a). The lack of excitement of the TiO_2 surface under ultrasound waves with different frequencies is also reported (Taghizadeh and Seifi-Aghjekohal 2015, Ziylan-Yavař and Ince 2016).

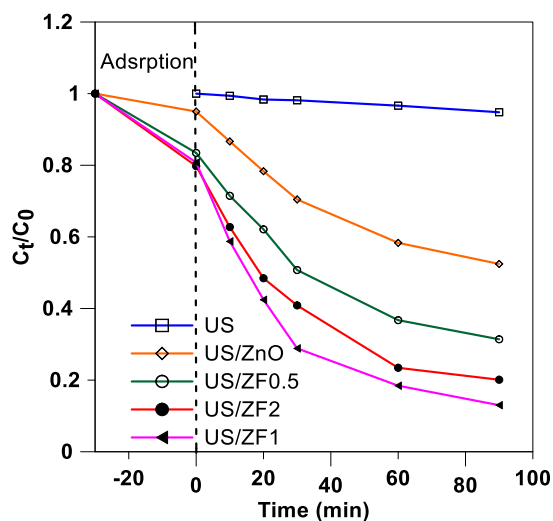


Figure 4.18. Removal ratio of AMP by different processes during 90 min treatment. Experimental conditions: $[\text{AMP}]_0 = 30 \text{ mg/L}$, $\text{pH} = 7$, $[\text{Catalyst}] = 1 \text{ g/L}$, temperature = $26 \pm 2 \text{ }^\circ\text{C}$ and ultrasonic power = 100 W

In this study, although, $\text{Zn}(\text{OH})\text{F}$ sonocatalysts possessed lower specific surface area compared to ZnO , they showed higher removal efficiencies. The removal of AMP by adsorption on ZnO was 5 % after 30 min, while by using ZF1 as sonocatalyst, the adsorption capacity of catalyst was enhanced and about 20% removal was achieved after 30 min. The improvement of adsorption capacity by using $\text{Zn}(\text{OH})\text{F}$ may be attributed to the presence of fluorine as the most electronegative element in the structure of catalyst, and attraction of AMP from its negative moiety. The highest removal efficiency was achieved by using ZF1 , while the removal efficiency of AMP by using ZF2 was lower than ZF1 . A reduction in photocatalytic activity of $\text{Zn}(\text{OH})\text{F}$ by increasing the fluorine content is also reported (Yang et al. 2017b). Considering that optical properties of ZF1 , such as PL emission intensity, are different from ZnO , the generation of

electrons and holes pair by sonoluminescence phenomenon is most likely occurred in this study. Beside OH^\bullet -mediated oxidation pathway, the sonogenerated holes on the surface of ZF1 play a decisive role in eliminating AMP. This is due to the fact that fluorine is the most electronegative element and it holds the generated electron in the conduction band and restrains the electron and hole recombination (Liu et al. 2012). By holding the electrons, the lifetime of generated holes can be extended to oxidize the hydroxide ions to OH^\bullet and to further oxidize the AMP molecules. Since the generated holes are strong oxidants and the adsorption of AMP onto the surface of ZF1 was enhanced compared to ZnO, using ZF1 as sonocatalyst can effectively promote the elimination of AMP. The significant contribution of holes to the removal of AMP is verified by the notable decline in the removal efficiency in the presence of hole-scavengers such as chloride and iodide ions as shown in Fig. 4.20. The benefits of utilizing ultrasound irradiation are the generation of hydroxyl radicals (Eq. 4.10), reduction of mass transfer limitations, continuous cleaning/renewing of the catalyst surface, reduction of chemical consumption and sludge generation rates, and formation of more active sites due to the disaggregating flocs of particles (Eren and Ince 2010, Ziylan-Yavaş and Ince 2016). Moreover, sonication can enhance oxidation via the continued removal of intermediate compounds and by-products from the surface of catalyst, thus improving the availability and clarity of surfaces for the ensuing reactions (Pang et al. 2010). Consequently, the rates of subsequent reactions, i.e. adsorption–oxidation–desorption of AMP will increase. Considering the results of screening experiments, the ZF1 catalyst which demonstrated a better performance than other sonocatalysts, was selected for investigation in the subsequent experiments.

4.3.2.2. Effect of operating parameters on the AMP sonocatalytic degradation rate

Effect of catalyst dosage

Fig. 4.19(a) shows the degradation rate of AMP by sonocatalytic process as a function of ZF1 dosage (0-2 g/L). As mentioned before, in the absence of sonocatalyst, the removal of AMP was insignificant. The rate of AMP removal was increased from 6.1×10^{-4} to $1.99 \times 10^{-2} \text{ min}^{-1}$ by increasing the ZF1 dosage from 0 to 1.5 g/L. This is due to the enhancement of active sites for the adsorption of AMP, direct oxidation by holes and generation of reactive radicals (Pang and Abdullah 2013). The enhancement of degradation rate in the presence of sonocatalyst in ultrasonic degradation system has been reported before (Pandit et al. 2001). This occurs because

of increases in the formation rate of cavities, by providing more nuclei, and by the higher generation of free radicals (Anju et al. 2012). It is reported that the optimum catalyst dosage depends on the initial contaminant concentration (Neppolian et al. 2002, Pang et al. 2011) as well as the shape, size and geometry of utilized sonoreactor (Anju et al. 2012). The excessive dosage of sonocatalyst can possibly suppress the transmission of ultrasound waves near the catalyst surface (Pang and Abdullah 2013). Moreover, the high dosage of catalyst may cause sound attenuation, flash light screening and restriction of contaminant molecules diffusion into the solution, producing adverse effects on the removal efficiency of contaminants (Pang and Abdullah 2013, Yin et al. 2011). In addition, the aggregation of catalyst particles which is likely to occur at high catalyst dosages, reduces the number of available active sites on the surface of catalysts (Anju et al. 2012). Consequently, the increase of catalyst concentration from 1.5 g/L to 2 g/L did not have a significant impact on the removal efficiency or removal rate of AMP. Therefore, all further experiments were carried out at the catalyst dosage of 1.5 g/L.

Effect of initial solution pH

The solution pH is a decisive parameter in the sonocatalytic degradation, since the ionization state of organic contaminants and the surface charge of catalysts are significantly influenced by pH value (Kang et al. 2015, Pang and Abdullah 2013, Wang et al. 2009a). Fig. 4.19(b) shows that the degradation rate of AMP is influenced by the solution pH, and the highest degradation rate of $2.24 \times 10^{-2} \text{ min}^{-1}$ was achieved at pH~5. Depending on the $\text{pH}_{(\text{zpc})}$ value, the surface of catalyst would be positively or negatively charged at pH values lower or higher than $\text{pH}_{(\text{zpc})}$, respectively. Besides, when the solution pH is higher than the acid-base dissociation constant (pK_a) of an organic compound, the corresponding compound mainly exists in anionic form in water (Pang and Abdullah 2013). As shown in Fig. 4.14, the $\text{pH}_{(\text{zpc})}$ of ZF1 was determined to be 7.6. Therefore, when the solution pH is less than 7.6, the surface of ZF1 is positively charged. On the other hand, the pK_a of AMP is 2.5, and at pH values higher than 2.5, AMP is in anionic form. For these reasons, the pH value between 2.5 and 7.6 is the most favorable pH range in this study, due to the attractive forces between the anionic form of AMP molecules and the positively charged catalyst surface. Moreover, in acidic condition, due to the accumulation of hydronium ion at the interface, the bubble interface becomes positively charged. This phenomenon not only

increases the number of bubbles in the solution, due to reduced coalescence of individual bubbles (Sasi et al. 2015), but it also attracts the negatively-charged AMP inside the bubble interface. The enhancement of reaction rate by reducing the solution pH during sonochemical degradation has been reported before (Anju et al. 2012, Nalini Vijaya Laxmi et al. 2010, Wu et al. 2001). Under basic condition, not only the hydroxyl radicals combine to form H₂O₂, which has a lower oxidation potential (Kang et al. 2015), but also due to the presence of OH⁻ ions, the produced hydrogen peroxide will decompose to form water and oxygen without producing oxidative radicals (Mirzaei et al. 2017b). In the examined pH range, the lowest degradation rate of 1.14×10⁻² min⁻¹ was achieved at pH~11. Besides, the oxidation potential of hydroxyl radicals under acidic condition is higher than that under basic condition. The standard redox potential of H₂O/ OH• couple is 2.59 V and 1.64 V at pH 0 and pH 14, respectively (Hassani et al. 2017). It is reported that the most stable form of OH• radicals is produced at pH values of 2–4 (Mohajeri et al. 2010). However, at very acidic condition, catalyst nanoparticles could be partially dissolved into the solution, which reduces the removal efficiency. Finally, at pH values lower than 3, AMP possesses neutral charge, which hinders its adsorption on the positively charged catalysts. Therefore, pH of 5 was selected as the optimum pH value for the ensuing experiments in this study.

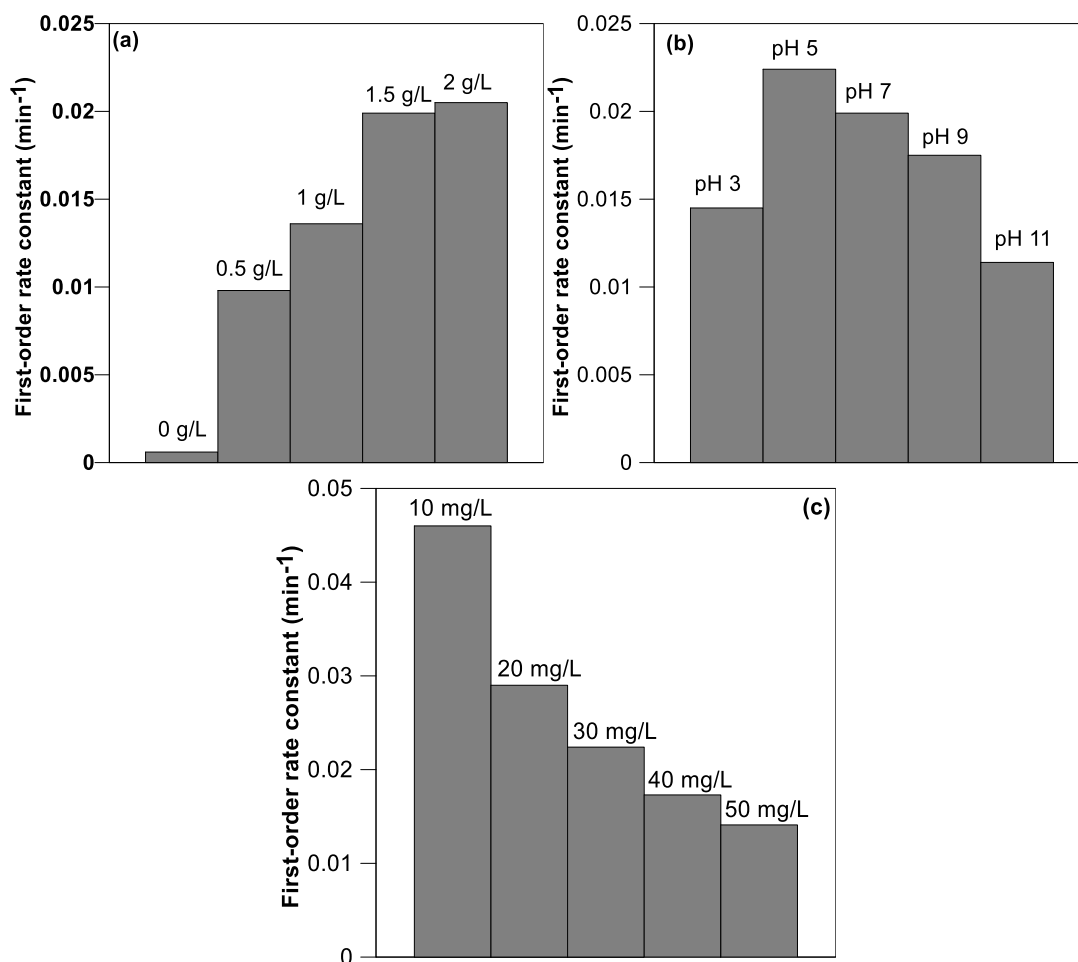


Figure 4.19. (a) Effect of ZF1 loading (pH=7, [AMP]₀ = 30 mg/L), (b) pH of solution ([catalyst]₀ = 1.5 g/L, [AMP]₀ = 30 mg/L), and (c) initial concentration of AMP ([catalyst]₀ = 1.5 g/L, pH=5) on the rate of AMP removal in sonocatalytic process.

Effect of initial AMP concentration

The concentration of contaminants in the influent stream of water treatment plants is not constant and varies with time (Mirzaei et al. 2017a). Therefore, it is important to evaluate the dependence of contaminant removal efficiency on the initial concentration of contaminants (Wang et al. 2009a). The degradation study was carried out at the concentration range of 10-50 mg/L, while keeping other operating parameters constant (catalyst dosage =1.5 g/L, pH 5 and ultrasound power =100 W). As seen in Fig. 4.19(c), the initial concentration of AMP and the sonodegradation rate are inversely related. The removal rate constant was $4.6 \times 10^{-2} \text{ min}^{-1}$ when the initial concentration was 10 mg/L, while the removal rate decreased to $1.41 \times 10^{-2} \text{ min}^{-1}$ when

the experiment was conducted with 50 mg/L initial AMP concentration. The reduction of sonocatalytic degradation rate at higher concentrations of contaminants has been reported before (Anju et al. 2012). At higher concentrations of AMP, the active sites of ZF1 are occupied by AMP and intermediate compounds. This prohibits sonocatalyst particles to absorb heat and energy that are generated by acoustic cavitation, and reduces the generation of reactive species (Hassani et al. 2017, Pang et al. 2011). However, Anju et al. (2012) reported that the saturation of semiconductor surface occurred at higher initial concentrations of contaminants during sonocatalysis in comparison with photocatalysis. This is due to the *in situ* regeneration of catalyst surface by the microstreaming phenomenon, where cavitation causes the formation of miniature eddies and a jet of fluid directed onto the catalyst particle (Adewuyi 2001). At high concentrations of contaminants, higher amounts of radicals are needed. Therefore, the removal rate of AMP decreased with the increase in its concentration.

Effects of the presence of scavengers in water on AMP degradation

Organic and inorganic ions are commonly present in the water and wastewater effluents and may influence the efficiency of contaminant removal by their radical scavenging properties (Khataee et al. 2015, Sasi et al. 2015). The governing mechanism for the effect of ions on sonochemical elimination of organic compounds is not well established. Several researchers reported that the presence of ions reduced the removal efficiency of contaminants in water (Hassani et al. 2017, Zhang et al. 2015), while some reports presented an insignificant effect of ions on the overall sonochemical elimination of contaminants (Moumeni and Hamdaoui 2012, Wang and Lim 2010), and yet other works highlighted that sonochemical or sonocatalytic degradation of organic contaminants was accelerated in the presence of ions (Jyothi et al. 2017, Ziylan-Yavaş and Ince 2016). As shown in Fig. 4.20 the removal efficiency of AMP after 90 min reaction was reduced from 97.2 % in deionized water to 78.1, 66.4, 57.1, 42.9 and 28.3% in the presence of nitrate, sulfate, carbonate, chloride and iodide ions, respectively. It is reported that the presence of anions in the solution slows down the penetration of US waves into the system (Jyothi et al. 2017). Besides, the reaction of inorganic ions with OH• radicals leads to the formation of less reactive radicals by the following reactions (Hassani et al. 2017, Mirzaei et al. 2017b, Sasi et al. 2015) :





Considering Eqs. (4.13-4.16) carbonate ion presents the highest competition for hydroxyl radicals as it has the highest rate constant. Guillard et al. (2005) concluded that the decline in efficiency is due to the formation of an inorganic salt layer at the surface of catalyst. As mentioned before, at pH values lower than $\text{pH}_{(\text{zpc})}$ the surface of catalysts is positively charged. Therefore, all examined anions can be adsorbed onto the surface of ZF1 and they can compete with AMP for adsorption on sonocatalyst. The adsorption of various anions on the surface of semiconductors is also reported before (Jyothi et al. 2017). In this regard, the decline of removal efficiency in the presence of divalent anions such as sulfate and carbonate was more pronounced than that obtained in the presence of nitrate, which is a monovalent anion. However, the negative effect of chloride was higher than that observed with divalent anions. This is because chloride anions can scavenge both produced holes (Eqs. 4.17 and 4.18) and hydroxyl radicals (Eq. 4.13) during the sonocatalytic reaction (Karaca et al. 2016).



The presence of iodide ions in the solution showed the strongest inhibition effect on removal of AMP. It is reported that iodide ions can act as the scavenger of both holes ($k = 1.2 \times 10^{10} \text{ M}^{-1}\text{s}^{-1}$) and hydroxyl radicals ($k = 1.1 \times 10^{10} \text{ M}^{-1}\text{s}^{-1}$), resulting in a significant reduction in the degradation efficiency (Hassani et al. 2017, Ziylan-Yavaş and Ince 2016). Therefore, a significant reduction of the removal efficiency in the presence of hole scavengers (iodide and chloride) further confirmed the contribution of both mechanisms, i.e. direct oxidation by holes and oxidation by hydroxyl radicals in the elimination of AMP in US/ZF1 system, as suggested before.

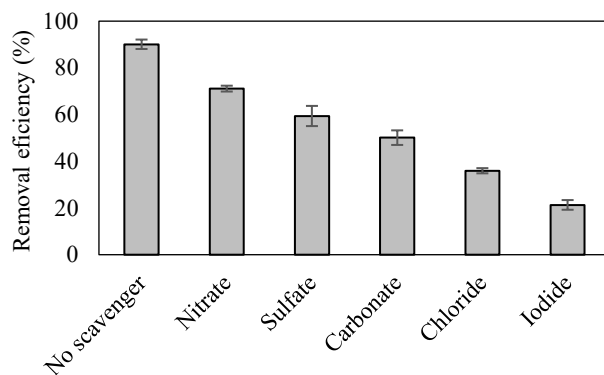


Figure 4.20. Effect of scavengers on the removal efficiency of AMP. Experimental conditions: $[AMP]_0 = 30 \text{ mg/L}$, $[ZF1] = 1.5 \text{ g/L}$, $pH=5$, $[scavenger]_0 = 30 \text{ mg/L}$, reaction time = 90 min, temperature = $26 \pm 2 \text{ }^\circ\text{C}$ and ultrasonic power = 100 W.

4.3.2.3. COD and TOC removal

Since many intermediate products may be formed during the oxidation process, the removal of parent contaminants does not reflect their respective mineralization (Xia and Lo 2016). Therefore, COD and TOC removals were evaluated as mineralization indicators for the degradation of AMP. As shown in Fig. 4.21 approximately 61 and 46% COD and TOC removal were achieved after 120 min of reaction at the optimum operating conditions. Notably, about 97.2 % AMP removal was achieved after 90 min of reaction, while TOC removal during this period was 40%, suggesting that AMP was transformed into intermediate products during the treatment process. The reductions of COD and TOC were faster during the first 60 min of treatment. This occurred because the removal of AMP in the initial stages of process is likely due to the aromatic ring cleavage by the continuous attack of hydroxyl radicals (Ghauch et al. 2009). Thereafter, a steady decrease in the removal rate of COD and TOC was observed by the formation of stable intermediates such as aliphatic acids, which are very persistent toward oxidation (Sasi et al. 2015).

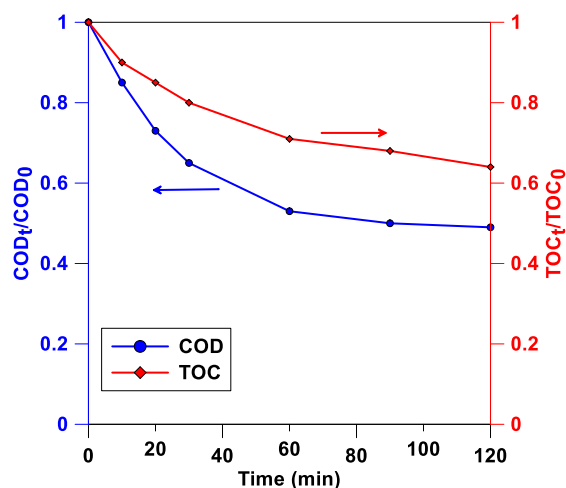


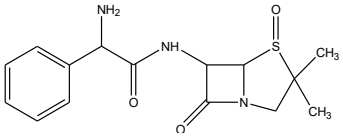
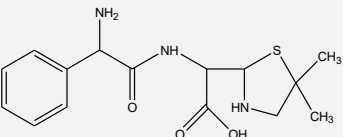
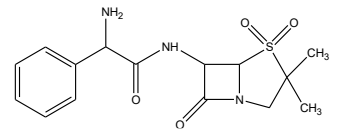
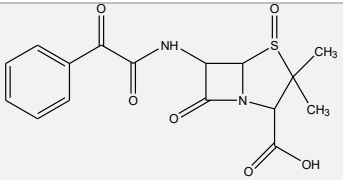
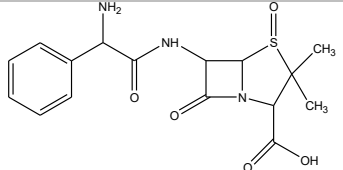
Figure 4.21. TOC and COD removal during the sonocatalytic degradation of AMP. Experimental conditions: $[AMP]_0 = 30 \text{ mg/L}$, $[ZF1] = 1.5 \text{ g/L}$, $\text{pH}=5$, temperature = $26 \pm 2 \text{ }^\circ\text{C}$ and ultrasonic power = 100 W .

4.3.2.4. By-product formation

Despite the high removal efficiency of AMP, Fig. 4.21 shows that AMP was not completely mineralized to water and carbon dioxide during the sonocatalytic process, even after 120 min reaction. Several potential by-products with relatively similar structure to AMP that may possess antibacterial activities were examined in the treated samples after 90 min reaction by US, US/ZnO and US/ZF1 processes. They include oxidized form of AMP, molecular hydration at β -lactam ring, oxidation of amine group into a carbonyl group, hydration at β -lactam ring followed by decarboxylation, oxidation of sulfur moiety and the combination of above. In addition, the intensity of peaks was compared as the indicators of by-products concentrations. The ampicillin molecule can change into the dimer form through aminolysis at the β -lactam carbonyl moiety by the amine group of a second molecule (Lu and Feng 2007). It is reported that the aromatic ring of β -lactam of AMP is the predominant hydroxylation reaction site for the hydroxyl radical reaction (Ghauch et al. 2009). Therefore, the generated OH^\bullet radicals during the treatment can attack the amine functional group where molecules are attached together. Table 4.8 and Fig. 4.22(a) show that the peak intensity of AMP during the US/ZF1 process was about 5 and 35 times less than that observed in the US/ZnO and US processes, respectively, which further confirmed the higher efficiency of AMP removal in the US/ZF1 process. The relative peak intensity of by-product $[m/z 322.12]$, which was produced by the oxidation of sulfur moiety and by losing CO and H_2O , was about 55 and 92% lower in the US/ZnO and US/ ZF1 processes, respectively, compared to

the intensity obtained in the US process (Fig. 4.22(b)). In addition, the peak intensity of generated by-product [m/z 349.09] was about 23% and 50% lower when US/ZnO and US/ZF1 processes were used to treat the AMP solution, respectively, than the level observed during sonolysis (Fig. 4.22(e)). Nevertheless, by-product [m/z 338.12] was produced at the same peak intensity during the three examined processes (Fig. 4.23(d)), and the intensity of compound [m/z 324.14] was higher during sonocatalysis compared to its intensity during the sonolysis process (Fig. 4.22(c)). The oxidized form of AMP (hydroxylation, +16 Da) was not detected in the treated solution by sonocatalysis processes and it was only observed during the sonolysis process (Fig. 4.22(f)).

Table 4.8. By-products identified during the sonocatalytic degradation of AMP after 90 min reaction by US, US/ZnO and US/ZF1 processes.

Chemical formula	Structure	[M+H] ⁺	Intensity of peak		
			Without catalyst	ZnO	ZF1
C ₁₅ H ₁₉ N ₃ O ₃ S Ampicillin – CO, -H ₂ O, +O, (-28)		322.12	1.8×10 ⁴	8×10 ³ (-55%)	1.5×10 ³ (-91.6%)
C ₁₅ H ₂₁ N ₃ O ₃ S Ampicillin + H ₂ O, -CO ₂ , (-26)		324.14	2.2×10 ³	7×10 ³ (+218%)	1.8×10 ⁴ (+718%)
C ₁₅ H ₁₉ N ₃ O ₄ S Ampicillin + O ₂ , -COOH, (-12)		338.12	1.3×10 ⁴	1.3×10 ⁴ (~ 0%)	1.3×10 ⁴ (~ 0%)
C ₁₆ H ₁₆ N ₂ O ₅ S Ampicillin + O, -NH ₂ , -H, (-1)		349.09	3×10 ³	2.3×10 ³ (-23%)	1.5×10 ³ (-50%)
C ₁₆ H ₁₉ N ₃ O ₅ S Ampicillin + O, (+16)		366.11	2×10 ⁴	N.D (-100%)	N.D (-100%)

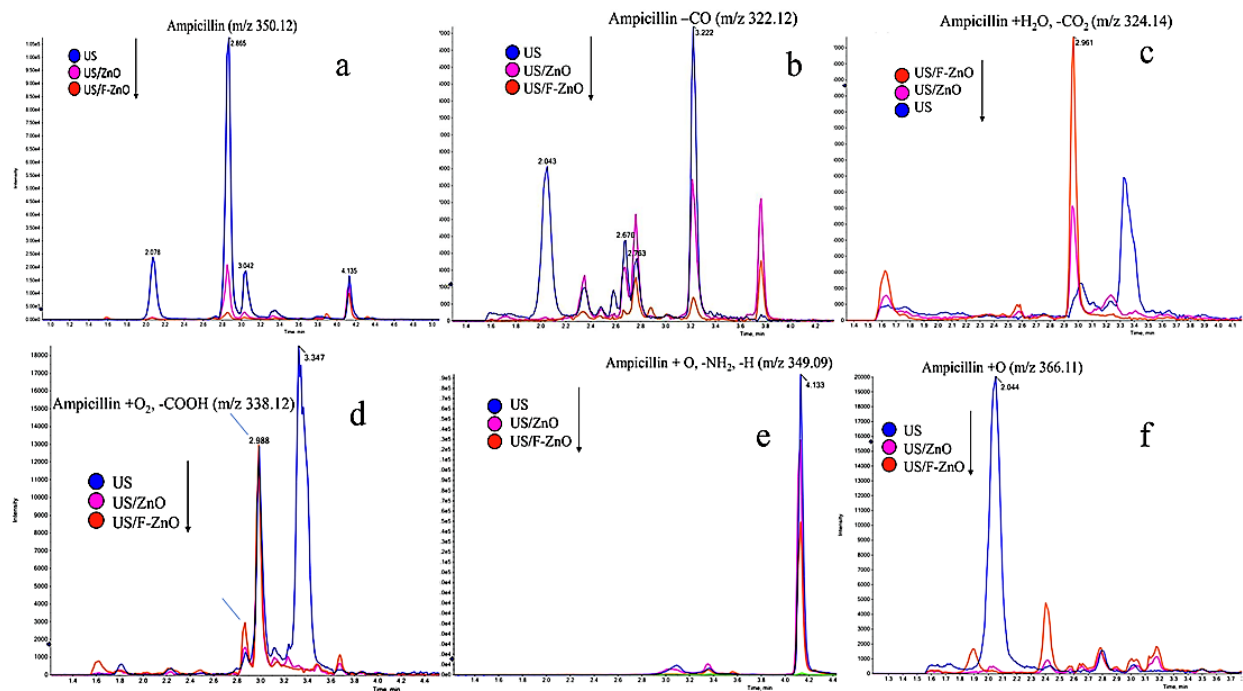


Figure 4.22. LC-HR-MS/MS extracted-ion screening chromatograms of (a) ampicillin, $[m/z=350.12]$, (b) ampicillin $-CO, -H_2O, +O$, $[m/z=312.12]$, (c) ampicillin $+H_2O, -CO_2$, $[m/z=324.14]$, (d) ampicillin $+O_2, -COOH$, $[m/z=338.12]$, (e) ampicillin $+O, -NH_2, -H$, $[m/z=349.09]$, (f) ampicillin $+O$, $[m/z=366.11]$.

4.3.2.5. Toxicity assessment

As mentioned above, the partial mineralization of contaminants may lead to the formation of intermediate compounds and by-products which are sometimes more toxic than their precursors (Sasi et al. 2015). Fig. 4.23 shows the percentage inhibition (PI) of solution corresponding to different treatment courses by ZF1 in sonocatalytic degradation of AMP at the optimum operating conditions. The results indicated a high percentage of solution inhibition as 42% PI against *E. coli* bacteria. The results of inhibition assays obtained after 30 min treatment showed that the degradation of AMP led to the generation of intermediate products which showed toxicity (PI >10%), although about half of the toxicity observed with the initial untreated samples. However, the continuation of treatment up to 60 min, led to the reduction of toxicity and lowered the inhibition to “non-toxic” range ($-10\% < PI < 10\%$).

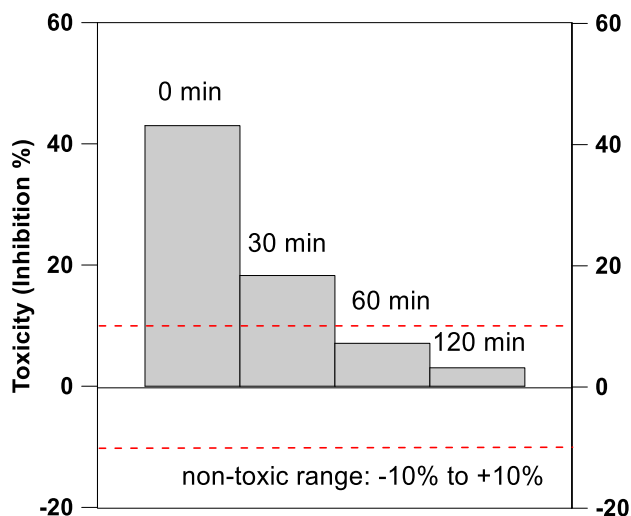


Figure 4.23. Changes in toxicities (as measured by the inhibition to *E. coli* bacteria) before treatment and after different stages of sonocatalytic degradation of AMP by ZF1 at the optimum condition.

Fig. 4.24 shows the magnified images of cultured plates with zone of inhibition for the *E. coli* strain. The initial sample of AMP was added to well number 0, while the treated solution by ZF1 after 60 min and 120 min reaction was added to wells number 1 and 2, respectively. The zone of inhibition around the initial sample (untreated) and the remarkable growth of bacterial colonies around the treated sample further confirmed the effectiveness of applied sonocatalytic degradation in decreasing the toxicity of AMP solution.

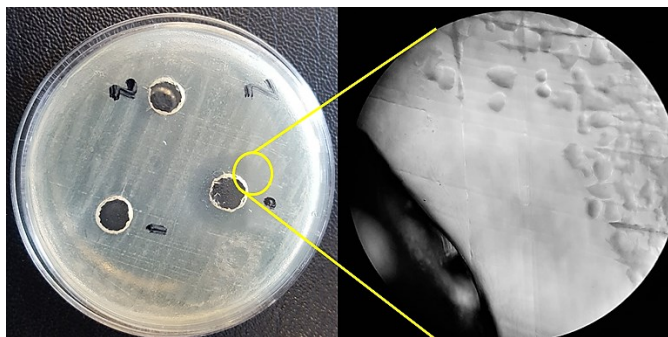


Figure 4.24. Magnified images of the growth inhibition zone of AMP solution against *E. coli* bacteria before treatment and after 1 and 2h treatment by US/ZF1 process at the optimum condition.

4.3.2.6. Stability of catalyst

The stability and reusability of a catalyst during long-term water treatment operations are among the most important characteristics of that catalyst (Hassani et al. 2017). In order to evaluate the stability of the developed sonocatalyst, ZF1 nanoparticles were used in four catalytic cycles. After each treatment process, nanoparticles were separated by centrifugation, washed with deionized water several times, dried at 105 °C and were utilized in the next experimental run. The results of stability experiments, illustrated in Fig. 4.25(a) showed that the developed sonocatalyst nanoparticles were stable in consecutive trials, and only about 5% decline in the removal efficiency was observed after four experimental runs.

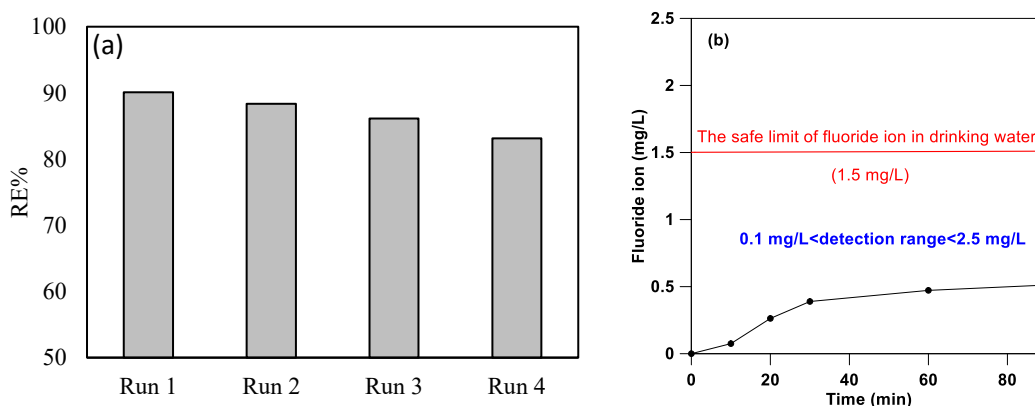


Figure 4.25. (a) Reusability of the F-ZnO nanoparticles within four consecutive experimental runs. (b) Fluoride ion concentration into the solution. Experimental conditions: $[AMP]_0 = 30 \text{ mg/L}$, $[F\text{-ZnO}] = 1.5 \text{ g/L}$, $\text{pH}=5$, $\text{temperature} = 26 \pm 2 \text{ }^\circ\text{C}$ and $\text{ultrasonic power} = 100 \text{ W}$.

As mentioned before, the generation of holes on the surface of sonocatalyst nanoparticles increases the removal efficiency of contaminant by direct oxidation of AMP and/or by the generation of reactive radicals. However, the generated holes may result in self-corrosion of zinc catalyst based on reaction (3.9). The adsorption capacity of the developed sonocatalyst (Zn(OH)F) for AMP was increased compared to ZnO. It is possible that the molecules of AMP adsorbed on the surface of sonocatalyst were not only removed from the water by direct oxidation, but they also protected the surface of catalyst from self-corrosion by consuming the produced holes. Fig. 4.25(b) shows the concentration of fluoride ion into the solution. As seen, even under severe condition of ultrasonic radiation, the amount of fluoride ion leached into the

solution is much lower than the safe limit of fluoride ion concentration in drinking water which confirms the high stability of synthesized catalyst.

4.3.3. Conclusions and remarks related to the catalytic performance of Zn(OH)F for the removal of AMP

The sonocatalyst Zn(OH)F was synthesized by solvothermal process, using ZnO and NH₄F as precursors with different molar ratio. After selecting the optimized catalyst in screening experiments, the sonocatalytic degradation of ampicillin antibiotic in water by bare ZnO and optimized Zn(OH)F (ZF1) was investigated in terms of AMP removal and mineralization, detoxification of solution, and the remaining by-products at the end of process. Preliminary results revealed that the sonocatalytic performance of ZF1 (US/ZF1) was significantly greater than that of bare ZnO (US/ZnO) and sonolysis (US) for the treatment of AMP solution. The effects of catalyst dosage, solution pH and initial AMP concentration on the rate of AMP removal were evaluated. Under the optimum operating conditions, the removal percentage of AMP by ZF1 was ~97% after 90 min reaction, while 51 and 36% COD and TOC removal were achieved after 120 min reaction, respectively. The formation of several by-products with chemical structures relatively similar to that of AMP during the sonolysis and sonocatalysis was evaluated by LC-HR-MS/MS method. LC-HR-MS/MS results showed that the concentration of most by-products, which were produced after 90 min reaction by US/ ZF1 process, was considerably lower than those obtained during sonolysis and US/ZnO processes. The study of ZF1 stability revealed that the degradation efficiency of AMP was reduced by only 5% after four repetitive experiments.

In spite of high stability of synthesized catalyst and low amount fluoride ion leachate from the structure, the separation of photocatalyst from solution after treatment is an important limitation of catalysts. In the following section the ZnO-based photocatalyst with high stability and magnetic properties was synthesized and its performance was evaluated for removal of SMX.

4.4. Removal of SMX by Fe₃O₄@Zn-O@g-C₃N₄

4.4.1. Experimental condition

The experimental conditions in this section are similar to those reported in Section (4.1.1).

4.4.2. Results and discussion

4.4.2.1. Characterization of photocatalysts

The XRD patterns of g-C₃N₄, ZnO, Fe-ZnO and FZG composites are shown in Fig. 4.26(a). The appearance of strong and narrow peaks confirmed that the synthesized photocatalysts were well crystallized. The peaks of pristine ZnO are in agreement with the hexagonal crystal phase of ZnO (JCPDS 65-3411). Three sharp peaks at 31.7°, 34.2° and 36.2° are assigned to (100), (002) and (101) faces of ZnO, respectively. The strong peaks of (100), (002) and (101) and the peaks with low intensities of (102) and (110) directions indicate the multi-directional growth of ZnO crystallites, which produce hierarchical structure. During the crystallization process, the adsorption of ethylene glycol on different surfaces of catalyst leads to preferential growth of ZnO crystallites at different rates, forming a petal-like morphology (Wang et al. 2010a). Both Fe-ZnO and FZG photocatalysts consist of Fe₃O₄ peaks at 31°, 35° and 43°, which are compatible with Fe₃O₄ peaks (JCPDS: 19-0629). In the case of g-C₃N₄, two distinct peaks at 13.1° and 27.1° correspond to the (100) and (002) diffraction planes, respectively (Pan et al. 2012). These two peaks can be clearly seen in the magnified XRD pattern of FZG in the inset of Fig. 4.26(a) which shows the growth of g-C₃N₄ on the surface of Fe-ZnO particles. There are no traces of other phases, indicating the high purity of photocatalyst and the successful preparation of FZG composite. The N₂ adsorption-desorption isotherms and pore size distribution curves of FZG1 are presented in Fig. 4.26(b). The presence of a H3 hysteric loop in typical IV-type isotherms indicates the mesoporous structure (Kumar et al. 2018). The mesoporous structure is beneficial for reducing mass transfer limitations and light harvesting in photocatalytic processes. Fig. 4.26(c) shows the pore size distribution of FZG1, which was determined by using the BJH method. The wide distribution of pore size further confirms the existence of pores at various sizes, which is preferable for accessibility of compounds to/from the catalytic sites (Li et al. 2016). The BET surface areas of four photocatalysts, i.e. ZnO, g-C₃N₄, Fe-ZnO and FZG1 were also evaluated. The specific surface area of ZnO sample was measured to be 28.95 m²/g. The presence of Fe₃O₄ nanoparticles on the structure of catalysts reduced the BET surface from 28.95 to 14.07 m²/g. The g-C₃N₄ sample had a relatively low specific surface area at 37.85 m²/g.

Various specific surface areas are reported for g-C₃N₄. For instance, Wang et al. (2017) reported the value of 10 m²/g, while the specific surface area reported by Zou et al. (2017b) is 275 m²/g. This difference is observed since the exfoliated g-C₃N₄ nanosheets can readily re-stack and form thick layers, leading to partial loss of their BET surface area (Wang et al. 2017). The coating of g-C₃N₄ onto the Fe-ZnO surfaces increased the specific surface area of catalyst to 18.14 m²/g. Therefore, the *in situ* growth of g-C₃N₄ on the Fe-ZnO surface not only led to the proper formation of an interface to charge transfer, but it also enhanced the specific surface area of FZG1 nanocomposite compared to Fe-ZnO. This enhancement favors light absorption and provides higher active sites for the photocatalytic process (Kumar et al. 2014). The DRS test was also examined in order to evaluate the optical properties of ZnO, g-C₃N₄, and the composites (Fig. 4.26(d)). As expected, the pristine ZnO could only absorb UV light spectrum and the corresponding band gap was ~3.2 eV which is compatible with the reported band gap for ZnO (He et al. 2015). The pure g-C₃N₄ has an absorption edge at 460 nm, corresponding to the band gap of 2.7 eV which is consistent with the reports in the literature (Zou et al. 2017b). The band gap of all the photocatalysts were calculated by using Eq. (4.4) and presented in Fig. 4.26(e). Interestingly, as shown in Fig. 4.26(d) the *in situ* growth of g-C₃N₄ on the ZnO surface increased the visible light absorption of FZG1. The potentials of conduction band and valence band edges of photocatalysts are calculated by using Eqs. (4.5) and (4.6) and listed in Table 4.9. PL spectroscopy is the emission of fluorescence, generated from the recombination of photo-induced e⁻/h⁺ pairs. Hence, the PL intensity is an indicator of the recombination rate of charge carriers (Kumar et al. 2014). In this study, PL spectroscopy test was conducted at an excitation wavelength of 325 nm. As seen in Fig. 4.26(f), g-C₃N₄ shows a strong photoluminescence with an emission peak at about 440 nm. The higher photoluminescence corresponds to the higher recombination of photo-induced electron and holes and lower quantum yield (Kumar et al. 2017). Interestingly, the addition of Fe₃O₄ to the structure of catalyst reduced the emission peak in PL spectra in Fe-ZnO compared to the bare ZnO. The addition of g-C₃N₄ to the Fe-ZnO followed by the formation of FZG1 further reduced the recombination of e⁻/h⁺ pairs and the PL emission due to strong interactions between Fe-ZnO and g-C₃N₄. The PL results demonstrated that the presence of Fe₃O₄ and the conjugation of Fe-ZnO and g-C₃N₄ promote the separation and the efficiency of photo-generated electron-hole pairs. However, the presence of Fe₃O₄ demonstrated a stronger effect.

Table 4.9. Band gap parameters for single photocatalysts

Photocatalyst	X (PAE)	E_{VB} (eV)	E_{CB} (eV)	E_g (eV)
ZnO	5.79	2.815	-0.235	3.05
g-C ₃ N ₄	4.73	1.58	-1.12	2.7

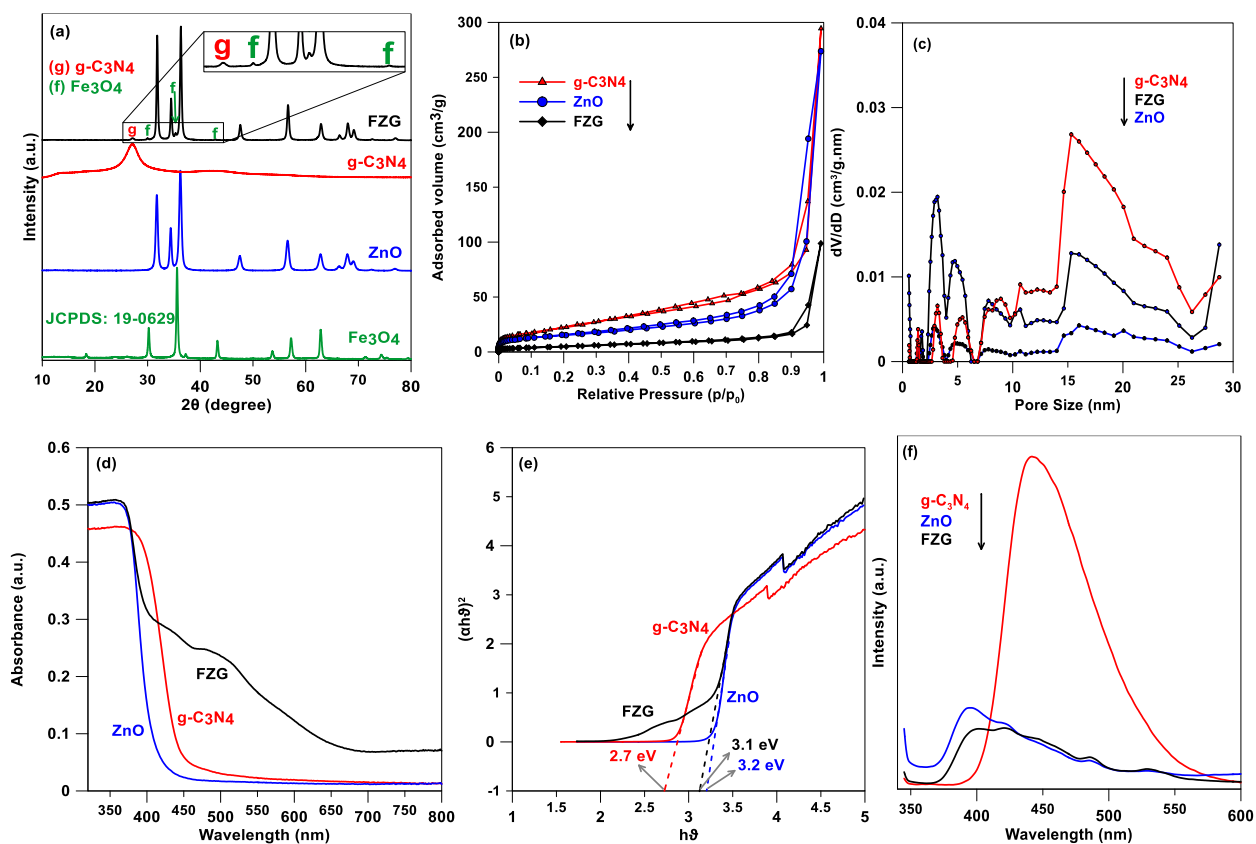


Figure 4.26. (a) XRD spectra of Fe₃O₄, pristine ZnO, g-C₃N₄ and FZG, inset: magnified XRD pattern of FZG and presence of g-C₃N₄ and Fe₃O₄ peaks; (b) Nitrogen adsorption/desorption isotherm of ZnO, g-C₃N₄ and FZG; (c) pore size distribution of ZnO, g-C₃N₄ and FZG; (d) DRS spectra of pristine ZnO, g-C₃N₄ and FZG; (e) Tauc plot of pristine ZnO, g-C₃N₄ and FZG; and (f) PL spectra of pristine ZnO, g-C₃N₄ and FZG excited at 325 nm.

The results obtained from the FTIR (Fig. 4.27) demonstrated that a strong chemical interaction occurred between ZnO and g-C₃N₄. The peak at 808 cm⁻¹ is related to the s-triazine ring vibrations in pure g-C₃N₄ (Kumar et al. 2014, Zhang et al. 2017a). However, this peak on the FZG1 sample shifted to the lower wavenumber (804 cm⁻¹). The observed red shift is caused by the formation of chemical bonds between ZnO and g-C₃N₄ in the conjugated system (Kumar

et al. 2014, Wang et al. 2017). This strong chemical interaction not only shows the formation of robust heterojunction structure, but it also facilitates the interfacial charge transfer between ZnO and g-C₃N₄ in the photocatalytic processes (Kumar et al. 2014).

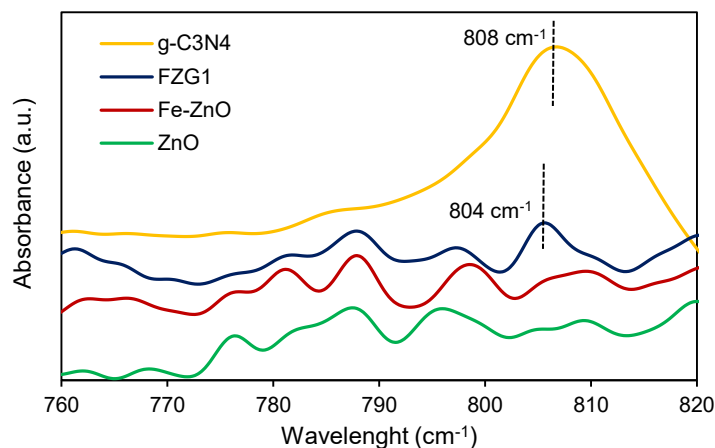


Figure 4.27. FTIR spectra of ZnO, g-C₃N₄, Fe-ZnO and FZG1.

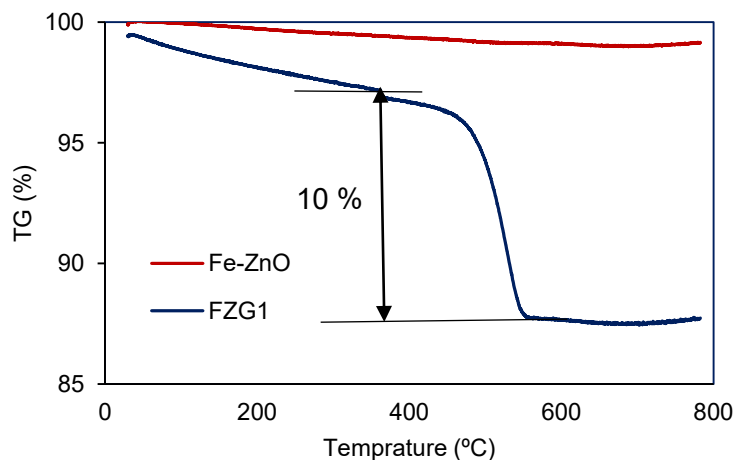


Figure 4.28. TGA curve of Fe-ZnO and FZG1.

The thermogravimetric analysis (TGA) was used to estimate the g-C₃N₄ content in the FZG1. As seen in Fig. 4.28 two weight loss regions are apparent in the TGA curve for FZG1. The first loss which occurred at 340 °C is related to water evaporation (about 1%). The major weight loss, which started at 490 °C and lasted until the temperature reached 700 °C, indicated the burning

and decomposition of g-C₃N₄ from the FZG1 structure. Therefore, the weight percentage of g-C₃N₄ was equal to the major weight loss of composite photocatalyst which was determined to be 10% in the FZG1 structure. However, for Fe-ZnO, only a slight slope of weight loss was observed, which corresponded to the evaporation of water molecules from the structure of catalyst. Fig. 4.29 shows the variation of zeta potential as a function of solution pH. As seen, the p*H*_(ZPC) is calculated as 3 which is close to the reported value for g-C₃N₄ (Shen et al. 2015).

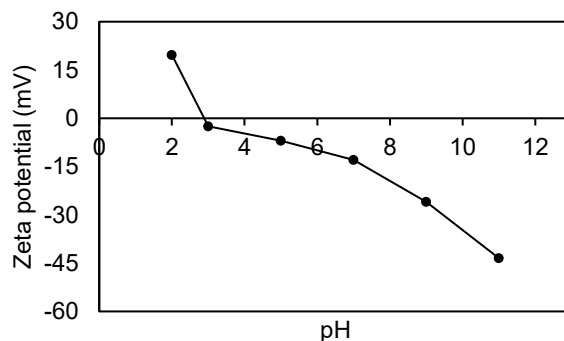


Figure 4.29. Zeta-potential of FZG as a function of pH value (Radjenovic and Petrovic 2017).

SEM images were used to investigate the morphology of photocatalysts. Fig. 4.30(a) shows the SEM images of the synthesized petal-like photocatalyst with approximately 4 μ m planar dimensions. The detailed morphology of the petal-like ZnO is shown in Fig. 4.30(b) and (c), which revealed that the thickness of petals is about 40-50 nm, and the entire architecture is assembled from several nano-petals with a smooth planar surface. The smooth surface of petals in ZnO and Fe-ZnO is probably due to Ostwald ripening during self-assembly crystallization (Zhong et al. 2006). The role of urea was crucial in this process. In a control experiment under the same synthesizing conditions, no particulate was collected in the absence of urea. The hydrolysis of urea provides steady and continuous supply of OH⁻ ions to react with zinc ions which control the growth speed of nuclei (Yan and Xue 2005). Such unique structure of ZnO is related to an appropriate portion of EG as the growth director in the solvent (Lv et al. 2015, Wang et al. 2010a). The SEM images with high magnification in Fig. 4.30(g-i) indicate the coating of ZnO nano-petals with g-C₃N₄, which produced the rough surfaces of photocatalyst. In addition, the smooth surface of Fe-ZnO was changed to porous structure after coating with g-

C₃N₄. This porous structure is beneficial since it improves the mass transport through the photocatalyst (Lv et al. 2015) and light trapping (Li et al. 2016). The presence of all elements i.e. Fe, Zn, O, N and C are verified by the EDS results (Fig. 4.31).

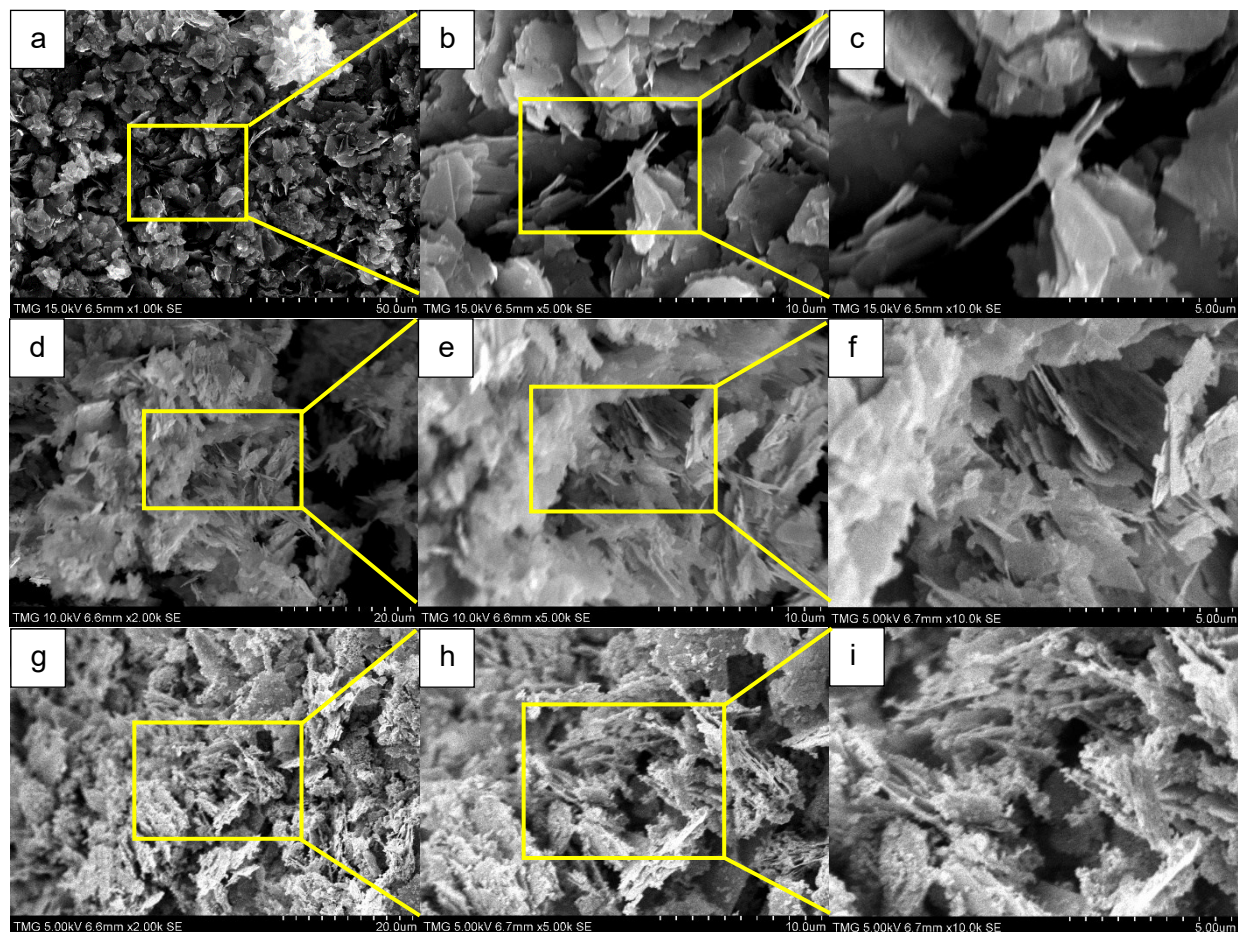


Figure 4.30. SEM images of ZnO (a-c), Fe-ZnO (d-f) and FZG1 (g-i) in three different magnifications.

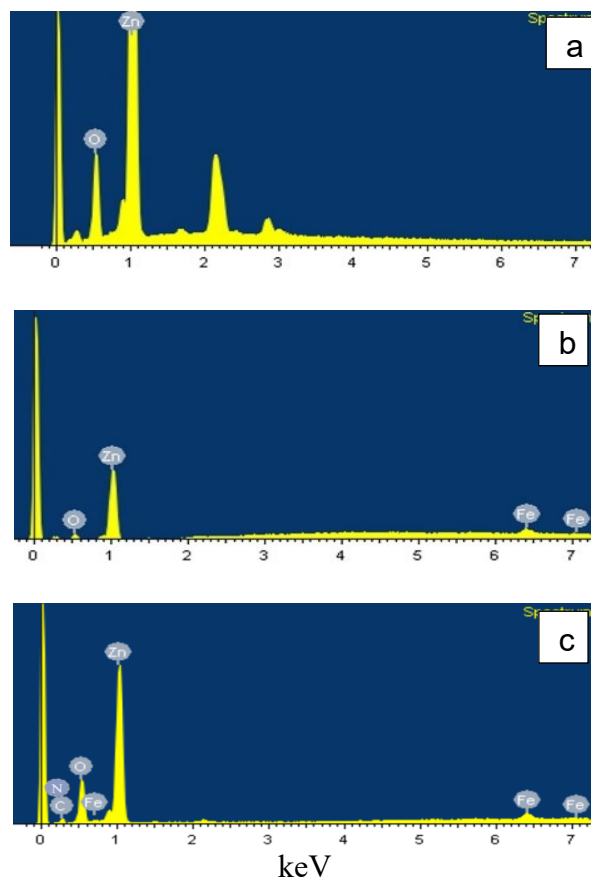


Figure 4.31. EDS spectra of (a) ZnO, (b) Fe-ZnO and (c) FZG1.

Fig. 4.32(a) shows the TEM images of quasi-monodispersed nanoparticles with sizes between 20 and 40 nm. The Fe_3O_4 nanoparticles are dispersed into the photocatalyst structure, which caused the magnetic properties of Fe-ZnO and FZG. High-angle annular dark-field (HAADF) imaging is a powerful tool for characterization of material with close atomic numbers. In this technique, the signal has a linear proportional to the thickness and atomic number of the examined sample (Chalasani and Vasudevan 2013). As shown in the inset of Fig. 4.32(a), the bright regions correspond to Fe_3O_4 . The iron nanoparticles are dispersed in the structure of specimen, while the agglomeration of iron oxide occurred in some areas. Fig. 4.32(b) shows the coalescence of nano-plates and the presence of Fe_3O_4 at the size of approximately 10 nm. As seen in Fig. 4.32(c), the FZG contains pores which may have been produced by the decomposition of urea during the *in situ* formation of $\text{g-C}_3\text{N}_4$ at the annealing stage (Zhu et al. 2014). The $\text{g-C}_3\text{N}_4$ protective layer with the thickness of about 3-4 nm provided a coating on the ZnO surface, thus favoring the charge carrier transfer between the interface of ZnO and $\text{g-C}_3\text{N}_4$,

extending the light harvesting range of Fe-ZnO and enhancing the photostability of photocatalyst. The inset of Fig. 4.32(d) shows the SAED pattern of the FZG nanocomposite, which confirms the polycrystalline nature of the composite.

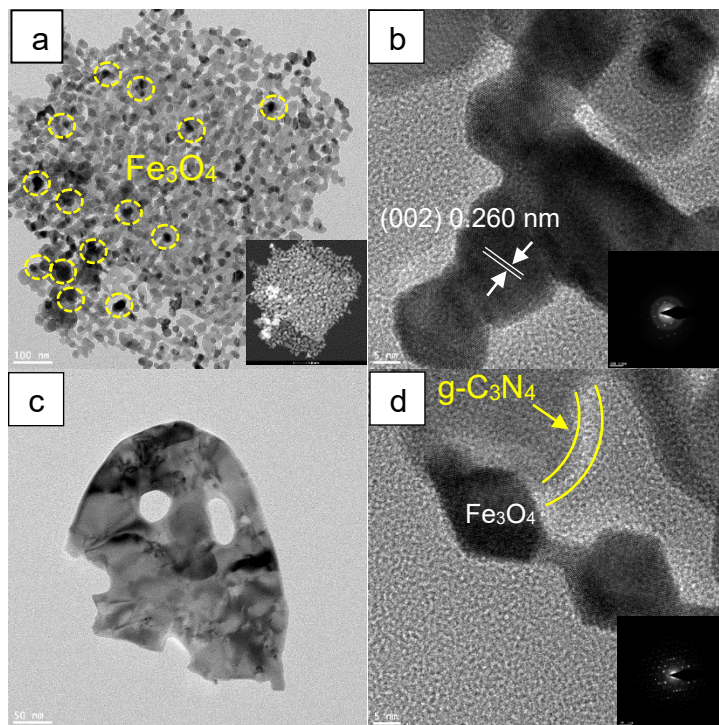


Figure 4.32. (a), TEM images of Fe-ZnO, inset: HAADF-STEM imaging Fe-ZnO, (b), high resolution TEM image of Fe-ZnO sample, inset: SEAD pattern for Fe-ZnO, (c-d) TEM images of FZG1, inset: SEAD pattern for FZG1.

The magnetic properties of Fe-ZnO and FZG1 samples were investigated at room temperature and the results are displayed in Fig. 4.33. Both samples showed the hysteresis loop, indicating a superparamagnetic behavior without any noticeable remanence. The saturation magnetizations of the Fe₃O₄-ZnO and FZG1 samples were 3.7 and 2.7 emu/g, respectively. The lower saturation magnetization of FZG1 compared to Fe-ZnO was due to the covering of the magnetic photocatalyst by g-C₃N₄ as a non-magnetic protective layer.

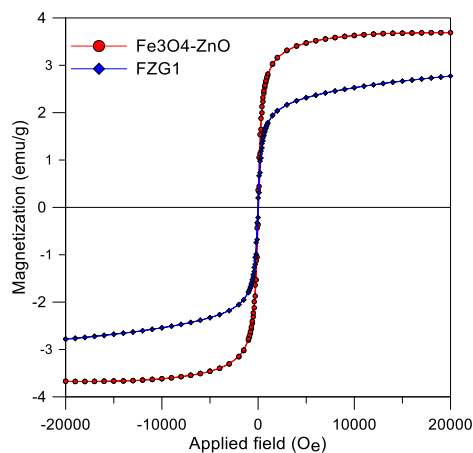


Figure 4.33. Magnetization curves of Fe_3O_4 -ZnO and FZG1.

4.4.2.2. Optimization of photocatalysts

The photocatalytic performance of photocatalysts was evaluated by the SMX degradation as illustrated in Fig. 4.34. As shown, a relatively high removal of SMX was achieved by direct photolysis in the absence of photocatalyst. This is due to the high overlap of employed low pressure UV lamp with maximum absorption wavelength of SMX which has been reported before (Luo et al. 2018, Willach et al. 2018). However, our previous study showed that the direct photolysis of SMX leads to a low extent of mineralization and formation of brownish by-products (Mirzaei et al. 2018c). In the photocatalytic processes, the removal of SMX by adsorption on photocatalysts after 30 min circulation in the dark was insignificant. Moreover, it was expected that the presence of Fe_3O_4 nanoparticles on the ZnO structure would improve the removal efficiency of SMX by facilitating the charge transfer and by reducing recombination of electron and hole pairs. However, this enhancement was not significant. This may be due the reduction of specific surface area of Fe-ZnO compared to ZnO as mentioned in Section 4.4.2.1. Apparently, the presence $g-C_3N_4$ in conjugated structure (FZG) considerably increased the SMX removal compared to bare ZnO and Fe-ZnO due to the enhancement of quantum yield by reducing the recombination rate of e^-/h^+ pairs. The coating of $g-C_3N_4$ at equal initial weight ratio (FZG1), which led to the formation of tertiary composite of different semiconductors, showed the best performance with 95.1% removal after 90 min, indicating that the amount of $g-C_3N_4$ in conjugated system plays an important role in the photocatalytic degradation of SMX. This occurred because the addition of $g-C_3N_4$ up to the optimum value (about 10% in FZG1) improved both specific surface area and absorption yield by reducing the recombination of

photo-induced e^-/h^+ pairs in a conjugated system. Nevertheless, too much $g-C_3N_4$ as the protective layer reduces the penetration of light to the ZnO surface, which is the major section of composite photocatalyst. A high amount of $g-C_3N_4$ would agglomerate on the surface, reducing the availability of active sites and causing light screening effect (Li et al. 2017, Zou et al. 2017b). Moreover, the accumulated $g-C_3N_4$ on the surface can act as a recombination center for photo-generated electron and holes and reduce the quantum yield of photocatalyst (Zou et al. 2017b). The overall micrometer-sized structure of hierarchical micro/nanostructure of FZG1 causes mechanical robustness against aggregation and wear and tear, whereas their nano-dimension provides high light-harvesting as well as a high surface area (Hu et al. 2008). Moreover, mass transfer limitation could be reduced due to the interconnected micro/nano porous structure in hierarchical photocatalyst (Li et al. 2016).

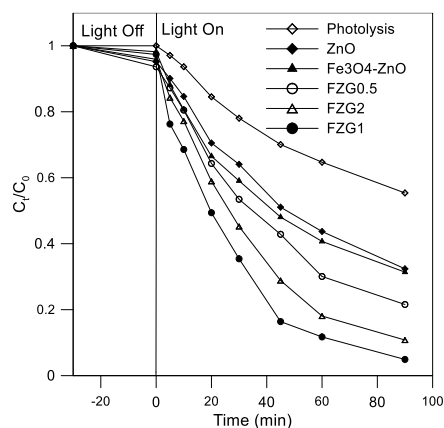
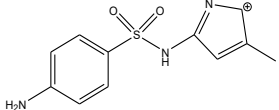
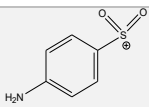
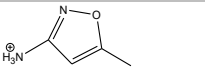
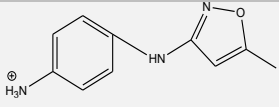
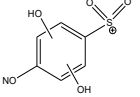


Figure 4.34. Photocatalytic degradation of SMX by photolysis and photocatalytic degradation by using ZnO, Fe_3O_4 -ZnO, FZG0.5, FZG1, and FZG2, experimental condition:

In order to evaluate the effect of $g-C_3N_4$ dose in hybrid photocatalysts, several potential by-products were examined in the treated samples after 90 min reaction by using FZG0.5, FZG1, FZG2 and bare ZnO. In addition, the intensity of peaks was compared as the indicators of by-products concentrations (Radjenovic and Petrovic 2017). A total of five by-products were identified by LC-HR-MS/MS method at the end of the reaction course (90 min), performed at 30 mg/L initial SMX concentration (Table 4.10) The structural assignment of detected by-products was based on accurate mass measurements and the proposed pseudo-molecular formula for SMX degradation reported in the literature (del Mar Gómez-Ramos et al. 2011, Ioannidou et al. 2017b,

Radjenovic and Petrovic 2017). The relative peak intensity of by-product [m/z 236.048], which was produced by losing the OH of isoxazole ring, was about 2, 100 and 65% lower in the UV/FZG0.5, UV/FZG1 and UV/FZG2 processes, respectively, compared to the intensity obtained in the UV/ZnO process. The cleavage of S–N bond resulting from the OH• attack on the sulfonamide bond led to the formation of [m/z 156.011] and [m/z 99.055]. In the case of [m/z 156.011] by-product, all composites showed better performance compared to bare ZnO, although FZG1 with 100% reduction showed the best performance. For [m/z 156.011] by-product, the relative peak intensity in comparison with bare ZnO was -46, -79 and +36% in the UV/FZG0.5, UV/FZG1 and UV/FZG2 processes, which further confirm the importance of g-C₃N₄ amount in the composite. In addition, [m/z 190.097] product was not detected in the treated solution by FZG1 and FZG2, while 31% reduction in the peak intensity was obtained by FZG0.5. Finally, the relative peak intensity of hydroxylation product of benzene ring ([m/z 201.98]) was about -71, -59 and -100% by UV/FZG0.5, UV/FZG1 and UV/FZG2 processes, respectively, compared to the intensity obtained in the UV/ZnO process.

Table 4.10. By-products identified during the photocatalytic degradation of SMX after 90 min reaction by UV/ZnO, UV/FZG0.5, UV/FZG1 and UV/FZG2 processes.

Chemical formula	Structure	[M+H] ⁺	t _r (min)	Intensity of peak			
				ZnO	FZG0.5	FZG1	FZG2
C ₁₀ H ₉ N ₃ O ₂ S		236.048	3.8	1261	1236 (-2%)*	N.D.# (-100%)	457 (-65%)
C ₆ H ₅ NO ₂ S		156.011	1.1	5835	2917 (-50%)*	N.D. (-100%)	2231 (-62%)
C ₄ H ₆ N ₂ O		99.055	0.92	58772	31638 (-46%)*	12356 (-79%)*	80018 (+36%)*
C ₁₀ H ₁₁ N ₃ O		190.097	0.95	3942	2707 (-31%)*	N.D. (-100%)	N.D. (-100%)
C ₆ H ₃ NO ₅ S		201.98	0.6	2561	748 (-71%)*	1056 (-59%)*	N.D. (-100%)

*(Changing percentage compared to the UV/ZnO process)

#N.D. = Not detected

A possible charge transfer mechanism is proposed to elucidate the enhanced photocatalytic activity of the FZG composite compared to bare ZnO for the SMX degradation (Fig. 4.35). As shown in Fig. 4.26(e) and Table 4.9, the band gap (E_g) of ZnO and g-C₃N₄ is calculated as 3.2 eV and 2.7 eV, respectively. The employed UV lamp in this study is able to excite the g-C₃N₄ and ZnO photocatalysts to generate electron/hole pairs. The valence and conduction band edge potential of a semiconductor can be determined by using Eq. (4.5) and Eq. (4.6) (Mirzaei et al. 2018a). As listed in Table 4.9, the conduction band edge potential of g-C₃N₄ is calculated as -1.12 eV which is more negative than that of ZnO with -0.31 eV. Moreover, the CB potential of Fe₃O₄ is reported as +1.21 eV (Kumar et al. 2018). Therefore, during the photocatalysis process, the photo-induced electrons transfer from CB of g-C₃N₄ to the CB of ZnO and further to Fe₃O₄ with a lower CB potential due to the heterojunction between g-C₃N₄, ZnO, and Fe₃O₄. As a result of electron deficiency of oxygen O₂ molecules (unpaired electrons) photo-induced electrons can then transfer to the dissolved oxygen to generate $O_2^{\cdot-}$ as an important reductant radical. In addition, electrons can directly participate in the reduction of SMX and the generated intermediates. The oxidation potential of photo-generated holes in the VB of g-C₃N₄ is determined as +1.58 eV which is significantly lower than the oxidation potential needed for the generation of hydroxyl radicals (+2.69 eV). However, the redox potential of holes in the VB of ZnO with 2.89 eV is high enough to generate hydroxyl radicals. Meanwhile, these holes can directly oxidize SMX or the formed intermediates during the photocatalytic process. It is reported that the charge transfer between semiconductors effectively reduces the electron-hole pairs recombination rate and prolongs the lifetime of the generated charge carriers (Kumar et al. 2018), which was confirmed by the reduction in PL emission intensity in this study (Fig. 4.26(f)).

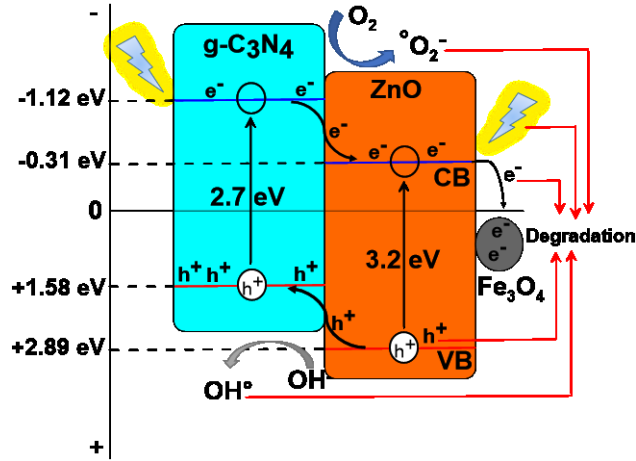


Figure 4.35. Band positions diagram and charge carriers transfer between ZnO, g-C₃N₄ and Fe₃O₄.

Considering that FZG1 photocatalyst showed the best performance for SMX removal and formation of lower by-products, this catalyst was selected for the ensuing experiments.

4.4.2.3. Experimental design and data analysis

The corresponding range of independent parameters including photocatalyst amount (X_1), pH of solution (X_2) and airflow rate (X_3) had been determined based on the preliminary experiments, as presented in Table 4.11.

Table 4.11. Ranges and levels of independent variables for SMX removal by using Fe₃O₄-ZnO@g-C₃N₄.

Independent variables (Unit)	Units	Level				
		-2	-1	0	+1	+2
Photocatalyst concentration (X_1)	g/L	0.4	0.5	0.6	0.7	0.8
pH of solution (X_2)	-	3	5	7	9	11
Airflow rate (X_3)	L/min	0.5	1	1.5	2	2.5

Table 4.12 presents the conditions of 20 experimental runs, and the experimental and predicted values of SMX degradation as the removal percentage. From the data in Table 4.12 a second-order polynomial equation was obtained to express the relationship between the response (Y) and process parameters (Eq. 4.19):

$$Y(\%) = -144.47 + 380.67X_1 + 22.20X_2 + 53.44X_3 - 431.61X_1^2 - 1.58X_2^2 - 21.26X_3^2 + 5.54X_1X_2 + 77.98X_1X_3 - 4.14X_2X_3 \quad (4.19)$$

where Y is the SMX removal efficiency after 60 min reaction expressed in %.

Table 4.12. Experimental design conditions and responses of each experimental run.

Run	Coded values of parameters			Actual values of parameters			Y (SMX removal efficiency %)	
	X ₁	X ₂	X ₃	X ₁	X ₂	X ₃	Actual ^a	Predicted ^b
1	+1	+1	+1	0.7	9	2.0	75.12	73.51
2	-1	-1	-1	0.5	5	1.0	72.91	73.73
3	0	-2	0	0.6	3	1.5	74.00	74.76
4	-1	-1	+1	0.5	5	2	84.00	81.67
5	0	0	+2	0.6	7	2.5	72.13	74.91
6	0	0	0	0.6	7	1.5	88.35	88.72
7	0	0	0	0.6	7	1.5	88.30	88.72
8	0	0	0	0.6	7	1.5	88.69	88.72
9	0	0	0	0.6	7	1.5	89.00	88.72
10	0	+2	0	0.6	11	1.5	52.00	52.02
11	+2	0	0	0.8	7	1.5	75.12	75.15
12	+1	-1	+1	0.7	5	2.0	92.16	90.95
13	+1	+1	-1	0.7	9	1.0	65.00	66.55
14	0	0	-2	0.6	7	0.5	62.00	60.00
15	+1	-1	-1	0.7	5	1.0	67.00	67.41
16	0	0	0	0.6	7	1.5	88.46	88.72
17	0	0	0	0.6	7	1.5	88.72	88.72
18	-1	+1	-1	0.5	9	1.0	68.00	68.42
19	-1	+1	+1	0.5	9	2.0	61.00	59.80
20	-2	0	0	0.4	7	1.5	67.00	67.75

^a actual SMX removal determined by experiment.

^b predicted SMX removal calculated according to Eq. (4.19) by Minitab V.16 software.

Statistically, a small p -value (<0.05) and a large F -value indicate the significance of a model or a parameter (Hou et al. 2012). As shown in Table 4.13, due to a high F -value (733.41) and very low probability ($p < 0.0001$), the regression model for SMX removal was found to be highly significant (Xiao et al. 2017). The predicted R^2 and adjusted R^2 values are 0.9896 and 0.9802, respectively. These values, which are close to one, further confirm that the model is adequate for

the regression of data. Judging by the F -values of variables, the order in which the independent parameters affected the SMX removal efficiency was: solution pH > photocatalyst concentration > airflow rate.

Table 4.13. ANOVA test for the response function Y .

Term	Degree of freedom	Sum of squares	Mean square	F-value	P-value
Model	9	2622.40	291.38	105.32	0.000
Linear	3	794.02	264.67	95.66	0.000
Square	3	1559.74	519.91	187.92	0.000
Interaction	3	268.64	89.55	32.37	0.000
X ₁	1	54.80	54.80	19.81	0.001
X ₂	1	516.99	516.99	186.86	0.000
X ₃	1	222.23	222.23	80.32	0.000
X ₁ .X ₁	1	139.04	468.39	169.30	0.000
X ₂ .X ₂	1	710.46	1007.81	364.26	0.000
X ₃ .X ₃	1	710.24	710.24	256.71	0.000
X ₁ .X ₂	1	9.83	9.83	3.55	0.089
X ₁ .X ₃	1	121.60	121.60	43.95	0.000
X ₂ .X ₃	1	137.20	137.20	49.59	0.000
Residual error	10	27.67	2.77		
Lack of fit	5	27.31	5.46	77.26	0.000
Pure error	5	0.35	0.07		
Total	19	2650.06			

$$R^2 = 0.9896, R^2 (adj.) = 0.9802$$

4.4.2.4. Effect of operating parameters on the removal efficiency of SMX

Fig. 4.36(a) and (b) present the variations of SMX removal as a function of the photocatalyst concentration (X_1) and solution pH (X_2) by 3D and contour plots, respectively. The dependence of SMX removal on the catalyst concentration (X_1) and airflow rate (X_3) is illustrated in Fig. 4.36(c) and (d) by 3D and contour plots, respectively. As seen, the SMX removal efficiency

increased by the increase of catalyst concentration up to the optimum value (0.65 g/L) and then it decreased. By increasing the catalyst concentration, the number of active sites, photon adsorption and contaminant adsorption increase, which lead to the direct elimination of contaminants or the generation of higher amounts of reactive species such as e^- , h^+ , OH^\bullet , and $O_2^{\bullet-}$ (Mirzaei et al. 2016). However, the increase of catalyst concentration higher than the optimum value decreased the penetration of light, due to the shielding effect of high photocatalyst concentration, and increasing the agglomeration and sedimentation of nanoparticles and reducing the accessibility of contaminants to the active sites (Gong and Chu 2015, Neppolian et al. 2002). Moreover, it is reported that at high photocatalyst loading, the photoexcited photocatalysts may be deactivated by collision with ground state photocatalysts (Neppolian et al. 2002).

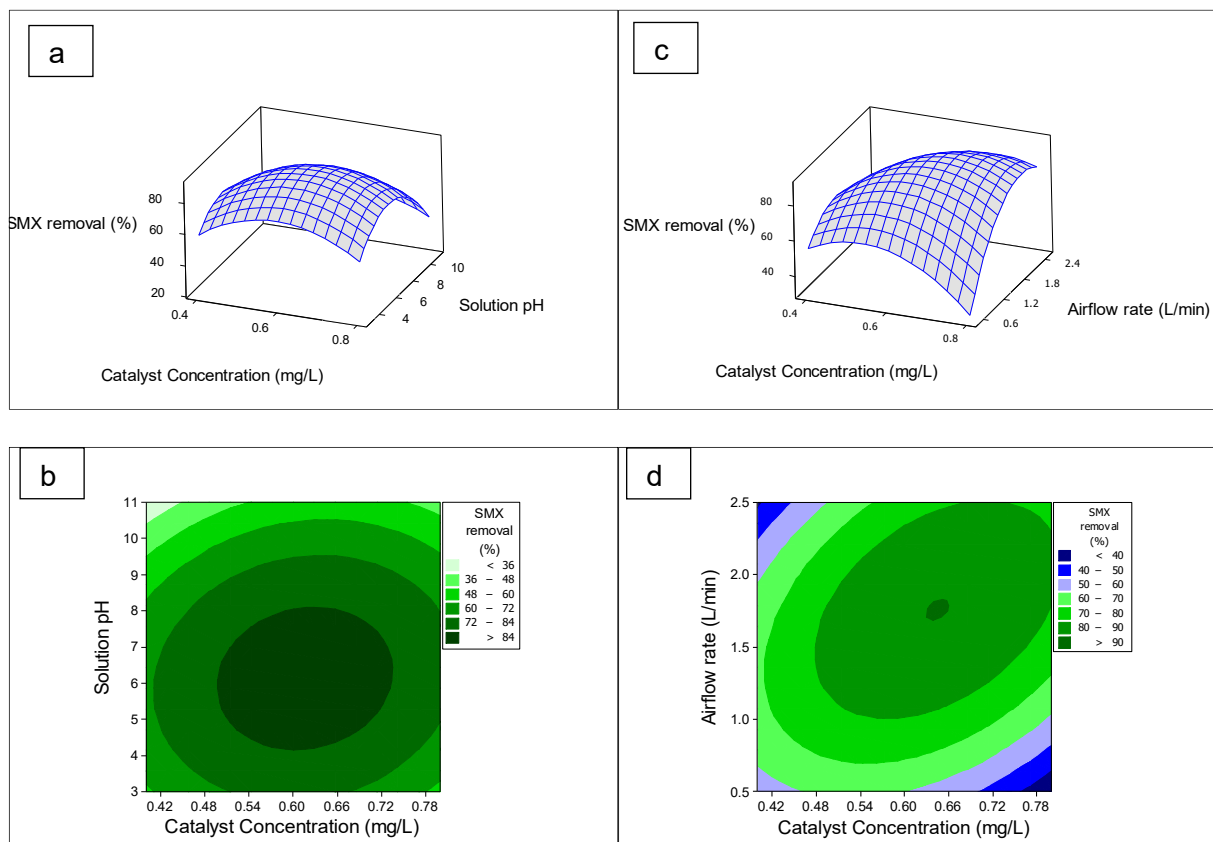


Figure 4.36. (a-b) 3D and contours surface plots of SMX degradation efficiency (%) for catalyst dosage vs pH, (c-d) catalyst dosage vs airflow rate.

As shown in Fig. 4.29, the zero point charge of FZG is determined as ~ 3 . Therefore, during all reported experiments, the surface of photocatalyst was negatively charged. On the other hand, when the pH of solution is higher than pK_{a1} and lower than pK_{a2} , SMX is mainly present in the neutral molecular state (Radke et al. 2009, Xiao et al. 2017), which has a higher light absorption capacity compared to the anionic or cationic forms (Niu et al. 2013). The pK_{a1} and pK_{a2} of SMX are 1.85 and 5.60, respectively (Xiao et al. 2017). The different molecular forms of SMX at different pH values are shown in Fig. 4.37.

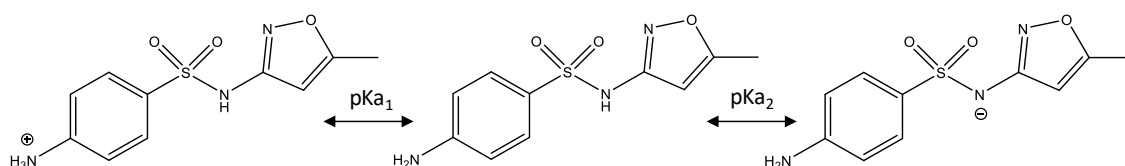


Figure 4.37. Different forms of sulfamethoxazole (SMX) at various pH values (Radjenovic and Petrovic 2017).

Fig. 4.36 shows that very acidic conditions are disadvantageous to SMX removal by the FZG composite. This happens because in strong acidic condition, both SMX and surface of FZG are positively charged and the adsorption capacity of photocatalyst toward SMX is reduced due to the repulsion force. Therefore, direct oxidation by photo-induced holes will be prevented at strong acidic condition. Generally, by increasing the pH value the efficiency of photocatalytic oxidation increases (Mirzaei et al. 2016), since the number of hydroxyl ions as the main precursor of hydroxyl radicals increases (Mirzaei et al. 2017b). However, at pH values more than the pK_{a2} of SMX, the photocatalyst surface and SMX are both negatively charged. Therefore, the removal efficiency decreases by increasing the pH value higher than 6, due to the repulsion force. Moreover, the affinity of reactive oxidants such as OH^\bullet radicals is generally lower to react with negatively charged compounds, leading to the reduction of SMX removal efficiency (Boreen et al. 2004, Gong and Chu 2015, Radke et al. 2009). As shown in Table 4.14, pH of 5.67 is suggested by the Minitab 16 statistical software as the optimum pH for SMX removal which is very close to the pK_{a2} of SMX.

It has been previously shown that aeration is an important factor in the photocatalysis process since it controls the dissolved oxygen concentration and the availability of oxygen molecules in

the solution (Chin et al. 2007, Nishio et al. 2006). As seen in Fig. 4.36(c) and (d) the increase of airflow rate up to the optimum value (1.89 L/min) had a positive effect on SMX removal. This is due to the fact that dissolved oxygen is strongly electrophilic and acts as the most important electron acceptor from the conduction band of photocatalyst (Lin et al. 2009, Pelaez et al. 2011). Dissolved oxygen molecules supplied to the liquid from air reduce the effect of unfavorable recombination of electrons and holes in the photocatalysis process (Nishio et al. 2006). Moreover, the extent of aeration can affect the size of photocatalyst aggregates and the accessible surface area (Chin et al. 2007). Nevertheless, the airflow rate higher than the optimum value led to the decrease of SMX removal, which could be attributed to the presence of a high number of air bubbles that reduce light penetration into the solution by the scattering effect caused by the smooth surface of bubbles (Mirzaei et al. 2016). Moreover, the surface of photocatalyst becomes highly oxygenated at high airflow rates. This limits the adsorption of contaminants and hydroxyl ions at active sites, which are essential to the direct oxidation of contaminants and OH[•] radical generation, respectively (Lin et al. 2009). In order to evaluate the accuracy of the developed model to predict the optimum values of parameters for “maximizing” the SMX removal as the target objective, a verifying experiment was conducted under the optimized condition. As shown in Table 4.14 the SMX removal achieved after 60 min reaction is close to the predicted values from Eq. 4.19, which further confirms that the adopted strategy to optimize the SMX removal process by RSM was successful.

Table 4.14. Optimum values of operating conditions and comparison of experimental and predicted values for SMX removal under the optimal conditions^a.

Parameter	Optimum values
Photocatalyst dosage (g/L) (X ₁)	0.65
pH of solution (X ₂)	5.67
Airflow rate (L/min) (X ₃)	1.89
Predicted SMX removal (%) after 60 min ^b	92.51 %
Experimental SMX removal (%) after 60 min	90.4 %

^a The initial SMX concentration is 30 mg/L

^b The values were calculated from Eq. (4.19)

There have been numerous reports on the photocatalytic degradation of SMX using UV lamps. It is reported that in comparison with UVA or UVB lamps, using UVC lamp would

enhance the removal efficiency due to synergistic effects of photolysis and photocatalytic mechanisms (Kim and Kan 2016, Nasuhoglu et al. 2011, Rioja et al. 2014). However, most reported studies on SMX removal have employed UV lamps emitting radiation either in UVA or UVB range. For comparison, Table 4.15 has summarized only the reported studies on photocatalytic removal of SMX by using UVC lamp. It should be noted that several parameters such as photoreactor design, catalyst dosage, solution pH, water matrix, initial SMX concentrations, etc. can also affect the photocatalytic efficiency (Mirzaei et al. 2018c). Interestingly, a high extent of mineralization at a relatively short treatment time was achieved in this study, which is comparable with previously reported SMX removal under UVC, as listed in Table 4.15.

Table 4.15. Comparison of reported efficiencies of removal and mineralization of SMX by photocatalytic process under UVC irradiation.

Photocatalyst	Light source	Experimental condition	Efficiency	Ref.
TiO ₂ Degussa P25 [Photocatalyst] = 0.5 g/L	UVC, Lamp Power: n.a.	[SMX] ₀ = 12 mg/L Volume = 1600 mL Solution pH = n.a.	<ul style="list-style-type: none"> • 100% SMX removal (30 min) • 87% COD removal (360 min) • Toxicity increased after treatment 	(Nasuhoglu et al. 2011)
Biochar-supported TiO ₂ [Photocatalyst] = 5 g/L	UVC, Lamp Power: 15W	[SMX] ₀ = 10 mg/L Volume = 100 mL Solution pH = 4	<ul style="list-style-type: none"> • 91% SMX removal (360 min) • 81% COD removal (360 min). • Toxicity substantially reduced after 360 min treatment. 	(Kim and Kan 2016)
Fluorinated ZnO [Photocatalyst] = 1.48 g/L	UVC, Lamp Power: 10W	[SMX] ₀ = 1mM Volume = 1000 mL Solution pH = 4.8	<ul style="list-style-type: none"> • 95% SMX removal (30 min) • 80% COD removal (90 min) • Toxicity substantially reduced after 30 min treatment. 	(Mirzaei et al. 2018c)
TiO ₂ Degussa P25 [Photocatalyst] = 0.5 g/L	UV-LED, λ_{\max} = 250 nm, Output power: 10 mW	[SMX] ₀ = 20 mg/L Volume = 150 mL Solution pH = 4	<ul style="list-style-type: none"> • About 100% SMX removal (60 min) • 59.9% TOC removal (180 min) 	(Eskandarian et al. 2016)
Au-Cu/TiO ₂ [Photocatalyst] = 0.5 g/L	UV-LED, λ_{\max} = 250 nm, Lamp Power: n.a.	[SMX] ₀ = 30 mg/L Volume = 250 mL Solution pH = 5.5	<ul style="list-style-type: none"> • 100% SMX removal (45 min) • ~40% TOC removal (90 min) 	(Zanella et al. 2017)
ZnO [Photocatalyst] = 1.5 g/L	UVC, Lamp Power: 30W	[SMX] ₀ = 10 mg/L Volume = 200 mL Solution pH = 4	<ul style="list-style-type: none"> • 80% SMX removal (60 min) • 20.8% TOC removal (360 min) 	(Pourmoslemi et al. 2016)
Magnetic ZnO@g-C ₃ N ₄ [Photocatalyst] = 0.65 g/L	UVC, Lamp Power: 10W	[SMX] ₀ = 30 mg/L Volume = 1000 mL Solution pH = 5.67	<ul style="list-style-type: none"> • ~100% SMX removal (90 min) • 64% COD removal (90 min) • 45% TOC removal (90 min) • Toxicity substantially reduced after 90 min treatment. 	This study

4.4.2.5. Kinetics of SMX removal

As shown in Fig. 4.38 the first-order rate constant for SMX removal by FZG was 0.0385 min^{-1} which is about 2.3 times higher than the rate obtained by using commercial ZnO, further confirming the improvement of photocatalytic activities in composite form. The effect of natural radical scavengers on the rate of SMX removal was evaluated in the presence of 1 mM calcium sulfate, sodium chloride, sodium nitrate or sodium bicarbonate under the optimum conditions for SMX removal. As seen from Fig. 4.38(b) the rate of SMX removal decreased in the presence of all examined anions due to their radical scavenging effects, while chloride ion showed the most inhibitory effect. This may be due to the properties of chloride that can act as both hole and hydroxyl radical scavenger (Karaca et al. 2016). The rate constant of SMX removal was reduced from 0.0385 to 0.0235 min^{-1} in the presence of chloride. Since the surface of FZG is negatively charged under optimum conditions, the adsorption of anions on the surface of FZG is unlikely to occur, suggesting that the observed reduction of SMX removal rate constant is mostly related to the reactions of OH^\bullet radicals with the examined anions. Following the effect of chloride, the extent of reduction of SMX removal rate constant in the presence of scavengers correlated with the rate constants of reactions between OH^\bullet radicals and scavengers, which have been reported to be 3.9×10^8 , 1.5×10^6 and $5 \times 10^5 \text{ M}^{-1}\text{s}^{-1}$ for carbonate, nitrate and sulfate, respectively (Sasi et al. 2015). Accordingly, the rate constant of SMX removal was reduced from 0.0385 min^{-1} to 0.0272, 0.0308 and 0.0342 min^{-1} in the presence of carbonate, sulfate and nitrate, respectively.

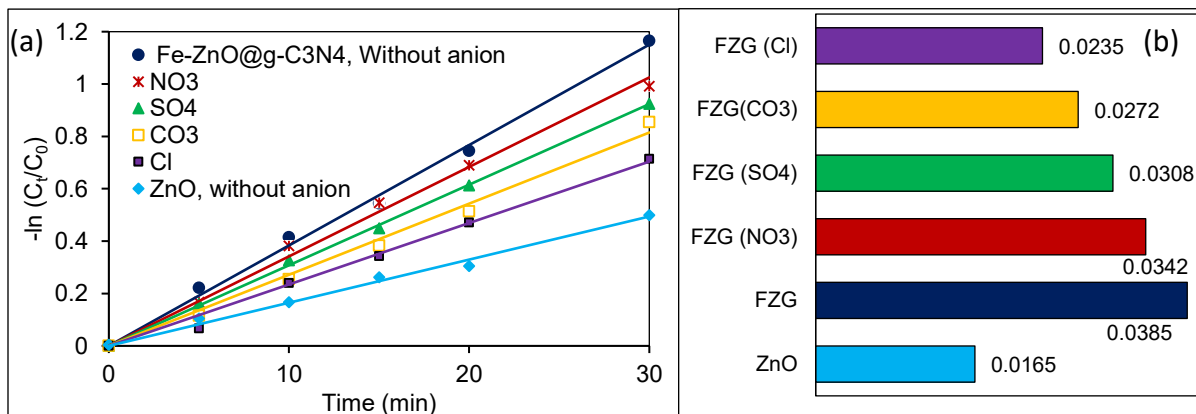


Figure 4.38. (a) First-order kinetic plots for SMX removal by commercial ZnO and FZG in the absence and presence of anions; (b) first-order kinetic rate constants. Experimental condition: $[\text{SMX}]_0 = 30 \text{ mg/L}$, $[\text{catalyst}]_0 = 0.65 \text{ g/L}$, $\text{pH} = 5.87$, $\text{airflow rate} = 1.89 \text{ L/min}$, $[\text{scavenger}]_0 = 1 \text{ mM}$.

4.4.2.6. COD and TOC removal

As shown in Fig. 4.39, under the optimum operating conditions, the removal of COD and TOC was approximately 64% and 45%, respectively, after 90 min of reaction. However, during this period about 99% SMX removal was achieved, suggesting that SMX was transformed into persistent by-products during the treatment process. Considering that the generated by-products may be more toxic than their parent compounds, the possible change in the solution toxicity after the treatment process was assessed.

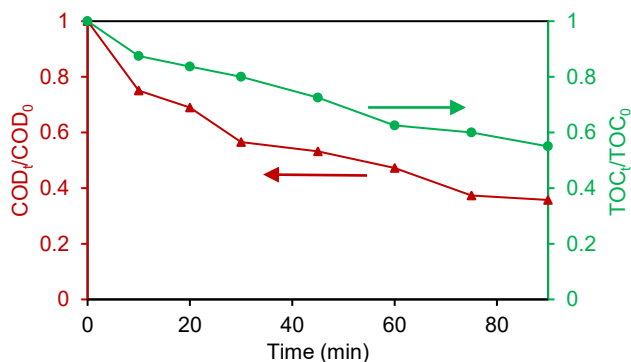


Figure 4.39. Degree of mineralization of SMX as COD and TOC removal; experimental condition: $[SMX]_0 = 30$ mg/L, $[catalyst]_0 = 0.65$ g/L, $pH = 5.87$, airflow rate = 1.89 L/min.

4.4.2.7. Toxicity assessment

Fig. 4.40 illustrates the percentage inhibition (PI) of SMX solution at different treatment times using photocatalytic degradation by FZG under optimum operating conditions. The results showed a high percentage of solution inhibition (27%) against *E. coli* bacteria before treatment. After 20 min treatment, the toxicity of SMX solution as PI was considerably reduced, although it was still above the “non-toxic” range ($-10\% < PI < 10\%$). Longer treatment times up to 60 and 90 min led to the reduction of PI to 6% and 5% respectively, which are lower than the toxic inhibition region boundaries.

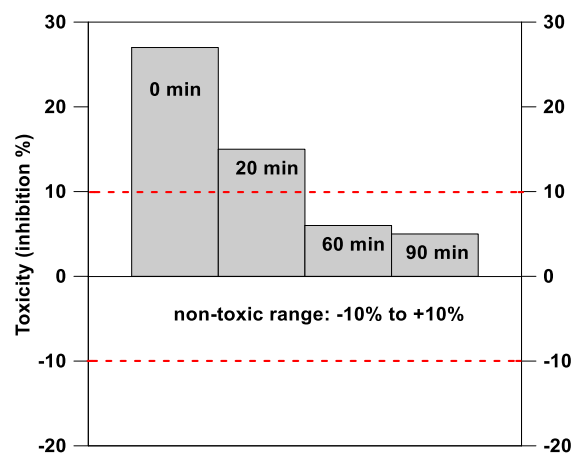


Figure 4.40. Changes in toxicity as the percentage inhibition of *E. coli* bacteria before and after the treatment of SMX solution by FZG under the optimum conditions.

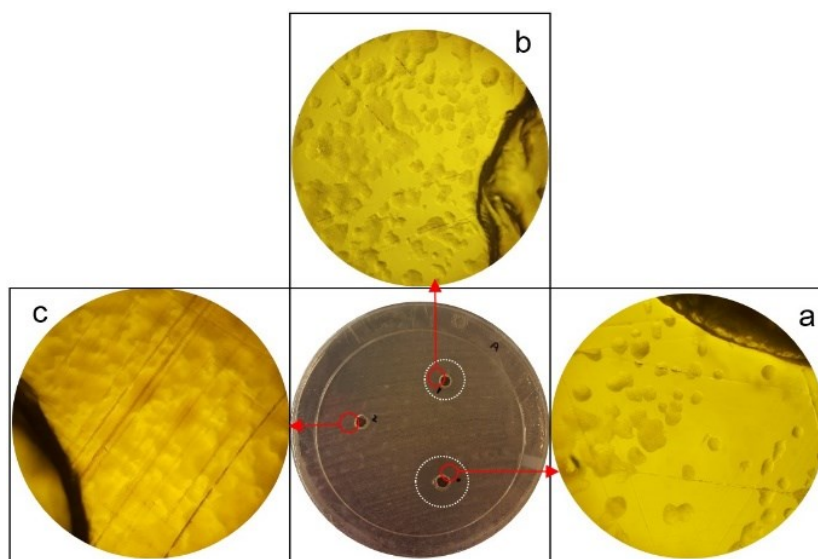


Figure 4.41. Well-agar diffusion method and magnified images of wells after (a) 0 min, (b) 20 min, and (c) 60 min treatment.

The results of agar-well diffusion method utilized to further evaluate the change of solution toxicity are shown in Fig. 4.41. As shown in Fig. 4.41(a) the initial SMX solution was toxic to *E. coli* and a clear inhibition zone was formed around well number 0. The diameter of this inhibition zone was reduced after 20 min treatment while it was totally removed after 60 min reaction, further confirming the efficiency of catalytic process for toxicity reduction. The magnified images of inhibition zones after 20 min and 60 min treatment and the growth of *E. coli* colonies around wells are shown in Fig. 4.41(b) and (c) respectively.

4.4.2.8. Transformation pathway and by-product formation

During the photocatalytic oxidation process, numerous degradation products (DPs) may be formed due to the non-selective nature of $\text{OH}\cdot$ radicals (Hu et al. 2007a). A total of eleven DPs were identified by LC-HR-MS/MS method at various time intervals during a 60 min reaction course, performed at 30 mg/L initial SMX concentration. The analysis was performed in positive ionization modes and the structural assignment of detected DPs was based on accurate mass measurements and the proposed pseudo-molecular formula for SMX degradation reported in the literature (del Mar Gómez-Ramos et al. 2011, Ioannidou et al. 2017a, Radjenovic and Petrovic 2017). The evolution profile of DPs based on their peak intensities are illustrated in Fig. 4.42(a) and (b) for high-intensity and low-intensity DPs, respectively. The proposed degradation pathways are illustrated in Fig. 4.43. The extracted ion chromatograms (XICs) of detected degradation products are shown in Fig. S1 in appendix. The product of hydroxylation of isoxazole ring or benzene ring (DP 300) was detected with a relatively high peak intensity. This DP remained stable and unchanged during the reaction course and its probable derivatives (DPs with $[\text{M}+\text{H}]^+ > 254$) were not detected. The resistance of hydroxylated form of SMX during the oxidation process is reported before (Hu et al. 2007a). As shown in Fig. 4.43 the cleavage of S–N bond resulting from the $\text{OH}\cdot$ attack on the sulfonamide bond and the subsequent abstraction of sulfone moiety is a main transformation pathway proposed in this study for the degradation of SMX. A number of organic intermediates accumulate during the first 30 min of degradation, but the intensity of their peaks was considerably reduced at longer degradation times. Most of the detected DPs contained nitrogen but not sulfur, indicating that sulfone moiety of SMX is more labile compared to nitrogen which is consistent with the results reported by Hu et al. (Hu et al. 2007a). While the concentrations of identifiable organic DPs were reduced below detection limits at longer treatment times, the formation of more stable by-products during the reaction is evident from the lower rates of TOC and COD removal compared to their initial rates. Although the mineralization of parent contaminant was not completed, the reported treatment is sufficient to remove the antimicrobial activity of solution, as confirmed by toxicity assays.

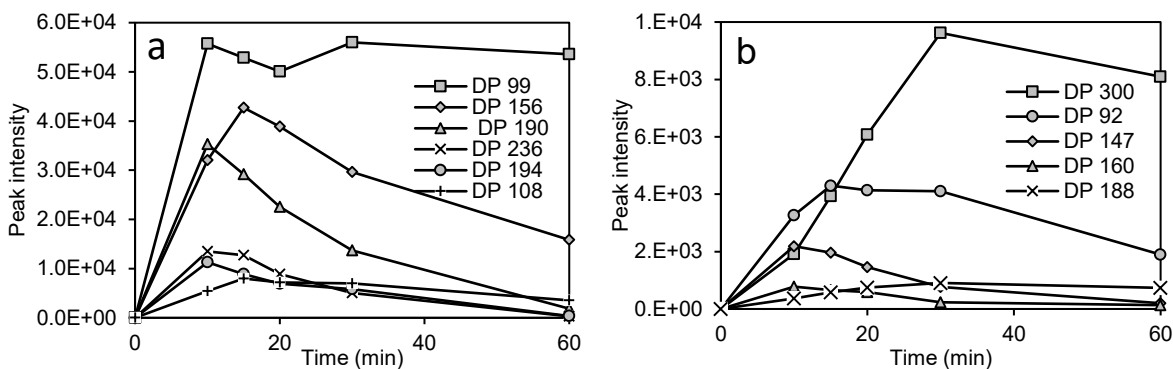


Figure 4.42. Evolution of major degradation products (DPs) with (a) high-peaks intensities and (b) low intensities in photocatalytic degradation of SMX under optimum conditions.

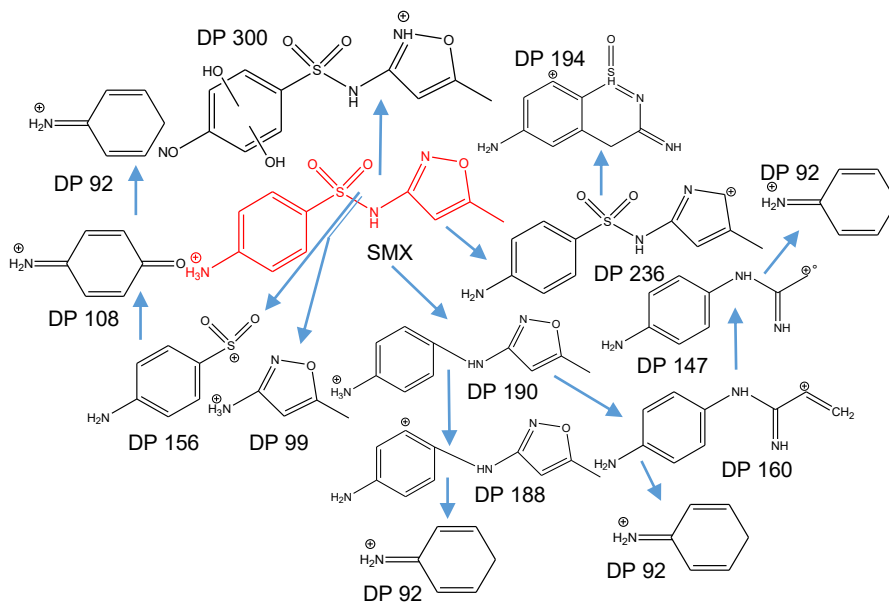


Figure 4.43. Proposed degradation pathway of SMX by photocatalytic degradation by using FZG.

4.4.2.9. Stability of the synthesized catalyst

The reusability of FZG1 was evaluated after 5 consecutive experimental runs as illustrated in Fig. 4.44(a). The FZG1 nanoparticles were readily and quickly separated from the aqueous solution in 1 min, whereas the ZnO suspensions did not clarify by gravity even after 90 min. After each experiment, the photocatalyst particles were separated and washed several times with deionized water and were dried at 100 °C overnight and then they were used in the subsequent experiment. As shown in Fig. 4.44(a), no significant decrease in the activity of FZG1 was

observed after five experimental runs, which indicate the high stability of the synthesized photocatalyst. The photocorrosion of ZnO mainly occurs due to the self-oxidation of ZnO based on Eq. (3.9).

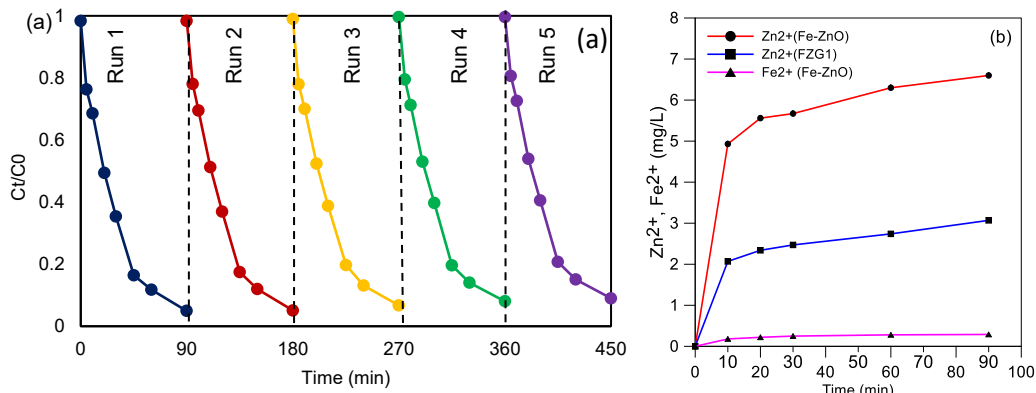


Figure 4.44 (a) Recyclability of FZG1 photocatalyst (five successive experiments) for the degradation of SMX, (b) release of zinc and iron ions into the solution as a function of time for Fe-ZnO and FZG1, experimental conditions: $[SMX]_0 = 30$ mg/L catalyst dosage: 0.5 g/L, initial solution pH=7, air flow rate = 1.5 L/min

In this regard, certain strategies have been proposed to slow down the self-oxidation rate and increase the stability of ZnO. For instance, hybridization with carbon materials such as C₆₀ (Fu et al. 2008), carbon nanotube (Han et al. 2014), graphite-like carbon layers (Zhang et al. 2009b), graphene (Chen et al. 2013) and monomolecular-layer polyaniline (PANI) (Zhang et al. 2009a) are used to suppress the photocorrosion of ZnO. Despite the relative success of the previously proposed processes to inhibit the photocorrosion of ZnO, the use of g-C₃N₄ as the protective layer, as presented in this study, provides the following important benefits: First, g-C₃N₄ protects the surface of photocatalyst against self-oxidation, and second, it improves the efficiency of SMX removal as a conjugated semiconductor by generating electron and hole pairs, thus facilitating the charge separation and increasing the specific surface area. In addition, based on Eq. (3.9), the release of Zn²⁺ ion into the solution was used as the indicator of photocorrosion. As seen from Fig. 4.44(b), the concentration of Zn²⁺ in the solution increased during the treatment course for both Fe-ZnO and FZG1. However, the release of Zn²⁺ from FZG1 into the treated solution was considerably lower than the release from Fe-ZnO which further indicates the effectiveness of g-C₃N₄ as the protective layer. As shown in Fig. 4.44(b), the release of iron ions into the solution was also investigated in an effort to evaluate the stability of photocatalyst. Due

to the low content of Fe_3O_4 in the photocatalyst structure, the maximum amount of iron ion after 90 min reaction was measured to be 0.29 (mg/L) for Fe-ZnO, while in the case of FZG1 the iron concentration was lower than the detection limit of atomic absorption spectrometer (0.11 mg/L) even after 90 min reaction. This result further confirms the higher stability of FZG1 compared to Fe-ZnO. Moreover, it is reported that a hierarchical structure of semiconductor leads to the higher stability against aggregation (Li et al. 2016, Wang et al. 2010a). Thus, the self-oxidation of photocatalyst, which is initiated by aggregation, will be hindered by hierarchical configuration. The high stability of FZG1 synthesized in this study could be attributed to the synergistic effect of hierarchical micro/nanostructure, reduced aggregation and the use of g- C_3N_4 as an effective protective layer.

4.4.3. Conclusions and remarks related to the removal of SMX by $\text{Fe}_3\text{O}_4@\text{ZnO}@g\text{-C}_3\text{N}_4$

In this phase of research, a petal-like photocatalyst, $\text{Fe}_3\text{O}_4\text{-ZnO}@g\text{-C}_3\text{N}_4$ (FZG) with different g- C_3N_4 to ZnO ratios was synthesized with hierarchical structure. The FZG1 photocatalyst, having the weight ratio of 1:1 for the initial urea and $\text{Fe}_3\text{O}_4\text{-ZnO}$ (Fe-ZnO), presented the highest sulfamethoxazole (SMX) degradation rate, which was 2.6 times higher than that of pristine ZnO. After selecting the best photocatalyst, the effect of catalyst dosage (0.4-0.8 g/L), solution pH (3-11) and airflow rate (0.5-2.5 L/min) on the SMX removal efficiency and the optimization of process was studied by RSM. Besides the facile separation, the performance of photocatalyst was improved due to the function of iron oxide as an electron acceptor that reduced the electron/hole recombination rate. The coating of g- C_3N_4 on the Fe-ZnO surface not only acted as a protective layer for ZnO against photocorrosion, but it also enhanced the photocatalytic activity of the catalyst for SMX degradation through the heterojunction mechanism. Under the optimum conditions, i.e. 0.65 g/L photocatalyst concentration, pH=5.6 and airflow rate=1.89 L/min, 90.4% SMX removal was achieved after 60 min reaction. The first-order kinetic rate constant for SMX removal by using FZG was 0.0384 min^{-1} while the rate constant by commercial ZnO was 0.0165 min^{-1} . Moreover, under the optimum conditions, about 64% COD removal and 45% TOC removal and a considerable reduction in toxicity were observed. The analysis of generated intermediates during the photocatalytic degradation of SMX was conducted by LC-HR-MS/MS method and a degradation pathway was proposed.

The majority of studies in photocatalysis nowadays emphasize the need for visible-driven photocatalysts for sustainable solar-based water treatment technology. It is reported that approximately 45% of published papers in photocatalysis targeted visible light activity or sunlight-driven treatment (Cates 2017). However, the efficiency of visible-driven photocatalysts, high area footprints that would result in replacing UV lamp reactors with solar irradiation and high energy consumption in the case of replacing visible with UV lamp, should also be considered. Consequently, in the following section, a UV/Visible driven photocatalyst was synthesized and its performance for removal of AMX was evaluated.

4.5. Removal of AMX by magnetic fluorinated g-C₃N₄ under UV and visible light

4.5.1. Experimental condition

The photocatalytic experiments with UV and visible light were performed in batch mode of operation. The schematic diagram of UV-driven cylindrical photoreactor is provided in Fig. 3.1 and Fig. 3.2(a). A 500 W halogen lamp with a UV cutoff filter (>400 nm) was used as the light source in visible-driven experiments as shown in Fig. 3.2(b). In both UV and visible-driven experiments, photocatalysts at 1 g/L concentration were used and the pH of solution was adjusted to 7. Millipore Milli-Q deionized water (DIW) was used to prepare AMX solution at 0.25 mM initial concentration and air at 1.5 L/min flowrate was bubbled into the solution. The solution temperature was maintained at 25 °C by using a cooling water system. Before irradiation, the solution was circulated for 60 min to ensure the achievement of adsorption/desorption equilibrium.

4.5.2. Results and discussion

4.5.2.1. Characterization of photocatalysts

Fig. 4.45(a) shows the XRD patterns of Fe₃O₄, bare g-C₃N₄, and nanocomposites with different Fe₃O₄ contents. The peaks at $2\theta = 18.3^\circ, 30.2^\circ, 35.6^\circ, 43.2^\circ, 53.6^\circ, 57.1^\circ, 62.6^\circ$ and 74.2° are indexed as (111), (220), (311), (400), (422), (511), (440), and (553) planes of magnetite (JCPDS: 19-0629) (Hou et al. 2016). These sharp narrow peaks indicate that Fe₃O₄ is highly crystalline. For the bare g-C₃N₄, the small peak at 13.2° corresponds to the tri-s-triazine unit plane (100) (Shen et al. 2016), while the peak at 27.6° is indexed to the (200) plane which arises from the interlayer-stacking of the conjugated aromatic segments (Zhao et al. 2014). Both corresponding peaks of GF are sharper than that of bare g-C₃N₄. This is due to the rearrangement

of g-C₃N₄ structure during the hydrothermal exfoliation process (Han et al. 2016, Zhao et al. 2014). Moreover, as shown in Fig. 4.46 the (002) peak of g-C₃N₄ is shifted from 27.1° to 27.6°, indicating a decreased gallery distance between the layers during the hydrothermal process (Dong et al. 2017). This happens because during the NH₄F-assisted exfoliation, strong acid (HF) is produced by the hydrolysis of NH₄F which leads to the cleavage of g-C₃N₄ layers. The cleavage of g-C₃N₄ layers by strong acids such as HCl (Dong et al. 2017, Ma et al. 2014, Zhang et al. 2014) and H₃PO₄ (Shi et al. 2016) has been reported before. Compared with the pure counterparts, the XRD patterns of FeGF composites contain the peaks of both Fe₃O₄ and g-C₃N₄, and the intensity of Fe₃O₄ peaks gradually increases with the increasing of Fe₃O₄ content. At a higher Fe₃O₄ percentage (FeGF2 and FeGF3) even the weak peaks of Fe₃O₄, such as those in the (440) and (553) planes are detectable.

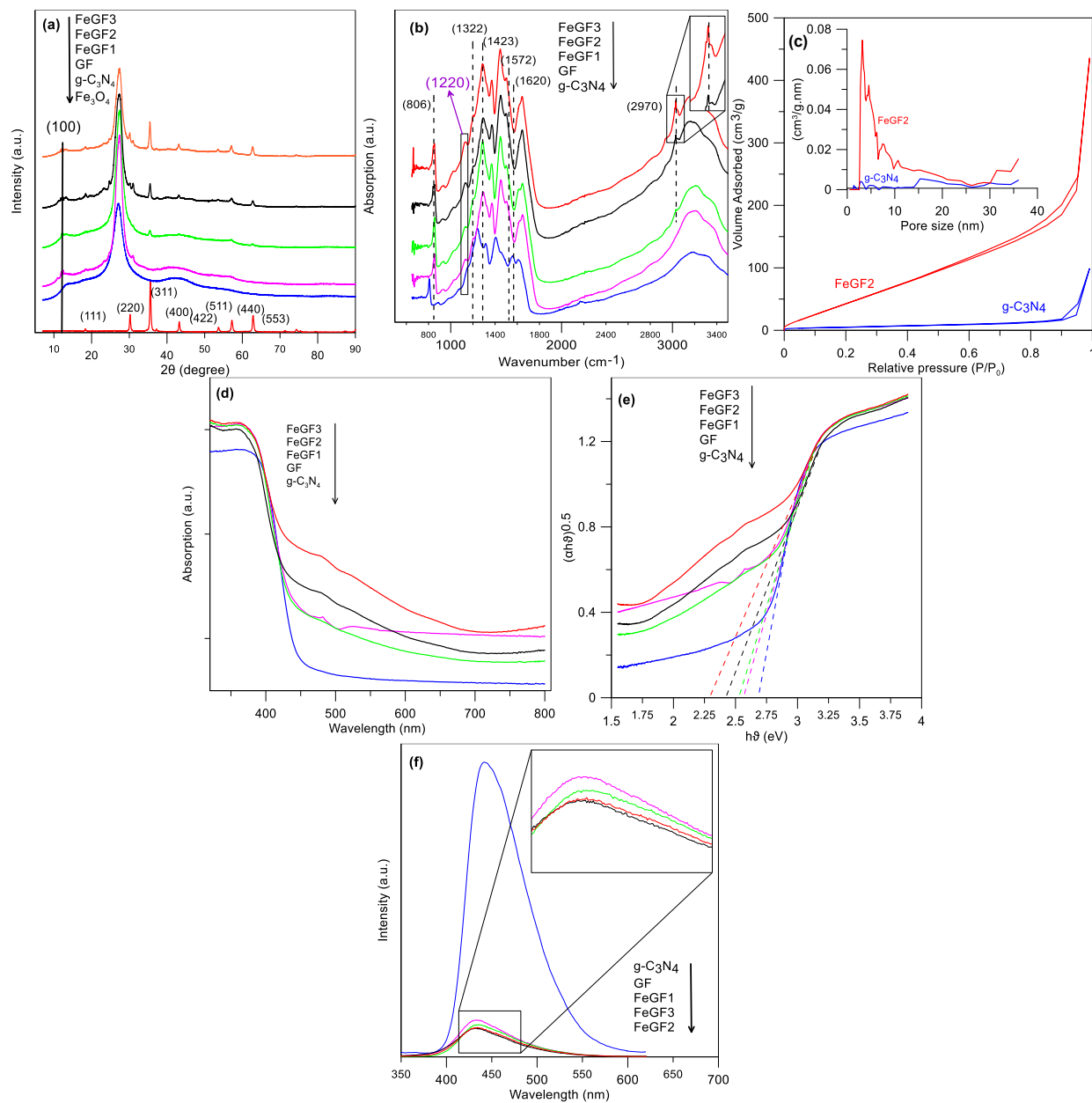


Figure 4.45. (a) XRD patterns, (b) FTIR spectra, (c) Nitrogen adsorption–desorption isotherms (inset: pore size distribution), (d) UV–vis diffuse reflectance spectra, (e) PL emission spectra, and (f) band gaps (E_g) of g-C₃N₄, GF, FeGF1, FeGF2 and FeGF3

This indicates that Fe₃O₄ has been successfully introduced into the g-C₃N₄ structure and both are in good combination in the composites.

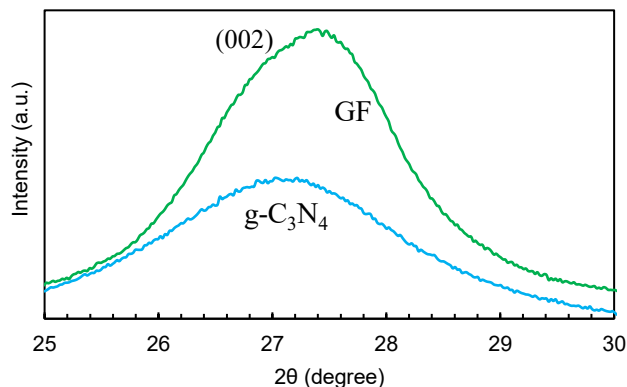


Figure 4.46. Magnified (002) peak of XRD pattern of $g\text{-C}_3\text{N}_4$ and exfoliated $g\text{-C}_3\text{N}_4$ (GF).

Fig. 4.45(b) shows the FTIR spectra of bare $g\text{-C}_3\text{N}_4$, GF and FeGF composites. In all samples, the band at 806 cm^{-1} corresponds to the breathing mode of triazine units (Shen et al. 2016). The absorption band at 1620 cm^{-1} is attributed to C=N stretching (Wang et al. 2012), while the peaks at 1322 , 1423 and 1572 cm^{-1} can be attributed to the stretching modes of aromatic C-N (Ge et al. 2012). As shown, all these peaks shifted to a higher wavelength after fluorination, indicating the strong interaction between the fluorine element and the s-triazine ring. The broad bands at around 3100 cm^{-1} are related to the N-H stretching vibration modes (Yan et al. 2009) which indicates that the amino functional group still existed in all samples (Xie et al. 2016). The broad bands at $3200\text{-}3600\text{ cm}^{-1}$ correspond to the physically adsorbed H_2O molecules (Shen et al. 2016). A peak at 2970 cm^{-1} is observed for the FeGF composites and its intensity is increased by increasing the Fe_3O_4 content of composites which results from the C-H vibration (Tang et al. 2017). As shown in Fig. 4.45(b), the fluorination of $g\text{-C}_3\text{N}_4$ led to the formation of a new band at 1220 cm^{-1} , which is related to the stretching mode of C-F bond (Wang et al. 2010b). Fig. 4.45(c) shows the N_2 adsorption-desorption isotherms and pore size distribution of $g\text{-C}_3\text{N}_4$ and FeGF2 samples. As seen, both isotherms are recognized as type IV with the hysteresis loop. The BET surface area of FeGF2 sample was $242.71\text{ m}^2/\text{g}$ which is about 6 times higher than that of bare $g\text{-C}_3\text{N}_4$ with $37.85\text{ m}^2/\text{g}$. The enhancement of specific surface area is due to the exfoliation of $g\text{-C}_3\text{N}_4$ sheets by the acid-assisted hydrothermal treatment (Zhang et al. 2014) and/or results from the presence of in-plane pores and the crumpled layered structure (Shi et al. 2016). Compared to bare $g\text{-C}_3\text{N}_4$, the hysteresis loops of FeGF2 become larger and shifts to a lower relative pressure, indicating the formation of enlarged mesopores

during exfoliation (Dong et al. 2014). The pore volumes of g-C₃N₄ and FeGF2 were calculated as 0.082 cm³/g and 0.427 cm³/g, respectively. The corresponding pore size distributions measured by BJH method are provided in the inset of Fig. 4.45(c). For both photocatalysts, pores are broadly distributed. The pore size distribution curve of FeGF2 shows a sharp peak at ~3.1 nm and a broad distribution in the range of 5–30 nm, which demonstrates that the micro/mesoporous structure of FeGF2 was well developed, while that of bare g-C₃N₄ has only negligible peaks. This dramatically increased the BET surface area, while the micro/mesoporous structure of FeGF2 should be beneficial for photocatalysis because it facilitates the mass transfer of reagents and the light harvesting by the multiple scattering effect. It also provides more catalytic active sites for photoredox reaction compared to bare g-C₃N₄ (Cui et al. 2012, Shi et al. 2016). The photocatalytic activity closely depends on the optical absorption ability of photocatalysts (Zhu et al. 2018). The UV–vis absorption spectra of g-C₃N₄, GF and FeGF composites are shown in Fig. 4.45(d). Clearly, all photocatalysts showed absorption in both UV and visible light region. Interestingly, fluorination enhanced the absorption in visible region and reduced the band gap from 2.7 eV to 2.52 eV compared to bare g-C₃N₄. The red shift of UV-vis spectrum by fluorination is different from protonation where g-C₃N₄ experienced a blue shift, suggesting that the process involved the doping of fluorine into the C-N matrix rather than the physical surface adsorption of F⁻ ions (Wang et al. 2010b). Moreover, the addition of Fe₃O₄ into the structure further increased the visible light absorption and strengthened the absorption intensity with the increase of Fe₃O₄ content. The higher light absorption of FeGF composites can be attributed to the intercalation effect of Fe₃O₄ nanoparticles which causes multiple absorption of reflected light in the interior space between layers (Zhu et al. 2017). Fig. 4.45(e) illustrates the band gap (E_g) calculation of samples. As shown, the E_g of g-C₃N₄ was 2.7 eV which is compatible with previous reports (Miao et al. 2017, Wang et al. 2010b). Due to the narrower E_g of Fe₃O₄, the band gap of FeGF composites decreased from 2.7 to ~2.3 eV for FeGF3. As shown in Fig. 4.45(f), the excited g-C₃N₄ sample showed a strong PL emission which is caused by recombination of charge carriers (Zhang et al. 2013, Zhu et al. 2017). The strong PL emission behavior of g-C₃N₄ is consistent with previous studies (Dong et al. 2014, He et al. 2014). The PL emission was significantly weakened in the case of GF by fluorination. Addition of Fe₃O₄ further reduced the PL emission. Nevertheless, compared to FeGF2, the FeGF3 sample showed a slightly higher PL emission. The reduction in PL peak intensity is associated with the charge

carrier separation, which is beneficial for the enhancement of photocatalytic activity (Dong et al. 2014).

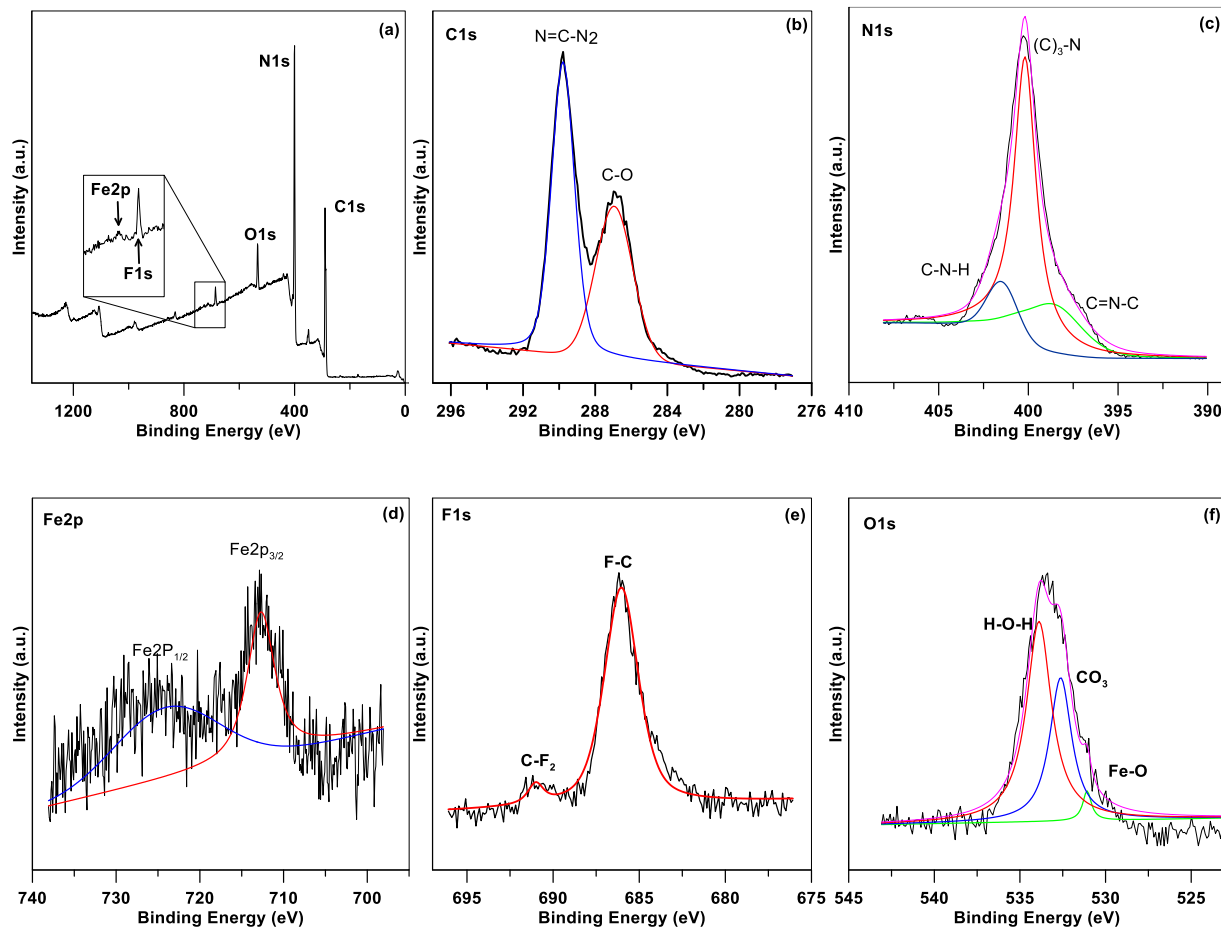


Figure 4.47. XPS survey spectra (a), high-resolution XPS spectra of the C1s region (b), N1s region (c), Fe2p (d), F1s (e) and O1s region (f) of FeGF2.

The XPS survey spectra and high-resolution spectra of FeGF2 elements are presented in Fig. 4.47. The survey spectra in Fig. 4.47(a) show that the FeGF2 sample is mainly composed of C and N elements, as expected. The high-resolution XPS spectra of C1s in Fig. 4.47(b) can be fitted into two peaks at 286.8 and 289.9 eV, corresponding to C–O from the adsorbed CO₂ (Zhu et al. 2015) and 289.9 eV corresponding to N=C–N₂ coordination (Leong et al. 2015). The high resolution of N1s (Fig. 4.47(c)) consists of three peaks at 398.6, 399.6 and 401.3 eV which are characteristics of C=N–C, (C)₃–N and C–N–H, respectively (Leong et al. 2015). In Fig. 4.47(d), two peaks located at 711.7 eV and 724.8 eV are attributed to Fe2p_{3/2} and Fe2p_{1/2}, respectively

(Dong and Wu 2017). Because of the high electronegativity, fluorine is most certainly bound to carbon rather than to nitrogen (Wang et al. 2010b). As shown in Fig. 4.47(e), the peak at 686.2 eV of F1s spectra is attributed to the F-C bond (Zha et al. 2017). The XPS peak at 686.2 eV and the FTIR band at 1220 cm^{-1} indicated that fluorine has been attached to C as the C-F bond rather than to other elements (Wang et al. 2010b). The weak peak at the binding energy of 692 eV is associated with CF_2 (Struzzi et al. 2017). In Fig. 4.47(f), the three peaks of oxygen in the FeGF2 sample were attributed to O-Fe (530.1 eV), CO_3^{2-} (532.540 eV) and H-O-H (533.1 eV) (Jiang et al. 2015).

The morphology of FeGF samples was investigated by the SEM techniques. As shown in Fig. 4.48(a-c), the FeGF1 sample shows aggregation of many wrinkled sheets with irregular shapes and pyramid-like structure and relatively smooth faces in certain parts. As seen in Fig. 4.48(d-f), the hydrothermal exfoliation of FeGF2 up to $180\text{ }^\circ\text{C}$ changed a part of the sample to a curvy sheet as marked with arrows.

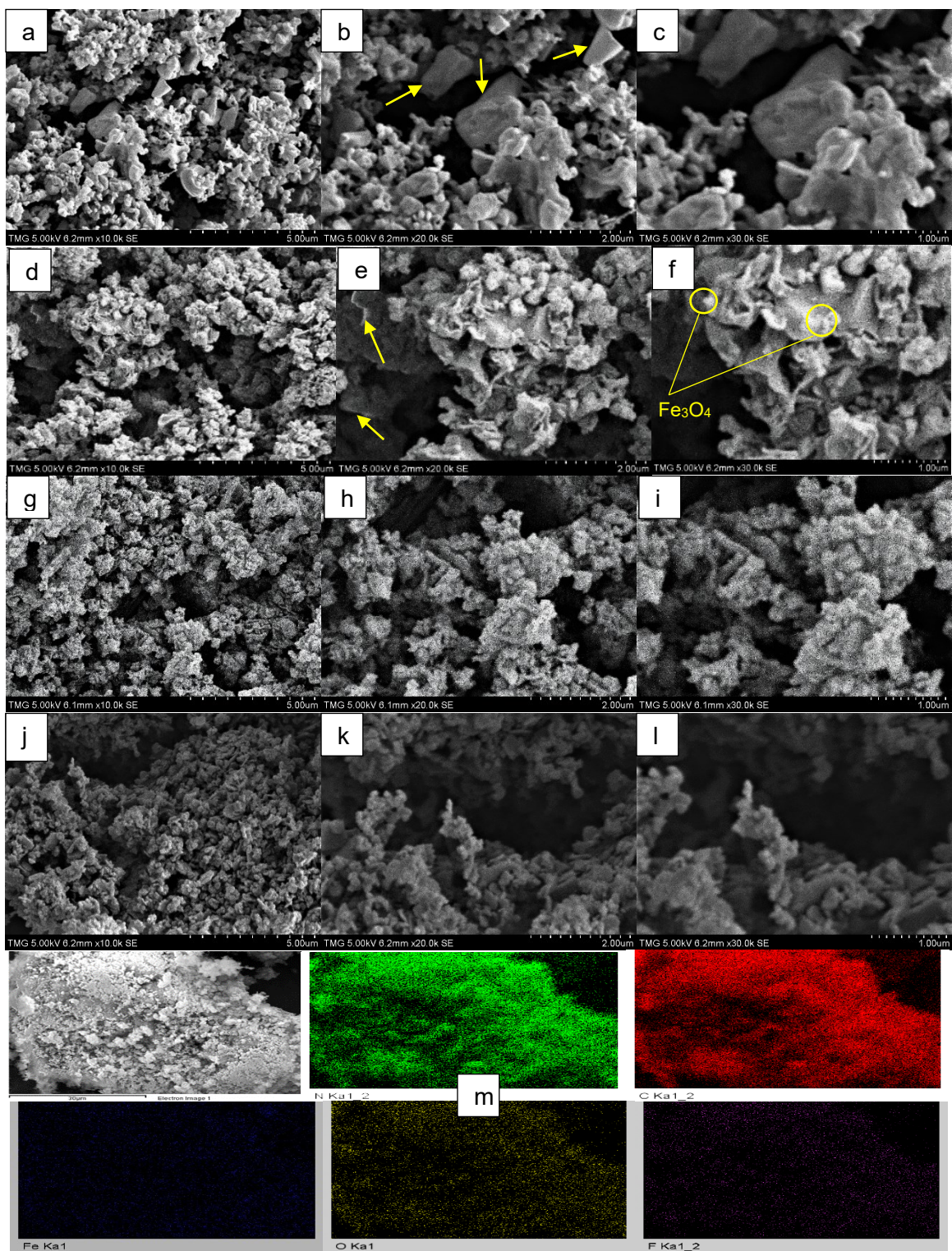


Figure 4.48. (a-c) SEM images of FeGF1, (d-f) FeGF2, (g-i) FeGF3, (j-l) Fe₃O₄ samples at different magnifications, (m) elemental mapping of N, C, Fe, O and F of FeGF2.

The small particles of Fe_3O_4 are clearly observed on FeGF2 (Fig. 4.48(f)). However, as shown in Fig. 4.48(g-i), in the case of FeGF3, the Fe_3O_4 particles agglomerated on the GF, which reduces the active sites of the photocatalyst. The SEM images Fe_3O_4 at different magnifications are shown in Fig. 4.48(j-l). In addition, EDS mapping images of FeGF2 are presented in Fig. 4.48(m) where the N, C, O, Fe, and F elements are clearly detected, further confirming that the Fe_3O_4 particles have been deposited uniformly on the fluorinated g- C_3N_4 .

TEM was employed to further examine the morphology of mesoporous FeGF2 (Fig. 4.49). A two-dimensional sheet-like structure consisting of wrinkles was observed in the FeGF2 sample which is similar to crumpled graphene (Luo et al. 2012). Fig. 4.49(a) shows the distribution of Fe_3O_4 nanoparticles on the porous g- C_3N_4 sheets. The high resolution image of FeGF2 in Fig. 4.49(b) shows the decoration of Fe_3O_4 , at the size of less than 30 nm, on the surface of g- C_3N_4 sheets. The porous structure FeGF2 is clearly shown in Fig. 4.49(c). Fig. 4.49(d) shows the HAADF image of FeGF2 sample. Since, in the HAADF the contrast of image is strongly dependent on the atomic number (Z) and number of atoms in a column (samples thickness) (Li et al. 2008), this method has proven to be a powerful tool for the detection of compounds with different atomic number, thickness and porosity (Leary et al. 2012). Accordingly, in Fig. 4.49(d), the bright spots in the HAADF image show the decoration of Fe_3O_4 nanoparticles on g- C_3N_4 sheets, while the dark cores display the mesoporous structure.

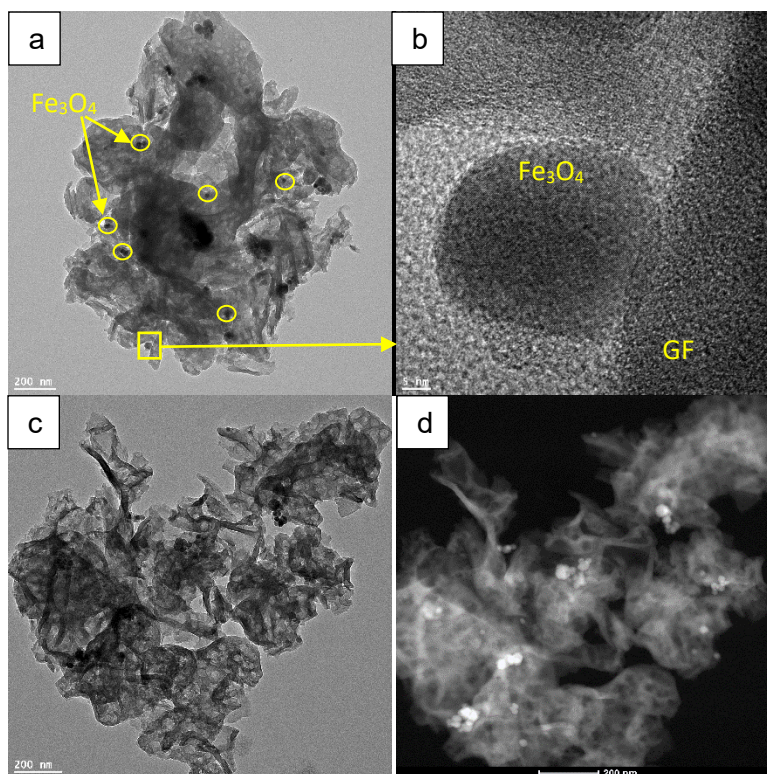


Figure 4.49. (a-c), TEM images of FeGF2 samples, (d) high angle annular dark field (HAADF) STEM image of FeGF2.

4.5.2.2. Photocatalytic performance and kinetics of contaminant removal

As seen in Fig. 4.50(a), in the absence of photocatalysts, the AMX concentration was slightly reduced during the reaction course by photolysis. This is due to the low absorption of AMX molecules at the maximum emission intensity of low pressure UV lamp (Fig. 4.51) It has been reported that fluorination may change the adsorption capacity of photocatalysts towards organic compounds (Liu et al. 2012). As shown in Fig. 4.50(a), the adsorption of AMX was slightly enhanced by fluorination. In addition, fluorination promotes the generation of mobile free OH^\bullet radicals instead of surface bounded radicals (Mirzaei et al. 2018c). Considering that the oxidation potential of mobile OH^\bullet radicals (2.3 eV vs NHE) is higher than that of attached surface radicals (1.5-1.7 eV vs NHE), fluorination would increase the oxidation potential of OH^\bullet radicals and removal efficiency of AMX. A significant enhancement of photocatalytic activity of g- C_3N_4 after fluorination for the oxidation of benzene to phenol has been reported (Wang et al. 2010b). Moreover, most photocatalytic reactions take place on the surface of photocatalysts and the application of fluorination changes the kinetics and mechanism of reaction (Mirzaei et al.

2017a, Mirzaei et al. 2018c). Fluorination, also led to a stable dispersion of photocatalyst in the solution which is beneficial for the photocatalytic process. As shown in Fig. 4.52 the GF particles were stable even after 24 h, while, the g-C₃N₄ particles precipitated after 30 min. It is worth noting that in this study, other parameters such as the specific surface area and adsorption capacity were enhanced simultaneously. Moreover, based on Fig. 4.45(f), the PL intensity which is an indicator of recombination of the excited electrons and holes was drastically reduced after fluorination. Although fluorination enhanced the AMX removal efficiency, the overall effects of fluorination on photocatalytic reactions are complex and need further investigation. As shown in Fig. 4.50(a), the presence of Fe₃O₄ nanoparticles in the FG structure further enhanced the AMX removal efficiency. This improvement may be associated with the formation of heterojunction between Fe₃O₄ and GF. However, the photocatalytic activity of FeGF3 was reduced compared to FeGF2. In fact, the highest AMX removal was obtained by using the UV/FeGF2 process. The decline in photocatalytic activity may be caused by the excess Fe₃O₄ nanoparticles covering the photocatalyst active sites, thus producing a shielding effect (He et al. 2014, Zhu et al. 2018). Moreover, the excess amount of Fe₃O₄ in the photocatalyst can serve as the recombination center for electrons and holes (Zhou et al. 2013b) which is consistent with the slight enhancement of PL emission for FeGF3 in comparison with FeGF2 (Fig. 4.50(f)). The photocatalytic activity of FeGF2 for AMX removal was also evaluated under visible light. As shown in Fig. 4.50(a) the removal percentage of AMX by using visible light was lower than 40% even after 2 h treatment. The kinetics of AMX removal were studied by using the pseudo-first-order kinetics model (Eq. 3.7). The rate constant for different photocatalysts under UV irradiation are shown in Fig. 4.50(b). FeGF2 exhibited the highest rate constant as $2.15 \times 10^{-2} \text{ min}^{-1}$.

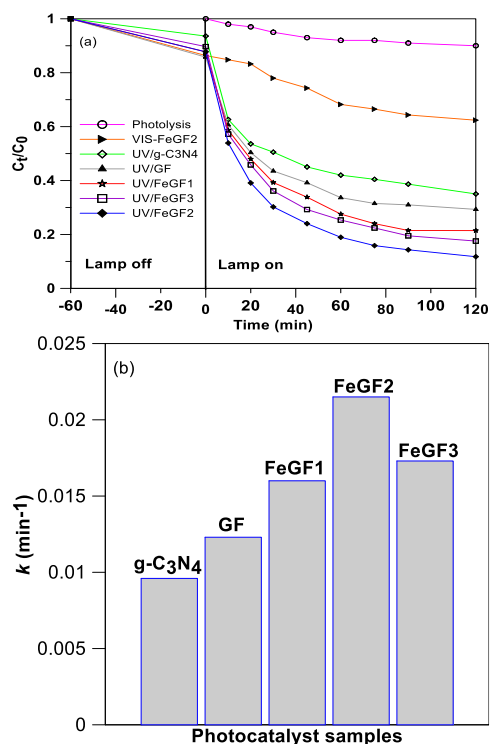


Figure 4.50. (a) Photocatalytic activity of photocatalysts for the degradation of AMX under UV and visible light, (b), apparent first-order rate constant; experimental condition: $[AMX]_0 = 0.25$ mM, pH 7, $[photocatalyst]_0 = 1$ g/L, $[scavenger]_0 = 2.5$ mM, airflow rate = 1.5 L/min.

4.5.2.3. Mechanism of reaction

It is reported that hydroxyl radicals (OH^\bullet), photo-induced holes (h^+), and superoxide radicals ($O_2^{\bullet-}$) are the main reactive species during the photocatalytic degradation of organic pollutants (Cao et al. 2015). Under the light irradiation, the excited FeGF2 will generate electrons and holes (Eq. 4.20). Afterward, the photo-induced electrons rapidly move to the surface of FeGF2 and further to the Fe_3O_4 nanoparticles (Eq. 4.21) (Zhou et al. 2013b). These electrons can be subsequently transferred to dissolved oxygen and produce superoxide radicals (Eq. 4.22). The produced holes can also participate in the direct oxidation of AMX and generate intermediate compounds, by-products and/or ions (Eq. 4.23). However, the redox ability of holes is not strong enough to generate hydroxyl radicals (+2.38 eV vs NHE for OH^\bullet/OH^\ominus) (Zhu et al. 2017). Nevertheless, hydroxyl radicals may be produced by superoxides in an indirect pathway (Eqs. 4.24 and 4.25) (Dong et al. 2014).





Accordingly, experiments were conducted in the presence of 2.5 mM TBA, EDTA, and BQ as scavengers of OH^{\bullet} , h^+ and $O_2^{\bullet -}$ species, respectively. As shown in Fig. 4.53, the highest inhibition effect was observed when EDTA was added to the reaction, followed by TBA and BQ, respectively. Therefore, holes play an important role in the photocatalytic degradation of AMX by FeGF2 under UV irradiation, followed by hydroxyl and superoxide radicals. The dominant role of holes in AMX removal is consistent with the observations of Yang et al. (Yang et al. 2017a) for the degradation of AMX. The presence of fluorine, which is the most electronegative element, on the surface of photocatalyst reduces the formation and contribution of $^{\circ}O_2^-$ by holding the electrons (Mirzaei et al. 2018c, Yu et al. 2009), while promoting the role of holes as strong species which can oxidize AMX or the generated intermediates on the surface of FeGF2 which has a high surface area.

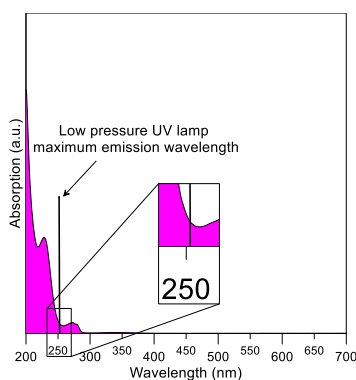


Figure 4.51. Absorbance spectrum of AMX in water and the maximum emission wavelength of UVC lamp.

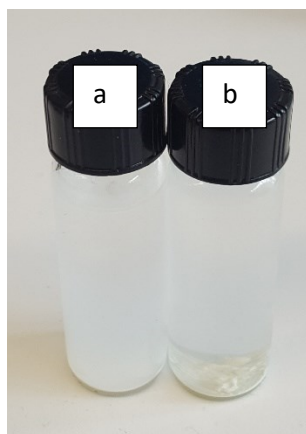


Figure 4.52. (a) Photographs of GF nanosheets after storage for 24 h and (b) bare $g\text{-C}_3\text{N}_4$ nanosheets after storage for 30 min.

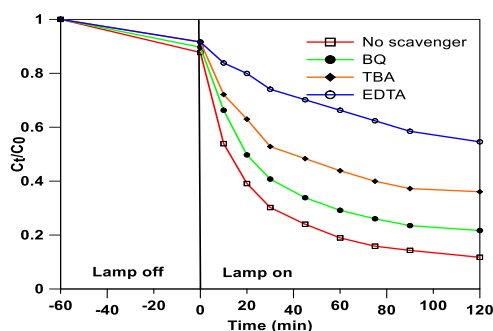


Figure 4.53. Species-trapping experiments for degradation of AMX by FeGF2 photocatalysts; experimental condition: $[\text{AMX}]_0 = 0.25 \text{ mM}$, pH 7, $[\text{photocatalyst}] = 1 \text{ g/L}$, $[\text{scavenger}]_0 = 2.5 \text{ mM}$ airflow rate = 1.5 L/min.

4.5.2.4. Identification of intermediates and AMX degradation pathway

The identification of main transformation products (TPs) formed during the UV/ $g\text{-C}_3\text{N}_4$ and UV/FeGF2 processes was conducted in an effort to propose a pathway for AMX degradation and to identify the potential intermediate compounds and by-products that may contribute to the solution toxicity (Fig. 4.54). The employed analytical methods allowed the detection of thirteen intermediate compounds during the degradation of AMX by the UV/FeGF2 process, and fourteen intermediates during its degradation by the UV/ $g\text{-C}_3\text{N}_4$ process. The first possible pathway is the hydroxylation (+16 Da) of AMX which may occur at different positions of the AMX molecule such as benzoic ring or nitrogen moiety (**TP 382**). The identification of the exact position of hydroxylation on the AMX molecule is difficult by solely relying on the employed method of analysis. However, almost all detected intermediates consisted of the thiazolidine ring

(C₆H₁₀NO₂S) and fragment [*m/z* =160.04] in their mass spectrum (data is not shown), suggesting that the thiazolidine ring of AMX is not susceptible to hydroxylation. This observation suggests that the benzoic ring or amine group of AMX which possess electrophilic characteristics is more prone to radical attack. Nevertheless, the presence of [*m/z*=189.06] fragment which corresponds to the C₇H₁₃N₂O₂S formula (Fig. 4.55) implies that the OH• radical most likely attached to nitrogen rather than to the benzoic ring. This intermediate can further lose the amine moiety and produce **TP 365**. Another possible transformation pathway involves the loss of amine group of AMX which leads to the formation of **TP 349**. The detection of **TP 349** has been reported in the literature (Gozlan et al. 2013, Kanakaraju et al. 2015), and showed the highest peak intensity in both UV/g-C₃N₄ and UV/FeGF2 processes. The loss of C=O from four-membered β-lactam ring of **TP 349** produces **TP 321** which is detected in both processes with lower peak intensities compared to **TP 349**. However, the hydroxylation product of **TP 349** which led to the formation of **TP 383** was only detected in the UV/g-C₃N₄ process. Moreover, as seen in Fig. 4.56 the detection of [*m/z*=155.015] fragment suggests that OH• radical most likely attached to both benzoic ring and nitrogen moiety rather than to benzoic ring alone. The opening of the four-membered β-lactam ring of the AMX is another possible degradation pathway which was also reported before (Trovo et al. 2011). This degradation pathway yielded the formation of AMX penicilloic acid (**TP 384**) (Kanakaraju et al. 2015). The hydroxylation of AMX penicilloic acid produces the **TP 400** which can further be transformed by losing amine and CO₂ groups, resulting in the formation of **TP 323**. The loss of amine group and the removal of β-lactam ring are two probable means of producing by-products from AMX penicilloic acid with the subsequent production of **TP 367** and AMX penicilloic acid (**TP 340**), respectively, in accordance with the observations of Pe´rez-Parada et al. (2011). The intermediate compounds formed by the opening of the four-membered β-lactam ring of AMX were detected at higher peak intensities in both processes compared to TPs with β-lactam ring. Amoxicillin sodium (**TP 388**) was also detected with very low peak intensities only in the UV/FeGF2 process, and its peak intensity was reduced during the reaction course. As shown in Fig. 4.57(a-b) the peak intensity of most transformation products increased up to 30 minutes in the UV/g-C₃N₄ process and then decreased with the progress of the process. The long chain products possibly broke into short chain compounds such as **TP 208**, **TP 160** and **TP 114**. As seen in Fig. 4.57(c-d) the intensity of intermediates during the UV/FeGF2 process was considerably lower than those in the UV/g-

C₃N₄ process. Moreover, the reduction in peak intensity was shown after 10 min for most compounds. The **TP 139** with low peak intensity was also detected during the UV/FeGF2 process. Further oxidation of intermediates led to the mineralization of compounds in the solution and the generation of ions such as nitrate and nitrite.

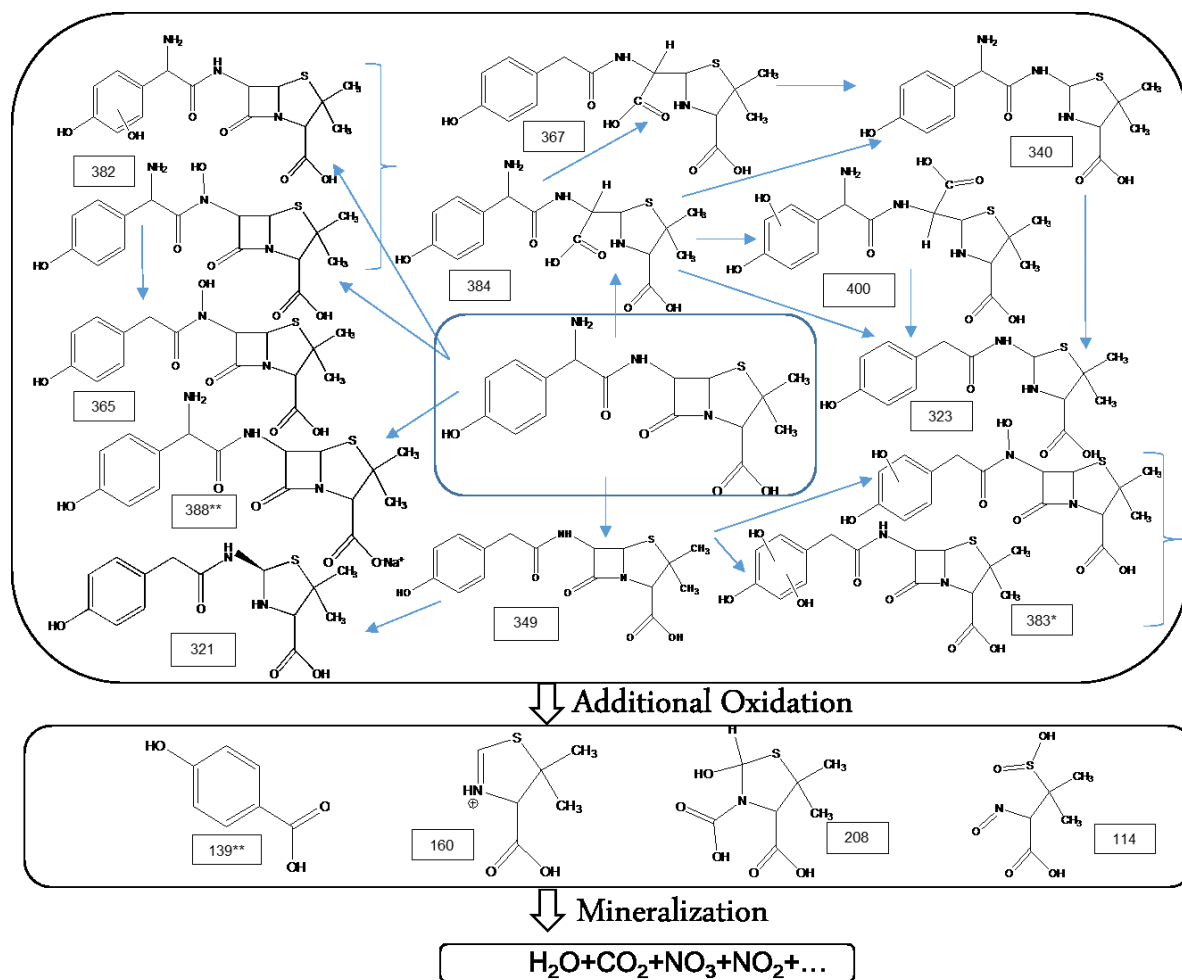


Figure 4.54. Schematic diagram of the proposed photocatalytic degradation mechanisms of AMX under UV light. The transformation products (TPs) marked with (*) were detected during UV/g-C₃N₄ process and TPs marked with (**) were detected during UV/FeGF2 processes.

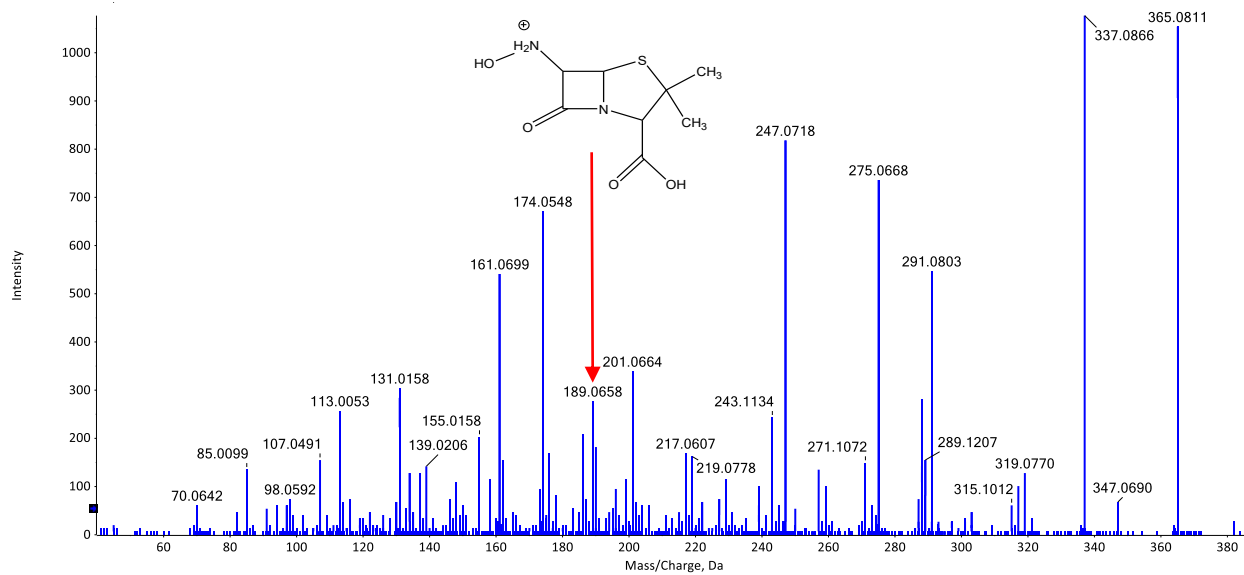


Figure 4.55. Presence of $[m/z=189.06]$ fragment during hydroxylation

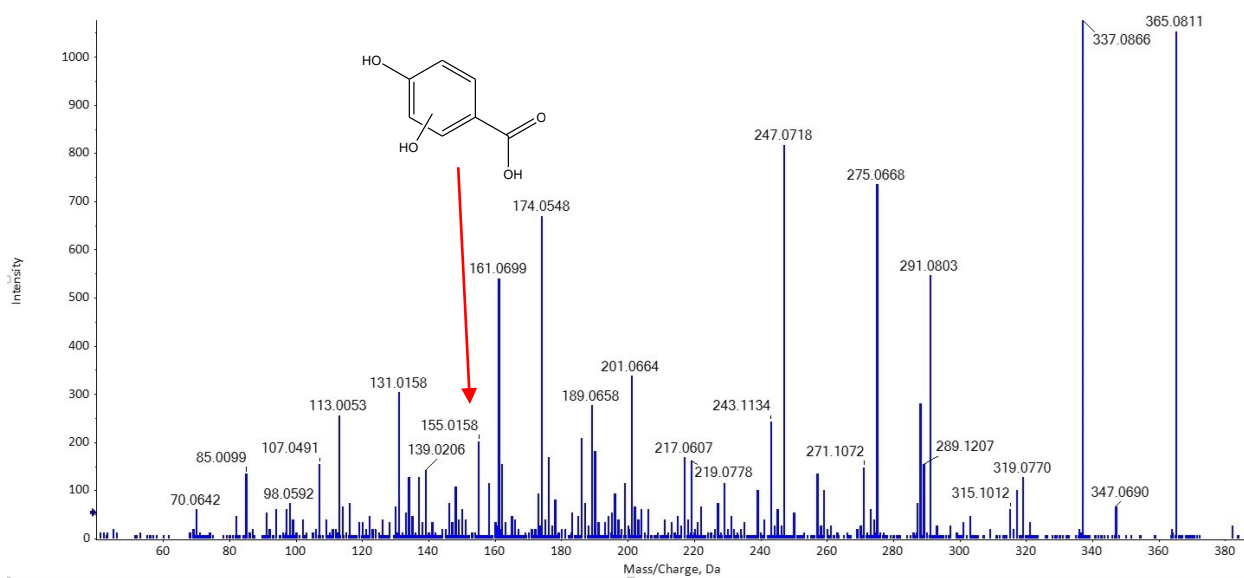


Figure 4.56. Presence of $[m/z=155.015]$ fragment during the hydroxylation of **TP 349**.

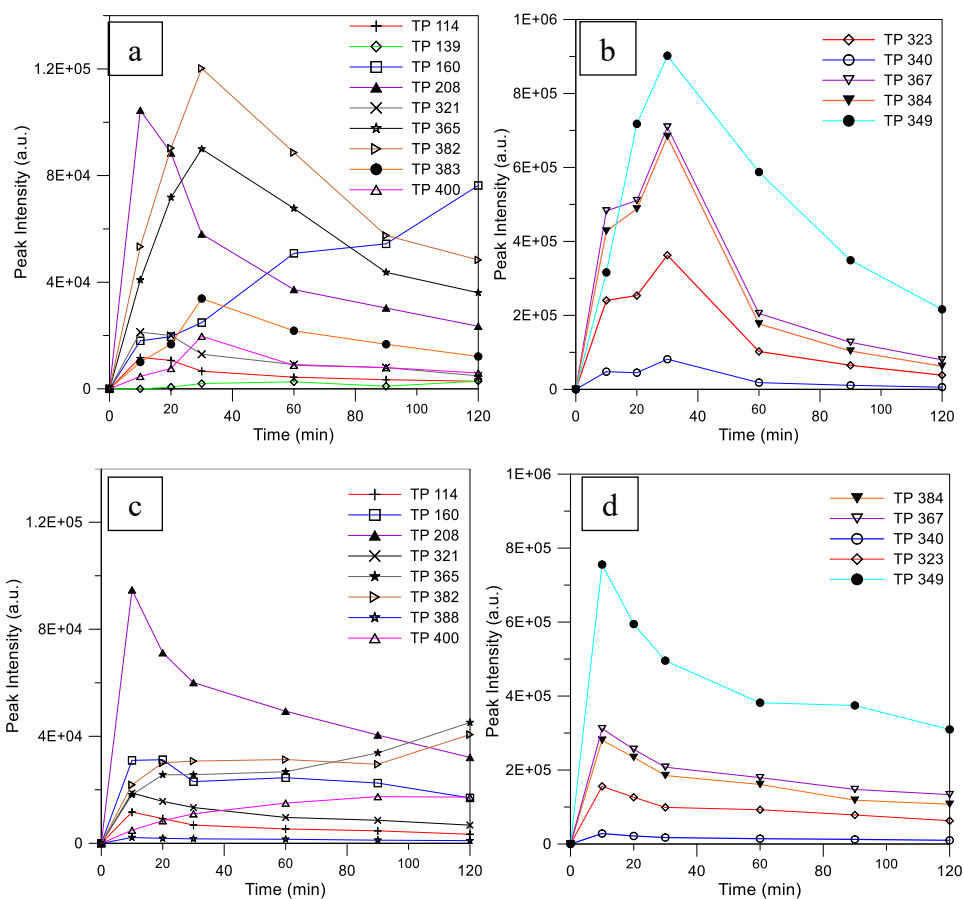


Figure 4.57. Evolution of transformation products (TP) with low (a) and high (b) peak intensities during the UV/g-C₃N₄ process; and with low (c) and high (d) peak intensities during the UV/FeGF2 process.

4.5.2.5. Mineralization

The removal of TOC and the formation of nitrate and nitrite as indicators of mineralization were evaluated. As shown in Fig. 4.58(a), all examined processes showed some extent of AMX mineralization. However, the UV/FeGF2 process with almost 60% TOC removal after 2 h showed the highest efficiency for the mineralization of AMX, followed by the UV/g-C₃N₄ and Vis/FeGF2 processes with 42% and 16%, respectively. Fig. 4.58(a) shows that the mineralization rate was relatively high during the first 30 min of the photocatalytic process and then decreased as the process proceeded. The intermediate compounds formed during the examined processes may be more resistant to further degradation, as observed before during the photocatalytic degradation of AMX by the UV/TiO₂ process (Kanakaraju et al. 2015). The presence of sulfur in most detected TPs indicate that nitrogen and amine moiety are more susceptible to radical attack compared to sulfur. Therefore, the formation of the oxidized nitrogenous compounds such as

nitrate and nitrite were monitored as indicators of mineralization. As seen in Fig. Fig. 4.58(b) during the UV/g-C₃N₄ and UV/FeGF2 processes, the concentration of nitrate and nitrite increased as the process progressed. However, the concentration of nitrate produced by the UV/FeGF2 process was considerably higher than that formed by the UV/g-C₃N₄ process. The concentrations of nitrate and nitrite during the Vis/FeGF2 process were consistently lower than the detection limit of employed measurement techniques.

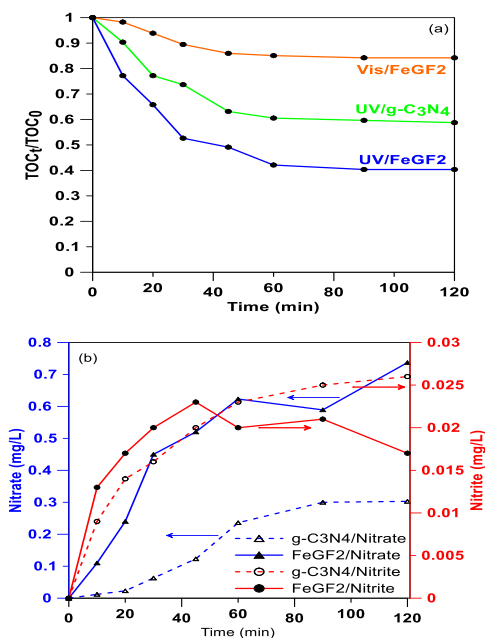


Figure 4.58. (a) TOC removal during UV/g-C₃N₄ and UV/FeGF2 and Vis/FeGF2 processes; evolution of nitrate and nitrite UV/g-C₃N₄ and UV/FeGF2 processes.

4.5.2.6. Toxicity assessment

As shown in Fig. 4.59(a) total mineralization was not achieved during the photocatalytic experiments even after 2 h. Therefore, toxicity assays using *E. coli* bacteria were conducted to evaluate the antibiotic activity prior and after the treatment operations. As seen in Fig. 4.59(a) the AMX solution before treatment significantly inhibited the growth of *E. coli* on the surface of agar, while bacterial growth was clearly observed after the onset of photocatalytic processes. Since no inhibition was detected in the control plate, the observed changes in bacterial growth were attributed to AMX degradation. As shown by the UV/G petri dishes in Fig. 4.59(a), the bare g-C₃N₄ was relatively effective for the detoxification of solution under UV light after 1 and 2 h of treatment. However, this process was not able to totally suppress the antibacterial activity of

AMX solution. The FeGF2 photocatalyst was also examined for the detoxification of AMX solution. The results showed that although the Vis/FeGF2 process was relatively effective, it did not produce a complete detoxification of solution. On the other hand, a complete detoxification, identified by the reduction of toxicity below the minimum inhibitory level for *E. coli*, was obtained by employing UV light during the UV/FeGF2 process (see UV/FeGF2/2h plate in Fig. 4.59(a)).

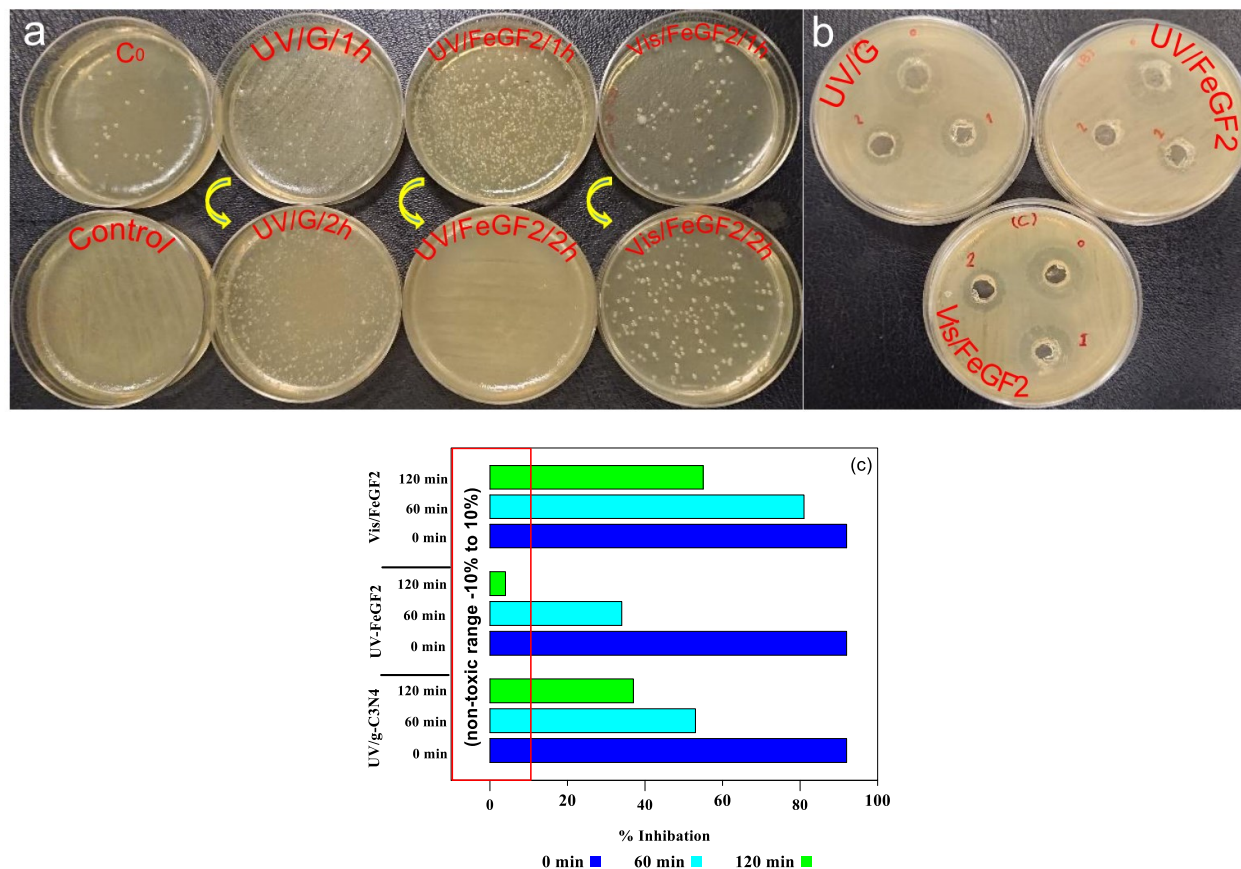


Figure 4.59. Evaluation of changes in the toxicity of AMX solution by using (a), petri dish (b), agar-well diffusion and (c) inhibition percentage (Toxtrac™ kit) in UV/g-C₃N₄, UV/FeGF2 and Vis/FeGF2 processes.

These results were also confirmed by the agar-well diffusion method. As shown in Fig. 4.59(b), by using FeGF2 in the presence of UV light, the diameter of inhibition zone was reduced after 1 h and eventually disappeared after 2 h treatment. However, under visible light, an inhibition zone still existed even after 2 h treatment. Fig. 4.59(c) shows the percentage inhibition (PI) of solution by the UV/g-C₃N₄, UV/FeGF2 and Vis/FeGF2 processes at two time intervals. A high inhibition percentage of AMX solution towards *E. coli* growth was shown before the

treatment. One hour treatment of solution reduced the inhibition percentage from 92% to 53%, 34% and 81% by the UV/g-C₃N₄, UV/FeGF2 and Vis/FeGF2 processes, respectively. The increase of treatment time up to 120 min decreased the toxicity of solution in all processes. However, only the solutions treated by the UV/FeGF2 process exhibited toxicity levels within the non-toxic range, indicating the effectiveness of UV/FeGF2 process in the reduction of toxicity.

4.5.2.7. Stability of photocatalyst

The magnetic properties of Fe₃O₄ and FeGF2 samples were investigated at room temperature and the results are presented in Fig. 4.60(a). The hysteresis loop in both samples indicates a superparamagnetic behavior without any noticeable remanence. Due to the low percentage of Fe₃O₄ in the FeGF2, the saturation magnetization of FeGF2 was lower than bare Fe₃O₄. Nevertheless, the magnetic properties of FeGF2 were high enough to enable its separation from the treated solution by magnetic force (Inset of Fig. 4.60(a)). The FeGF2 particles were found to be highly stable and could be reused in repeated operational runs without a significant reduction in their activity. The high stability of photocatalyst is also confirmed by XPS spectra of fresh and spent FeGF2 (Fig. 4.61). As shown in Fig. 4.60(b), no noticeable reduction in AMX removal was observed after four cyclic operations, which indicates the high stability of photocatalyst particles.

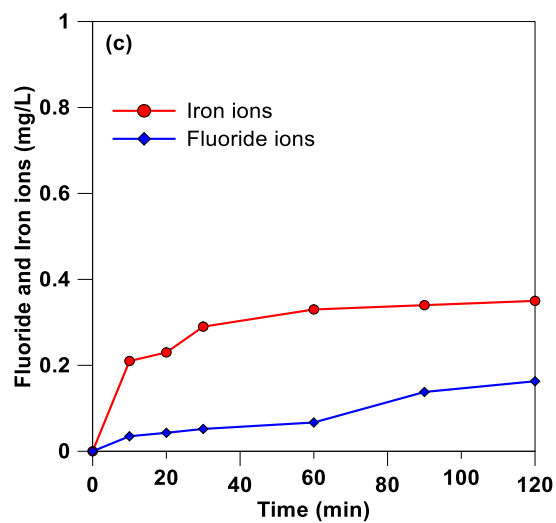
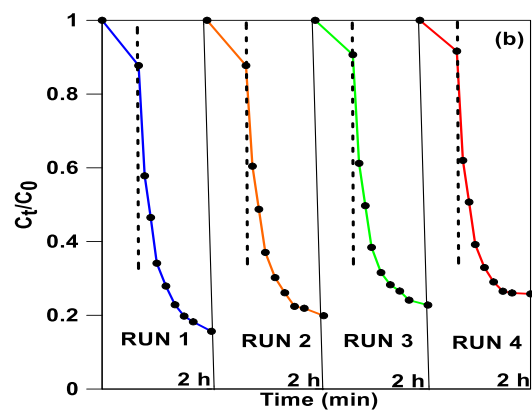
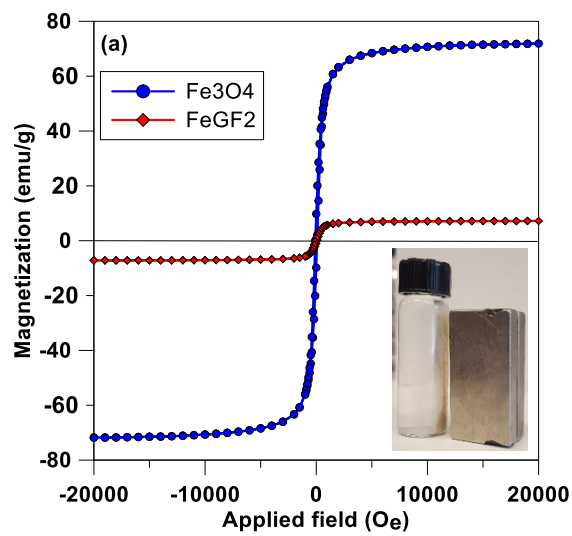


Figure 4.60. (a) Magnetization curves of Fe_3O_4 and FeGF_2 , (b) repeated photocatalytic degradation of AMX by FeGF_2 under UV irradiation, (c) fluoride ion leaching from FeGF_2 structure during UV/ FeGF_2 process.

Moreover, the concentrations of fluoride and iron ions during the reaction course were measured in order to assess possible leaching of fluoride and iron ions from the photocatalysts that may reduce the photocatalyst activity. The monitoring of fluoride ion concentration in the treated water is also important since concentrations up to 1.5 mg/L fluoride is beneficial, especially to children for calcification of dental enamel (Srimurali et al. 1998), while prolonged exposure to F^- ion at higher concentrations leads to dental and skeletal fluorosis (Mohapatra et al. 2009). A maximum concentration of 1.5 mg/L of fluoride ion in drinking water has been set as the limit by World Health Organization (WHO) (Klauson et al. 2010). As shown in Fig. 4.60(c), after 120 min reaction, the concentration of F^- was about 0.16 mg/L, which was considerably lower than the permitted concentration. The high-resolution XPS spectra of fresh and spent FeGF2 for Fe2p (Fig. 4.61(a)) and F1s (4.61(b)) are relatively similar. These results further verify the high stability of FeGF2 photocatalyst.

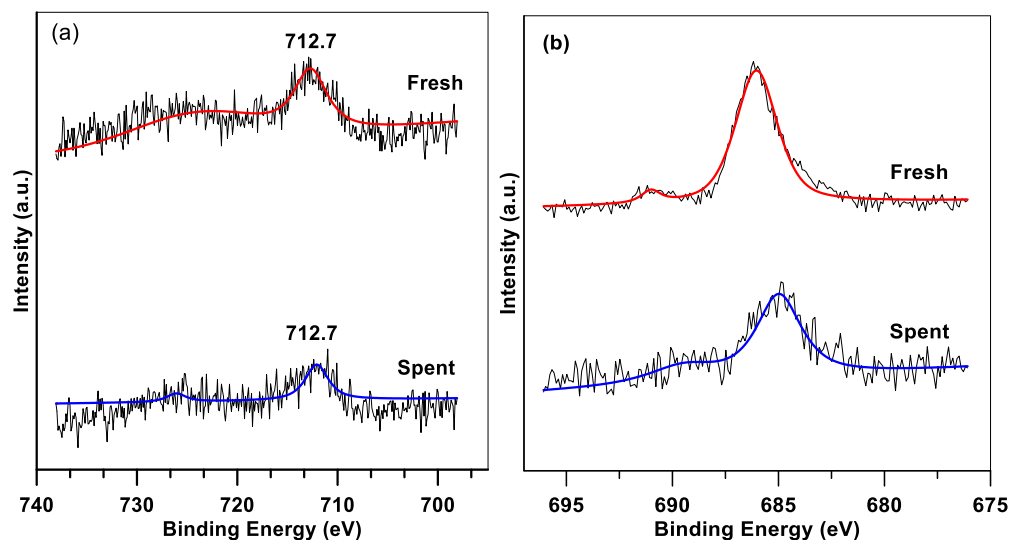


Figure 4.61. High-resolution XPS spectra of fresh and spent FeGF2 of (a) Fe2p and (b) F1s

4.5.3. Conclusions and remarks

A novel fluorinated graphite carbon nitride photocatalyst with magnetic properties was synthesized by a facile hydrothermal method and used for degradation of amoxicillin (AMX) in water. Compared to the bulk $g-C_3N_4$, magnetic fluorinated $Fe_3O_4/g-C_3N_4$ (FeGF) with a high specific surface area ($243 \text{ m}^2 \cdot \text{g}^{-1}$) and easy separation from aqueous solution by magnet, led to

improved photocatalytic activity in terms of AMX removal and mineralization as well as detoxification of the solution. The results showed that in comparison with a 500 W visible lamp, using a UV lamp (10 W) was considerably more effective for AMX removal, its mineralization and detoxification of the solution. Based on the measurement of accurate masses of the transformation products and their main fragments, a degradation pathway for AMX was proposed. The peak intensities of most transformation products (TPs) generated by using the modified photocatalyst under UV light (UV/FeGF2) process were significantly lower than those generated by using the pristine g-C₃N₄, suggesting that UV/FeGF2 process produced a higher extent of mineralization and a lower accumulation of transformation by-products. Based on the use of inexpensive precursor and modifier, simple preparation, good photocatalytic activity and low energy consumption, the proposed method can guide the development of low-cost and high-performance photocatalysts.

5. Conclusions and Recommendations

Despite the conduct of numerous studies on photocatalytic degradation of contaminants during the last twenty years, this technology has scarcely demonstrated the capability to survive outside laboratories. The main limitations of photocatalysis are high energy consumption, separation and recovery of photocatalyst from solution and stability of photocatalysts. Therefore, the main objective of this research was defined as the development of “novel photocatalysts for effective removal of antibiotics from water with low energy consumption”. This objective was accomplished in different steps as follows:

- 1) In order to maximize the UV light utilization, a cylindrical stainless steel photoreactor was designed and built with a low energy consuming UV lamp (10W).
- 2) The effect of post synthesis surface fluorination was evaluated by the addition of NH_4F as a source of fluoride ion into the solution for the removal of SMX. The results showed that surface fluorination increased the efficiency of removal in terms of SMX removal, mineralization and detoxification of solution and increasing the rate of removal reaction.
- 3) Effects of operating parameters including catalyst concentration in the solution, pH of solution and airflow rate were examined. Results showed that the operating parameters considerably affect the efficiency of removal.
- 4) Response surface methodology based on central composite design was employed to optimize the operating parameters in order to maximize SMX removal.
- 5) *In situ* fluorination of ZnO was accomplished by synthesizing $\text{Zn}(\text{OH})\text{F}$, and the AMP removal was examined by using $\text{Zn}(\text{OH})\text{F}$ under ultrasound irradiation. At the end of process (90 min) the concentration of fluoride ions which were leached from structure was lower than the allowed value for drinking water.
- 6) $\text{Fe}_3\text{O}_4\text{-ZnO}@g\text{-C}_3\text{N}_4$ was synthesized in order to enhance the stability of ZnO and facile separation of photocatalyst from solution after treatment by magnetic force.
- 7) Mesoporous fluorinated $\text{Fe}_3\text{O}_4@g\text{-C}_3\text{N}_4$ was synthesized as UV/Visible-driven photocatalyst for the removal of AMX, and its performance was compared under visible and UV light.

- 8) All synthesized photocatalysts were characterized by using various characterization tests including: XRD, FTIR, SEM, TEM, EDS, XPS, BET, PL spectra, VSM and zeta potential analyzer.
- 9) The stability of photocatalysts was evaluated in consecutive runs. No significant reduction in the performance of Zn(OH)F, Fe₃O₄-ZnO@g-C₃N₄ and Fe₃O₄@g-C₃N₄ was shown after four runs.
- 10) The photocatalytic performance was determined in terms of antibiotic removal, mineralization, detoxification of the solution, and by-products formation.

5.1. Conclusions, remarks and contribution of research

In this study the removal efficiencies of three emerging contaminants, namely, sulfamethoxazole, ampicillin and amoxicillin were evaluated in terms of contaminant removal and mineralization, detoxification of the solution and by-product formation. In this study, we showed that the energy consumption of photocatalysis process can be considerably reduced by using immersed lamp with short emitting wavelength ($\lambda_{\max}=254$ nm) to compensate for the low UV light intensity of low-energy-consuming lamps. As shown in Table 4.5, UVA ($\lambda_{\max}=365$ nm) is the most widely used lamp in photocatalysis processes. This is due to the lower price of medium pressure (UVA) lamps compared to low pressure (UVC) UV lamps. However, considering the lower energy consumption of UVC lamp, increasing the removal efficiency of emerging contaminants by photolysis (beside photocatalysis) and ability of UVC for disinfection, the overall operating cost of process by using UVC would be much lower than using UVA. However, a comprehensive study is needed to evaluate the feasibility and cost evaluation of photocatalysis process.

The conclusive outcomes of the research can be summarized as follow:

1) *Reduction of energy consumption*

Based on equation (3.10), the energy consumption during AOPs depends on the rate of degradation reaction. Comparison of the energy consumption in this study with previously-reported studies which had considered photocatalytic degradation of SMX under UV irradiation, showed considerably lower *electrical energy per order* (E_{EO}) as compared in Table 4.5. The main reason for low energy consumption in this study is the high rate of removal reaction as a result of the following:

- i) Using a cylindrical narrow photoreactor which led to utilizing all emitted radiation and increasing the quantum yield.
- ii) Enhancing the removal efficiency and removal rate by slowing down the recombination rate of charge carriers by surface modification.
- iii) Utilizing low energy consuming UV lamp with low wavelength (UVC) to increase the removal rate by photolysis besides the photocatalysis process.
- iv) Optimizing the operating parameters including catalyst dosage, pH of solution and airflow rate to maximize the removal rate of contaminants.

Although, energy consumption in this study is substantially reduced, the consumed energy is almost equal to the energy consumed in the UV/H₂O₂ process. Due to its catalytic nature, photocatalysis is usually labeled as an “energy-saving” process. This statement would be reliable if the problems associated with the recovery of catalyst are solved and photocatalysts can be recovered and reused for several runs. In this case, the long-term process cost for photocatalysis would be much less than the other AOPs, such as UV/H₂O₂ or UV/O₃, where the oxidation agents are consumed during the process. Synthesizing magnetic photocatalysts with high stability is the second conclusive achievement of this research.

2) *Developing magnetic photocatalysts with high stability*

As mentioned earlier, the photocorrosion is a crucial obstacle to the potential large-scale application of photocatalysis process. In practical applications, photocatalysts that can sustain several cycles of use, along with properties that enable low-cost recovery from effluent streams is needed.

The photocatalytic activity and stability can be improved by using composite photocatalysts, owing to the heterojunction mechanism. However, the poor attachment of photocatalysts restricts the charge transfer between interfaces. In this study, we synthesized graphitic carbon nitride (g-C₃N₄) by *in situ* condensation of urea on the surface of ZnO. By using this method, a uniform layer of g-C₃N₄ was obtained and acted as the protective layer and reduced the photocorrosion of ZnO. Moreover, the use of g-C₃N₄ as the protective layer of ZnO in this study not only protects the surface of photocatalyst against self-oxidation but it also improves the efficiency of SMX removal as a conjugated semiconductor by generating more electron and hole pairs, facilitating the charge separation and increasing the specific surface area. Moreover, Fe₃O₄ as magnetic core

facilitated the separation of particles from solution after the process and also acted as a conductor of electrons to dissolved oxygen. Consequently, the developed photocatalyst ($\text{Fe}_3\text{O}_4\text{-ZnO@g-C}_3\text{N}_4$) showed a high durability and comparable performance for the removal of SMX as shown in Table 4.15. The obtained results in this study presented a new approach to the development of modified photocatalysts, which can expand practical applications of photocatalytic processes for water and wastewater treatment.

5.2. Recommendations for future work

Based on the findings of this research, the following recommendations are made to further improve the efficiency of photocatalysis process:

- In photocatalysis, nanoparticles with complex structures have emerged. However, considering the issue of catalyst separation from solution, larger and more robust materials are needed. In recent years, many types of photocatalysts have been developed that perform well at laboratory scale, but their production at large-scale and their durability in long-term applications have not been established yet. The development of larger photocatalysts (macroporous) with high stability and the ability for low-cost recovery from effluent streams is strongly recommended, even though these particles may produce lower concentrations of hydroxyl radicals.
- Hierarchical photocatalysts possess macro scale dimension (for easy separation) and mesoporous structure for increasing the specific surface area, light harvesting and photocatalytic activity. Therefore, the synergetic effects of different dimensional levels often lead to significant improvement of the performance of hierarchical photocatalysts.
- Over the past decades, a large volume of research has been devoted to the optimization of operating parameters and materials development. However, less attention has been paid to the process engineering and design of photoreactors, which are indeed critically important for the overall AOPs performance. Quantum yield, mass transfer coefficient, residence time, light distribution profile and energy consumption depend on the reactor design.
- Investigating the removal of emerging contaminants in real water bodies such as river and lake water as well as the effluent of water treatment plants is important. In the real

water matrix, not only the concentration of emerging contaminants is extremely low and their measurement is difficult, the presence of a mixture of emerging contaminants would complicate the removal process.

- Since advanced oxidation processes for complete mineralization of contaminants are usually expensive and require high amounts of energy and/or chemicals, their combination with a biological treatment (as a pre-treatment or post-treatment stage) is a promising approach to reducing operating costs.
- Comparing the efficiency of photocatalysis process with other more frequently applied technologies such as Fenton, O₃, O₃/UV, and H₂O₂/UV process in terms of contaminant removal and mineralization, by-products formation, energy consumption and especially scalability of process is important.

References

- Abazari, R., Mahjoub, A.R. and Sanati, S. (2016) Magnetically recoverable Fe₃O₄-ZnO/AOT nanocomposites: Synthesis of a core-shell structure via a novel and mild route for photocatalytic degradation of toxic dyes. *Journal of Molecular Liquids* 223, 1133-1142.
- Abdel Aal, A., Mahmoud, S.A. and Aboul-Gheit, A.K. (2009) Sol-Gel and Thermally Evaporated Nanostructured Thin ZnO Films for Photocatalytic Degradation of Trichlorophenol. *Nanoscale Research Letters* 4(7), 627-634.
- Abellán, M., Bayarri, B., Giménez, J. and Costa, J. (2007) Photocatalytic degradation of sulfamethoxazole in aqueous suspension of TiO₂. *Applied Catalysis B: Environmental* 74(3), 233-241.
- Abellán, M., Giménez, J. and Esplugas, S. (2009) Photocatalytic degradation of antibiotics: the case of sulfamethoxazole and trimethoprim. *Catalysis Today* 144(1), 131-136.
- Adamek, E., Baran, W., Ziemiańska, J. and Sobczak, A. (2012) Effect of FeCl₃ on sulfonamide removal and reduction of antimicrobial activity of wastewater in a photocatalytic process with TiO₂. *Applied Catalysis B: Environmental* 126, 29-38.
- Adewuyi, Y.G. (2001) Sonochemistry: Environmental Science and Engineering Applications. *Industrial & Engineering Chemistry Research* 40(22), 4681-4715.
- Alsager, O.A., Alnajrani, M.N. and Alhazzaa, O. (2018) Decomposition of antibiotics by gamma irradiation: Kinetics, antimicrobial activity, and real application in food matrices. *Chemical Engineering Journal* 338, 548-556.
- Anju, S.G., Yesodharan, S. and Yesodharan, E.P. (2012) Zinc oxide mediated sonophotocatalytic degradation of phenol in water. *Chemical Engineering Journal* 189-190, 84-93.
- Arabatzis, I.M., Stergiopoulos, T., Andreeva, D., Kitova, S., Neophytides, S.G. and Falaras, P. (2003) Characterization and photocatalytic activity of Au/TiO₂ thin films for azo-dye degradation. *Journal of Catalysis* 220(1), 127-135.
- Ba-Abbad, M.M., Kadhum, A.A.H., Mohamad, A.B., Takriff, M.S. and Sopian, K. (2013) Visible light photocatalytic activity of Fe³⁺-doped ZnO nanoparticle prepared via sol-gel technique. *Chemosphere* 91(11), 1604-1611.
- Ballesteros Martín, M.M., Sánchez Pérez, J.A., Acién Fernández, F.G., Casas López, J.L., García-Ripoll, A.M., Arques, A., Oller, I. and Malato Rodríguez, S. (2008) Combined photo-Fenton and biological oxidation for pesticide degradation: Effect of photo-treated intermediates on biodegradation kinetics. *Chemosphere* 70(8), 1476-1483.
- Benhebal, H., Chaib, M., Leonard, A., Lambert, S.D. and Crine, M. (2012) Photodegradation of phenol and benzoic acid by sol-gel-synthesized alkali metal-doped ZnO. *Materials Science in Semiconductor Processing* 15(3), 264-269.
- Benito, A., Penadés, A., Lliberia, J.L. and Gonzalez-Olmos, R. (2017) Degradation pathways of aniline in aqueous solutions during electro-oxidation with BDD electrodes and UV/H₂O₂ treatment. *Chemosphere* 166, 230-237.
- Bhuyan, B., Paul, B., Purkayastha, D.D., Dhar, S.S. and Behera, S. (2016) Facile synthesis and characterization of zinc oxide nanoparticles and studies of their catalytic activity towards ultrasound-assisted degradation of metronidazole. *Materials Letters* 168, 158-162.

- Bohdziewicz, J., Kudlek, E. and Dudziak, M. (2016) Influence of the catalyst type (TiO₂ and ZnO) on the photocatalytic oxidation of pharmaceuticals in the aquatic environment. *Desalination and Water Treatment* 57(3), 1552-1563.
- Boix, C., Ibáñez, M., Fabregat-Safont, D., Morales, E., Pastor, L., Sancho, J.V., Sánchez-Ramírez, J.E. and Hernández, F. (2016) Behaviour of emerging contaminants in sewage sludge after anaerobic digestion. *Chemosphere* 163, 296-304.
- Boreen, A.L., Arnold, W.A. and McNeill, K. (2004) Photochemical fate of sulfa drugs in the aquatic environment: sulfa drugs containing five-membered heterocyclic groups. *Environmental science & technology* 38(14), 3933-3940.
- Cai, M., Thorpe, D., Adamson, D.H. and Schniepp, H.C. (2012) Methods of graphite exfoliation. *Journal of Materials Chemistry* 22(48), 24992-25002.
- Cao, S., Low, J., Yu, J. and Jaroniec, M. (2015) Polymeric photocatalysts based on graphitic carbon nitride. *Advanced Materials* 27(13), 2150-2176.
- Carbonaro, S., Sugihara, M.N. and Strathmann, T.J. (2013) Continuous-flow photocatalytic treatment of pharmaceutical micropollutants: activity, inhibition, and deactivation of TiO₂ photocatalysts in wastewater effluent. *Applied Catalysis B: Environmental* 129, 1-12.
- Castañeda, C., Tzompantzi, F. and Gómez, R. (2016) Photocatalytic reduction of 4-nitrophenol on in situ fluorinated sol-gel TiO₂ under UV irradiation using Na₂SO₃ as reducing agent. *Journal of Sol-Gel Science and Technology* 80(2), 426-435.
- Catalá, M., Domínguez-Morueco, N., Migens, A., Molina, R., Martínez, F., Valcárcel, Y., Mastroianni, N., López de Alda, M., Barceló, D. and Segura, Y. (2015) Elimination of drugs of abuse and their toxicity from natural waters by photo-Fenton treatment. *Science of The Total Environment* 520, 198-205.
- Cater, S.R., Stefan, M.I., Bolton, J.R. and Safarzadeh-Amiri, A. (2000) UV/H₂O₂ Treatment of Methyl tert-Butyl Ether in Contaminated Waters. *Environmental Science & Technology* 34(4), 659-662.
- Cates, E.L. (2017) Photocatalytic water treatment: so where are we going with this?. *Environmental Science & Technology*, 51(2), 757-758
- Chalasanani, R. and Vasudevan, S. (2013) Cyclodextrin-functionalized Fe₃O₄@ TiO₂: reusable, magnetic nanoparticles for photocatalytic degradation of endocrine-disrupting chemicals in water supplies. *ACS nano* 7(5), 4093-4104.
- Chen, J., Li, G., Huang, Y., Zhang, H., Zhao, H. and An, T. (2012) Optimization synthesis of carbon nanotubes-anatase TiO₂ composite photocatalyst by response surface methodology for photocatalytic degradation of gaseous styrene. *Applied Catalysis B: Environmental* 123, 69-77.
- Chen, X., Wei, J., Hou, R., Liang, Y., Xie, Z., Zhu, Y., Zhang, X. and Wang, H. (2016) Growth of gC₃N₄ on mesoporous TiO₂ spheres with high photocatalytic activity under visible light irradiation. *Applied Catalysis B: Environmental* 188, 342-350.
- Chen, Y.-C. and Smirniotis, P. (2002) Enhancement of Photocatalytic Degradation of Phenol and Chlorophenols by Ultrasound. *Industrial & Engineering Chemistry Research* 41(24), 5958-5965.
- Chen, Y., Chen, F. and Zhang, J. (2009) Effect of surface fluorination on the photocatalytic and photo-induced hydrophilic properties of porous TiO₂ films. *Applied Surface Science* 255(12), 6290-6296.

- Chen, Y. and Liu, K. (2016) Preparation and characterization of nitrogen-doped TiO₂/diatomite integrated photocatalytic pellet for the adsorption-degradation of tetracycline hydrochloride using visible light. *Chemical Engineering Journal* 302, 682-696.
- Chen, Z., Zhang, N. and Xu, Y.-J. (2013) Synthesis of graphene-ZnO nanorod nanocomposites with improved photoactivity and anti-photocorrosion. *CrystEngComm* 15(15), 3022-3030.
- Cheng, D., Ngo, H.H., Guo, W., Liu, Y., Chang, S.W., Nguyen, D.D., Nghiem, L.D., Zhou, J. and Ni, B. (2018) Anaerobic membrane bioreactors for antibiotic wastewater treatment: Performance and membrane fouling issues. *Bioresource Technology* 267, 714-724.
- Chi, G.T., Churchley, J. and Huddersman, K.D. (2013) Pilot-Scale Removal of Trace Steroid Hormones and Pharmaceuticals and Personal Care Products from Municipal Wastewater Using a Heterogeneous Fenton's Catalytic Process. *International Journal of Chemical Engineering* 2013, 10.
- Chiarello, G.L., Dozzi, M.V., Scavini, M., Grunwaldt, J.-D. and Selli, E. (2014) One step flame-made fluorinated Pt/TiO₂ photocatalysts for hydrogen production. *Applied Catalysis B: Environmental* 160, 144-151.
- Chin, S.S., Lim, T.M., Chiang, K. and Fane, A.G. (2007) Factors affecting the performance of a low-pressure submerged membrane photocatalytic reactor. *Chemical Engineering Journal* 130(1), 53-63.
- Choina, J., Bagabas, A., Fischer, C., Flechsig, G.U., Kosslick, H., Alshammari, A. and Schulz, A. (2015) The influence of the textural properties of ZnO nanoparticles on adsorption and photocatalytic remediation of water from pharmaceuticals. *Catalysis Today* 241, Part A, 47-54.
- Chong, M.N., Jin, B., Chow, C.W.K. and Saint, C. (2010) Recent developments in photocatalytic water treatment technology: A review. *Water Research* 44(10), 2997-3027.
- Chun, S.Y., An, S.W., Lee, S.J., Kim, J.T. and Chang, S.W. (2014) Optimization of sulfamethoxazole degradation by TiO₂/hydroxyapatite composite under ultraviolet irradiation using response surface methodology. *Korean Journal of Chemical Engineering* 31(6), 994-1001.
- Comparelli, R., Fanizza, E., Curri, M.L., Cozzoli, P.D., Mascolo, G. and Agostiano, A. (2005) UV-induced photocatalytic degradation of azo dyes by organic-capped ZnO nanocrystals immobilized onto substrates. *Applied Catalysis B: Environmental* 60(1-2), 1-11.
- Cui, Y., Huang, J., Fu, X. and Wang, X. (2012) Metal-free photocatalytic degradation of 4-chlorophenol in water by mesoporous carbon nitride semiconductors. *Catalysis Science & Technology* 2(7), 1396-1402.
- del Mar Gómez-Ramos, M., Mezcuca, M., Agüera, A., Fernández-Alba, A.R., Gonzalo, S., Rodríguez, A. and Rosal, R. (2011) Chemical and toxicological evolution of the antibiotic sulfamethoxazole under ozone treatment in water solution. *Journal of hazardous materials* 192(1), 18-25.
- Dhir, A., Prakash, N.T. and Sud, D. (2012) Comparative studies on TiO₂/ZnO photocatalyzed degradation of 4-chlorocatechol and bleach mill effluents. *Desalination and Water Treatment* 46(1-3), 196-204.
- Ding, F., Yang, D., Tong, Z., Nan, Y., Wang, Y., Zou, X. and Jiang, Z. (2017) Graphitic carbon nitride-based nanocomposites as visible-light driven photocatalysts for environmental purification. *Environmental Science: Nano* 4(7), 1455-1469.
- Ding, S., Niu, J., Bao, Y. and Hu, L. (2013) Evidence of superoxide radical contribution to demineralization of sulfamethoxazole by visible-light-driven Bi₂O₃/Bi₂O₂CO₃/Sr₆Bi₂O₉ photocatalyst. *Journal of hazardous materials* 262, 812-818.
- Divband, B., Khatamian, M., Eslamian, G.R.K. and Darbandi, M. (2013) Synthesis of Ag/ZnO nanostructures by different methods and investigation of their photocatalytic efficiency for 4-nitrophenol degradation. *Applied Surface Science* 284, 80-86.

- Długosz, M., Żmudzki, P., Kwiecień, A., Szczubiałka, K., Krzek, J. and Nowakowska, M. (2015) Photocatalytic degradation of sulfamethoxazole in aqueous solution using a floating TiO₂-expanded perlite photocatalyst. *Journal of Hazardous Materials* 298, 146-153.
- Dolar, D., Gros, M., Rodriguez-Mozaz, S., Moreno, J., Comas, J., Rodriguez-Roda, I. and Barceló, D. (2012) Removal of emerging contaminants from municipal wastewater with an integrated membrane system, MBR-RO. *Journal of Hazardous Materials* 239-240, 64-69.
- Dong, C., Ma, Z., Qie, R., Guo, X., Li, C., Wang, R., Shi, Y., Dai, B. and Jia, X. (2017) Morphology and Defects Regulation of Carbon Nitride by Hydrochloric Acid to Boost Visible Light Absorption and Photocatalytic Activity. *Applied Catalysis B: Environmental*.
- Dong, F., Li, Y., Wang, Z. and Ho, W.-K. (2015) Enhanced visible light photocatalytic activity and oxidation ability of porous graphene-like g-C₃N₄ nanosheets via thermal exfoliation. *Applied Surface Science* 358, 393-403.
- Dong, F., Wang, Z., Li, Y., Ho, W.-K. and Lee, S. (2014) Immobilization of polymeric g-C₃N₄ on structured ceramic foam for efficient visible light photocatalytic air purification with real indoor illumination. *Environmental science & technology* 48(17), 10345-10353.
- Dong, Y., Wang, Q., Wu, H., Chen, Y., Lu, C.H., Chi, Y. and Yang, H.H. (2016) Graphitic carbon nitride materials: sensing, imaging and therapy. *Small* 12(39), 5376-5393.
- Dong, Z. and Wu, Y. (2017) Magnetically separable photocatalyst of direct Z-scheme g-C₃N₄ nanosheets/natural hematite ore hybrids. *Journal of Photochemistry and Photobiology A: Chemistry* 336, 156-163.
- Ebadi, A., Soltan Mohammadzadeh, J.S. and Khudiev, A. (2009) What is the correct form of BET isotherm for modeling liquid phase adsorption? *Adsorption* 15(1), 65-73.
- El-Kemary, M., El-Shamy, H. and El-Mehasseb, I. (2010) Photocatalytic degradation of ciprofloxacin drug in water using ZnO nanoparticles. *Journal of Luminescence* 130(12), 2327-2331.
- Elmolla, E.S. and Chaudhuri, M. (2010a) Comparison of different advanced oxidation processes for treatment of antibiotic aqueous solution. *Desalination* 256(1-3), 43-47.
- Elmolla, E.S. and Chaudhuri, M. (2010b) Degradation of amoxicillin, ampicillin and cloxacillin antibiotics in aqueous solution by the UV/ZnO photocatalytic process. *Journal of hazardous materials* 173(1), 445-449.
- Eren, Z. and Ince, N.H. (2010) Sonolytic and sonocatalytic degradation of azo dyes by low and high frequency ultrasound. *Journal of Hazardous Materials* 177(1-3), 1019-1024.
- Erto, A., Di Natale, F., Musmarra, D. and Lancia, A. (2015) Modeling of single and competitive adsorption of cadmium and zinc onto activated carbon. *Adsorption* 21(8), 611-621.
- Erto, A., Lancia, A. and Musmarra, D. (2011) A modelling analysis of PCE/TCE mixture adsorption based on Ideal Adsorbed Solution Theory. *Separation and Purification Technology* 80(1), 140-147.
- Escher, B.I., Bramaz, N., Richter, M. and Lienert, J. (2006) Comparative Ecotoxicological Hazard Assessment of Beta-Blockers and Their Human Metabolites Using a Mode-of-Action-Based Test Battery and a QSAR Approach. *Environmental Science & Technology* 40(23), 7402-7408.
- Eskandarian, M.R., Choi, H., Fazli, M. and Rasoulifard, M.H. (2016) Effect of UV-LED wavelengths on direct photolytic and TiO₂ photocatalytic degradation of emerging contaminants in water. *Chemical Engineering Journal* 300, 414-422.

- Eskandarloo, H., Badiei, A., Behnajady, M.A. and Ziarani, G.M. (2016) Ultrasonic-assisted degradation of phenazopyridine with a combination of Sm-doped ZnO nanoparticles and inorganic oxidants. *Ultrasonics Sonochemistry* 28, 169-177.
- Etacheri, V., Roshan, R. and Kumar, V. (2012) Mg-Doped ZnO Nanoparticles for Efficient Sunlight-Driven Photocatalysis. *ACS Applied Materials & Interfaces* 4(5), 2717-2725.
- Farzadkia, M., Esrafil, A., Baghapour, M.A., Shahamat, Y.D. and Okhovat, N. (2014) Degradation of metronidazole in aqueous solution by nano-ZnO/UV photocatalytic process. *Desalination and Water Treatment* 52(25-27), 4947-4952.
- Feng, X., Guo, H., Patel, K., Zhou, H. and Lou, X. (2014) High performance, recoverable Fe₃O₄ZnO nanoparticles for enhanced photocatalytic degradation of phenol. *Chemical Engineering Journal* 244, 327-334.
- Fleming, A. (1944) The discovery of penicillin. *British Medical Bulletin* 2(1), 4-5.
- Foo, K.Y. and Hameed, B.H. (2010) Insights into the modeling of adsorption isotherm systems. *Chemical Engineering Journal* 156(1), 2-10.
- Friedmann, D., Mendive, C. and Bahnemann, D. (2010) TiO₂ for water treatment: parameters affecting the kinetics and mechanisms of photocatalysis. *Applied Catalysis B: Environmental* 99(3), 398-406.
- Fu, H., Xu, T., Zhu, S. and Zhu, Y. (2008) Photocorrosion inhibition and enhancement of photocatalytic activity for ZnO via hybridization with C₆₀. *Environmental science & technology* 42(21), 8064-8069.
- Gao, N., Liu, C.-X., Xu, Q.-M., Cheng, J.-S. and Yuan, Y.-J. (2018) Simultaneous removal of ciprofloxacin, norfloxacin, sulfamethoxazole by co-producing oxidative enzymes system of *Phanerochaete chrysosporium* and *Pycnoporus sanguineus*. *Chemosphere* 195, 146-155.
- Gaya, U.I. and Abdullah, A.H. (2008) Heterogeneous photocatalytic degradation of organic contaminants over titanium dioxide: A review of fundamentals, progress and problems. *Journal of Photochemistry and Photobiology C: Photochemistry Reviews* 9(1), 1-12.
- Gaya, U.I., Abdullah, A.H., Zainal, Z. and Hussein, M.Z. (2009) Photocatalytic treatment of 4-chlorophenol in aqueous ZnO suspensions: Intermediates, influence of dosage and inorganic anions. *Journal of Hazardous Materials* 168(1), 57-63.
- Ge, L., Zuo, F., Liu, J., Ma, Q., Wang, C., Sun, D., Bartels, L. and Feng, P. (2012) Synthesis and efficient visible light photocatalytic hydrogen evolution of polymeric g-C₃N₄ coupled with CdS quantum dots. *The Journal of Physical Chemistry C* 116(25), 13708-13714.
- Ghauch, A., Tuqan, A. and Assi, H.A. (2009) Antibiotic removal from water: Elimination of amoxicillin and ampicillin by microscale and nanoscale iron particles. *Environmental Pollution* 157(5), 1626-1635.
- Gmurek, M., Bizukojć, M., Mosinger, J. and Ledakowicz, S. (2015) Application of photoactive electrospun nanofiber materials with immobilized meso-tetraphenylporphyrin for parabens photodegradation. *Catalysis Today* 240, 160-167.
- Gong, H. and Chu, W. (2015) Photodegradation of Sulfamethoxazole with a Recyclable Catalyst. *Industrial & Engineering Chemistry Research* 54(51), 12763-12769.
- Gong, H. and Chu, W. (2018) Permanganate with a double-edge role in photodegradation of sulfamethoxazole: Kinetic, reaction mechanism and toxicity. *Chemosphere* 191, 494-502.

- Gozlan, I., Rotstein, A. and Avisar, D. (2013) Amoxicillin-degradation products formed under controlled environmental conditions: Identification and determination in the aquatic environment. *Chemosphere* 91(7), 985-992.
- Guillard, C., Puzenat, E., Lachheb, H., Houas, A. and Herrmann, J.-M. (2005) Why inorganic salts decrease the TiO₂ photocatalytic efficiency. *International Journal of Photoenergy* 7(1), 1-9.
- Güyer, G.T. and Ince, N.H. (2011) Degradation of diclofenac in water by homogeneous and heterogeneous sonolysis. *Ultrasonics sonochemistry* 18(1), 114-119.
- Han, C., Yang, M.-Q., Weng, B. and Xu, Y.-J. (2014) Improving the photocatalytic activity and anti-photocorrosion of semiconductor ZnO by coupling with versatile carbon. *Physical Chemistry Chemical Physics* 16(32), 16891-16903.
- Han, Q., Wang, B., Gao, J., Cheng, Z., Zhao, Y., Zhang, Z. and Qu, L. (2016) Atomically thin mesoporous nanomesh of graphitic C₃N₄ for high-efficiency photocatalytic hydrogen evolution. *ACS nano* 10(2), 2745-2751.
- Hao, R., Wang, G., Tang, H., Sun, L., Xu, C. and Han, D. (2016) Template-free preparation of macro/mesoporous g-C₃N₄/TiO₂ heterojunction photocatalysts with enhanced visible light photocatalytic activity. *Applied Catalysis B: Environmental* 187, 47-58.
- Hariharan, C. (2006) Photocatalytic degradation of organic contaminants in water by ZnO nanoparticles: Revisited. *Applied Catalysis A: General* 304, 55-61.
- Hassani, A., Khataee, A., Karaca, S., Karaca, C. and Gholami, P. (2017) Sonocatalytic degradation of ciprofloxacin using synthesized TiO₂ nanoparticles on montmorillonite. *Ultrasonics Sonochemistry* 35, 251-262.
- Hayat, K., Gondal, M.A., Khaled, M.M., Ahmed, S. and Shemsi, A.M. (2011) Nano ZnO synthesis by modified sol gel method and its application in heterogeneous photocatalytic removal of phenol from water. *Applied Catalysis A: General* 393(1-2), 122-129.
- He, Y., Wang, Y., Zhang, L., Teng, B. and Fan, M. (2015) High-efficiency conversion of CO₂ to fuel over ZnO/g-C₃N₄ photocatalyst. *Applied Catalysis B: Environmental* 168, 1-8.
- He, Y., Zhang, L., Teng, B. and Fan, M. (2014) New application of Z-scheme Ag₃PO₄/g-C₃N₄ composite in converting CO₂ to fuel. *Environmental science & technology* 49(1), 649-656.
- Hong, R.Y., Zhang, S.Z., Di, G.Q., Li, H.Z., Zheng, Y., Ding, J. and Wei, D.G. (2008) Preparation, characterization and application of Fe₃O₄/ZnO core/shell magnetic nanoparticles. *Materials Research Bulletin* 43(8), 2457-2468.
- Hou, D., Goei, R., Wang, X., Wang, P. and Lim, T.-T. (2012) Preparation of carbon-sensitized and Fe-Er codoped TiO₂ with response surface methodology for bisphenol A photocatalytic degradation under visible-light irradiation. *Applied Catalysis B: Environmental* 126, 121-133.
- Hou, L., Wang, L., Royer, S. and Zhang, H. (2016) Ultrasound-assisted heterogeneous Fenton-like degradation of tetracycline over a magnetite catalyst. *Journal of Hazardous Materials* 302, 458-467.
- Hu, J.-S., Zhong, L.-S., Song, W.-G. and Wan, L.-J. (2008) Synthesis of Hierarchically Structured Metal Oxides and their Application in Heavy Metal Ion Removal. *Advanced Materials* 20(15), 2977-2982.
- Hu, L., Flanders, P.M., Miller, P.L. and Strathmann, T.J. (2007a) Oxidation of sulfamethoxazole and related antimicrobial agents by TiO₂ photocatalysis. *Water research* 41(12), 2612-2626.

- Hu, L., Flanders, P.M., Miller, P.L. and Strathmann, T.J. (2007b) Oxidation of sulfamethoxazole and related antimicrobial agents by TiO₂ photocatalysis. *Water research* 41(12), 2612-2626.
- Hu, X., Liu, B., Deng, Y., Chen, H., Luo, S., Sun, C., Yang, P. and Yang, S. (2011) Adsorption and heterogeneous Fenton degradation of 17 α -methyltestosterone on nano Fe₃O₄/MWCNTs in aqueous solution. *Applied Catalysis B: Environmental* 107(3-4), 274-283.
- Huang, D., Yan, X., Yan, M., Zeng, G., Zhou, C., Wan, J., Cheng, M. and Xue, W. (2018) Graphitic Carbon Nitride-Based Heterojunction Photoactive Nanocomposites: Applications and Mechanism Insight. *ACS Applied Materials & Interfaces* 10(25), 21035-21055.
- Ikehata, K., Jodeiri Naghashkar, N. and Gamal El-Din, M. (2006) Degradation of aqueous pharmaceuticals by ozonation and advanced oxidation processes: a review. *Ozone: Science and Engineering* 28(6), 353-414.
- Ioannidou, E., Frontistis, Z., Antonopoulou, M., Venieri, D., Konstantinou, I., Kondarides, D.I. and Mantzavinos, D. (2017a) Solar photocatalytic degradation of sulfamethoxazole over tungsten-Modified TiO₂. *Chemical Engineering Journal* 318, 143-152.
- Ioannidou, E., Frontistis, Z., Antonopoulou, M., Venieri, D., Konstantinou, I., Kondarides, D.I. and Mantzavinos, D. (2017b) Solar photocatalytic degradation of sulfamethoxazole over tungsten-Modified TiO₂. *Chemical Engineering Journal* 318, 143-152.
- Ivetić, T.B., Dimitrievska, M.R., Finčur, N.L., Đaćanin, L.R., Gúth, I.O., Abramović, B.F. and Lukić-Petrović, S.R. (2014) Effect of annealing temperature on structural and optical properties of Mg-doped ZnO nanoparticles and their photocatalytic efficiency in alprazolam degradation. *Ceramics International* 40(1, Part B), 1545-1552.
- Jiang, H.-Y., Liu, G., Wang, T., Li, P., Lin, J. and Ye, J. (2015) In situ construction of α -Bi₂O₃/gC₃N₄/ β -Bi₂O₃ composites and their highly efficient photocatalytic performances. *RSC Advances* 5(113), 92963-92969.
- Jyothi, K., Yesodharan, S. and Yesodharan, E. (2014) Ultrasound (US), ultraviolet light (UV) and combination (US+ UV) assisted semiconductor catalysed degradation of organic pollutants in water: oscillation in the concentration of hydrogen peroxide formed in situ. *Ultrasonics sonochemistry* 21(5), 1787-1796.
- Jyothi, K.P., Yesodharan, S. and Yesodharan, E.P. (2018) Contaminant salts as enhancers of sonocatalytic degradation of organic water pollutants: Effect of concentration, reaction time and adsorption on the efficiency of enhancement and the fate of concurrently formed H₂O₂. *Journal of Environmental Chemical Engineering*. 6(3), 3574-3589
- Kamat, P.V., Huehn, R. and Nicolaescu, R. (2002) A "Sense and Shoot" Approach for Photocatalytic Degradation of Organic Contaminants in Water. *The Journal of Physical Chemistry B* 106(4), 788-794.
- Kanakaraju, D., Kockler, J., Motti, C.A., Glass, B.D. and Oelgemöller, M. (2015) Titanium dioxide/zeolite integrated photocatalytic adsorbents for the degradation of amoxicillin. *Applied Catalysis B: Environmental* 166, 45-55.
- Kang, K., Jang, M., Cui, M., Qiu, P., Na, S., Son, Y. and Khim, J. (2015) Enhanced sonocatalytic treatment of ibuprofen by mechanical mixing and reusable magnetic core titanium dioxide. *Chemical Engineering Journal* 264, 522-530.
- Kansal, S.K., Singh, M. and Sud, D. (2007) Studies on photodegradation of two commercial dyes in aqueous phase using different photocatalysts. *Journal of Hazardous Materials* 141(3), 581-590.
- Karaca, M., Kıranşan, M., Karaca, S., Khataee, A. and Karimi, A. (2016) Sonocatalytic removal of naproxen by synthesized zinc oxide nanoparticles on montmorillonite. *Ultrasonics Sonochemistry* 31, 250-256.

- Kayvani Fard, A., McKay, G., Manawi, Y., Malaibari, Z. and Hussien, M.A. (2016) Outstanding adsorption performance of high aspect ratio and super-hydrophobic carbon nanotubes for oil removal. *Chemosphere* 164, 142-155.
- Khataee, A., Kayan, B., Gholami, P., Kalderis, D., Akay, S. and Dinpazhoh, L. (2017a) Sonocatalytic degradation of Reactive Yellow 39 using synthesized ZrO₂ nanoparticles on biochar. *Ultrasonics sonochemistry* 39, 540-549.
- Khataee, A., Saadi, S. and Vahid, B. (2017b) Kinetic modeling of sonocatalytic degradation of reactive orange 29 in the presence of lanthanide-doped ZnO nanoparticles. *Ultrasonics Sonochemistry* 34, 98-106.
- Khataee, A., Soltani, R.D.C., Karimi, A. and Joo, S.W. (2015) Sonocatalytic degradation of a textile dye over Gd-doped ZnO nanoparticles synthesized through sonochemical process. *Ultrasonics sonochemistry* 23, 219-230.
- Khataee, A., Vahid, B., Saadi, S. and Joo, S.W. (2016) Development of an empirical kinetic model for sonocatalytic process using neodymium doped zinc oxide nanoparticles. *Ultrasonics sonochemistry* 29, 146-155.
- Kim, H.-i., Choi, Y., Hu, S., Choi, W. and Kim, J.-H. (2018) Photocatalytic hydrogen peroxide production by anthraquinone-augmented polymeric carbon nitride. *Applied Catalysis B: Environmental* 229, 121-129.
- Kim, J., Choi, W. and Park, H. (2010) Effects of TiO₂ surface fluorination on photocatalytic degradation of methylene blue and humic acid. *Research on Chemical Intermediates* 36(2), 127-140.
- Kim, J.R. and Kan, E. (2016) Heterogeneous photocatalytic degradation of sulfamethoxazole in water using a biochar-supported TiO₂ photocatalyst. *Journal of environmental management* 180, 94-101.
- Klauson, D., Babkina, J., Stepanova, K., Krichevskaya, M. and Preis, S. (2010) Aqueous photocatalytic oxidation of amoxicillin. *Catalysis Today* 151(1-2), 39-45.
- Kong, J.-Z., Li, A.-D., Li, X.-Y., Zhai, H.-F., Zhang, W.-Q., Gong, Y.-P., Li, H. and Wu, D. (2010) Photo-degradation of methylene blue using Ta-doped ZnO nanoparticle. *Journal of Solid State Chemistry* 183(6), 1359-1364.
- Kovacic, M., Kopicic, N., Kusic, H., Stangar, U.L., Dionysiou, D.D. and Bozic, A.L. (2017) Reactivation and reuse of TiO₂-SnS₂ composite catalyst for solar-driven water treatment. *Environmental Science and Pollution Research*, 1-14.
- Krzeminski, P., Tomei, M.C., Karaolia, P., Langenhoff, A., Almeida, C.M.R., Felis, E., Gritten, F., Andersen, H.R., Fernandes, T., Manaia, C.M., Rizzo, L. and Fatta-Kassinos, D. (2019) Performance of secondary wastewater treatment methods for the removal of contaminants of emerging concern implicated in crop uptake and antibiotic resistance spread: A review. *Science of The Total Environment* 648, 1052-1081.
- Kudo, A. and Miseki, Y. (2009) Heterogeneous photocatalyst materials for water splitting. *Chemical Society Reviews* 38(1), 253-278.
- Kumar, A., Kumar, A., Sharma, G., Al-Muhtaseb, A.a.H., Naushad, M., Ghfar, A.A. and Stadler, F.J. (2018) Quaternary magnetic BiOCl/g-C₃N₄/Cu₂O/Fe₃O₄ nano-junction for visible light and solar powered degradation of sulfamethoxazole from aqueous environment. *Chemical Engineering Journal* 334, 462-478.
- Kumar, A., Kumar, A., Sharma, G., Naushad, M., Stadler, F.J., Ghfar, A.A., Dhiman, P. and Saini, R.V. (2017) Sustainable nano-hybrids of magnetic biochar supported g-C₃N₄/FeVO₄ for solar powered degradation of noxious pollutants-Synergism of adsorption, photocatalysis & photo-ozonation. *Journal of Cleaner Production* 165, 431-451.
- Kumar, S., Baruah, A., Tonda, S., Kumar, B., Shanker, V. and Sreedhar, B. (2014) Cost-effective and eco-friendly synthesis of novel and stable N-doped ZnO/gC₃N₄ core-shell nanoplates with excellent visible-light responsive photocatalysis. *Nanoscale* 6(9), 4830-4842.

- Kumar, S.G. and Rao, K.S.R.K. (2015) Zinc oxide based photocatalysis: tailoring surface-bulk structure and related interfacial charge carrier dynamics for better environmental applications. *RSC Advances* 5(5), 3306-3351.
- Lam, S.-m., Sin, J.-c., Abdullah, A.Z. and Mohamed, A.R. (2013) Photocatalytic degradation of resorcinol, an endocrine disrupter, by TiO₂ and ZnO suspensions. *Environmental Technology* 34(9), 1097-1106.
- Leary, R., Saghi, Z., Armbrüster, M., Wowsnick, G., Schlögl, R., Thomas, J.M. and Midgley, P.A. (2012) Quantitative High-Angle Annular Dark-Field Scanning Transmission Electron Microscope (HAADF-STEM) Tomography and High-Resolution Electron Microscopy of Unsupported Intermetallic GaPd₂ Catalysts. *The Journal of Physical Chemistry C* 116(24), 13343-13352.
- Lee, K.M., Lai, C.W., Ngai, K.S. and Juan, J.C. (2016) Recent developments of zinc oxide based photocatalyst in water treatment technology: A review. *Water Research* 88, 428-448.
- Leong, K.H., Liu, S.L., Sim, L.C., Saravanan, P., Jang, M. and Ibrahim, S. (2015) Surface reconstruction of titania with g-C₃N₄ and Ag for promoting efficient electrons migration and enhanced visible light photocatalysis. *Applied Surface Science* 358, 370-376.
- Li, H., Bian, Z., Zhu, J., Zhang, D., Li, G., Huo, Y., Li, H. and Lu, Y. (2007) Mesoporous Titania Spheres with Tunable Chamber Structure and Enhanced Photocatalytic Activity. *Journal of the American Chemical Society* 129(27), 8406-8407.
- Li, X., Yu, J. and Jaroniec, M. (2016) Hierarchical photocatalysts. *Chemical Society Reviews* 45(9), 2603-2636.
- Li, Y., Lv, K., Ho, W., Dong, F., Wu, X. and Xia, Y. (2017) Hybridization of rutile TiO₂ (rTiO₂) with gC₃N₄ quantum dots (CN QDs): An efficient visible-light-driven Z-scheme hybridized photocatalyst. *Applied Catalysis B: Environmental* 202, 611-619.
- Li, Y., Wang, Y., Liu, L., Wang, D. and Zhang, W. (2014) Ag/ZnO hollow sphere composites: reusable photocatalyst for photocatalytic degradation of 17 α -ethinylestradiol. *Environmental Science and Pollution Research* 21(7), 5177-5186.
- Li, Y., Xie, W., Hu, X., Shen, G., Zhou, X., Xiang, Y., Zhao, X. and Fang, P. (2010) Comparison of Dye Photodegradation and its Coupling with Light-to-Electricity Conversion over TiO₂ and ZnO. *Langmuir* 26(1), 591-597.
- Li, Z.-Y., Shao, L.-L. and Zhang, C.-L. (2015) Fin-and-tube condenser performance modeling with neural network and response surface methodology. *International Journal of Refrigeration* 59, 124-134.
- Li, Z., Young, N., Di Vece, M., Palomba, S., Palmer, R., Bleloch, A., Curley, B., Johnston, R., Jiang, J. and Yuan, J. (2008) Three-dimensional atomic-scale structure of size-selected gold nanoclusters. *Nature* 451(7174), 46.
- Lin, L., Wang, H. and Xu, P. (2017) Immobilized TiO₂-reduced graphene oxide nanocomposites on optical fibers as high performance photocatalysts for degradation of pharmaceuticals. *Chemical Engineering Journal* 310, 389-398.
- Lin, Y., Ferronato, C., Deng, N., Wu, F. and Chovelon, J.-M. (2009) Photocatalytic degradation of methylparaben by TiO₂: multivariable experimental design and mechanism. *Applied Catalysis B: Environmental* 88(1-2), 32-41.
- Liu, S., Yu, J., Cheng, B. and Jaroniec, M. (2012) Fluorinated semiconductor photocatalysts: Tunable synthesis and unique properties. *Advances in Colloid and Interface Science* 173, 35-53.

- Liu, S., Yu, J. and Jaroniec, M. (2010) Tunable Photocatalytic Selectivity of Hollow TiO₂ Microspheres Composed of Anatase Polyhedra with Exposed {001} Facets. *Journal of the American Chemical Society* 132(34), 11914-11916.
- Liu, Y. and Gao, W. (2014) Photodegradation of Endocrine Disrupting Chemicals by ZnO Nanorod Arrays. *Molecular Crystals and Liquid Crystals* 603(1), 194-201.
- Liu, Y., Goebel, J. and Yin, Y. (2013) Templated synthesis of nanostructured materials. *Chemical Society Reviews* 42(7), 2610-2653.
- Liu, Z., Bai, H., Xu, S. and Sun, D.D. (2011) Hierarchical CuO/ZnO “corn-like” architecture for photocatalytic hydrogen generation. *International Journal of Hydrogen Energy* 36(21), 13473-13480.
- Lu, C.-Y. and Feng, C.-H. (2007) Identification of dimer impurities in ampicillin and amoxicillin by capillary LC and tandem mass spectrometry. *Journal of Separation Science* 30(3), 329-332.
- Lu, F., Cai, W. and Zhang, Y. (2008) ZnO Hierarchical Micro/Nanoarchitectures: Solvothermal Synthesis and Structurally Enhanced Photocatalytic Performance. *Advanced Functional Materials* 18(7), 1047-1056.
- Luo, J., Zhao, X., Wu, J., Jang, H.D., Kung, H.H. and Huang, J. (2012) Crumpled Graphene-Encapsulated Si Nanoparticles for Lithium Ion Battery Anodes. *The Journal of Physical Chemistry Letters* 3(13), 1824-1829.
- Luo, S., Wei, Z., Spinney, R., Zhang, Z., Dionysiou, D.D., Gao, L., Chai, L., Wang, D. and Xiao, R. (2018) UV direct photolysis of sulfamethoxazole and ibuprofen: An experimental and modelling study. *Journal of hazardous materials* 343, 132-139.
- Lv, H., Ji, G., Yang, Z., Liu, Y., Zhang, X., Liu, W. and Zhang, H. (2015) Enhancement photocatalytic activity of the graphite-like C₃N₄ coated hollow pencil-like ZnO. *Journal of Colloid and Interface Science* 450, 381-387.
- Ma, T.Y., Tang, Y., Dai, S. and Qiao, S.Z. (2014) Proton-Functionalized Two-Dimensional Graphitic Carbon Nitride Nanosheet: An Excellent Metal-/Label-Free Biosensing Platform. *Small* 10(12), 2382-2389.
- Ma, X., Li, H., Liu, T., Du, S., Qiang, Q., Wang, Y., Yin, S. and Sato, T. (2017) Comparison of photocatalytic reaction-induced selective corrosion with photocorrosion: Impact on morphology and stability of Ag-ZnO. *Applied Catalysis B: Environmental* 201, 348-358.
- Mahalakshmi, M., Arabindoo, B., Palanichamy, M. and Murugesan, V. (2007) Photocatalytic degradation of carbofuran using semiconductor oxides. *Journal of Hazardous Materials* 143(1-2), 240-245.
- Mahdavi, R. and Talesh, S.S.A. (2017) Sol-gel synthesis, structural and enhanced photocatalytic performance of Al doped ZnO nanoparticles. *Advanced Powder Technology*. 28, 1418-1425
- Mai, F.D., Chen, C.C., Chen, J.L. and Liu, S.C. (2008) Photodegradation of methyl green using visible irradiation in ZnO suspensions: Determination of the reaction pathway and identification of intermediates by a high-performance liquid chromatography–photodiode array–electrospray ionization–mass spectrometry method. *Journal of Chromatography A* 1189(1-2), 355-365.
- Matamoros, V., Arias, C.A., Nguyen, L.X., Salvadó, V. and Brix, H. (2012) Occurrence and behavior of emerging contaminants in surface water and a restored wetland. *Chemosphere* 88(9), 1083-1089.
- Miao, X., Shen, X., Wu, J., Ji, Z., Wang, J., Kong, L., Liu, M. and Song, C. (2017) Fabrication of an all solid Z-scheme photocatalyst gC₃N₄/GO/AgBr with enhanced visible light photocatalytic activity. *Applied Catalysis A: General* 539, 104-113.

- Minero, C., Mariella, G., Maurino, V., Vione, D. and Pelizzetti, E. (2000) Photocatalytic Transformation of Organic Compounds in the Presence of Inorganic Ions. 2. Competitive Reactions of Phenol and Alcohols on a Titanium Dioxide–Fluoride System. *Langmuir* 16(23), 8964-8972.
- Mirzaei, A., Chen, Z., Haghghat, F. and Yerushalmi, L. (2016) Removal of pharmaceuticals and endocrine disrupting compounds from water by zinc oxide-based photocatalytic degradation: A review. *Sustainable Cities and Society* 27, 407-418.
- Mirzaei, A., Chen, Z., Haghghat, F. and Yerushalmi, L. (2017a) Enhanced adsorption of anionic dyes by surface fluorination of zinc oxide: A straightforward method for numerical solving of the ideal adsorbed solution theory (IAST). *Chemical Engineering Journal* 330, 407-418.
- Mirzaei, A., Chen, Z., Haghghat, F. and Yerushalmi, L. (2017b) Removal of pharmaceuticals from water by homo/heterogenous Fenton-type processes—A review. *Chemosphere* 174, 665-688.
- Mirzaei, A., Chen, Z., Haghghat, F. and Yerushalmi, L. (2018a) Hierarchical magnetic petal-like Fe₃O₄-ZnO@g-C₃N₄ for removal of sulfamethoxazole, suppression of photocorrosion, by-products identification and toxicity assessment. *Chemosphere* 205, 463-474.
- Mirzaei, A., Ebadi, A. and Khajavi, P. (2013) Kinetic and equilibrium modeling of single and binary adsorption of methyl tert-butyl ether (MTBE) and tert-butyl alcohol (TBA) onto nano-perfluorooctyl alumina. *Chemical Engineering Journal* 231, 550-560.
- Mirzaei, A., Yerushalmi, L., Chen, Z. and Haghghat, F. (2018b) Photocatalytic degradation of sulfamethoxazole by hierarchical magnetic ZnO@g-C₃N₄: RSM optimization, kinetic study, reaction pathway and toxicity evaluation. *Journal of Hazardous Materials* 359, 516-526.
- Mirzaei, A., Yerushalmi, L., Chen, Z., Haghghat, F. and Guo, J. (2018c) Enhanced photocatalytic degradation of sulfamethoxazole by zinc oxide photocatalyst in the presence of fluoride ions: Optimization of parameters and toxicological evaluation. *Water Research* 132, 241-251.
- Mohajeri, S., Aziz, H.A., Isa, M.H., Zahed, M.A. and Adlan, M.N. (2010) Statistical optimization of process parameters for landfill leachate treatment using electro-Fenton technique. *Journal of Hazardous Materials* 176(1-3), 749-758.
- Mohapatra, M., Anand, S., Mishra, B.K., Giles, D.E. and Singh, P. (2009) Review of fluoride removal from drinking water. *Journal of Environmental Management* 91(1), 67-77.
- Mohd Omar, F., Abdul Aziz, H. and Stoll, S. (2014) Aggregation and disaggregation of ZnO nanoparticles: Influence of pH and adsorption of Suwannee River humic acid. *Science of The Total Environment* 468-469, 195-201.
- Mompelat, S., Le Bot, B. and Thomas, O. (2009) Occurrence and fate of pharmaceutical products and by-products, from resource to drinking water. *Environment International* 35(5), 803-814.
- Moumeni, O. and Hamdaoui, O. (2012) Intensification of sonochemical degradation of malachite green by bromide ions. *Ultrasonics sonochemistry* 19(3), 404-409.
- Mousavi, M., Habibi-Yangjeh, A. and Pouran, S.R. (2018) Review on magnetically separable graphitic carbon nitride-based nanocomposites as promising visible-light-driven photocatalysts. *Journal of Materials Science: Materials in Electronics*, 1-29.
- Muñoz-Fernandez, L., Sierra-Fernandez, A., Flores-Carrasco, G., Milošević, O. and Rabanal, M.E. (2017) Solvothermal synthesis of Ag/ZnO micro/nanostructures with different precursors for advanced photocatalytic applications. *Advanced Powder Technology* 28(1), 83-92.

- Nakada, N., Shinohara, H., Murata, A., Kiri, K., Managaki, S., Sato, N. and Takada, H. (2007) Removal of selected pharmaceuticals and personal care products (PPCPs) and endocrine-disrupting chemicals (EDCs) during sand filtration and ozonation at a municipal sewage treatment plant. *Water Research* 41(19), 4373-4382.
- Nalini Vijaya Laxmi, P., Saritha, P., Rambabu, N., Himabindu, V. and Anjaneyulu, Y. (2010) Sonochemical degradation of 2-chloro-5-methyl phenol assisted by TiO₂ and H₂O₂. *Journal of Hazardous Materials* 174(1), 151-155.
- Nasuhoglu, D., Yargeau, V. and Berk, D. (2011) Photo-removal of sulfamethoxazole (SMX) by photolytic and photocatalytic processes in a batch reactor under UV-C radiation (λ_{max} = 254nm). *Journal of hazardous materials* 186(1), 67-75.
- Neppolian, B., Choi, H., Sakthivel, S., Arabindoo, B. and Murugesan, V. (2002) Solar/UV-induced photocatalytic degradation of three commercial textile dyes. *Journal of hazardous materials* 89(2-3), 303-317.
- Nishio, J., Tokumura, M., Znad, H.T. and Kawase, Y. (2006) Photocatalytic decolorization of azo-dye with zinc oxide powder in an external UV light irradiation slurry photoreactor. *Journal of Hazardous Materials* 138(1), 106-115.
- Niu, J., Zhang, L., Li, Y., Zhao, J., Lv, S. and Xiao, K. (2013) Effects of environmental factors on sulfamethoxazole photodegradation under simulated sunlight irradiation: kinetics and mechanism. *Journal of Environmental Sciences* 25(6), 1098-1106.
- Noorpoor, A.R. and Nazari Kudahi, S. (2016) Analysis and study of CO₂ adsorption on UiO-66/graphene oxide composite using equilibrium modeling and ideal adsorption solution theory (IAST). *Journal of Environmental Chemical Engineering* 4(1), 1081-1091.
- Oller, I., Malato, S. and Sánchez-Pérez, J.A. (2011) Combination of Advanced Oxidation Processes and biological treatments for wastewater decontamination—A review. *Science of The Total Environment* 409(20), 4141-4166.
- Ou, H., Lin, L., Zheng, Y., Yang, P., Fang, Y. and Wang, X. (2017) Tri-s-triazine-Based Crystalline Carbon Nitride Nanosheets for an Improved Hydrogen Evolution. *Advanced Materials* 29(22), 1700008.
- Palominos, R.A., Mondaca, M.A., Giraldo, A., Peñuela, G., Pérez-Moya, M. and Mansilla, H.D. (2009) Photocatalytic oxidation of the antibiotic tetracycline on TiO₂ and ZnO suspensions. *Catalysis Today* 144(1-2), 100-105.
- Pan, C., Xu, J., Wang, Y., Li, D. and Zhu, Y. (2012) Dramatic Activity of C₃N₄/BiPO₄ Photocatalyst with Core/Shell Structure Formed by Self-Assembly. *Advanced Functional Materials* 22(7), 1518-1524.
- Pandit, A.B., Gogate, P.R. and Mujumdar, S. (2001) Ultrasonic degradation of 2:4:6 trichlorophenol in presence of TiO₂ catalyst. *Ultrasonics sonochemistry* 8(3), 227-231.
- Pang, Y.L. and Abdullah, A.Z. (2013) Fe³⁺ doped TiO₂ nanotubes for combined adsorption–sonocatalytic degradation of real textile wastewater. *Applied Catalysis B: Environmental* 129, 473-481.
- Pang, Y.L., Abdullah, A.Z. and Bhatia, S. (2010) Effect of annealing temperature on the characteristics, sonocatalytic activity and reusability of nanotubes TiO₂ in the degradation of Rhodamine B. *Applied Catalysis B: Environmental* 100(1-2), 393-402.
- Pang, Y.L., Abdullah, A.Z. and Bhatia, S. (2011) Optimization of sonocatalytic degradation of Rhodamine B in aqueous solution in the presence of TiO₂ nanotubes using response surface methodology. *Chemical Engineering Journal* 166(3), 873-880.

- Papailias, I., Todorova, N., Giannakopoulou, T., Ioannidis, N., Boukos, N., Athanasekou, C.P., Dimotikali, D. and Trapalis, C. (2018) Chemical vs thermal exfoliation of g-C₃N₄ for NO_x removal under visible light irradiation. *Applied Catalysis B: Environmental* 239, 16-26.
- Pardeshi, S.K. and Patil, A.B. (2008) A simple route for photocatalytic degradation of phenol in aqueous zinc oxide suspension using solar energy. *Solar Energy* 82(8), 700-705.
- Pare, B., Jonnalagadda, S.B., Tomar, H., Singh, P. and Bhagwat, V.W. (2008) ZnO assisted photocatalytic degradation of acridine orange in aqueous solution using visible irradiation. *Desalination* 232(1-3), 80-90.
- Park, H. and Choi, W. (2004) Effects of TiO₂ Surface Fluorination on Photocatalytic Reactions and Photoelectrochemical Behaviors. *The Journal of Physical Chemistry B* 108(13), 4086-4093.
- Patil, A.B., Patil, K.R. and Pardeshi, S.K. (2010) Ecofriendly synthesis and solar photocatalytic activity of S-doped ZnO. *Journal of Hazardous Materials* 183(1-3), 315-323.
- Pelaez, M., Armah, A., O'Shea, K., Falaras, P. and Dionysiou, D.D. (2011) Effects of water parameters on the degradation of microcystin-LR under visible light-activated TiO₂ photocatalyst. *Water research* 45(12), 3787-3796.
- Peng, F., Wang, H., Yu, H. and Chen, S. (2006) Preparation of aluminum foil-supported nano-sized ZnO thin films and its photocatalytic degradation to phenol under visible light irradiation. *Materials Research Bulletin* 41(11), 2123-2129.
- Pérez-Parada, A., Agüera, A., Gómez-Ramos, M.d.M., García-Reyes, J.F., Heinzen, H. and Fernández-Alba, A.R. (2011) Behavior of amoxicillin in wastewater and river water: identification of its main transformation products by liquid chromatography/electrospray quadrupole time-of-flight mass spectrometry. *Rapid Communications in Mass Spectrometry* 25(6), 731-742.
- Pourmoslemi, S., Mohammadi, A., Kobarfard, F. and Assi, N. (2016) Photocatalytic removal of two antibiotic compounds from aqueous solutions using ZnO nanoparticles. *Desalination and Water Treatment* 57(31), 14774-14784.
- Prieto-Rodríguez, L., Miralles-Cuevas, S., Oller, I., Fernández-Ibáñez, P., Agüera, A., Blanco, J. and Malato, S. (2012) Optimization of mild solar TiO₂ photocatalysis as a tertiary treatment for municipal wastewater treatment plant effluents. *Applied Catalysis B: Environmental* 128, 119-125.
- Prieto-Rodríguez, L., Oller, I., Klamerth, N., Agüera, A., Rodríguez, E.M. and Malato, S. (2013) Application of solar AOPs and ozonation for elimination of micropollutants in municipal wastewater treatment plant effluents. *Water Research* 47(4), 1521-1528.
- Pronin, I.A., Kaneva, N.V., Bozhinova, A.S., Averin, I.A., Papazova, K.I., Dimitrov, D.T. and Moshnikov, V.A. (2014) Photocatalytic oxidation of pharmaceuticals on thin nanostructured Zinc Oxide films. *Kinetics and Catalysis* 55(2), 167-171.
- Qamar, M. and Muneer, M. (2009) A comparative photocatalytic activity of titanium dioxide and zinc oxide by investigating the degradation of vanillin. *Desalination* 249(2), 535-540.
- Qi, D., Xing, M. and Zhang, J. (2014) Hydrophobic Carbon-Doped TiO₂/MCF-F Composite as a High Performance Photocatalyst. *The Journal of Physical Chemistry C* 118(14), 7329-7336.
- Qin, D., Lu, W., Wang, X., Li, N., Chen, X., Zhu, Z. and Chen, W. (2016) Graphitic Carbon Nitride from Burial to Re-emergence on Polyethylene Terephthalate Nanofibers as an Easily Recycled Photocatalyst for Degrading Antibiotics under Solar Irradiation. *ACS applied materials & interfaces* 8(39), 25962-25970.

- Rabindranathan, S., Devipriya, S. and Yesodharan, S. (2003) Photocatalytic degradation of phosphamidon on semiconductor oxides. *Journal of Hazardous Materials* 102(2–3), 217-229.
- Radjenovic, J. and Petrovic, M. (2017) Removal of sulfamethoxazole by electrochemically activated sulfate: Implications of chloride addition. *Journal of Hazardous Materials* 333, 242-249.
- Radke, M., Lauwigi, C., Heinkele, G., Mürdter, T.E. and Letzel, M. (2009) Fate of the antibiotic sulfamethoxazole and its two major human metabolites in a water sediment test. *Environmental science & technology* 43(9), 3135-3141.
- Ramasundaram, S., Seid, M.G., Choe, J.W., Kim, E.-J., Chung, Y.C., Cho, K., Lee, C. and Hong, S.W. (2016) Highly reusable TiO₂ nanoparticle photocatalyst by direct immobilization on steel mesh via PVDF coating, electrospraying, and thermal fixation. *Chemical Engineering Journal* 306, 344-351.
- Rioja, N., Benguria, P., Peñas, F. and Zorita, S. (2014) Competitive removal of pharmaceuticals from environmental waters by adsorption and photocatalytic degradation. *Environmental Science and Pollution Research* 21(19), 11168-11177.
- Ryu, J., Kim, W., Kim, J., Ju, J. and Kim, J. (2017) Is surface fluorination of TiO₂ effective for water purification? The degradation vs. mineralization of phenolic pollutants. *Catalysis Today* 282, Part 1, 24-30.
- Saien, J., Azizi, A. and Soleymani, A.R. (2014) Optimized photocatalytic conversion of Ni (II) ions with very low titania nanoparticles at different temperatures; kinetics and energy consumption. *Separation and Purification Technology* 134, 187-195.
- Samadi, M., Zirak, M., Naseri, A., Khorashadizade, E. and Moshfegh, A.Z. (2016) Recent progress on doped ZnO nanostructures for visible-light photocatalysis. *Thin Solid Films* 605, 2-19.
- Sangari, M., Umadevi, M., Mayandi, J. and Pinheiro, J.P. (2015) Photocatalytic degradation and antimicrobial applications of F-doped MWCNTs/TiO₂ composites. *Spectrochimica Acta Part A: Molecular and Biomolecular Spectroscopy* 139, 290-295.
- Sasi, S., Rayaroth, M.P., Devadasan, D., Aravind, U.K. and Aravindakumar, C.T. (2015) Influence of inorganic ions and selected emerging contaminants on the degradation of Methylparaben: A sonochemical approach. *Journal of Hazardous Materials* 300, 202-209.
- Sauvé, S. and Desrosiers, M. (2014) A review of what is an emerging contaminant. *Chemistry Central Journal* 8(1), 15.
- Sepulveda-Guzman, S., Reeja-Jayan, B., de la Rosa, E., Torres-Castro, A., Gonzalez-Gonzalez, V. and Jose-Yacaman, M. (2009) Synthesis of assembled ZnO structures by precipitation method in aqueous media. *Materials Chemistry and Physics* 115(1), 172-178.
- Serpone, N., Maruthamuthu, P., Pichat, P., Pelizzetti, E. and Hidaka, H. (1995) Exploiting the interparticle electron transfer process in the photocatalysed oxidation of phenol, 2-chlorophenol and pentachlorophenol: chemical evidence for electron and hole transfer between coupled semiconductors. *Journal of Photochemistry and Photobiology A: Chemistry* 85(3), 247-255.
- Shamsuddin, N., Das, D.B. and Starov, V.M. (2015) Filtration of natural organic matter using ultrafiltration membranes for drinking water purposes: Circular cross-flow compared with stirred dead end flow. *Chemical Engineering Journal* 276, 331-339.
- Shankar, M.V., Anandan, S., Venkatachalam, N., Arabindoo, B. and Murugesan, V. (2004) Novel thin-film reactor for photocatalytic degradation of pesticides in an aqueous solution. *Journal of Chemical Technology & Biotechnology* 79(11), 1279-1285.

- Sharma, G., Kumar, D., Kumar, A., Ala'a, H., Pathania, D., Naushad, M. and Mola, G.T. (2017a) Revolution from monometallic to trimetallic nanoparticle composites, various synthesis methods and their applications: A review. *Materials Science and Engineering: C* 71, 1216-1230.
- Sharma, M., Vaidya, S. and Ganguli, A.K. (2017b) Enhanced photocatalytic activity of gC₃N₄-TiO₂ nanocomposites for degradation of Rhodamine B dye. *Journal of Photochemistry and Photobiology A: Chemistry* 335, 287-293.
- Shayegan, Z., Razzaghi, M., Niaei, A., Salari, D., Tabar, M.T.S. and Akbari, A.N. (2013) Sulfur removal of gas oil using ultrasound-assisted catalytic oxidative process and study of its optimum conditions. *Korean Journal of Chemical Engineering* 30(9), 1751-1759.
- Shemer, H., Kunukcu, Y.K. and Linden, K.G. (2006) Degradation of the pharmaceutical Metronidazole via UV, Fenton and photo-Fenton processes. *Chemosphere* 63(2), 269-276.
- Shen, C., Chen, C., Wen, T., Zhao, Z., Wang, X. and Xu, A. (2015) Superior adsorption capacity of g-C₃N₄ for heavy metal ions from aqueous solutions. *Journal of colloid and interface science* 456, 7-14.
- Shen, M., Zhang, L. and Shi, J. (2018) Converting CO₂ into fuels by graphitic carbon nitride-based photocatalysts. *Nanotechnology* 29(41), 412001.
- Shen, S., Zhao, D., Chen, J., Guo, L. and Mao, S.S. (2016) Enhanced photocatalytic hydrogen evolution over graphitic carbon nitride modified with Ti-activated mesoporous silica. *Applied Catalysis A: General* 521, 111-117.
- Shi, L., Chang, K., Zhang, H., Hai, X., Yang, L., Wang, T. and Ye, J. (2016) Drastic Enhancement of Photocatalytic Activities over Phosphoric Acid Protonated Porous g-C₃N₄ Nanosheets under Visible Light. *Small* 12(32), 4431-4439.
- Shimizu, N., Ogino, C., Dadjour, M.F. and Murata, T. (2007) Sonocatalytic degradation of methylene blue with TiO₂ pellets in water. *Ultrasonics sonochemistry* 14(2), 184-190.
- Sin, J.-C., Lam, S.-M., Lee, K.-T. and Mohamed, A.R. (2013) Degrading two endocrine-disrupting chemicals from water by UV irradiation with the presence of nanophotocatalysts. *Desalination and Water Treatment* 51(16-18), 3505-3520.
- Soltani, R.D.C., Jorfi, S., Ramezani, H. and Purfadakari, S. (2016) Ultrasonically induced ZnO-biosilica nanocomposite for degradation of a textile dye in aqueous phase. *Ultrasonics sonochemistry* 28, 69-78.
- Srimurali, M., Pragathi, A. and Karthikeyan, J. (1998) A study on removal of fluorides from drinking water by adsorption onto low-cost materials. *Environmental pollution* 99(2), 285-289.
- Struzzi, C., Scardamaglia, M., Reckinger, N., Colomer, J.-F., Sezen, H., Amati, M., Gregoratti, L., Snyders, R. and Bittencourt, C. (2017) Fluorination of suspended graphene. *Nano Research* 10(9), 3151-3163.
- Su, T., Deng, H., Benskin, J.P. and Radke, M. (2016) Biodegradation of sulfamethoxazole photo-transformation products in a water/sediment test. *Chemosphere* 148, 518-525.
- Subramonian, W., Wu, T.Y. and Chai, S.-P. (2017) Photocatalytic degradation of industrial pulp and paper mill effluent using synthesized magnetic Fe₂O₃-TiO₂: Treatment efficiency and characterizations of reused photocatalyst. *Journal of Environmental Management* 187, 298-310.
- Sugden, R., Kelly, R. and Davies, S. (2016) Combatting antimicrobial resistance globally. *Nature Microbiology* 1, 16187.

- Taghizadeh, M.T. and Seifi-Aghjekohal, P. (2015) Sonocatalytic degradation of 2-hydroxyethyl cellulose in the presence of some nanoparticles. *Ultrasonics sonochemistry* 26, 265-272.
- Takata, T. and Domen, K. (2009) Defect Engineering of Photocatalysts by Doping of Aliovalent Metal Cations for Efficient Water Splitting. *The Journal of Physical Chemistry C* 113(45), 19386-19388.
- Talebian, N., Nilforoushan, M.R. and Memarnezhad, P. (2012) Photocatalytic activities of multilayered ZnO-based thin films prepared by sol-gel route: effect of SnO₂ heterojunction layer. *Journal of Sol-Gel Science and Technology* 65(2), 178-188.
- Tang, X., Ni, L., Han, J. and Wang, Y. (2017) Preparation and characterization of ternary magnetic g-C₃N₄ composite photocatalysts for removal of tetracycline under visible light. *Chinese Journal of Catalysis* 38(3), 447-457.
- Teixeira, S., Gurke, R., Eckert, H., Kühn, K., Fauler, J. and Cuniberti, G. (2016) Photocatalytic degradation of pharmaceuticals present in conventional treated wastewater by nanoparticle suspensions. *Journal of Environmental Chemical Engineering* 4(1), 287-292.
- Terzić, S., Senta, I., Ahel, M., Gros, M., Petrović, M., Barcelo, D., Müller, J., Knepper, T., Martí, I., Ventura, F., Jovančić, P. and Jabučar, D. (2008) Occurrence and fate of emerging wastewater contaminants in Western Balkan Region. *Science of The Total Environment* 399(1-3), 66-77.
- Tijani, J., Fatoba, O. and Petrik, L.F. (2013) A Review of Pharmaceuticals and Endocrine-Disrupting Compounds: Sources, Effects, Removal, and Detections. *Water, Air, & Soil Pollution* 224(11), 1-29.
- Trovo, A.G., Nogueira, R.F.P., Agüera, A., Fernandez-Alba, A.R. and Malato, S. (2011) Degradation of the antibiotic amoxicillin by photo-Fenton process-chemical and toxicological assessment. *Water research* 45(3), 1394-1402.
- Velegraki, T., Poulios, I., Charalabaki, M., Kalogerakis, N., Samaras, P. and Mantzavinos, D. (2006) Photocatalytic and sonolytic oxidation of acid orange 7 in aqueous solution. *Applied Catalysis B: Environmental* 62(1-2), 159-168.
- Veloutsou, S., Bizani, E. and Fytianos, K. (2014) Photo-Fenton decomposition of β -blockers atenolol and metoprolol; study and optimization of system parameters and identification of intermediates. *Chemosphere* 107, 180-186.
- Vogna, D., Marotta, R., Napolitano, A., Andreozzi, R. and d'Ischia, M. (2004) Advanced oxidation of the pharmaceutical drug diclofenac with UV/H₂O₂ and ozone. *Water Research* 38(2), 414-422.
- Vu, T.T., del Río, L., Valdés-Solís, T. and Marbán, G. (2013) Fabrication of wire mesh-supported ZnO photocatalysts protected against photocorrosion. *Applied Catalysis B: Environmental* 140, 189-198.
- Wang, J., Jiang, Z., Zhang, L., Kang, P., Xie, Y., Lv, Y., Xu, R. and Zhang, X. (2009a) Sonocatalytic degradation of some dyestuffs and comparison of catalytic activities of nano-sized TiO₂, nano-sized ZnO and composite TiO₂/ZnO powders under ultrasonic irradiation. *Ultrasonics sonochemistry* 16(2), 225-231.
- Wang, J., Liu, P., Fu, X., Li, Z., Han, W. and Wang, X. (2009b) Relationship between Oxygen Defects and the Photocatalytic Property of ZnO Nanocrystals in Nafion Membranes. *Langmuir* 25(2), 1218-1223.
- Wang, J., Sun, W., Zhang, Z., Xing, Z., Xu, R., Li, R., Li, Y. and Zhang, X. (2008a) Treatment of nano-sized rutile phase TiO₂ powder under ultrasonic irradiation in hydrogen peroxide solution and investigation of its sonocatalytic activity. *Ultrasonics sonochemistry* 15(4), 301-307.

- Wang, J., Xia, Y., Zhao, H., Wang, G., Xiang, L., Xu, J. and Komarneni, S. (2017) Oxygen defects-mediated Z-scheme charge separation in gC₃N₄/ZnO photocatalysts for enhanced visible-light degradation of 4-chlorophenol and hydrogen evolution. *Applied Catalysis B: Environmental* 206, 406-416.
- Wang, J., Zhuan, R. and Chu, L. (2019) The occurrence, distribution and degradation of antibiotics by ionizing radiation: An overview. *Science of The Total Environment* 646, 1385-1397.
- Wang, N., Chen, Z., Zhu, L., Jiang, X., Lv, B. and Tang, H. (2007) Synergistic effects of cupric and fluoride ions on photocatalytic degradation of phenol. *Journal of photochemistry and photobiology A: chemistry* 191(2), 193-200.
- Wang, Q., Chen, C., Zhao, D., Ma, W. and Zhao, J. (2008b) Change of Adsorption Modes of Dyes on Fluorinated TiO₂ and Its Effect on Photocatalytic Degradation of Dyes under Visible Irradiation. *Langmuir* 24(14), 7338-7345.
- Wang, X., Cai, W., Lin, Y., Wang, G. and Liang, C. (2010a) Mass production of micro/nanostructured porous ZnO plates and their strong structurally enhanced and selective adsorption performance for environmental remediation. *Journal of Materials Chemistry* 20(39), 8582-8590.
- Wang, X. and Lim, T.-T. (2010) Solvothermal synthesis of C–N codoped TiO₂ and photocatalytic evaluation for bisphenol A degradation using a visible-light irradiated LED photoreactor. *Applied Catalysis B: Environmental* 100(1), 355-364.
- Wang, X., Maeda, K., Thomas, A., Takanabe, K., Xin, G., Carlsson, J.M., Domen, K. and Antonietti, M. (2009c) A metal-free polymeric photocatalyst for hydrogen production from water under visible light. *Nature materials* 8(1), 76.
- Wang, Y., Bai, X., Pan, C., He, J. and Zhu, Y. (2012) Enhancement of photocatalytic activity of Bi₂WO₆ hybridized with graphite-like C₃N₄. *Journal of Materials Chemistry* 22(23), 11568-11573.
- Wang, Y., Di, Y., Antonietti, M., Li, H., Chen, X. and Wang, X. (2010b) Excellent visible-light photocatalysis of fluorinated polymeric carbon nitride solids. *Chemistry of Materials* 22(18), 5119-5121.
- Wang, Y. and Hong, C.-S. (2000) TiO₂-mediated photomineralization of 2-chlorobiphenyl: the role of O₂. *Water research* 34(10), 2791-2797.
- Wang, Z.L. (2004) Zinc oxide nanostructures: growth, properties and applications. *Journal of physics: condensed matter* 16(25), R829.
- Watkinson, A.J., Murby, E.J. and Costanzo, S.D. (2007) Removal of antibiotics in conventional and advanced wastewater treatment: Implications for environmental discharge and wastewater recycling. *Water Research* 41(18), 4164-4176.
- Wenhua, L., Hong, L., Sao'an, C., Jianqing, Z. and Chunan, C. (2000) Kinetics of photocatalytic degradation of aniline in water over TiO₂ supported on porous nickel. *Journal of Photochemistry and Photobiology A: Chemistry* 131(1-3), 125-132.
- Willach, S., Lutze, H.V., Eckey, K., Löppenber, K., Lüling, M., Wolbert, J.-B., Kujawinski, D.M., Jochmann, M.A., Karst, U. and Schmidt, T.C. (2018) Direct Photolysis of Sulfamethoxazole Using Various Irradiation Sources and Wavelength Ranges—Insights from Degradation Product Analysis and Compound-Specific Stable Isotope Analysis. *Environmental science & technology* 52(3), 1225-1233.
- Wirunmongkol, T., O-Charoen, N. and Pavasupree, S. (2013) Simple Hydrothermal Preparation of Zinc Oxide Powders Using Thai Autoclave Unit. *Energy Procedia* 34, 801-807.

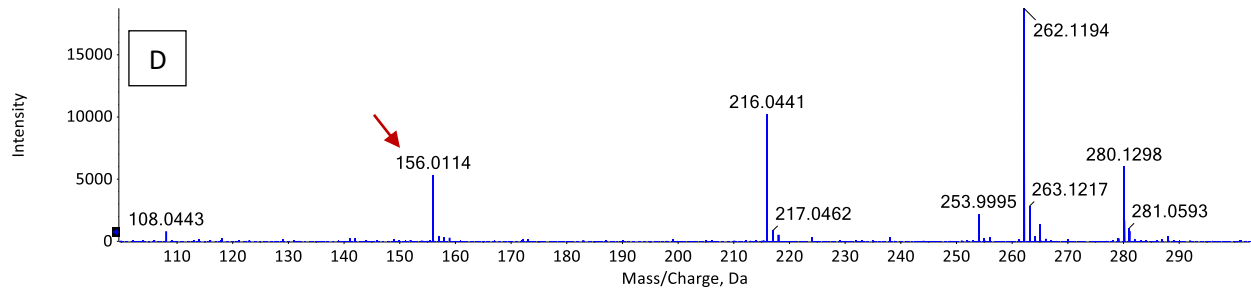
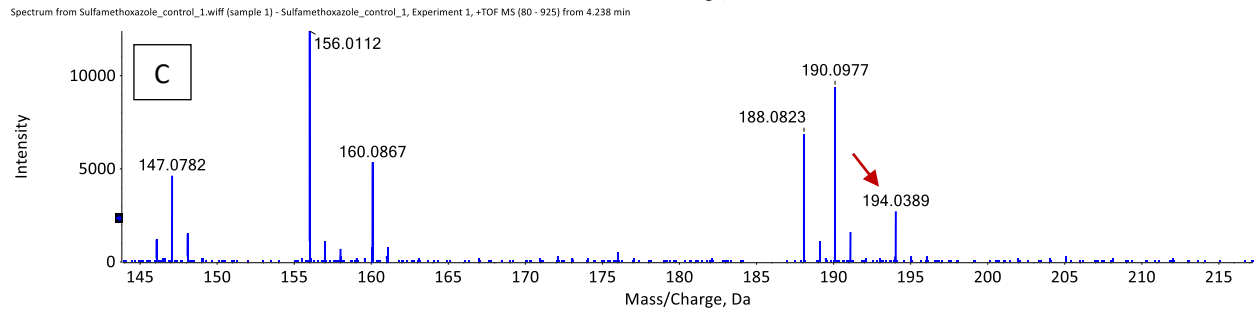
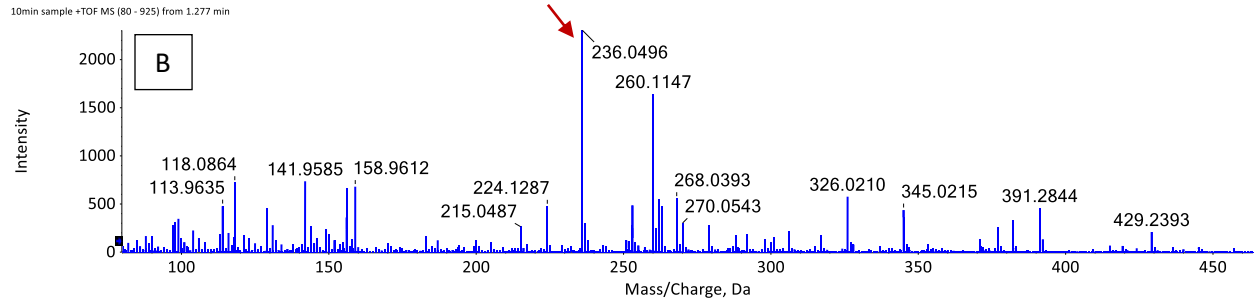
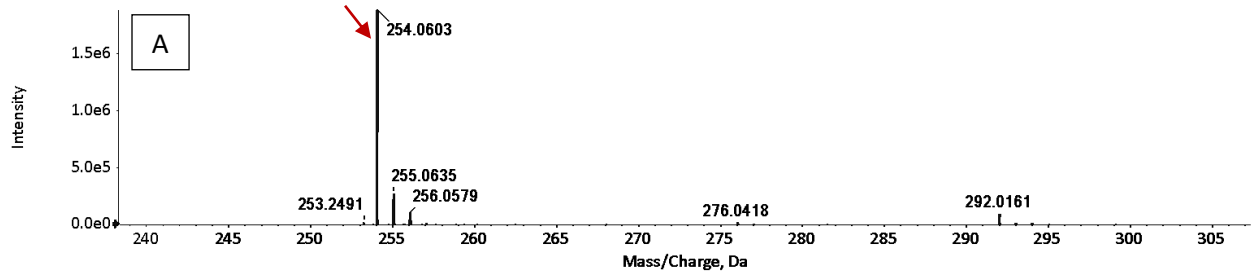
- Wu, C.-H. (2004) Comparison of azo dye degradation efficiency using UV/single semiconductor and UV/coupled semiconductor systems. *Chemosphere* 57(7), 601-608.
- Wu, C. and Huang, Q. (2010) Synthesis of Na-doped ZnO nanowires and their photocatalytic properties. *Journal of Luminescence* 130(11), 2136-2141.
- Wu, C., Liu, X., Wei, D., Fan, J. and Wang, L. (2001) Photosonochemical degradation of Phenol in water. *Water research* 35(16), 3927-3933.
- Wu, L., Lian, J., Sun, G., Kong, X. and Zheng, W. (2009) Synthesis of zinc hydroxyfluoride nanofibers through an ionic liquid assisted microwave irradiation method. *European Journal of Inorganic Chemistry* 2009(20), 2897-2900.
- Xekoukoulotakis, N.P., Drosou, C., Brebou, C., Chatzisyneon, E., Hapeshi, E., Fatta-Kassinos, D. and Mantzavinos, D. (2011) Kinetics of UV-A/TiO₂ photocatalytic degradation and mineralization of the antibiotic sulfamethoxazole in aqueous matrices. *Catalysis Today* 161(1), 163-168.
- Xia, D. and Lo, I.M. (2016) Synthesis of magnetically separable Bi₂O₄/Fe₃O₄ hybrid nanocomposites with enhanced photocatalytic removal of ibuprofen under visible light irradiation. *Water research* 100, 393-404.
- Xia, J., Wang, A., Liu, X. and Su, Z. (2011) Preparation and characterization of bifunctional, Fe₃O₄/ZnO nanocomposites and their use as photocatalysts. *Applied Surface Science* 257(23), 9724-9732.
- Xiao, Y., Song, X., Liu, Z., Li, R., Zhao, X. and Huang, Y. (2017) Photocatalytic removal of cefazolin using Ag₃PO₄/BiOBr under visible light and optimization of parameters by response surface methodology. *Journal of Industrial and Engineering Chemistry* 45, 248-256.
- Xie, M., Wei, W., Jiang, Z., Xu, Y. and Xie, J. (2016) Carbon nitride nanowires/nanofibers: a novel template-free synthesis from a cyanuric chloride-melamine precursor towards enhanced adsorption and visible-light photocatalytic performance. *Ceramics International* 42(3), 4158-4170.
- Xing, M., Qi, D., Zhang, J., Chen, F., Tian, B., Bagwas, S. and Anpo, M. (2012) Super-hydrophobic fluorination mesoporous MCF/TiO₂ composite as a high-performance photocatalyst. *Journal of Catalysis* 294, 37-46.
- Xiong, T., Dong, F. and Wu, Z. (2014) Enhanced extrinsic absorption promotes the visible light photocatalytic activity of wide band-gap (BiO)₂CO₃ hierarchical structure. *RSC Advances* 4(99), 56307-56312.
- Xu, Y., Lv, K., Xiong, Z., Leng, W., Du, W., Liu, D. and Xue, X. (2007) Rate enhancement and rate inhibition of phenol degradation over irradiated anatase and rutile TiO₂ on the addition of NaF: new insight into the mechanism. *The Journal of Physical Chemistry C* 111(51), 19024-19032.
- Yan, C. and Xue, D. (2005) Novel self-assembled MgO nanosheet and its precursors. *The Journal of Physical Chemistry B* 109(25), 12358-12361.
- Yan, S., Li, Z. and Zou, Z. (2009) Photodegradation performance of g-C₃N₄ fabricated by directly heating melamine. *Langmuir* 25(17), 10397-10401.
- Yang, C.-C., Huang, C.-L., Cheng, T.-C. and Lai, H.-T. (2015) Inhibitory effect of salinity on the photocatalytic degradation of three sulfonamide antibiotics. *International Biodeterioration & Biodegradation* 102, 116-125.
- Yang, C., You, X., Cheng, J., Zheng, H. and Chen, Y. (2017a) A novel visible-light-driven In-based MOF/graphene oxide composite photocatalyst with enhanced photocatalytic activity toward the degradation of amoxicillin. *Applied Catalysis B: Environmental* 200, 673-680.

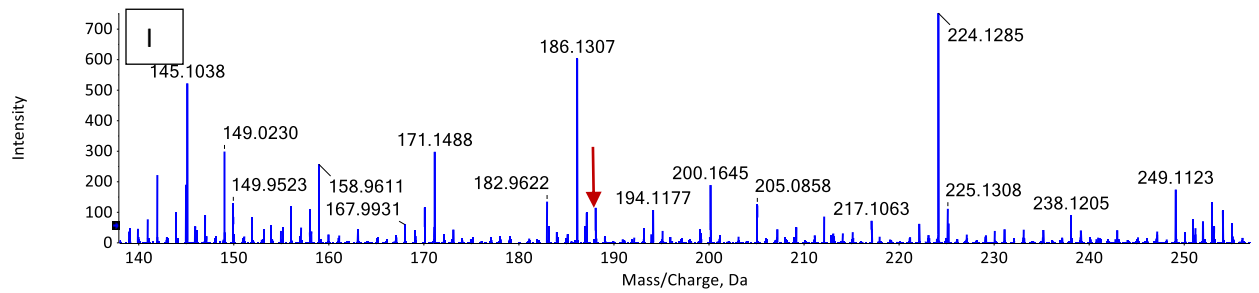
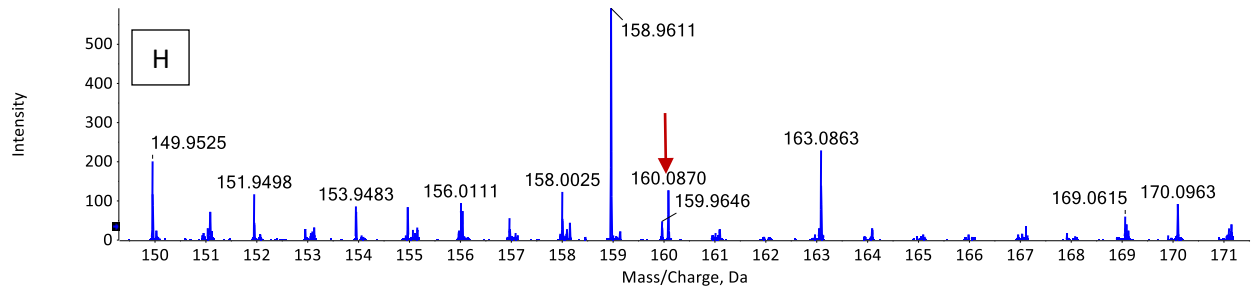
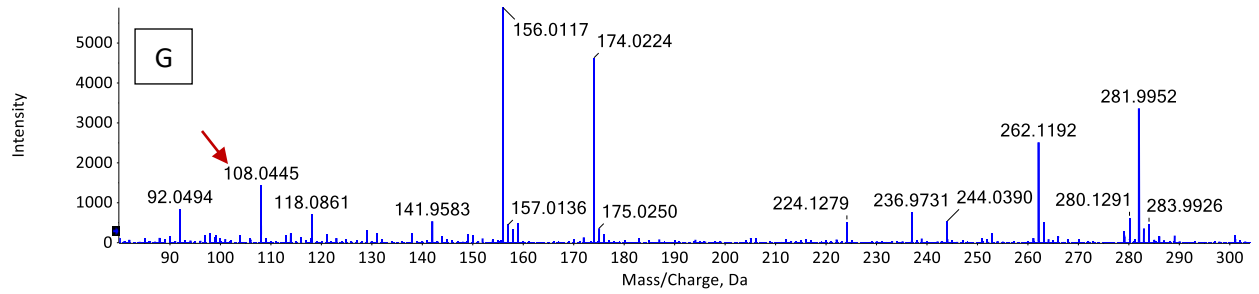
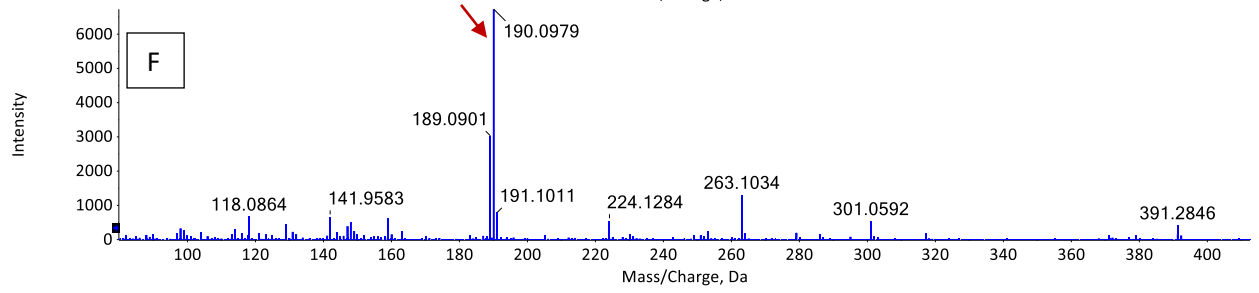
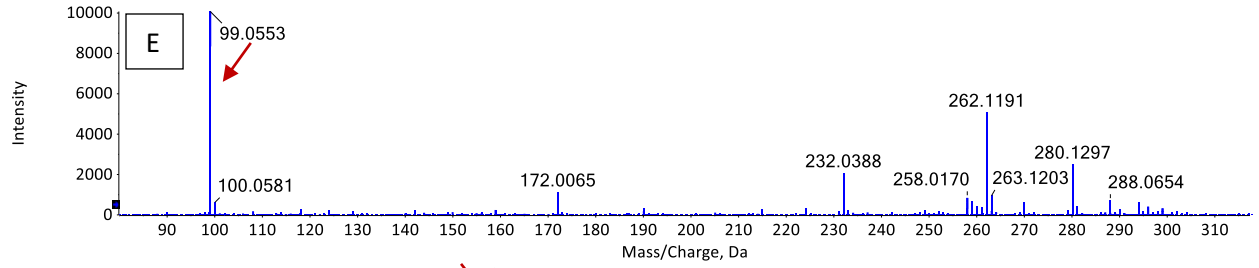
- Yang, H., Teng, F., Gu, W., Liu, Z., Zhao, Y., Zhang, A., Liu, Z. and Teng, Y. (2017b) A simple post-synthesis conversion approach to Zn(OH)F and the effects of fluorine and hydroxyl on the photodegradation properties of dye wastewater. *Journal of Hazardous Materials* 333, 250-258.
- Yin, L., Gao, J., Wang, J., Wang, B., Jiang, R., Li, K., Li, Y. and Zhang, X. (2011) Enhancement of sonocatalytic performance of TiO₂ by coating Er³⁺:YAlO₃ in azo dye degradation. *Separation and Purification Technology* 81(1), 94-100.
- Yu, C., Yang, K., Xie, Y., Fan, Q., Yu, J.C., Shu, Q. and Wang, C. (2013) Novel hollow Pt-ZnO nanocomposite microspheres with hierarchical structure and enhanced photocatalytic activity and stability. *Nanoscale* 5(5), 2142-2151.
- Yu, J., Liu, W. and Yu, H. (2008) A One-Pot Approach to Hierarchically Nanoporous Titania Hollow Microspheres with High Photocatalytic Activity. *Crystal Growth & Design* 8(3), 930-934.
- Yu, J., Wang, W., Cheng, B. and Su, B.-L. (2009) Enhancement of Photocatalytic Activity of Mesoporous TiO₂ Powders by Hydrothermal Surface Fluorination Treatment. *The Journal of Physical Chemistry C* 113(16), 6743-6750.
- Yu, J.C., Wang, X. and Fu, X. (2004) Pore-Wall Chemistry and Photocatalytic Activity of Mesoporous Titania Molecular Sieve Films. *Chemistry of Materials* 16(8), 1523-1530.
- Yu, J.C., Yu, J., Ho, W., Jiang, Z. and Zhang, L. (2002) Effects of F-doping on the photocatalytic activity and microstructures of nanocrystalline TiO₂ powders. *Chemistry of materials* 14(9), 3808-3816.
- Yu, W., Zhang, J. and Peng, T. (2016) New insight into the enhanced photocatalytic activity of N-, C- and S-doped ZnO photocatalysts. *Applied Catalysis B: Environmental* 181, 220-227.
- Yuan, S., Gou, N., Alshwabkeh, A.N. and Gu, A.Z. (2013) Efficient degradation of contaminants of emerging concerns by a new electro-Fenton process with Ti/MMO cathode. *Chemosphere* 93(11), 2796-2804.
- Zanella, R., Avella, E., Ramírez-Zamora, R.M., Castellón-Barraza, F. and Durán-Álvarez, J.C. (2017) Enhanced photocatalytic degradation of sulfamethoxazole by deposition of Au, Ag and Cu metallic nanoparticles on TiO₂. *Environmental technology*, 1-12.
- Zha, J., Ali, S.S., Peyroux, J., Batisse, N., Claves, D., Dubois, M., Kharitonov, A.P., Monier, G., Darmanin, T. and Guittard, F. (2017) Superhydrophobicity of polymer films via fluorine atoms covalent attachment and surface nano-texturing. *Journal of Fluorine Chemistry* 200, 123-132.
- Zhang, D., Wang, Q., Wang, L. and Zhang, L. (2015) Magnetically separable CdFe₂O₄/graphene catalyst and its enhanced photocatalytic properties. *Journal of Materials Chemistry A* 3(7), 3576-3585.
- Zhang, H., Zong, R. and Zhu, Y. (2009a) Photocorrosion inhibition and photoactivity enhancement for zinc oxide via hybridization with monolayer polyaniline. *The Journal of Physical Chemistry C* 113(11), 4605-4611.
- Zhang, L., Cheng, H., Zong, R. and Zhu, Y. (2009b) Photocorrosion suppression of ZnO nanoparticles via hybridization with graphite-like carbon and enhanced photocatalytic activity. *The Journal of Physical Chemistry C* 113(6), 2368-2374.
- Zhang, L., He, X., Xu, X., Liu, C., Duan, Y., Hou, L., Zhou, Q., Ma, C., Yang, X. and Liu, R. (2017a) Highly active TiO₂/gC₃N₄/G photocatalyst with extended spectral response towards selective reduction of nitrobenzene. *Applied Catalysis B: Environmental* 203, 1-8.
- Zhang, L., Qi, H., Yan, Z., Gu, Y., Sun, W. and Zewde, A.A. (2017b) Sonophotocatalytic inactivation of *E. coli* using ZnO nanofluids and its mechanism. *Ultrasonics sonochemistry* 34, 232-238.

- Zhang, M., Liu, Y.-S., Zhao, J.-L., Liu, W.-R., He, L.-Y., Zhang, J.-N., Chen, J., He, L.-K., Zhang, Q.-Q. and Ying, G.-G. (2018) Occurrence, fate and mass loadings of antibiotics in two swine wastewater treatment systems. *Science of The Total Environment* 639, 1421-1431.
- Zhang, S., Li, J., Wang, X., Huang, Y., Zeng, M. and Xu, J. (2014) In situ ion exchange synthesis of strongly coupled Ag@ AgCl/g-C₃N₄ porous nanosheets as plasmonic photocatalyst for highly efficient visible-light photocatalysis. *ACS applied materials & interfaces* 6(24), 22116-22125.
- Zhang, S., Li, J., Zeng, M., Zhao, G., Xu, J., Hu, W. and Wang, X. (2013) In Situ Synthesis of Water-Soluble Magnetic Graphitic Carbon Nitride Photocatalyst and Its Synergistic Catalytic Performance. *ACS applied materials & interfaces* 5(23), 12735-12743.
- Zhao, L., Xia, M., Liu, Y., Zheng, B., Jiang, Q. and Lian, J. (2012) Structure and Photocatalysis of TiO₂/ZnO Double-Layer Film Prepared by Pulsed Laser Deposition. *MATERIALS TRANSACTIONS* 53(3), 463-468.
- Zhao, Y., Ma, J., Liu, J. and Bao, Y. (2017) Synthesis of fireworks-shaped ZnO/graphite-like carbon nanowires with enhanced visible-light photocatalytic activity and anti-photocorrosion. *Colloids and Surfaces A: Physicochemical and Engineering Aspects* 518, 57-63.
- Zhao, Y., Zhao, F., Wang, X., Xu, C., Zhang, Z., Shi, G. and Qu, L. (2014) Graphitic carbon nitride nanoribbons: graphene-assisted formation and synergic function for highly efficient hydrogen evolution. *Angewandte Chemie International Edition* 53(50), 13934-13939.
- Zhong, L.S., Hu, J.S., Liang, H.P., Cao, A.M., Song, W.G. and Wan, L.J. (2006) Self-Assembled 3D flowerlike iron oxide nanostructures and their application in water treatment. *Advanced Materials* 18(18), 2426-2431.
- Zhou, L.-J., Ying, G.-G., Liu, S., Zhao, J.-L., Yang, B., Chen, Z.-F. and Lai, H.-J. (2013a) Occurrence and fate of eleven classes of antibiotics in two typical wastewater treatment plants in South China. *Science of The Total Environment* 452-453, 365-376.
- Zhou, L., Zhang, W., Chen, L. and Deng, H. (2017) Z-scheme mechanism of photogenerated carriers for hybrid photocatalyst Ag₃PO₄/g-C₃N₄ in degradation of sulfamethoxazole. *Journal of Colloid and Interface Science* 487, 410-417.
- Zhou, X., Jin, B., Chen, R., Peng, F. and Fang, Y. (2013b) Synthesis of porous Fe₃O₄/g-C₃N₄ nanospheres as highly efficient and recyclable photocatalysts. *Materials Research Bulletin* 48(4), 1447-1452.
- Zhu, B., Xia, P., Ho, W. and Yu, J. (2015) Isoelectric point and adsorption activity of porous g-C₃N₄. *Applied Surface Science* 344, 188-195.
- Zhu, D., Liu, S., Chen, M., Zhang, J. and Wang, X. (2018) Flower-like-flake Fe₃O₄/g-C₃N₄ nanocomposite: Facile synthesis, characterization, and enhanced photocatalytic performance. *Colloids and Surfaces A: Physicochemical and Engineering Aspects* 537, 372-382.
- Zhu, L., Zheng, Y., Hao, T., Shi, X., Chen, Y. and Ou-Yang, J. (2009) Synthesis of hierarchical ZnO nanobelts via Zn (OH) F intermediate using ionic liquid-assistant microwave irradiation method. *Materials Letters* 63(28), 2405-2408.
- Zhu, Y.-P., Li, M., Liu, Y.-L., Ren, T.-Z. and Yuan, Z.-Y. (2014) Carbon-doped ZnO hybridized homogeneously with graphitic carbon nitride nanocomposites for photocatalysis. *The Journal of Physical Chemistry C* 118(20), 10963-10971.
- Zhu, Z., Yu, Y., Dong, H., Liu, Z., Li, C., Huo, P. and Yan, Y. (2017) Intercalation Effect of Attapulgite in g-C₃N₄ Modified with Fe₃O₄ Quantum Dots To Enhance Photocatalytic Activity for Removing 2-Mercaptobenzothiazole under Visible Light. *ACS Sustainable Chemistry & Engineering* 5(11), 10614-10623.

- Ziylan-Yavaş, A. and Ince, N.H. (2016) Enhanced photo-degradation of paracetamol on n-platinum-loaded TiO₂: The effect of ultrasound and OH/hole scavengers. *Chemosphere* 162, 324-332.
- Zou, T., Wang, C., Tan, R., Song, W. and Cheng, Y. (2017a) Preparation of pompon-like ZnO-PANI heterostructure and its applications for the treatment of typical water pollutants under visible light. *Journal of hazardous materials*.
- Zou, Y., Shi, J.-W., Ma, D., Fan, Z., Lu, L. and Niu, C. (2017b) In situ synthesis of C-doped TiO₂@gC₃N₄ core-shell hollow nanospheres with enhanced visible-light photocatalytic activity for H₂ evolution. *Chemical Engineering Journal* 322, 435-444.

Appendix A: Extracted ion chromatograms of SMX and its by-products





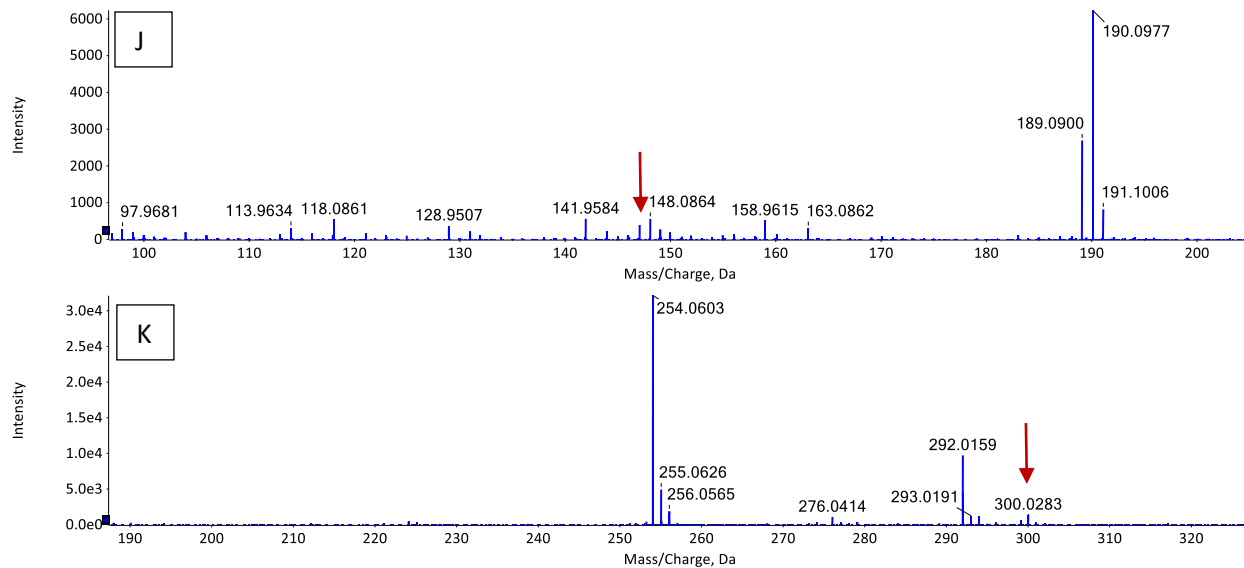


Fig. S1. Extracted ion chromatograms (XICs) of: (A) Sulfamethoxazole, (B) DP236, (C) DP194, (D) DP156, (E) DP99, (F) DP190, (G) DP108, (H) DP160, (I) DP188, (J) DP147, (K) DP300